Research Topics

Quantum dots for biological applications, volume II

Edited by
Md Palashuddin Sk, Gopinath Packirisamy, Krishna Misra,
Sameer Hussain and Mohammad Tariq

Published in
Frontiers in Bioengineering and Biotechnology
Frontiers in Molecular Biosciences

ISSN 1664-8714
ISBN 978-2-8325-4668-0
DOI 10.3389/978-2-8325-4668-0

About Frontiers

Frontiers is more than just an open access publisher of scholarly articles: it is a pioneering approach to the world of academia, radically improving the way scholarly research is managed. The grand vision of Frontiers is a world where all people have an equal opportunity to seek, share and generate knowledge. Frontiers provides immediate and permanent online open access to all its publications, but this alone is not enough to realize our grand goals.

Frontiers journal series

The Frontiers journal series is a multi-tier and interdisciplinary set of open-access, online journals, promising a paradigm shift from the current review, selection and dissemination processes in academic publishing. All Frontiers journals are driven by researchers for researchers; therefore, they constitute a service to the scholarly community. At the same time, the *Frontiers journal series* operates on a revolutionary invention, the tiered publishing system, initially addressing specific communities of scholars, and gradually climbing up to broader public understanding, thus serving the interests of the lay society, too.

Dedication to quality

Each Frontiers article is a landmark of the highest quality, thanks to genuinely collaborative interactions between authors and review editors, who include some of the world's best academicians. Research must be certified by peers before entering a stream of knowledge that may eventually reach the public - and shape society; therefore, Frontiers only applies the most rigorous and unbiased reviews. Frontiers revolutionizes research publishing by freely delivering the most outstanding research, evaluated with no bias from both the academic and social point of view. By applying the most advanced information technologies, Frontiers is catapulting scholarly publishing into a new generation.

What are Frontiers Research Topics?

Frontiers Research Topics are very popular trademarks of the *Frontiers journals series*: they are collections of at least ten articles, all centered on a particular subject. With their unique mix of varied contributions from Original Research to Review Articles, Frontiers Research Topics unify the most influential researchers, the latest key findings and historical advances in a hot research area.

Find out more on how to host your own Frontiers Research Topic or contribute to one as an author by contacting the Frontiers editorial office: frontiersin.org/about/contact

Quantum dots for biological applications, volume II

Topic editors
Md Palashuddin Sk — Aligarh Muslim University, India
Gopinath Packirisamy — Indian Institute of Technology Roorkee, India
Krishna Misra — Indian Institute of Information Technology, Allahabad, India
Sameer Hussain — Xi'an Jiaotong University, China
Mohammad Tariq — NOVA University of Lisbon, Portugal

Citation
Palashuddin Sk, M., Packirisamy, G., Misra, K., Hussain, S., Tariq, M., eds. (2024).
Quantum dots for biological applications, volume II. Lausanne: Frontiers Media SA.
doi: 10.3389/978-2-8325-4668-0

Table of contents

Frontiers in Bioengineering and Biotechnology

TYPE Editorial
PUBLISHED 13 March 2024
DOI 10.3389/fbioe.2024.1389974

Editorial: Quantum dots for biological applications, volume II

Sameer Hussain[1]*, Gopinath Packirisamy[2], Krishna Misra[3], Mohammad Tariq[4] and Md Palashuddin Sk[5]*

[1]School of Chemistry, Xi'an Jiaotong University, Xi'an, China, [2]Nanobiotechnology Laboratory, Department of Biosciences and Bioengineering, Indian Institute of Technology Roorkee, Roorkee, India, [3]Department of Applied Science, Indian Institute of Information Technology, Allahabad, India, [4]LAQV, REQUIMTE, Departamento de Química, Faculdade de Ciências e Tecnologia, Universidade NOVA de Lisboa, Caparica, Portugal, [5]Department of Chemistry, Aligarh Muslim University, Aligarh, India

OPEN ACCESS

EDITED AND REVIEWED BY
Gianni Ciofani,
Italian Institute of Technology (IIT), Italy

*CORRESPONDENCE
Sameer Hussain,
✉ sameer@xjtu.edu.cn
Md Palashuddin Sk,
✉ palashuddin.ch@amu.ac.in

RECEIVED 22 February 2024
ACCEPTED 04 March 2024
PUBLISHED 13 March 2024

CITATION
Hussain S, Packirisamy G, Misra K, Tariq M and Sk MP (2024), Editorial: Quantum dots for biological applications, volume II.
Front. Bioeng. Biotechnol. 12:1389974.
doi: 10.3389/fbioe.2024.1389974

KEYWORDS

quantum dots (QDs), carbon dots (Cdots), Se QDs, biosensing, bioimaging, healthcare, therapy

Editorial on the Research Topic
Quantum dots for biological applications, volume II

The use of quantum dots (QDs) which are nanomaterials typically measuring just a few nanometers in size, has revolutionized various research fields over the past decade including bioimaging and therapy. Fascinatingly, the Nobel Prize in Chemistry (2023) is also awarded for the discovery and development of QDs. QDs possess exceptional properties such as remarkable photostability, sensible fluorescence quantum yield (Φ) and a narrow emission band. As a result, they have become preferred over traditional organic fluorophores for a multitude of biological and biomedical applications. Two conventional techniques employed for the preparation of QDs are the bottom-up method and the top-down approach. Furthermore, QDs can be modified with specific ligands known as receptors for targeted applications. In recent years, QDs have showcased immense potential in sensing, imaging, drug delivery, tracking, and phototherapy. Despite various features, the toxicity of most QDs remains a significant challenge for researchers in this field. Therefore, the quest for biocompatible, less-toxic, and brightly luminescent QDs for use in biological systems is a captivating area of research.

This Research Topic aims to highlight and gather the state-of-the art advancements in the synthesis and biomedical applications of QDs. Consequently, researchers were invited to contribute studies focusing on new synthetic procedures, particularly sustainable and greener techniques, and explore their applications in biomedicine. Our Research Topic includes six original research articles, two full review papers, and one minireview, which delve into the synthesis of QDs for various biological applications, and provide insights into emerging trends. Subsequent section provideds a brief overview of the Articles and Review papers covered in the current Research Topic.

Alcoholic gastric ulcer (AGU) is a prevalent and severe gastrointestinal condition. The investigation into the anti-gastric ulcer properties of nanoparticles within the realm of nanomaterials has garnered significant attention from researchers. Kong et al. recently isolated carbon dots (Cdots) designated as FP-CDs, from aqueous extracts of *Fuligo Plantae* and evaluated their therapeutic potential against alcohol-induced gastric ulcer. This was achieved by examining macroscopic images and pathological alterations in gastric tissue, as well as measuring levels of inflammatory and oxidative stress markers. The study not only presents a new approach for exploring the active material component of *Fuligo Plantae*, but also establishes an initial groundwork for the potential clinical use of FP-CDs in treating alcoholic gastric ulcer. In their exciting research, Zhao et al. and co-workers successfully extracted a new type of fluorescent Cdots knows as CMRC-CDs, from *Chrysanthemum morifolium Ramat Carbonisata* using an environmentally friendly method. In murine models, CMRC-CDs were found to alleviate anxiety-like behavior induced by *m*-chlorophenylpiperazine (mCPP) in a dose-dependent manner and demonstrated promising anxiolytic properties. The findings of this study provide valuable insights into how Cdots obtained from traditional herbs could potentially be used to develop innovative, more effective, and safer therapies for anxiety disorders.

Ulcerative colitis (UC) is a bowel disease marked by persistent and progressive inflammation of the intestines. Zhao et al. successfully obtained Cdots, termed as SCR-CDs, from scrambled *Coptidis Rhizoma* using an innovative method. To assess the protective effects against UC, SCR-CDs were tested in a widely accepted mouse model induced by dextran sulfate sodium. The study demonstrated that SCR-CDs, with their diverse surface functional groups, exhibited hygroscopic capacity and hemostatic bioactivity, effectively alleviating key symptoms of UC, particularly bloody diarrhea. This study provides innovative perspectives on how pure plants can be carbonized to prepare Cdots, offering new insights. Furthermore, it holds significant potential in enhancing therapeutic strategies for ulcerative colitis.

Many natural compounds, including naringin, have poor bioavailability due to their low water solubility. Recently, Qu et al. and colleagues acquired Cdots (AFI-CDs) derived from *Aurantia Fructus Immatures*, which demonstrated an impressive solubilization effect, increasing the solubility of naringin by a factor of 216.72. This study provides fundamental insights into the solubilization mechanism of naringin using AFI-CDs, offering a new approach to address the difficulties linked with the low water solubility of drugs that are insoluble in water in the field of modern pharmaceutical science.

Liver fibrosis is a transitional phase in the advancement of liver disease, and currently, there is no recognized clinical therapy available for effective treatment of fibrosis. In their subsequent research, Qu et al. and colleagues acquired biocompatible Cdots (VSC-CDs) from *Vaccaria Semen Carbonisatum* using a one-step pyrolysis technique. Spherical shaped and negatively charged VSC-CDs exhibit a quantum yield of ~2.08%, with diameters in the range 1–5.5 nm. VSC-CDs, possessing ample chemical functional groups and excellent water dispersibility, not only improved liver function and mitigated liver damage in pathomorphology but also reduced the severity of liver fibrosis. The results of this study offer potential for the advancement of a new, eco-friendly, and efficient nanomedicine, providing a promising therapeutic approach for attenuating liver fibrosis in clinical settings.

The lack of vitamin D is linked to a range of conditions including osteoporosis, obesity, depression, digestive Research Topic, and infections. Consequently, it has become a subject of sinificant interest in the field of healthcare. Yue et al. developed a fluorescence immunochromatographic assay based on ZnCdSe/ZnS QDs for the prompt, visual and quantitative detection of 25-hydroxyvitamins D (25-OF VD) in human serum. The assay demonstrated good selectivity and a linear detection range of 5–100 ng/mL for 25-OH VD in phosphate buffer saline. This study represents a pioneering application of QDs for fast, visual and quantitative identification of 25-OH VD, holding significant promise for the clinical diagnosis of diseases linked to vitamin D.

Despite substantial advancements in research, cancer continues to be a highly fatal disease on a globe scale. The Review paper published by Omer et al. in this Research Topic magnificently summarizes the recent advancements in the usage of group-11 (Cu, Ag and Au) Cdots regarding their potential for early cancer diagnosis and therapy, which includes their nanohybrids, nanocomposites, heterostructures, and more. It specicially emphasizes the role of Cu-, Ag-, and Au-doped Cdots as nanotheranostic agents for cancer treatment in terms of imaging applications (e.g., fluoresecnce, photoacoustic, magnetic resonance imaging) and therapeutic applications (e.g., photodynamic, photothermal, multimodal). Based on extensive research, it is believed that Ag-, Cu- and Au-doped-Cdots are new emerging class of C-based fluorescent nanomaterials for cancer theranostics.

Mondal et al. highlighted the wide-ranging applications of Cdots in their Review paper, including bioimaging, gene therapy, phototherapy, medication delivery, and more. The initial section of the paper discussed various synthetic techniques, as well as the structure and properties of Cdots. The subsequent sections focused on recent advancements, future prospects, and multiple applications of Cdots and their composites, as well as hetero-atom-doped modifications, specifically in the field of bioimaging and therapy.

Selenium quantum dots (Se QDs) is a new type of fluorescent nanomaterial that provide various advantages including ultra-small particle size, distinct optical/surface properties, and low-toxicity. Consequently, Se QDs have become a promising player in the realm of non-metallic luminescent QDs, making them highly suitable for a wide range of biological applications. The sole Minireview published by Li Zhou et al. on this Research Topic elegantly summarizes preparation of various fluorescent Se QDs for biomedical applications such as detection of biomolecules, cell/tissue imaging and therapy. The review also discusses the existing challenges and future prospects of Se QDs in the domain of biosensing and bioimaging.

In summary, this Research Topic offers recent updates on biocompatible QDs derived from various plant sources using greener synthetic methods, highlighting their potential for diverse biomedical applications. These applications encompass the treatment of alcohol-induced gastric ulcers, anxiety disorders, ulcerative colitis, liver fibrosis, and diseases associated with vitamin D. The Review papers collected on this Research Topic also revealed that QDs represents a promising class of nanomaterials in the field of healthcare. Indeed, Se QDs has garnered substantial attention as an emerging type of fluorescent QDs in recent years. However, their low photostability when continuously exposed to excitation light poses a significant challenge and can greatly impact their fluorescence properties. Addressing this Research Topic remains a crucial and ongoing task in the field. Additionally, the challenges of cost-effective synthesis and large-scale industrial production of QDs are also significant hurdles that need to be addressed in the near future. Besides, the primary challenge for biomedical scientists persists in the form of the low toxicity and inadequate biocompatibility of most QDs. These limitations curtail the potential applications of QDs in biomedicine. Furthermore, the limited capability of numerous QDs to penetrate the blood-brain barrier poses a significant obstacle to their use in targeting brain tumors. Therefore, further research is warranted on the preparation of QDs with reasonable biocompatibility, good photostability, easy synthetic methods, and the ability to penetrate cells.

Author contributions

SH: Writing–original draft, Writing–review and editing. GP: Writing–review and editing. KM: Writing–review and editing. MT: Writing–review and editing. MPS: Writing–original draft, Writing–review and editing, Conceptualization, Project administration, Supervision.

Funding

The author(s) declare that no financial support was received for the research, authorship, and/or publication of this article.

Conflict of interest

The authors declare that the research was conducted in the absence of any commercial or financial relationships that could be construed as a potential conflict of interest.

The author(s) declared that they were an editorial board member of Frontiers, at the time of submission. This had no impact on the peer review process and the final decision.

Publisher's note

Frontiers in Molecular Biosciences

TYPE Original Research
PUBLISHED 07 July 2023
DOI 10.3389/fmolb.2023.1223621

OPEN ACCESS

EDITED BY
Gopinath Packirisamy,
Indian Institute of Technology Roorkee,
India

REVIEWED BY
Madhuri Sharon,
Walchand Centre for Research in
Nanotechnology and
Bionanotechnology, India
Mingzhen Zhang,
Xi'an Jiaotong University, China

*CORRESPONDENCE
Huihua Qu,
quhuihuadr@163.com
Hui Kong,
doris7629@126.com

†These authors have contributed equally to this work

RECEIVED 16 May 2023
ACCEPTED 29 June 2023
PUBLISHED 07 July 2023

CITATION
Zhao Y, Cheng G, Gao Y, Cui L, Zhao Y, Zhang Y, Tian Y, Zhao Y, Zhang Y, Qu H and Kong H (2023), Green synthetic natural carbon dots derived from *Fuligo Plantae* with inhibitory effect against alcoholic gastric ulcer.
Front. Mol. Biosci. 10:1223621.
doi: 10.3389/fmolb.2023.1223621

Green synthetic natural carbon dots derived from *Fuligo Plantae* with inhibitory effect against alcoholic gastric ulcer

Yusheng Zhao[1†], Guoliang Cheng[1†], Yushan Gao[1], Luming Cui[1], Yafang Zhao[1], Yifan Zhang[1], Yu Tian[1], Yan Zhao[1], Yue Zhang[2], Huihua Qu[3]* and Hui Kong[1]*

[1]School of Traditional Chinese Medicine, Beijing University of Chinese Medicine, Beijing, China, [2]School of Life Sciences, Beijing University of Chinese Medicine, Beijing, China, [3]Centre of Scientific Experiment, Beijing University of Chinese Medicine, Beijing, China

Introduction: *Fuligo Plantae* (FP), the ash that sticks to the bottom of pots or chimneys after weeds burn, has long been used for its hemostatic effects and treatment of gastrointestinal bleeding. Nevertheless, the active ingredient of FP still needs to be further explored.

Methods: The microstructure, optical and chemical properties of FP-CDs were characterized. An alcohol-induced gastric ulcer model was utilized to evaluate whether pre-administration of FP-CDs alleviated gastric bleeding symptoms and ameliorated gastric mucosal barrier disruption. In addition, the feces of each group of rats were extracted for 16S rDNA genome sequencing of intestinal flora.

Results: FP-CDs with a diameter ranging from 1.4–3.2 nm had abundant chemical groups, which may be beneficial to the exertion of inherent activity. FP-CDs alleviated alcohol-induced gastric ulcer, as demonstrated by activating the extrinsic coagulation pathway, alleviating inflammation, and suppressing oxidative stress levels. More interestingly, FP-CDs can improve the diversity and dysbiosis of intestinal flora in rats with alcohol-induced gastric ulcer.

Conclusion: These comes about illustrate the momentous inhibitory effects of FP-CDs on alcoholic gastric ulcer in rats, which give a modern methodology for investigating the effective ingredient of FP, and lay an experimental basis for the application of FP-CDs in the clinical treatment of alcoholic gastric ulcer.

KEYWORDS

***Fuligo Plantae*, carbon dots, alcoholic gastric ulcer, hemostasis, antiinflammatory, antioxidant, intestinal flora**

1 Introduction

Alcoholic gastric ulcer (AGU) is a common intense gastrointestinal disease. Oral intake of a large amount of alcohol will directly damage the gastric mucosa epithelial cells and destroy the gastric mucosal barrier, thereby causing acute gastric mucosal congestion, erosion, and even superficial ulcers (Liu et al., 2021; Ren et al., 2021). With the change of lifestyle, the incidence of alcohol-related diseases is increasing year by year. Epidemiological surveys have found that the probability of gastrointestinal diseases in people who drink is much higher than those who do not drink (Sumbul et al., 2011). Alcohol is one of the direct factors of acute gastric ulcer, which makes the research on the avoidance and treatment of alcohol-induced gastric ulcer and its mechanism a hot spot in gastric health research.

AGU is a heterogeneous disease with high incidence and complex etiology. Commonly used clinical drugs include histamine receptor antagonists, cytoprotective agents, antibiotics, proton pump inhibitors and prostaglandins analogs, but these treatment methods will produce adverse effects side effects, and have the disadvantages of easy recurrence and long course of treatment (Rickard, 2016; Maes et al., 2017; Rahman et al., 2021). Therefore, there is an urgent need for a more secure and lower-cost medicate to treat AGU. In this regard, the research on the anti-gastric ulcer activity of nanoparticles in the field of nanomaterials has attracted many scholars and showed good therapeutic effects.

As a novel type of carbon-based nanomaterials, carbon dots (CDs) with unique advantages such as predominant photoluminescence (Zhao et al., 2021), good biocompatibility (Cui et al., 2021), tunable chemical properties (Lin et al., 2017), and excellent water dispersibility (Vinoth Kumar et al., 2021) have attracted widespread attention in many fields, including bioimaging (Ansari et al., 2021), drug delivery (Chen et al., 2021) and cancer therapy (Nocito et al., 2021). Due to their significant advantages, the biological activities of CDs in medicine, including anti-tumor (Zhang W. et al., 2021), bacteriostatic (Wang et al., 2020), anti-viral (Tong et al., 2020), anti-inflammatory (Hu et al., 2021), immune regulation (Zhang M. et al., 2021), hemostasis (Yan et al., 2017), analgesia (Zhang et al., 2020), have been confirmed by various scientific experiments, which opens entirely novel drugs for the discovery of effective remission or cure of certain clinical diseases.

Fuligo Plantae (FP), named Zao-xia-hui in Chinese, is the ash that weeds attach to the bottom of the pot or chimney after burning, and has a long-time medicinal history. It is the finished product by gently scraping the ash from the bottom of the pot or chimney and sifting out impurities. Ancient Chinese classic medical books documented that FP can be utilized to treat diverse symptoms, such as hemorrhage, inflammation, food accumulation and jaundice. After observing that FP has a wide range of civil applications, we have extensive interest in whether it has a certain effect and its unexplained underlying mechanism. Interestingly, it is found that the high-temperature carbonization strategy of FP is exceptionally comparable to the one-step pyrolysis strategy to get ready CDs. Recently, we discovered the CDs from aqueous extracts of FPs by modern instruments including transmission electron microscopy and optical instruments, and used a series of strategies to extract FP-CDs. Therefore, it is speculated that FP-CDs with electron exchange capacity and diverse functional groups may be the effective ingredients within the treatment of bleeding gastric ulcer disease.

Herein, an alcohol-induced gastric ulcer model was used to evaluate whether pre-administration of FP-CDs ameliorated gastric mucosal barrier disruption and alleviated gastric bleeding symptoms. The therapeutic effect of FP-CDs was assessed by observing macroscopic images and pathological changes of gastric tissue, measuring the levels of inflammatory indicators and oxidative stress indicators, and further exploring the impact on the intestinal flora.

2 Materials and methods

2.1 Materials

Alcohol and chloral hydrate were purchased from Beijing Solarbio Science & Technology Co., Ltd. (Beijing, China). Dulbecco's Modified Eagle Medium (DMEM) and foetal bovine serum (FBS) were purchased from Corning Co., Ltd. (New York, United States). Cell counting kit-8 (CCK-8), tumour necrosis factor-α (TNF-α), interleukin (IL)-6 and IL-1β were brought from Beijing Bairuiji Biotechnology Co., Ltd. (Beijing, China). Alanine transaminase (ALT), aspartate aminotransferase (AST), Malondialdehyde (MDA), superoxide dismutase (SOD) and glutathione (GSH) kits were purchased from Nanjing Jiancheng Bioengineering Institute of China (Nanjing, China). The analytical grade chemicals and reagents were purchased from China National Pharmaceutical Industry Corporation Ltd. (Beijing, China). All the experiments were performed utilizing deionized water (DW).

2.2 Animals

Male grown-up Sprague–Dawley (SD) rats weighing 210.0 ± 10.0 g were purchased from Beijing Jinmuyang Co., Ltd. (Beijing, China) under the following rearing conditions: temperature (24.0 ± 1.0) °C, Relative humidity 55%–65%, 12 h light/dark cycle, free access to food and water.

2.3 Synthesis of FP-CDs

To put it succinctly, 50 g FP was ground into fine powder and boiled 2 times with DW in a 100°C water bath for 1 h each time. Subsequently, the water decoction was filtered with 0.22 μm organic microporous membrane and concentrated to 50 mL. At that point, the concentrated was dialyzed against 1,000 Da molecular weight dialysis membrane in a measuring utensil filled with DW. Finally, the gotten FP-CDs were put away at 4°C until assist use. The schematic diagram of the experimental protocol for the preparation of FP-CDs is exhibited in Figure 1.

2.4 Characterization of FP-CDs

The morphology, distribution and microstructure information of FP-CDs were revealed by transmission electron microscopy (TEM) (Tecnai G220, FEI Company, United States), while the atomic lattice spacing of FP-CDs was uncovered utilizing a high-resolution TEM (JEN-1230, Japan Electron Optics Laboratory, Japan). The emission wavelength and electronic transition characteristics of FP-CDs were gotten by utilizing ultraviolet (UV-Vis) spectrophotometer (CECIL, Cambridge, United Kingdom) and fluorescence (FL) spectrophotometer (F-4500, Tokyo, Japan) respectively. The functional group properties of FP-CDs were further characterized with Fourier transform infrared (FTIR) spectroscopy (Thermo Fisher, Fremont; California, United States) and X-ray photoelectron spectroscopy (XPS) (ESCALAB 250Xi, Thermo Fisher Scientific, United States).

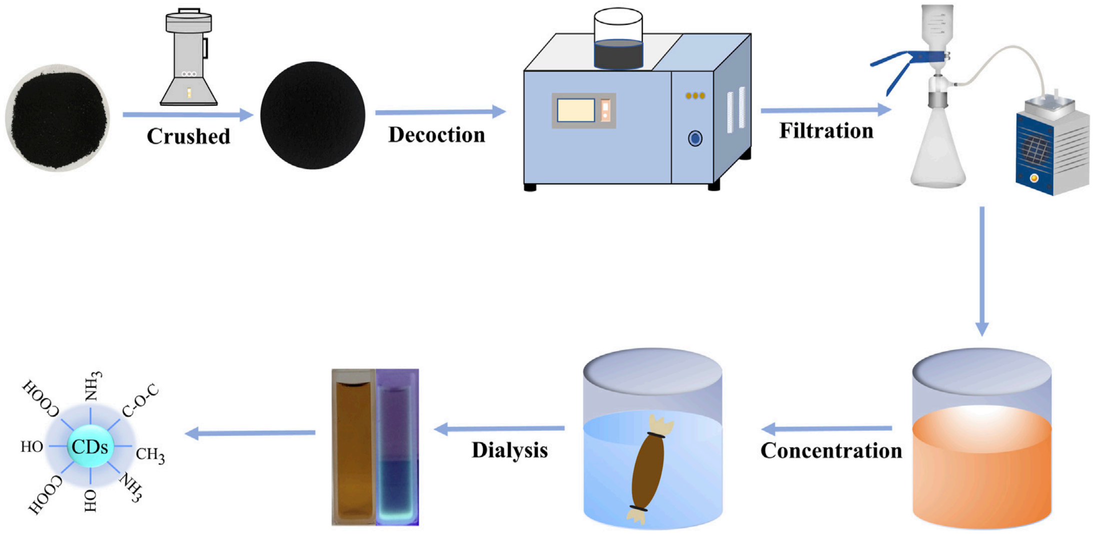

FIGURE 1
The flowchart for the preparation process of carbon dots derived from *Fuligo Plantae* (FP-CDs) by one-step calcination method.

The polydispersity index (PDI) value of FP-CDs was measured with dynamic light scattering (DLS).

2.5 Cytotoxicity assay of FP-CDs

In order to assess the hazards of FP-CDs and investigate its safety, the CCK-8 experiments were performed to recognize the cytotoxicity of FP-CDs to RAW 264.7 mouse macrophage, human gastric epithelial cell lines (GES-1) and human LO2 hepatocyte. The 3 cells were cultured in DMEM medium containing 20% fetal bovine serum in a humidified 5% CO_2 atmosphere at 37°C. Subsequently, the 3 cells were seeded in a 96-well plate at a density of 1×10^5 cells per 100 μL/well and incubated for 24 h, respectively. Then, different concentrations of FP-CDs (650, 325, 162.5, 81.25, 40.63, 20.31, 10.16 μg/mL) were added to the designated wells for 24 h and the control cells were treated with DMEM medium. After these plates were washed thrice with PBS, 10 μL of CCK-8 is added to the plate and incubated for 4 h. Additionally, a microplate reader (Biotek, Vermont, United States) was utilized to record the absorbance of each well. Finally, the cell viability (%) calculation formula is as follows:

$$\text{Cell Viability (\% of control)} = (\text{Ae} - \text{Ab}) / (\text{Ac} - \text{Ab}) \times 100 \quad (1)$$

where Ae, Ab, and Ac represent the absorbance of the experimental, blank and control groups, respectively, at 450 nm.

2.6 Biosafety experiment in rats

Twenty rats were randomly divided into the following two groups (n = 10 in each) according to the administration situation: control group (normal saline, 0.5 mL, i.g.), administration intervention group (FP-CDs, 9.98 mg/kg, i.g.). Next, the reaction and mortality of each group of mice within 24 h were observed for 5 consecutive days. After 4 days of administration, rats in each group fasted for 24 h during which they drank freely. On the 5th day of administration, after 3 h of administration, rats were anesthetized by intraperitoneal injection of 4% chloral hydrate (0.40 g/kg). Blood samples were collected from rats via the abdominal aorta by blood taking needles and vacuum blood collection tubes (Becton Dickinson Medical Instrument Co., Ltd., Shanghai, China) to detect indexes of hepatic function (ALT and AST). Subsequently, the heart, liver, spleen, lung, kidney, and thymus of rats in each group were extracted in 4% tissue fixation solution, and the organs of each group were observed by HE staining.

2.7 Coagulation parameter measurements

Sixty rats were randomly divided into the following six groups (n = 10 in each) according to the administration situation: control group (normal saline, 0.5 mL, i.g.), model (normal saline, 0.5 mL, i.g.), positive group (Yunnan Baiyao powder, 250 mg/kg, i.g.), and FP-CDs at different doses [low (L): 2.49 mg/kg, medium (M): 4.99 mg/kg, high (H): 9.98 mg/kg; i.g.). After 4 days of administration, rats in each group fasted for 24 h during which they drank freely. On the 5th day of administration, after 2 h of administration, all groups were given to 95% alcohol (10 mL/kg, i.g.) except the control group, which acquired an equal amount of normal saline. After being modelled with alcohol for 1 h, rats were anesthetized by intraperitoneal injection of 4% chloral hydrate (0.40 g/kg). Next, Abdominal aortic blood was infused into prepacked 3.2% sodium citrate (blood: citrate: 1:9, v/v) centrifuge tubes and permitted to respond for at slightest 30 min. Subsequently, blood samples were centrifuged at 750 × g for 15 min to get supernatant. Activated partial thromboplastin time (APTT), thrombin time (TT), prothrombin time (PT), and fibrinogen content (FIB) were determined utilizing a programmed coagulation analyser.

2.8 Models of alcohol-induced acute gastric ulcer model in rats and drug treatment

The AGC model was established as previously reported (Gao et al., 2020). A total of 60 SD rats were randomly divided into the following six groups ($n = 10$ in each) according to the administration situation: control group (normal saline, 0.5 mL, i.g.), model (normal saline, 0.5 mL, i.g.), positive (ranitidine, 50 mg/kg, i.g.) and FP-CDs at different doses [low (L): 2.49 mg/kg, medium (M): 4.99 mg/kg, high (H): 9.98 mg/kg; i.g.]. After 4 days of administration, rats in each group fasted for 24 h during which they drank freely. On the 5th day of administration, after 2 h of administration, all groups were given to 95% alcohol (10 mL/kg, i.g.) except the control group, which gotten an equal volume of normal saline.

2.9 The calculation of gastric ulcer area and gastric ulcer inhibition rate

After being modelled with alcohol for 1 h, rats were euthanized. Subsequently, the abdominal cavity was opened to separate the gastric tissue, cut along the more noteworthy curvature, and after that washed with ice-cold saline until there was no content or bloodshot. The stomach was stretched on a clean ice box with the mucous membrane facing up, and was instantly captured by a computerized camera to watch the ulcer zone. The ratio of mucosal ulcer area in each group was automatically assessed by ImageJ software (v1.8.0v, MD, United States). The ulcer index (UI) and percentage inhibition (Xin et al., 2021) were calculated by the following formulas:

$$\text{UI }(\%) = \text{zone of gastric ulcer}/\text{area of entirety stomach} \times 100 \quad (2)$$

Percentage Inhibition (%) = (UI in model group-UI in each group)/UI in model group × 100. (3)

2.10 Histopathological evaluation

After the gastric tissue was watched and captured, portion of the gastric tissue was quickly put in 4% paraformaldehyde, got dried out, embedded in paraffin, and recoloured with HE. The recoloured segments were shot and watched beneath a magnifying lens at amplifications of ×100 and 200 ×. Subsequently, the pathological changes of gastric mucosa in each group were used for comparative observation.

2.11 Examinations of biochemical indicators

The remaining portion gastric tissues of rats were weighed and processed with 9 times volume of pre-cooling PBS solution to make 10% gastric tissue homogenate. Next, the supernatant centrifuged at 750 × g for 15 min was utilized to detect the contents of inflammatory cytokines (TNF-α, IL-6, and IL-1β) and the contents of oxidative stress indicators (MDA, SOD, and GSH) utilizing corresponding kits according to the instructions.

2.12 16S rDNA genome sequencing for intestinal flora

New feces of each group of rats were collected with sterile forceps and put away at −80°C for gene sequencing. Total DNA in feces was extracted according to the instructions of the DNA extraction kit (MN NucleoSpin 96 Soi, US), and the V3-V4 region of 16S rDNA was opened with primers with barcodes. The primer sequences were 338F: ACTCCTACGGGAGGCAGCA, 806R: GGACTACHVGGGTWTCTAAT. The PCR amplification products were at that point recuperated by gel cutting and measured concurring to electrophoresis. Afterwards, the purified amplification products were blended in rise to sums, ligated with sequencing connectors, and sequenced using Illumina Novaseq 6,000 (Beijing Biomarker Cloud Technology Co., Ltd., China).

2.13 Statistical analysis

All data from experiment were carried out utilizing IBM SPASS (version 25.0, Chicago, IL). The values were represented as means ± standard deviation. Multiple comparisons were performed employing a one-way analysis of variance (ANOVA) followed by the least-significant difference (LSD) test. $p < 0.05$ and $p < 0.01$ were considered statistically significant.

3 Result

3.1 Characterization of FP-CDs

The TEM image (Figure 2A) directly exhibited that the FP-CDs were spherical-like particles consistently distributed within the field of vision without self-evident conglomeration. The particle sizes of FP-CDs were fundamentally scattered between 1.4 and 3.2 nm (Figure 2B), which acclimated to the normal distribution characteristics and was obtained by statistical analysis of more than 200 particles with the support of ImageJ software (Bhamore et al., 2019). As illustrated in Figure 2C, the high-resolution TEM image appeared well-resolved lattice fringes and a lattice spacing of 0.165 nm, which was near to the value of the crystal plane of graphite. These morphological findings are consistent and dependable with past survey reports (Wang et al., 2021).

The optical properties of FP-CDs were assist examined utilizing UV-Vis spectrophotometer and FL spectrophotometer. The UV-Vis spectra of FP-CDs (Figure 2D) displayed several distinct absorption peaks between 200 and 240 nm, which may be caused by the π-π* electronic transition of the conjugated C=C bonds and aromatic sp^2 domains (Sun et al., 2021). At the same time, the absorption peak around 300 nm may be caused by the n-π* electronic transition caused by the unsaturated heteroatom bond. As shown in Figure 2E, it can be seen from the FL spectra of FP-CDs that the maximum emission wavelength (EM_{max}) is at 490 nm when excited at 399 nm. Further analysis of the fluorescence characteristics (Figure 2F) can be found that as the excitation wavelength increases from 360 nm to 430 nm, the EM_{max} begins to red-shift and its fluorescence intensity showed up a drift of growing to start with and after that diminishing. According to literature reports (Wei et al., 2019), the optical

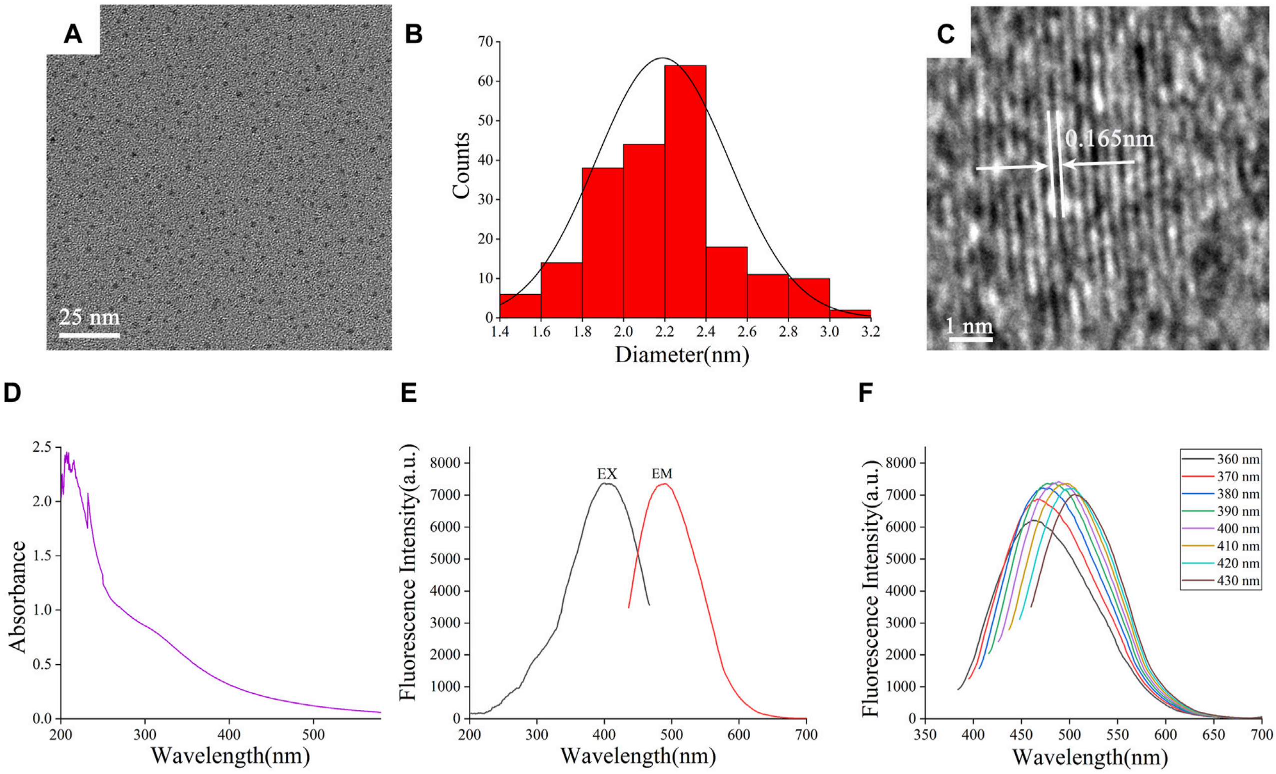

FIGURE 2
Morphological and optical characterizations of FP-CDs. **(A)** Transmission electron microscopy (TEM) images of FP-CDs displaying ultra-small particles. **(B)** Particle size distribution histogram of FP-CDs. **(C)** High-resolution TEM image of FP-CDs and lattice spacing of ASAC-CDs (in the middle). **(D)** Ultraviolet–visible spectrum. **(E)** Fluorescence spectra. **(F)** Fluorescence spectra of FP-CDs with different excitation wavelengths.

properties of CDs vary with size, which may lead to changes in the density of CDs and the properties of sp^2 sites. The phenomenon of the fluorescence wavelength red-shift is explained that it may be caused by the different emission traps on the surface of CDs of different sizes and the energy gap decreases with the increase of size under the condition of quantum confinement effect.

The plenteous surface chemical groups and element composition of FP-CDs were advance characterized and analysed by FTIR and XPS techniques. Within the FTIR spectra (Figure 3A), the intense peak at 3,447 cm^{-1} was credited to the stretching vibration of O-H and N-H bonds. The absorption peaks at 2,919 cm^{-1} indicated the existence of -CH bonds, which was related to the binding of methyl or methylene groups to aliphatic hydrocarbons in FP-CDs. The peak at 1,636 cm^{-1} belonged to the stretching vibration peak of -C=O bonds, while the weakly absorbed peak at 1,384 cm^{-1} was associated with -C-N bonds (Manchala et al., 2021). Moreover, the peak was observed at 1,047 cm^{-1} means the existence of C-O-C bonds (Muhammad et al., 2019). Therefore, these results demonstrate that FP-CDs with abundant hydroxyl, amino and carboxyl groups on the surface have better water solubility and hydrophilicity.

Furthermore, three apparent element peaks in XPS spectra (Figure 3B) were observed clearly at 284.81, 399.84 and 531.67 eV, indicating that the FP-CDs were basically made up of C (65.46%), N (9.75%), and O (24.78%). Three obvious peaks at 284.63, 285.85, and 287.91 eV in the C 1 s (Figure 3C) spectrum were attributed to the presence of C=C/C-C, C-O/C-N and C=O/C-N, respectively. The N 1 s spectrum (Figure 3D) was divided into two apparent peaks at 399.64 and 400.67 eV, which were consistent with C-N-C and N-H bonds. Moreover, the O 1 s spectrum (Figure 3F) was isolated into two evident peaks at 531.36 and 532.54 eV, which confirmed the presence of C-O and C=O bonds (Radnia et al., 2020; Luo et al., 2021). The XPS experimental results are basically consistent with the FTIR characterization, indicating that FP-CDs contain various groups including carboxyl, hydroxyl, and amino groups, which can be credited to the multiphoton dynamic forms in the diverse oxygen-containing functional groups. In addition, the dispersion stability of FP-CDs is usually measured by DLS method. The colloidal stability of FP-CDs in water and NaCl at 25°C for 3 days was studied by DLS. The results (Figure 3F) showed that the PDI of FP-CDs in water did not change significantly.

3.2 Biosafety evaluation

As potential unused nano-drug possessed a series of exceptional properties, CDs have been widely concerned about the security of clinical application. As shown in Figure 4A, FP-CDs with concentrations ranging from 10.16 to 650 μg/mL had little impact on the viability of RAW264.7, GES-1 and LO2 cells, and the overall survival rate was above 75%. In addition, FP-CDs even exhibited a certain promoting effect on cell viability at concentrations extending

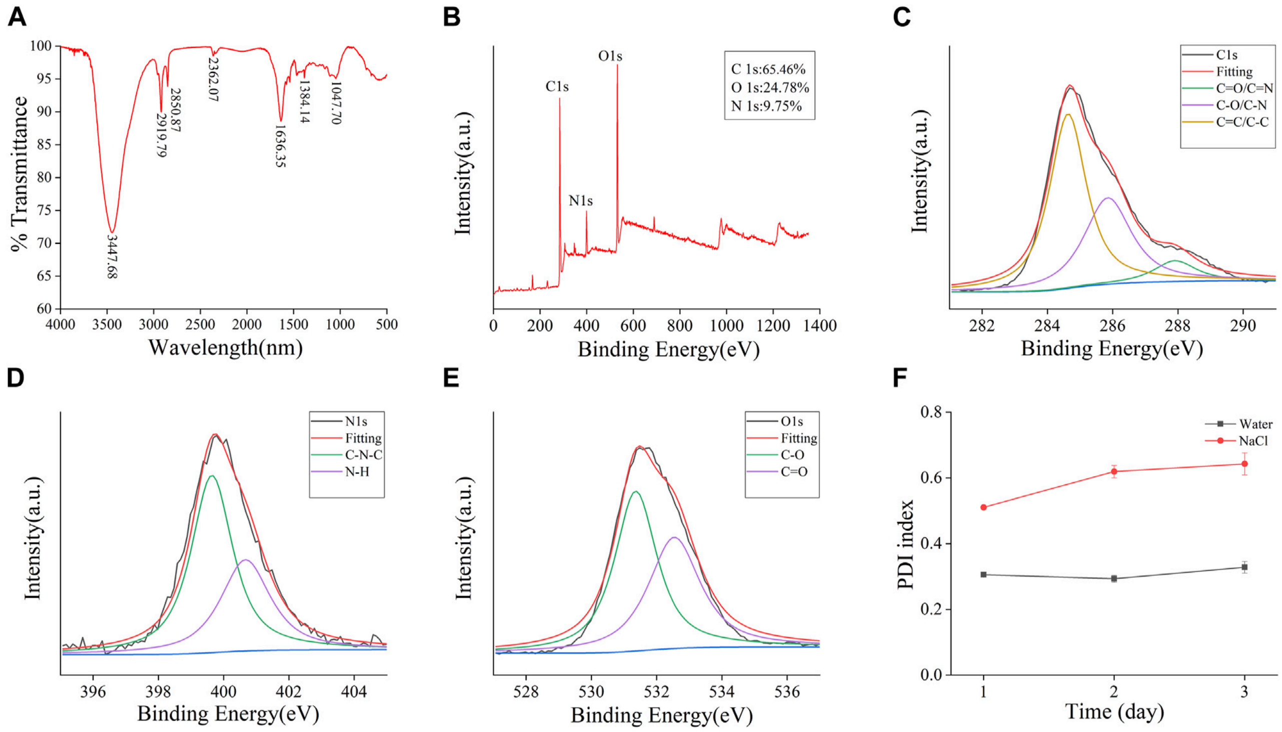

FIGURE 3
Functional groups and dynamic light scattering (DLS) analysis of the prepared FP-CDs. **(A)** Fourier transform infrared spectroscopy spectrum (FT-IR). **(B)** X-ray photoelectron spectroscopy survey (XPS), **(C)** C 1 s, **(D)** O 1 s, **(E)** N 1 s high-resolution survey spectrum and **(F)** The colloid stability of FP-CDs dispersed in water and NaCl measured by DLS.

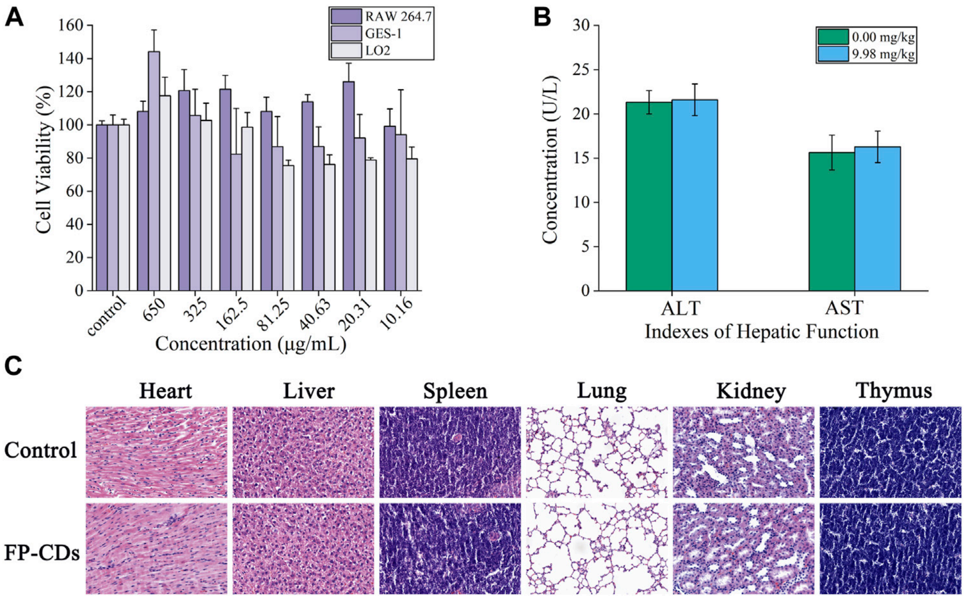

FIGURE 4
Biosafety experiment of FP-CDs. **(A)** Effect of different concentrations of FP-CDs on the viability of RAW264.7, GES-1 and LO2 cells via CCK-8 assay for 24 h. **(B)** Effects of FP-CDs (9.98 mg/kg) on indexes of hepatic function (ALT and AST) in normal rats. **(C)** Effect of FP-CDs (9.98 mg/kg) on pathological changes of the heart, liver, spleen, lung, kidney, and thymus in normal rats.

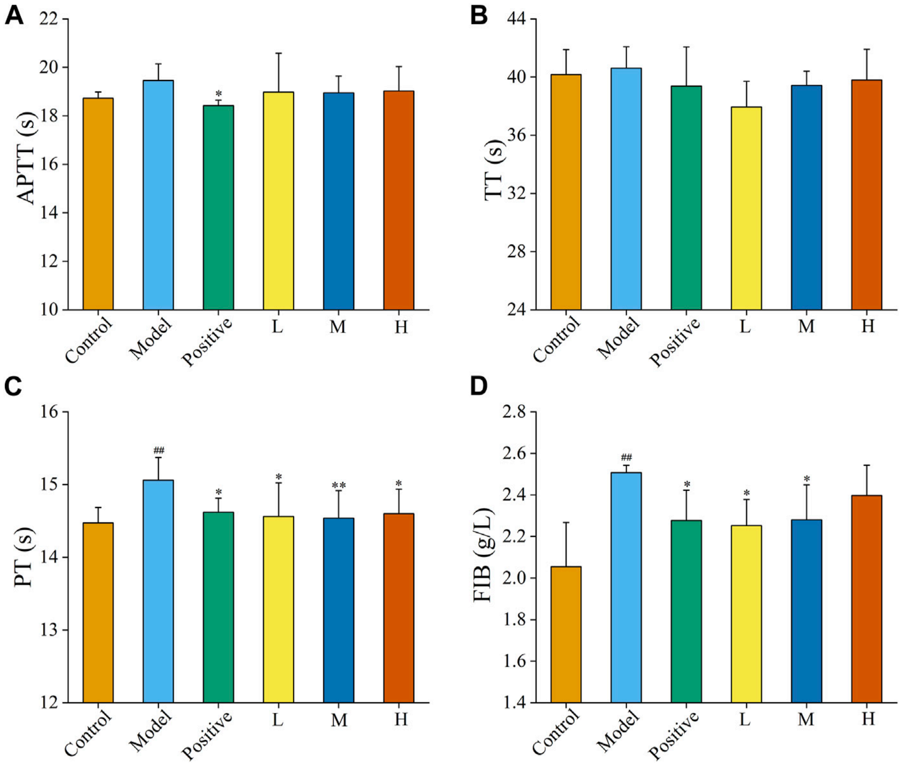

FIGURE 5
Effects on coagulation parameters. **(A)** activated partial thromboplastin time (APTT), **(B)** thrombin time (TT), **(C)** prothrombin time (PT), and **(D)** fibrinogen (FIB). Analysis of rats treated with control group, model group, positive (Yunnan Baiyao) group, or low (L), medium (M), or high (H) doses of FP-CDs (2.49, 4.99, and 9.98 mg/kg, respectively). Significantly different compared with the control group at $^{\#\#}p < 0.01$, significantly different compared to the model group at $^{**}p < 0.01$ and $^{*}p < 0.05$.

from 325 to 650 μg/mL. Animal serum biochemical parameters are one of the important indicators for evaluating organ function. As shown in Figure 4B, FP-CDs within the experimental dose range had no significant effect on indexes of hepatic function (ALT and AST) after continuous administration for 5 days, and there was no statistical difference between the groups compared with the normal group. Figure 4C showed that after 5 days of continuous intervention with FP-CDs, the structure of the heart, liver, spleen, lung, kidney, pancreas, and thymus of normal rats did not change significantly, which further suggests that FP-CDs have high security. The detection results of the biosafety experiment illustrated that FP-CDs have low toxicity, which has a certain potential reference value for the clinical use of nano-drugs in the future.

3.3 Effect of FP-CDs on the coagulation system

The haemostatic mechanism of FP-CDs evaluated by assessed four coagulation parameters (APTT, TT, PT, and FIB). As illustrated in Figures 5A, B, APTT and TT values were not essentially distinctive among the four treatment groups in comparison with the model group. Figures 5C, D exhibited that the values of PT and FIB in the model group were elevated ($p < 0.01$) in comparison with the control group. In addition, the PT and FIB values of Yunnan Baiyao group and FP-CDS group at low, medium, and high doses were alleviated in contrast with the model group ($p < 0.05$), which indicated that the haemostatic efficacy of FP-CDs may be related to the exogenous coagulation route.

3.4 FP-CDs ameliorated alcohol-induced structural abnormalities

As a gastric mucosal attack factor, excessive high concentration of alcohol can directly damage gastric mucosal tissue, stimulate gastrointestinal motility, and cause mucosal oedema, haemorrhage necrosis, and inflammation. In this experiment, the inhibitory efficacy of FP-CDs on AGU in rats caused by excessive oral alcohol was investigated by evaluating the morphological changes in the stomach of rats in each group, calculating the ratio of ulcer index and inhibition rate. Compared with the control group (Figure 6A), gastric tissue (Figure 6B) after oral alcohol administration exhibited marked spasms and extensive dark red streaks, demonstrating serious haemorrhage of the gastric mucosa. Moreover, in contrast to the model group, the gastric mucosal bleeding of rats treated with ranitidine (Figure 6C) and FP-CDs (Figures 6D–F) was significantly reduced, and only a few punctate haemorrhages were seen, suggesting that FP-CDs alleviated the damage of gastric tissue to varying degrees.

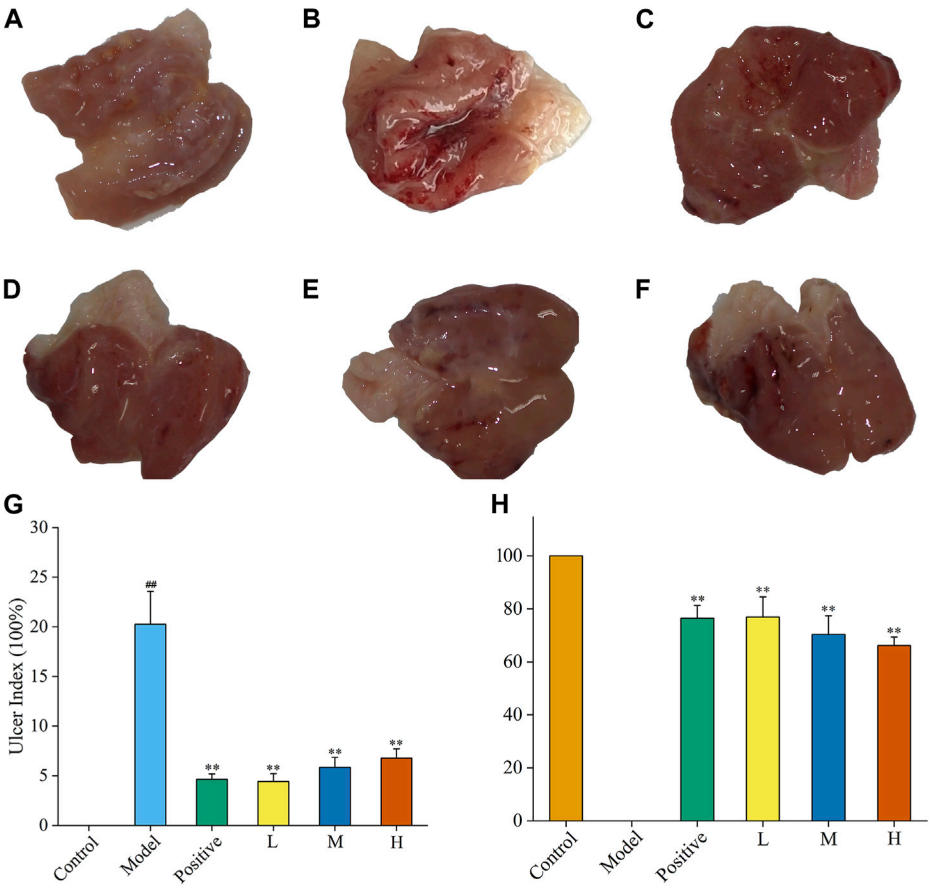

FIGURE 6
Effects of FP-CDs on the gastric mucosa in rats with alcohol-induced ulcers. **(A)** control group, **(B)** model group, **(C)**positive (ranitidine) group, **(D)** low (L), **(E)** medium (M), and **(F)** high (H) doses of FP-CDs (2.49, 4.99, and 9.98 mg/kg, respectively), **(G)** the ulcer index, **(H)** percentage inhibition of each group. Significantly different compared with the control group at $^{\#\#}p < 0.01$, significantly different compared to the model group at $^{**}p < 0.01$.

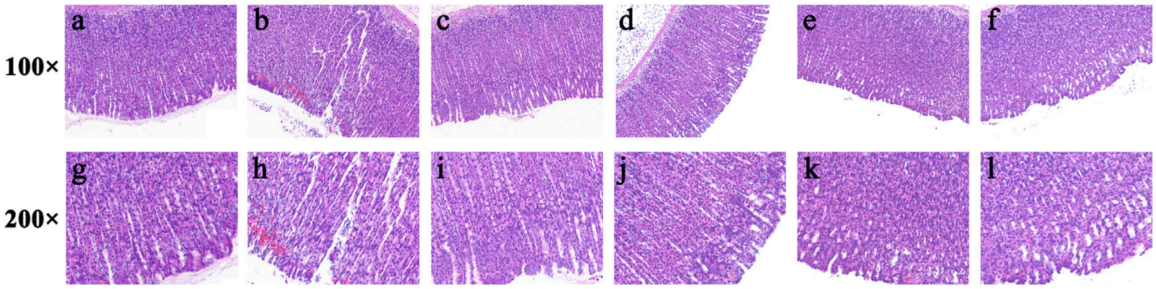

FIGURE 7
Effects of FP-CDs on histopathological changes in alcohol-induced gastric histopathological damage (magnification = × 100 and 200 ×). Histopathological sections of gastric tissue were stained with H&E. **(A,G)** control group, **(B,H)** model group, **(C,I)** positive (ranitidine) group, **(D,J)** low-dose FP-CDs group (2.49 mg/kg), **(E,K)** medium-dose FP-CDs group (4.99 mg/kg), and **(F,L)** high-dose FP-CDs group (9.98 mg/kg).

Moreover, the UI and inhibition rate were calculated by ImageJ computer program to quantify the change of the lesion area and assess the gastroprotective efficacy of FP-CDs. As illustrated in Figures 6G, H, the UI of the rats in the model group accounted for a higher proportion in comparison with the control group, indicating that the gastric mucosal injury caused by alcohol was obvious ($p < 0.01$). In sharp contrast, the pre-administration group treated with ranitidine and FP-CDs obviously alleviated the ulcer area and exhibited higher inhibition rate ($p < 0.01$), in which the low-dose FP-CDS group with an inhibition rate of more than 76% had a stronger inhibition effect on ulcer injury.

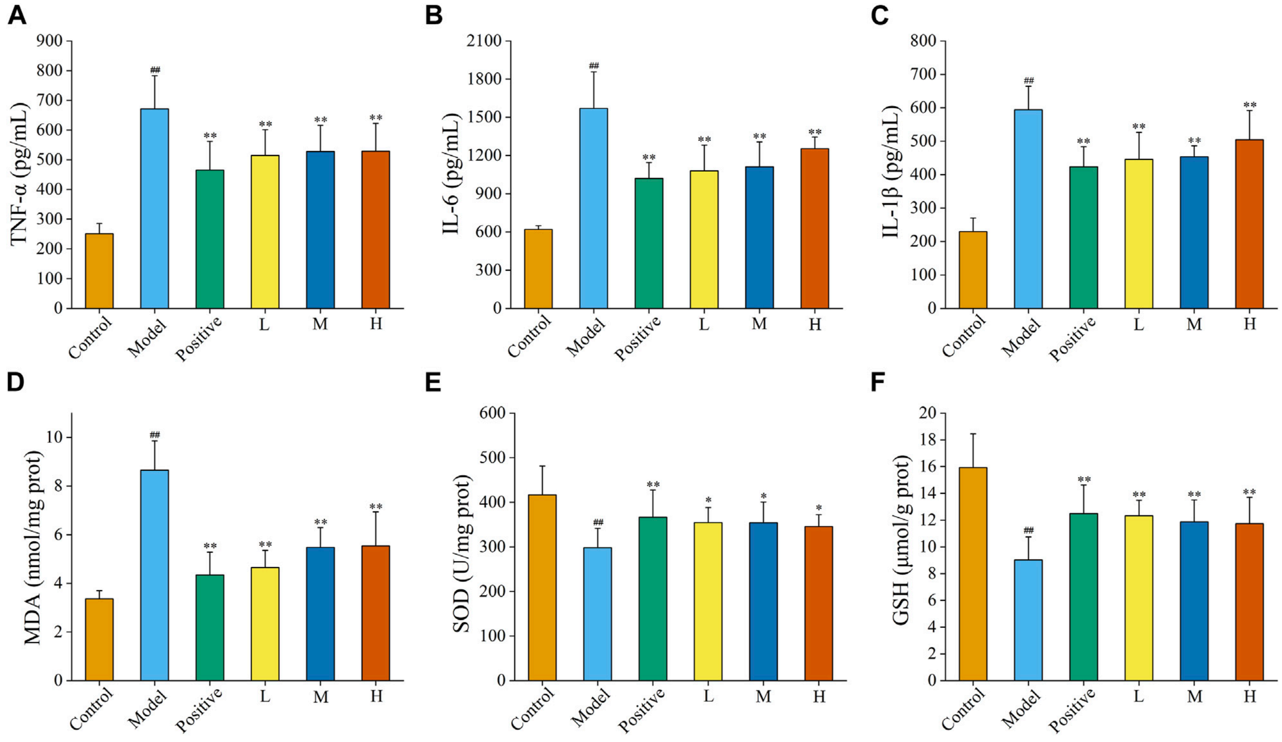

FIGURE 8
Effects of FP-CDs on inflammatory cytokines and oxidative stress in gastric tissue homogenate supernatant. **(A)** tumour necrosis factor-α (TNF-α), **(B)** interleukin (IL)-6, **(C)** IL-1β, **(D)** malondialdehyde (MDA), **(E)** superoxide dismutase (SOD), and **(F)** glutathione (GSH). Analysis of rats treated with control group, model group, positive (ranitidine) group, or low (L), medium (M), or high (H) doses of FP-CDs (2.49, 4.99, and 9.98 mg/kg, respectively). Significantly different compared with the control group at $^{\#\#}p < 0.01$, significantly different compared to the model group at $^{**}p < 0.01$ and $^{*}p < 0.05$.

Furthermore, haematoxylin and eosin (HE) staining showed that the gastric mucosa in the control group (Figures 7A, G) was flat and smooth, and the cells were arranged in an orderly manner. While necrosis of mucosal cells, increased inflammatory cells and severe intervillous haemorrhage were clearly observed in the model group (Figures 7B, H). In contrast, oral administration of ranitidine (Figures 7C, I) and different doses of FP-CDs (L: Figures 7D, J, M: Figures 7E, K, H: Figures 7F, L) during pre-treatment significantly alleviated haemorrhage, oedema, and inflammatory cell infiltration, which further suggested the inhibitory effect of FP-CDs on alcohol-induced injury.

3.5 FP-CDs inhibited alcohol-induced inflammatory response

Inflammation is one of the imperative underlying mechanisms of excess alcohol-induced AGU. As illustrated in Figure 8A, the contents of TNF-α within the model group (671.46 ± 111.51 pg/mL) was obviously upregulated ($p < 0.01$) in comparison to that of the control group (250.90 ± 34.69 pg/mL), suggesting that the model was successful ($p < 0.01$). Compared with that in the model group, the levels of TNF-α in the ranitidine (465.27 ± 96.79 pg/mL), low-dose (514.53 ± 86.66 pg/mL), medium-dose (527.82 ± 88.17 pg/mL) and high-dose (528.87 ± 93.51 pg/mL) groups produced a conspicuous reduction ($p < 0.01$).

Moreover, the content of IL-6 (Figure 8B) was obviously raised by alcohol in the model group (1,570.09 ± 287.61 pg/mL) compared to control group (620.17 ± 28.58 pg/mL), while the pre-administration of ranitidine (1,020.20 ± 124.22 pg/mL) and FP-CDs (L: 1,079.01 ± 201.86 pg/mL, M: 1,111.70 ± 195.81 pg/mL, H: 1,253.67 ± 91.96 pg/mL) could downregulate the index to varying degrees ($p < 0.01$).

Additionally, the level of IL-1β (Figure 8C) in the model group (594.18 ± 70.36 pg/mL, $p < 0.01$) also ascended in comparison to those in the control group (229.31 ± 40.83 pg/mL). In comparison to the model group, the levels of IL-1β in the ranitidine (423.21 ± 60.45 pg/mL), low-dose (445.49 ± 81.13 pg/mL), medium-dose (453.18 ± 32.92 pg/mL) and high-dose (504.20 ± 87.55 pg/mL) groups significantly decreased ($p < 0.01$).

3.6 FP-CDs attenuated alcohol-induced oxidative stress

Oxygen radicals in the body are associated with most causative factors for ulcers. Enhanced lipid peroxidase action and increased production of oxygen free radicals can trigger a decrease in cellular fluidity and peroxidation of membrane-structured unsaturated fatty acids, which can lead to cellular damage and further mucosal damage. In this study, changes in oxidative stress indicators were

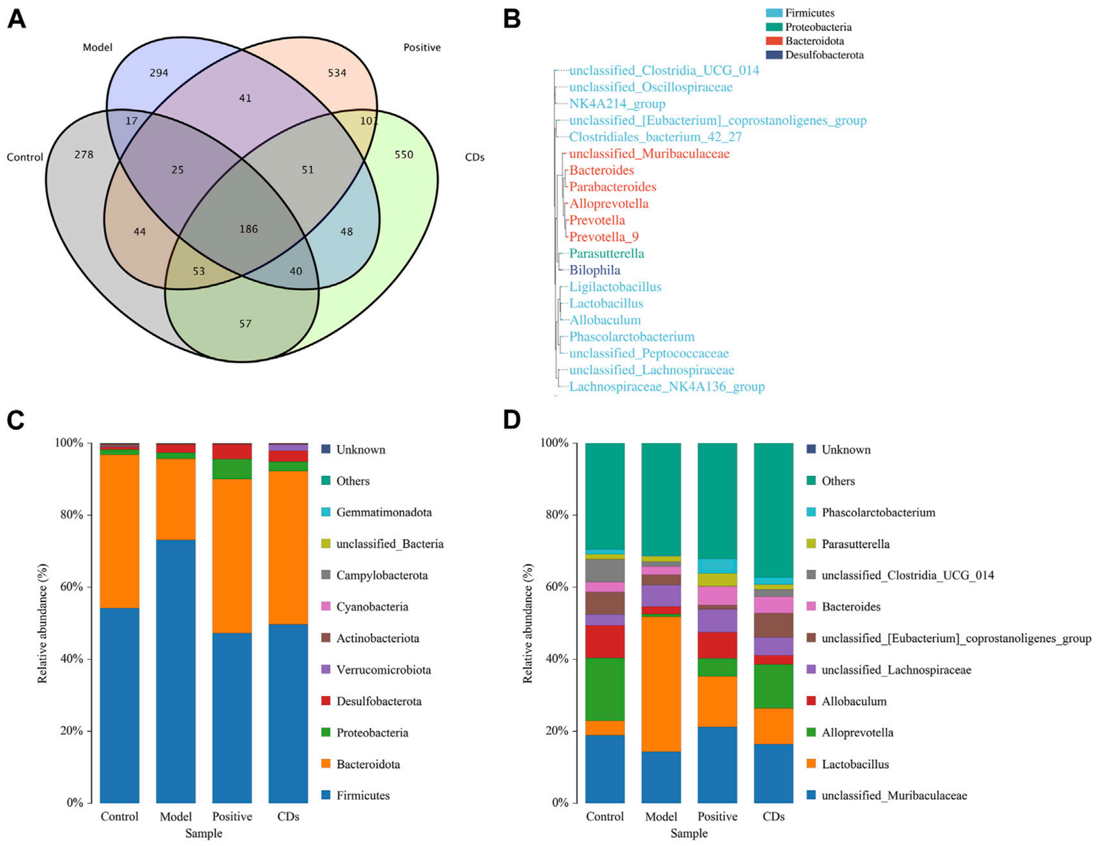

FIGURE 9
Effects of FP-CDs on the overall changes of intestinal flora in rats with alcohol-induced ulcers. **(A)** Venn diagram of intestinal flora of rats in each group, **(B)** schematic diagram of the phylogenetic tree at genus level for each group, **(C)** histogram of species distribution at phylum level for each group, **(D)** histogram of species distribution at genus level for each group.

assessed by measuring the amount of MDA, SOD, and GSH in the gastric tissue (Figures 8D–F).

After being disturbed by alcohol, the level of MDA in the model group (8.66 ± 1.20 nmol/mg port, $p < 0.01$) was significantly higher than that in the control group (3.37 ± 0.33 nmol/mg port, $p < 0.01$). Meanwhile, the levels of SOD and GSH in the model group (SOD: 298.24 ± 43.28 U/mg prot, GSH: 9.02 ± 1.72 μmol/g prot) was significantly descending in comparison to that of the control group (SOD: 416.59 ± 64.84 U/mg prot, GSH: 15.93 ± 2.53 μmol/g prot, $p < 0.01$), which indicated that the modelling was successful.

Conversely, the contents of MDA in the positive group (4.35 ± 0.94 nmol/mg port) and FP-CDs groups (L: 4.65 ± 0.70 nmol/mg port, M: 5.48 ± 0.81 nmol/mg port, H: 5.54 ± 1.40 nmol/mg port) were significantly relieved in comparison to the model group ($p < 0.01$). In addition, pre-treatment with ranitidine (SOD: 366.66 ± 61.01 U/mg prot, GSH: 12.50 ± 2.12 μmol/g prot, $p < 0.01$) and low- (SOD: 354.53 ± 33.81 U/mg prot, $p < 0.01$; GSH: 12.33 ± 1.15 μmol/g prot, $p < 0.05$), medium-(SOD: 354.20 ± 46.24 U/mg prot, $p < 0.01$; GSH: 11.88 ± 1.62 μmol/g prot, $p < 0.05$), and high-doses (SOD: 345.81 ± 26.76 U/mg prot, $p < 0.01$; GSH: 11.73 ± 1.96 μmol/g prot, $p < 0.05$) of FP-CDs generated a noteworthy increment within the levels of Grass and GSH.

3.7 Effects of FP-CDs on intestinal microflora and metabolism

The composition and abundance ratio of intestinal flora have a close relationship with the health status of the body, and maintain a dynamic balance in the continuous development and change. In the state of alcohol stimulation, various homeostatic balances of the body are disrupted, resulting in intestinal flora imbalance, which in turn leads to the occurrence of startling gastrointestinal diseases. Here, we further investigated the impact of the more effective low-dose FP-CDs group on the intestinal flora.

The Venn diagram (Figure 9A) exhibited that a total of 186 species of intestinal flora in each group were common, apart from which, the other common flora number in control group and model group was 268. In contrast, that of common flora in the positive and FP-CDs groups was 308 and 336, respectively. In addition, the phylogenetic tree of the features at the genus taxonomic level (Figure 9B) displayed that the same colour genus name represented the same phylum, and was mainly divided into *Firmicutes*, *Bacteroidota*, *Proteobacteria*, and *Desulfobacterota*. The histograms of species richness at the phylum level (Figure 9C) and genus level (Figure 9D) were clearly observed the species composition and proportion of each group of samples, which further reflected the changes of species among each group of samples. The ranitidine and FP-CDs groups could significantly adjust the levels of *Firmicutes* (ranitidine: 25.89%, FP-CDs: 23.48%) and *Bacteroidota* (ranitidine: 20.30%, FP-CDs: 20.07%) in comparison to that of the model group at the phylum level. According to the intestinal flora structure analysis at the genus level, compared with the model group, the positive group and FP-CDs group could call back the proportions of *Alloprevotella* (ranitidine: 4.26%, FP-CDs: 11.49%) and *Bacteroides* (ranitidine: 3.00%, FP-CDs: 2.31%). At the same time, the proportions of *Lactobacillus* (27.45%) and *Phascolarctobacterium* (1.66%) makes the composition of the intestinal flora in FP-CDs group close to the level of the control group in comparison to that of the model group. These results implied that FP-CDs reversed the diversity and dysbiosis of the intestinal flora in rats with AGU, and bring it closer to the content of the control group.

4 Discussion

CDs, as a new type of nanomaterials with unique advantages, has shown great application potential in biomedical fields such as biological imaging and tumour therapy (Ansari et al., 2021; Zhang W. et al., 2021). At present, A lot of research focus on the exploration of disease treatment and the expansion of application fields, while ignoring the problem of raw materials. Researchers are turning their consideration to green precursors with therapeutic properties after considering the need for low toxicity and avoiding transport of goods (Zhao et al., 2020). Compared with chemically derived CDs, Chinese herbal medicine-derived CDs have the advantages of abundant raw material sources, simple preparation methods, good biocompatibility, good water solubility, low toxicity, and low cost, and are an ideal CDs precursor material selection (LuMaHuang et al., 2021). More notably, Chinese herbal medicine is rich in a variety of active ingredients that make them a direct route to heteroatoms. Therefore, in recent years, the research on the biological activity of CDs derived from Chinese herbal medicine has become the focus of many scholars at home and abroad.

Charcoal drugs are a kind of characteristic Chinese medicines with extensive pharmacological effects formed after similar high temperature carbonization of Chinese medicines from different sources. However, its material basis is still controversial. High temperature carbonization is a critical procedure in the processing of charcoal drugs, which is like the bottom-up pyrolysis of CDs. Different process parameters change the chemical bond splitting mode of the compounds in the raw medicinal materials, which in turn leads to changes in the particle size, crystal structure and biological activity of the formed CDs. In the preliminary work, our team demonstrated that CDs is the active substance basis of charcoal drugs. We have confirmed that CDs derived from *Pollen Typhae Carbonisata* (Yan et al., 2017) and *Selaginella tamariscina Carbonisata* (Zhang et al., 2019) can stimulate endogenous and exogenous coagulation pathways respectively to play a haemostatic role. In addition, CDs derived from different charcoal drugs showed similar efficacy, such as *Radix Sophorae Flavescentis*

Carbonisata-based CDs (Hu et al., 2021) and *Atractylodes macrocephala Carbonisata*-based CDs (Kong et al., 2021) both showed a certain anti-ulcer effect. The same charcoal-derived CDs also have various pharmacological activities, such as CDs derived from *Phellodendri Chinensis Cortex Carbonisata*, which have haemostatic effects, reduce kidney damage caused by snake venom, and treat psoriasis (AkhtarMalikArshad et al., 2021; Zhang M. et al., 2021). Moreover, CDs derived from *Artemisiae Argyi Folium Carbonisata* perform a certain selective antibacterial effect as well as anti-frostbite effect (Wang et al., 2020; Zhou et al., 2021).

Based on the revelation of previous studies, we used FP as the only biomass precursors for the first time to extract and isolate FP-CDs. XPS and FTIR spectra were utilized to demonstrate the plentiful hydrophilic groups on the surface of FP-CDs, corresponding to good water solubility and diffusion in solution. CCK-8 experiments showed that FP-CDs showed extremely low toxicity to RAW 264.7, GES-1 and LO2 cells. The data of the four coagulation tests illustrated that the PT and FIB values of the FP-CDs group were decreased, which indicated that the haemostatic effect of FP-CDs was mainly related to the activation of the extrinsic coagulation pathway or the fibrinogen system. On this basis, the biological activity of FP-CDs was further explored.

Gastric ulcers are a common and frequent digestive tract illness. Although emotional and food factors will directly affect the cure of gastric ulcer, heavy drinking is still one of the main factors for the recurrence of the disease (Yang et al., 2021). Excessive consumption of alcohol not only causes direct stimulation to the gastric mucosa, but also increases the mucosal lipid peroxidation and cell damage induced by free radicals formed in the process of alcohol digestion system. Alcohol can cause damage to the submucosal blood vessels in the stomach, which can dilate the blood vessels and change the blood flow, causing small blood vessels to rupture and bleed (Sistani Karampour et al., 2019). In addition, alcohol can increase gastric acid secretion, gastrointestinal motility disorders, abnormal changes in intestinal flora, and aggravate oxidative stress and inflammatory responses (Kong et al., 2021). Meanwhile, free radicals are also generated during the alcohol metabolism. Once these free radicals cannot be effectively removed, it will cause antioxidant damage to major biological molecules such as lipids, proteins, and DNA, and finally lead to alcoholic gastric damage (Aziz et al., 2019).

Inflammation plays a key role in alcoholic gastric ulcer. Excessive alcohol intake will activate the microcirculation blood vessels on the gastric mucosa to produce inflammatory cytokines, and destroy the normal functioning of gastric tissue (Arab et al., 2019). As one of the indicators for evaluating apoptosis, TNF-α can stimulate the generation of other inflammatory cytokines, further lead to the activation of neutrophils and the production of acute phase reactive protein, which in turn influences the blood oxygen supply of gastric mucosa (Lian et al., 2020). IL-1β and IL-6 are also critical pro-inflammatory factors in the body, which can induce neutrophil aggregation, thereby aggravating the inflammatory response (Lin et al., 2021). The data of this research showed that the high, medium, and low dose groups of FP-CDs could reduce the levels of TNF-α, IL-6 and IL-1β in the gastric tissue of model rats to different degrees to alleviate the acute inflammatory response caused by alcohol, which may be one of the potential gastroprotective mechanisms of FP-CDs.

Oxidative stress refers to the nonstop generation of reactive oxygen species (ROS) that over-burdens the capacity of the natural antioxidant resistance system, resulting in DNA, protein, and lipid damage, and is one of the critical reasons for the occurrence of AGU (Grigor’eva, 2020). After alcohol acts on the body, it can increase the production of ROS, resulting in a maladjustment between the production of oxygen free radicals and the antioxidant potential in the body, which in turn induces the aggregation of inflammatory cells and aggravates stomach damage (Xue et al., 2019). As an oxidation product, the content of MDA increases with the destruction of lipid film structure and function. SOD and GSH are important antioxidant enzymes in the human body, which decrease the production of free radicals and improve the body's antioxidant capacity under excessive oxidative stress levels. From the experimental results, the high, medium, and low dose groups of FP-CDs can reduce the MDA content in the gastric tissue of model rats on the one hand, and at the same time ascend the levels of SOD and GSH, which indicates that FP-CDs can effectively inhibit alcohol-induced oxidative damage and improve the capacity to resist oxidation and purge free radicals.

The current commonly utilized anti-ulcer therapy may induce changes in the flora of each segment of the host's gastrointestinal tract and further lead to the occurrence of other gastrointestinal illness. Therefore, the development of new drugs without negative effects on intestinal homeostasis is urgently needed. Here, we evaluated the efficacy of FP-CDs on rat intestinal microflora. The composition structure and differences of intestinal flora in rats were analysed from the phylum level. In this experiment, *Firmicutes* and *Bacteroidetes* were the dominant phyla in each group, and the ratio of *Firmicutes* to *Bacteroidetes* (F/B) was an important index reflecting the disorder of intestinal flora (Mousa et al., 2019). The F/B value of the model group increased, which was reversed after FP-CDs intervention. Analysis of the composition and differences of rat intestinal flora at the subordinate level showed that FP-CDs could restore the proportion of beneficial bacteria such as *Alloprevotella* and *Lactobacillus*. In conclusion, FP-CDs can improve the diversity and dysbiosis of intestinal flora in rats with AGU.

5 Conclusion

In summary, under the premise of using FP as the sole precursor, novel fluorescent FP-CDs with characteristic biological activity and less harmfulness were extracted and isolated, and proved to be effective active ingredients against gastric ulcer. The inhibitory effect of FP-CDs on gastric ulcer may be related to the mitigation of the levels of inflammatory factors and oxidative stress. In addition, FP-CDs can inhibit the symptoms of alcoholic gastric ulcer by modulating the structure of intestinal flora. This study not only provides a novel tactics for investigating the effective material basis of FP, but also lays an exploratory foundation for the application of FP-CDs in the clinical treatment of alcoholic gastric ulcer.

Data availability statement

The raw data supporting the conclusions of this article will be made available by the authors, without undue reservation.

Ethics statement

All the animal experiments were performed in accordance with the Guide for the Care and Use of Laboratory Animals endorsed by the Committee of Ethics of Animal Experimentation of the Beijing University of Chinese Medicine (ethics code: BUCM-4-2021-102502-4021).

Author contributions

Authors' contributions: HK, HQ, and YnZ designed the study. YSZ and GC performed the research. LC, YiFZ, YaFZ, YT, and YeZ analyzed the data. YSZ wrote the manuscript. HK and HQ confirm the authenticity of all the raw data. YG carried out supplementary experiments and revisions in the process of manuscript revision. All authors contributed to the article and approved the submitted version.

Funding

This work was supported by Special Funds for Fundamental Research Expenses of the Central Universities (China, Grant number 90011451310030).

Conflict of interest

The authors declare that the research was conducted in the absence of any commercial or financial relationships that could be construed as a potential conflict of interest.

Publisher's note

References

AkhtarMalikArshad, M. S. A. H., Batool, S., Raza, A. R., Tabassum, T., et al. (2021). Protective effect of newly synthesized indole imines against ethanol-induced gastric ulcer in rats. *Biotechnol. Biotechnol. Equip.* 35 (1), 231–237. doi:10.1080/13102818.2020.1868330

Ansari, L., Hallaj, S., Hallaj, T., and Amjadi, M. (2021). Doped-carbon dots: Recent advances in their biosensing, bioimaging and therapy applications. *Colloids Surf. B Biointerfaces* 203, 111743. doi:10.1016/j.colsurfb.2021.111743

Arab, H. H., Salama, S. A., Eid, A. H., Kabel, A. M., and Shahin, N. N. (2019). Targeting MAPKs, NF-κB, and PI3K/AKT pathways by methyl palmitate ameliorates ethanol-induced gastric mucosal injury in rats. *J. Cell Physiol.* 234 (12), 22424–22438. doi:10.1002/jcp.28807

Aziz, R. S., Siddiqua, A., Shahzad, M., Shabbir, A., and Naseem, N. (2019). Oxyresveratrol ameliorates ethanol-induced gastric ulcer via downregulation of IL-6, TNF-α, NF-κB, and COX-2 levels, and upregulation of TFF-2 levels. *Biomed. Pharmacother.* 110, 554–560. doi:10.1016/j.biopha.2018.12.002

Bhamore, J. R., Jha, S., Park, T. J., and Kailasa, S. K. (2019). Green synthesis of multi-color emissive carbon dots from Manilkara zapota fruits for bioimaging of bacterial and fungal cells. *J. Photochem Photobiol. B* 191, 150–155. doi:10.1016/j.jphotobiol.2018.12.023

Chen, Y., Cheng, H., Wang, W., Jin, Z., Liu, Q., Yang, H., et al. (2021). Preparation of carbon dots-hematite quantum dots-loaded hydroxypropyl cellulose-chitosan nanocomposites for drug delivery, sunlight catalytic and antimicrobial application. *J. Photochem Photobiol. B* 219, 112201. doi:10.1016/j.jphotobiol.2021.112201

Cui, F., Sun, J., Ji, J., Yang, X., Wei, K., Xu, H., et al. (2021). Carbon dots-releasing hydrogels with antibacterial activity, high biocompatibility, and fluorescence performance as candidate materials for wound healing. *J. Hazard Mater* 406, 124330. doi:10.1016/j.jhazmat.2020.124330

Gao, R., Wu, Z., Wang, L., Liu, J., Deng, Y., Xiao, Z., et al. (2020). Green preparation of fluorescent nitrogen-doped carbon quantum dots for sensitive detection of oxytetracycline in environmental samples. *Nanomater. (Basel)* 10 (8), 1561. doi:10.3390/nano10081561

Grigor'eva, I. N. (2020). Gallstone disease, obesity and the firmicutes/bacteroidetes ratio as a possible biomarker of gut dysbiosis. *J. Pers. Med.* 11 (1), 13. doi:10.3390/jpm11010013

Hu, J., Luo, J., Zhang, M., Wu, J., Zhang, Y., Kong, H., et al. (2021). Protective effects of Radix Sophorae Flavescentis carbonisata-based carbon dots against ethanol-induced acute gastric ulcer in rats: Anti-inflammatory and antioxidant activities. *Int. J. Nanomedicine* 16, 2461–2475. doi:10.2147/IJN.S289515

Kong, H., Zhao, Y., Zhu, Y., Xiong, W., Luo, J., Cheng, J., et al. (2021). Carbon dots from Artemisiae argyi Folium Carbonisata: Strengthening the anti-frostbite ability. *Artif. Cells Nanomed Biotechnol.* 49 (1), 11–19. doi:10.1080/21691401.2020.1862134

Lian, Y. Z., Lin, I. H., Yang, Y. C., and Chao, J. C. J. (2020). Gastroprotective effect of Lycium barbarum polysaccharides and C-phycocyanin in rats with ethanol-induced gastric ulcer. *Int. J. Biol. Macromol.* 165 (Pt), 1519–1528. doi:10.1016/j.ijbiomac.2020.10.037

Lin, B., Yu, Y., Liu, F., Cao, Y., and Guo, M. (2017). Tunable and nontoxic fluorescent probes based on carbon dots for imaging of indole propionic acid receptor in plant tissues *in situ*. *J. Fluoresc.* 27 (4), 1495–1503. doi:10.1007/s10895-017-2089-z

Lin, K., Qu, H., Tan, Y., Deng, T., Gao, B., and Wei, N. (2021). Effects of the diphenylheptane extract of Alpinia officinarum rhizomes on ethanol-induced gastric ulcers in mice. *Iran. J. Basic Med. Sci.* 24 (5), 657–665. doi:10.22038/ijbms.2021.53644.12068

Liu, Y., Sui, D., Fu, W., Sun, L., Li, Y., Yu, P., et al. (2021). Protective effects of polysaccharides from Panax ginseng on acute gastric ulcers induced by ethanol in rats. *Food Funct.* 12 (6), 2741–2749. doi:10.1039/d0fo02947e

LuMaHuang, F. Y. H., Zhang, Y., Kong, H., Zhao, Y., et al. (2021). Edible and highly biocompatible nanodots from natural plants for the treatment of stress gastric ulcers. *Nanoscale* 13 (14), 6809–6818. doi:10.1039/d1nr01099a

Luo, W. K., Zhang, L. L., Yang, Z. Y., Guo, X. H., Wu, Y., et al. (2021). Herbal medicine derived carbon dots: Synthesis and applications in therapeutics, bioimaging and sensing. *J. Nanobiotechnology* 19 (1), 320. doi:10.1186/s12951-021-01072-3

Maes, M. L., Fixen, D. R., and Linnebur, S. A. (2017). Adverse effects of proton-pump inhibitor use in older adults: A review of the evidence. *Ther. Adv. Drug Saf.* 8 (9), 273–297. doi:10.1177/2042098617715381

Manchala, S., Gandamalla, A., Vempuluru, N. R., Muthukonda Venkatakrishnan, S., and Shanker, V. (2021). High potential and robust ternary LaFeO3/CdS/carbon quantum dots nanocomposite for photocatalytic H2 evolution under sunlight illumination. *J. Colloid Interface Sci.* 583, 255–266. doi:10.1016/j.jcis.2020.08.125

Mousa, A. M., El-Sammad, N. M., Hassan, S. K., Madboli, A. E. N. A., Hashim, A. N., Moustafa, E. S., et al. (2019). Antiulcerogenic effect of Cuphea ignea extract against ethanol-induced gastric ulcer in rats. *BMC Complement. Altern. Med.* 19 (1), 345. doi:10.1186/s12906-019-2760-9

Muhammad, W., Ullah, N., Haroon, M., and Abbasi, B. H. (2019). Optical, morphological and biological analysis of zinc oxide nanoparticles (ZnO NPs) using Papaver somniferum L. *RSC Adv.* 9 (51), 29541–29548. doi:10.1039/c9ra04424h

Nocito, G., Calabrese, G., Forte, S., Petralia, S., Puglisi, C., Campolo, M., et al. (2021). Carbon dots as promising tools for cancer diagnosis and therapy. *Cancers (Basel)* 13 (9), 1991. doi:10.3390/cancers13091991

Radnia, F., Mohajeri, N., and Zarghami, N. (2020). New insight into the engineering of green carbon dots: Possible applications in emerging cancer theranostics. *Talanta* 209, 120547. doi:10.1016/j.talanta.2019.120547

Rahman, Z., Dwivedi, D. K., and Jena, G. B. (2021). The intervention of tert-butylhydroquinone protects ethanol-induced gastric ulcer in type II diabetic rats: The role of Nrf2 pathway. *Can. J. Physiol. Pharmacol.* 99 (5), 522–535. doi:10.1139/cjpp-2020-0173

Ren, S., Wei, Y., Niu, M., Li, R., Wang, R., et al. (2021). Mechanism of rutaecarpine on ethanol-induced acute gastric ulcer using integrated metabolomics and network pharmacology. *Biomed. Pharmacother.* 138, 111490. doi:10.1016/j.biopha.2021.111490

Rickard, J. (2016). Surgery for peptic ulcer disease in sub-saharan africa: Systematic review of published data. *J. Gastrointest. Surg.* 20 (4), 840–850. doi:10.1007/s11605-015-3025-7

Sistani Karampour, N., Arzi, A., Rezaie, A., Pashmforoosh, M., and Kordi, F. (2019). Gastroprotective effect of zingerone on ethanol-induced gastric ulcers in rats. *Med. Kaunas.* 55 (3), 64. doi:10.3390/medicina55030064

Sumbul, S., Ahmad, M. A., Mohd, A., et al. (2011). Role of phenolic compounds in peptic ulcer: An overview. *J. Pharm. Bioallied Sci.* 3 (3), 361–367. doi:10.4103/0975-7406.84437

Sun, L., Zhang, H., Wang, Y., Xiong, Z., Zhao, X., and Xia, Y. (2021). Chitosan-derived N-doped carbon dots for fluorescent determination of nitrite and bacteria imaging. *Spectrochim. Acta A Mol. Biomol. Spectrosc.* 251, 119468. doi:10.1016/j.saa.2021.119468

Tong, T., Hu, H., Zhou, J., Deng, S., Zhang, X., Tang, W., et al. (2020). Glycyrrhizic-acid-based carbon dots with high antiviral activity by multisite inhibition mechanisms. *Small* 16 (13), e1906206. doi:10.1002/smll.201906206

Vinoth Kumar, J., Kavitha, G., Arulmozhi, R., Arul, V., Singaravadivel, S., and Abirami, N. (2021). Green sources derived carbon dots for multifaceted applications. *J. Fluoresc.* 31 (4), 915–932. doi:10.1007/s10895-021-02721-4

Wang, H., Zhang, M., Ma, Y., Wang, B., Shao, M., Huang, H., et al. (2020). Selective inactivation of Gram-negative bacteria by carbon dots derived from natural biomass: Artemisia argyi leaves. *J. Mater Chem. B* 8 (13), 2666–2672. doi:10.1039/c9tb02735a

Wang, T., Luo, H., Jing, X., Yang, J., Huo, M., and Wang, Y. (2021). Synthesis of fluorescent carbon dots and their application in ascorbic acid detection. *Molecules* 26 (5), 1246. doi:10.3390/molecules26051246

Wei, X., Li, L., Liu, J., Yu, L., Li, H., Cheng, F., et al. (2019). Green synthesis of fluorescent carbon dots from gynostemma for bioimaging and antioxidant in zebrafish. *ACS Appl. Mater Interfaces* 11 (10), 9832–9840. doi:10.1021/acsami.9b00074

Xin, Q., Shah, H., Xie, W., Wang, Y., Jia, X., Nawaz, A., et al. (2021). Preparation of blue- and green-emissive nitrogen-doped graphene quantum dots from graphite and their application in bioimaging. *Mater Sci. Eng. C Mater Biol. Appl.* 119, 111642. doi:10.1016/j.msec.2020.111642

Xue, Z., Shi, G., Fang, Y., Liu, X., Zhou, X., Feng, S., et al. (2019). Protective effect of polysaccharides from Radix Hedysari on gastric ulcers induced by acetic acid in rats. *Food Funct.* 10 (7), 3965–3976. doi:10.1039/c9fo00433e

Yan, X., Zhao, Y., Luo, J., Xiong, W., Liu, X., Cheng, J., et al. (2017). Hemostatic bioactivity of novel Pollen Typhae Carbonisata-derived carbon quantum dots. *J. Nanobiotechnology* 15 (1), 60. doi:10.1186/s12951-017-0296-z

Yang, R., Li, J., Xu, X., Xu, K., and Shi, J. (2021). Preventive and therapeutic effects of Lactobacillus rhamnosus SHA113 and its culture supernatant on alcoholic gastric ulcers. *Food Funct.* 12 (16), 7250–7259. doi:10.1039/d1fo00181g

Zhang, M., Cheng, J., Hu, J., Luo, J., Zhang, Y., Lu, F., et al. (2021b). Green Phellodendri Chinensis Cortex-based carbon dots for ameliorating imiquimod-induced psoriasis-like inflammation in mice. *J. Nanobiotechnology* 19 (1), 105. doi:10.1186/s12951-021-00847-y

Zhang, M., Cheng, J., Sun, Z., Kong, H., Zhang, Y., Wang, S., et al. (2019). Protective effects of carbon dots derived from Phellodendri Chinensis Cortex Carbonisata against deinagkistrodon acutus venom-induced acute kidney injury. *Nanoscale Res. Lett.* 14 (1), 377. doi:10.1186/s11671-019-3198-1

Zhang, M., Cheng, J., Zhang, Y., Kong, H., Wang, S., Luo, J., et al. (2020). Green synthesis of Zingiberis rhizoma-based carbon dots attenuates chemical and thermal stimulus pain in mice. *Nanomedicine (Lond)* 15 (9), 851–869. doi:10.2217/nnm-2019-0369

Zhang, W., Dang, G., Dong, J., Li, Y., Jiao, P., Yang, M., et al. (2021a). A multifunctional nanoplatform based on graphitic carbon nitride quantum dots for imaging-guided and tumor-targeted chemo-photodynamic combination therapy. *Colloids Surf. B Biointerfaces* 199, 111549. doi:10.1016/j.colsurfb.2020.111549

Zhao, P., Jin, B., Zhang, Q., and Peng, R. (2021). High-quality carbon nitride quantum dots on photoluminescence: Effect of carbon sources. *Langmuir* 37 (5), 1760–1767. doi:10.1021/acs.langmuir.0c02966

Zhao, Y., Zhang, Y., Kong, H., Zhang, M., Cheng, J., Luo, J., et al. (2020). Haemostatic nanoparticles-derived bioactivity of from Selaginella tamariscina Carbonisata. *Molecules* 25 (3), 446. doi:10.3390/molecules25030446

Zhou, B., Zhang, W., Wu, Y., Yang, Y., Wang, N., Li, J., et al. (2021). Improved efficacy of Panax notoginseng saponin loaded into BSP/alginate microspheres for the treatment of alcoholic gastric ulcers. *Int. J. Pharm.* 596, 120218. doi:10.1016/j.ijpharm.2021.120218

Frontiers in Molecular Biosciences

TYPE Original Research
PUBLISHED 13 July 2023
DOI 10.3389/fmolb.2023.1222415

OPEN ACCESS

EDITED BY
Md Palashuddin Sk,
Aligarh Muslim University, India

REVIEWED BY
Anupriya Baranwal,
RMIT University, Australia
Amaresh Kumar Sahoo,
Indian Institute of Information Technology, Allahabad, India
Madhulekha Gogoi,
North East Institute of Science and Technology (CSIR), India

*CORRESPONDENCE
Hui Kong,
doris7629@126.com
Huihua Qu,
quhuihuadr@163.com
Yan Zhao,
zhaoyandr@163.com

†These authors have contributed equally to this work and share first authorship

RECEIVED 14 May 2023
ACCEPTED 26 June 2023
PUBLISHED 13 July 2023

CITATION
Cui L, Zhang Q, Zhang Y, Li T, Li M, Yuan J, Wu Z, Zhang Y, Kong H, Qu H and Zhao Y (2023), Anxiolytic effects of Chrysanthemum morifolium Ramat Carbonisata-based carbon dots in mCPP-induced anxiety-like behavior in mice: a nature-inspired approach.
Front. Mol. Biosci. 10:1222415.
doi: 10.3389/fmolb.2023.1222415

Anxiolytic effects of Chrysanthemum morifolium Ramat Carbonisata-based carbon dots in mCPP-induced anxiety-like behavior in mice: a nature-inspired approach

Luming Cui[1†], Qian Zhang[2†], Yifan Zhang[1], Tingjie Li[3], Menghan Li[1], Jinye Yuan[1], Zhiyi Wu[1], Yue Zhang[4], Hui Kong[1*], Huihua Qu[5*] and Yan Zhao[1*]

[1]School of Traditional Chinese Medicine, Beijing University of Chinese Medicine, Beijing, China, [2]Qingdao Zhonghengneng Environmental Science Engineering Research Institute Co., Ltd, Qingdao, China, [3]School of Chinese Materia Medica, Beijing University of Chinese Medicine, Beijing, China, [4]School of Life Sciences, Beijing University of Chinese Medicine, Beijing, China, [5]Center of Scientific Experiment, Beijing University of Chinese Medicine, Beijing, China

Introduction: Anxiety disorders have emerged as a predominant health concern, yet existing pharmacological treatments for anxiety still present various challenges. Chrysanthemum morifolium Ramat Carbonisata (CMRC) has been utilized in China for approximately 400 years as a therapeutic intervention for anxiety disorders. In this study, a novel type of carbon dots derived from the decoction of Chrysanthemum morifolium Ramat Carbonisata (CMRC-CDs) was identified and isolated, and their morphological structure and functional groups were characterized. Furthermore, the effects of CMRC-CDs on m-chlorophenylpiperazine (mCPP)-induced anxiety-like behaviour in mice were examined and quantified. In order to investigate the potential mechanisms of their anxiolytic effects, concentrations of hypothalamic-pituitary-adrenal (HPA) axis hormones, amino acid neurotransmitters, and monoamine neurotransmitters were measured.

Methods: In this study, we synthesized CMRC-CDs and evaluated their potential anti-anxiety effects in a controlled experiment involving 48 male ICR mice. The mice were randomly divided into six groups, treated with CMRC-CDs at different doses for 14 days, and subjected to Open-Field (OF) and Elevated Plus Maze (EPM) tests. Post-behavioral evaluations, blood samples and brain tissues were collected for neurotransmitter and Hypothalamic-Pituitary-Adrenal (HPA) axis hormone quantification via ELISA. Additionally, cytotoxicity of CMRC-CDs was assessed using a Cell Counting Kit-8 (CCK-8) assay on RAW 264.7 cells.

Results and Discussion: CMRC-CDs were spherical and homogeneously dispersed, with diameters ranging from 1.4 to 4.0 nm and an abundance of chemical groups on their surface. In the open-field (OF) test, mice pre-treated with CMRC-CDs demonstrated an increased proportion of time spent in the central area and a higher frequency of entries into the central area. In the elevated plus maze (EPM) test, mice pre-treated with CMRC-CDs exhibited a greater number of entries into the open arm and an extended duration spent in the open arm. CMRC-CDs were observed to decrease serum concentrations of corticotropin-releasing hormone (CRH), adrenocorticotropic hormone (ACTH), and corticosterone (CORT). Furthermore, CMRC-CDs were found to increase γ-aminobutyric acid (GABA) and 5-hydroxytryptamine (5-HT) levels, while concurrently reducing glutamic acid (Glu) concentrations in brain tissue. CMRC-CDs demonstrated anxiolytic effects, which may be attributed to their modulation of hormones and neurotransmitters. This finding suggests the potential therapeutic value of CMRC-CDs in the clinical treatment of anxiety disorders.

KEYWORDS

carbon dots, Chrysanthemum morifolium Ramat, anxiety disorder, HPA axis, neurotransmitters

1 Introduction

The prevalence of mental disorders has steadily increased since 1990. By 2019, anxiety disorders had emerged as one of the leading causes of global burden, ranking 24th among the primary causes of disability-adjusted life years ("Global, Regional, and National Burden of 12 Mental Disorders in 204 Countries and Territories, 1990–2019: A Systematic Analysis for the Global Burden of Disease Study, 2019"2022). In recent years, the COVID-19 pandemic has further escalated the prevalence of anxiety disorders (Santomauro et al., 2021). According to one study estimate, one-third of adults experienced anxiety during the global coronavirus disease outbreak in 2019 (Delpino et al., 2022). Consequently, the treatment of anxiety disorders is garnering increased attention.

The pathophysiology of anxiety disorders remains an area ripe for further exploration, but it is generally believed to be closely associated with the hypothalamic-pituitary-adrenocortical (HPA) axis and neurotransmitter secretion (Meldrum, 2000; Jacobson, 2014; Olivier and Olivier, 2020). Currently, prevalent anti-anxiety medications include benzodiazepines, selective serotonin reuptake inhibitors (SSRIs), and serotonin-noradrenaline reuptake inhibitors (SNRIs). Nevertheless, these drugs present several challenges, such as benzodiazepines causing side effects like increased talkativeness, emotional release, excitement, and excessive movement; SSRIs leading to sexual dysfunction; and both causing potent withdrawal symptoms (Petursson, 1994; Mancuso et al., 2004; Bala et al., 2018; Horowitz and Taylor, 2019). These issues have prompted a search for and investigation into more effective and safer anti-anxiety drugs.

Carbon dots (CDs), featuring ultra-fine dimensions of below 10 nm, were first identified in 2004 (Cui et al., 2021). Due to their minimal cytotoxicity, superior biocompatibility, chemical stability, negligible toxicity, and substantial surface area-to-volume ratio, they are finding escalating usage in the realm of biomedical applications (Durán et al., 2016; Jaleel and Pramod, 2018; Singh et al., 2018; Ross et al., 2020; Khayal et al., 2021; Mansuriya and Altintas, 2021). A myriad of studies have underscored the potential of carbon dots, suggesting their prospective utility as innovative carriers for drug delivery systems targeting the central nervous system. These studies further posit that carbon dots may serve as a therapeutic intervention for an array of psychiatric and cognitive disorders (Ashrafizadeh et al., 2020; Henna et al., 2020). For instance, nanodiamonds have been observed to exhibit neuroprotective effects against Alzheimer's disease (Alawdi et al., 2017), graphene oxide has been shown to mitigate neurotoxicity and improve cognitive impairment (Ren et al., 2018; Chu et al., 2021), and graphene quantum dots have been found to enhance learning abilities (Xiao et al., 2016).

In recent years, the number of raw material options for synthesizing CDs has expanded significantly, and the extraction of CDs from various natural sources, especially plants, is attracting increasing attention due to its convenience and affordability. As a result, numerous studies have emerged on the biomedical applications of carbon dots derived from herbal medicines, particularly carbonized traditional herbs (Chen et al., 2019; Luo et al., 2021; Li et al., 2022). A variety of herbs used in traditional Chinese medicine to treat mental symptoms have been investigated for their active ingredients and mechanisms of action, such as Rhodiola rosea, ginseng, and Ginkgo biloba (S. Lee and Rhee, 2017; Liu et al., 2015; Xie et al., 2018; Panossian et al., 2010). However, the herbs that have been evaluated so far represent only a small proportion of those in daily use, suggesting that the effects and mechanisms of single herbs in improving mood disorders still warrant further research.

Given this background, we embarked on a study aimed at exploring the anxiolytic effects and underlying mechanisms of carbonized derivatives sourced from a commonly used and widely available traditional herb. Chrysanthemum morifolium Ramat (CMR), known as "Jv Hua" in Chinese, boasts a longstanding medicinal tradition within China. Chrysanthemum morifolium Ramat Carbonisata (CMRC) is a CMR product obtained through the carbonization process. It has been used as a sedative in China since its first documentation in the "Guide to Clinical Practice with Medical Records" over 300 years ago. Nevertheless, its efficacy and underlying mechanisms remain incompletely understood, highlighting the need for further investigation.

In this study, we synthesized CMRC-based carbon dots (CMRC-CDs) using an eco-friendly approach and evaluated their physicochemical properties, such as morphology and functional groups. We utilized a variety of analytical techniques, encompassing roadmaps, heat maps, and regional dwell times, to yield a thorough evaluation of the behavioral outcomes. These metrics were utilized to determine the capacity of CMRC-CDs to alleviate anxiety-like behavior induced by mCPP administration in mice. The underlying mechanisms of the anxiolytic effects were explored by measuring the levels of corticotropin-releasing hormone (CRH), adrenocorticotropic hormone (ACTH), corticosterone (CORT), 5-hydroxytryptamine (5-HT), dopamine (DA),

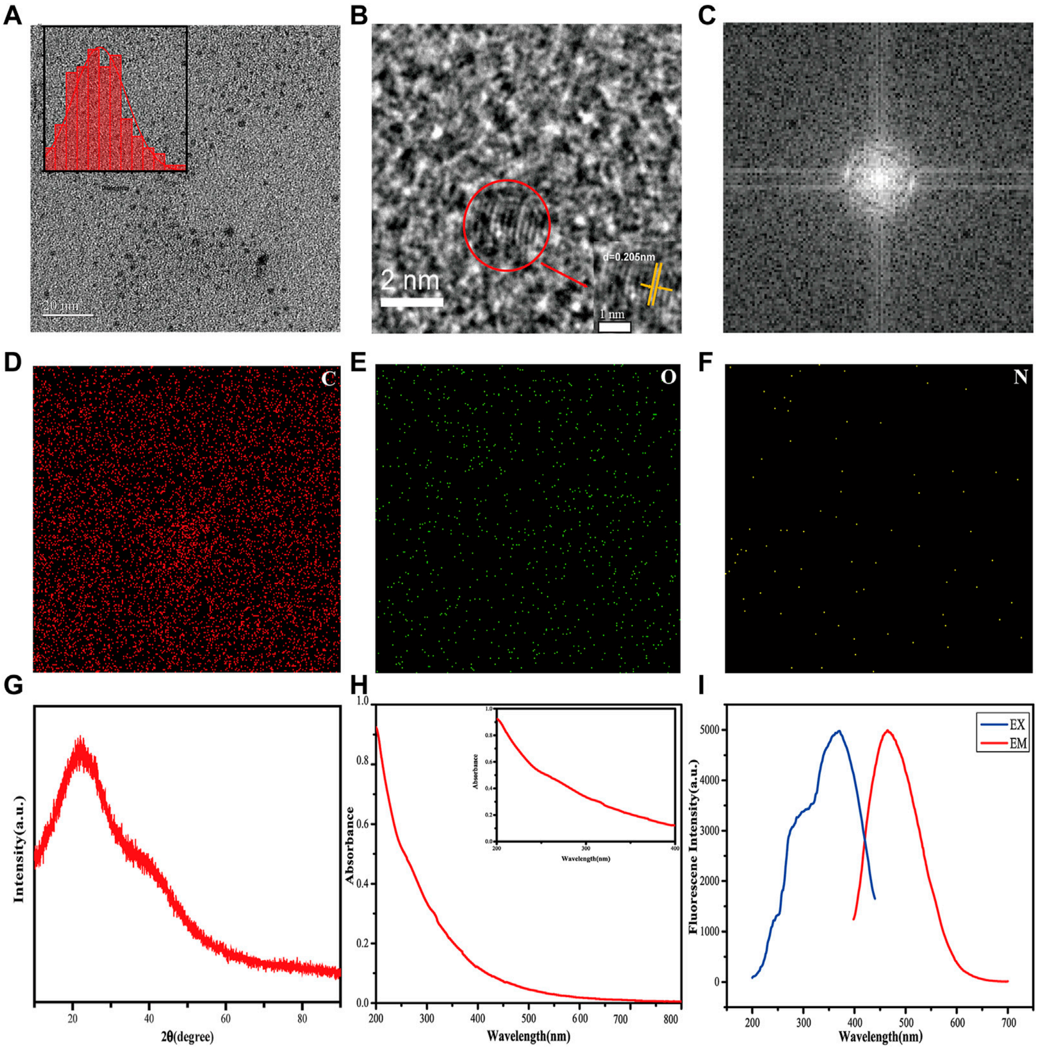

FIGURE 1
Characterization of CMRC-CDs. **(A)** Transmission electron microscopy (TEM) image of CMRC-CDs, with histogram depicting particle size distribution of CMRC-CDs. **(B)** High-resolution TEM (HRTEM) image of individual CMRC-CDs **(C)** FFT image processing was performed on CMCR-CDs. **(D–F)** TEM mapping of CMRC-CDs, showing the main elements in carbon dots, including C, O, and N. **(G)** XRD pattern spectrum of CMRC-CDs. **(H)** UV-vis absorption spectrum of CMRC-CDs. **(I)** Fluorescence excitation spectra and emission spectra of CMRC-CDs.

norepinephrine (NE), glutamic acid (Glu), and γ-aminobutyric acid (GABA). Our findings may provide a valuable contribution towards comprehending the anxiolytic properties of CMRC-CDs and offer valuable insights into the potential utility of carbon dots obtained from traditional herbs for the development of novel, efficacious, and safer anti-anxiety therapies.

2 Results

2.1 Analysis of the properties and features of CMRC-CDs

As depicted in Figure 1A, TEM micrographs reveal that the CMRC-CDs exhibit a nearly spherical morphology and are uniformly dispersed throughout the sample. The diameters of the CMRC-CDs span between 1.4 and 4.0 nm, with a majority of particles concentrated within the 1.8–2.8 nm interval. Furthermore, HRTEM imaging demonstrates a lattice spacing of 0.205 nm for the CMRC-CDs, as illustrated in Figure 1B. Figure 1C presents the results obtained from the Fast Fourier Transform (FFT) analysis performed on CMRC-CDs, facilitating a clearer visualization of the lattice structure.

Figures 1D–F depict TEM elemental mappings of the CMRC-CDs, illustrating the primary constituents within the carbon dots as carbon (C), oxygen (O), and nitrogen (N), while concurrently displaying their spatial distribution.

Figure 1G illustrates a distinct diffraction peak at 2θ = 22.0° in the X-ray diffraction (XRD) pattern of CMRC-CDs. When considered in conjunction with the High-Resolution Transmission Electron Microscopy (HRTEM) imaging results, it becomes apparent that CMRC-CDs represent a carbon structure that resides between amorphous and lattice morphologies.

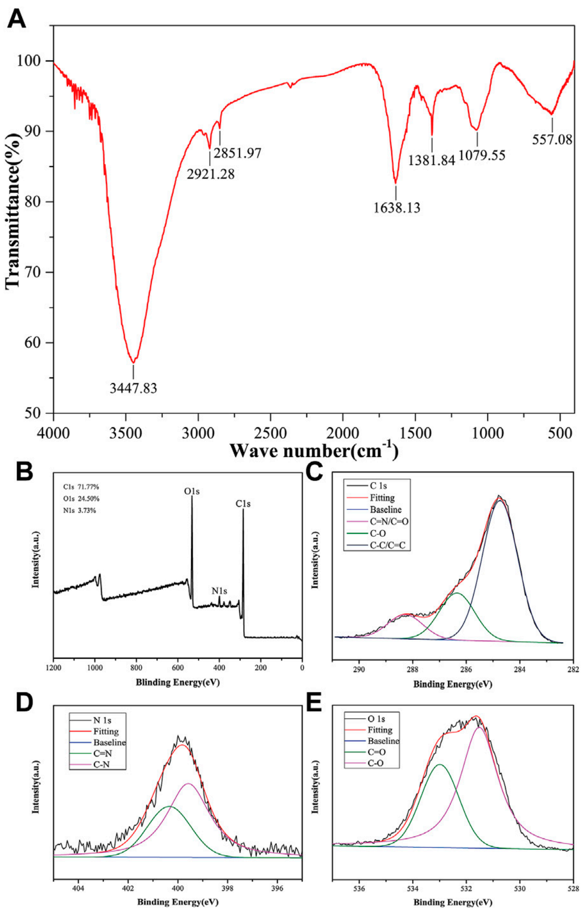

FIGURE 2
Elemental composition and functional group of CMRC-CDs. **(A)** Fourier transform infrared (FTIR) spectrum of CMRC-CDs. **(B)** Full survey spectrum of X-ray photoelectron spectroscopy (XPS). **(C–E)** High-resolution survey spectra of different elements by XPS.

In the aqueous solution, the UV-Vis absorption spectrum of the CMRC-CDs exhibited a subtle absorption peak at 310 nm, which is indicative of the π–π* electronic transitions of the aromatic C=C and C≡C bonds (Figure 1H) (Y. Zhang et al., 2021). Furthermore, the fluorescence characterization of the CMRC-CDs revealed a maximum emission at 465 nm upon excitation at a wavelength of 369 nm (Figure 1I).

To gain further insights into the surface functional groups of CMRC-CDs, FTIR spectroscopy was employed, and the corresponding results are presented in Figure 2A. Upon purification, the CMRC-CDs exhibited characteristic peaks at 3,447, 2,921, 2,851, 1,638, 1,381, 1,079, and 557 cm^{-1}. The peak observed at 3,447 cm^{-1} can be attributed to the stretching vibrations of O-H and N-H functional groups, whereas the C-H stretching vibrations are discernible through the peaks at 2,921 and 2,851 cm^{-1}, respectively (Atchudan et al., 2020). The peak arising at 1,639 cm^{-1} is associated with C=O groups, while the C-H and N-H functional groups give rise to the peak at 1,381 cm^{-1} (Muhammad et al., 2019). Lastly, the peak observed at 1,058 cm^{-1} can be ascribed to the C-O-C absorption vibrations (Muhammad et al., 2019; Wei et al., 2019).

XPS was utilized to execute an elemental analysis of CMRC-CDs; the obtained results revealed that CMRC-CDs primarily consist of carbon (71.77%), oxygen (24.50%), and nitrogen (3.73%). The binding energies corresponding to C 1s, O 1s, and N 1s are delineated by three distinct peaks in Figure 2B, observed respectively at 284.8, 531.8, and 400.0 eV. Three prominent peaks can be seen in the high-resolution C 1s XPS spectra with binding energies of 284.8, 286.4, and 288.3 eV, which are associated with the C-C/C=C, C-O, and C=N/C=O bonds, respectively (Figure 2C) (Godavarthi et al., 2017). Characteristic peaks are visible in the high-resolution O 1s spectra at 531.5 and 533.0 eV, which can be individually attributed to the C-O and C=O functional groups (Figure 2D). In the N 1s spectra, two peaks emerge, corresponding to the N-H and C=N bonds at approximately 399.6 and 400.3 eV, respectively (Figure 2E) (Li et al., 2019).

In conclusion, we conducted a comprehensive investigation of the physical appearance and elemental composition of CMRC-CDs using a combination of techniques, including TEM, HRTEM, TEM mapping, FTIR, and XPS. The consistent results from these methods indicate that the purified CMRC-CDs predominantly consist of carbon, oxygen, and nitrogen elements. The CMRC-CDs feature surface adornment with multiple functional groups, encompassing carbonyl, amino, and hydroxyl entities.

2.2 Effect of CMRC-CDs on mCPP-treated mice in the of test

Figure 3 delineates the spatiotemporal dynamics of mice during the open-field (OF) test. As depicted in Figure 3C, compared to the control group, which spent 18.75 ± 5.46% of the time in the central zone, the model group demonstrated a significant reduction, spending only 12.24 ± 2.99% of the time in the same area ($p < 0.01$). In contrast, central zone occupancy increased in the medium- (19.27 ± 3.23%), and low-dose groups (18.39 ± 3.91%) relative to the model group ($p < 0.05$), with a more pronounced enhancement observed in the positive and high-dose groups ($p < 0.01$). Figure 3D presents the frequency of central zone entries as a proportion of total entries across all areas. The model group demonstrated a marked reduction in central zone entry proportion (18.24 ± 4.85%) relative to the control group (39.83 ± 7.62%, $p < 0.01$). Conversely, the positive (43.99 ± 6.09%), high- (38.37 ± 6.39%), medium- (34.55 ± 3.12%), and low-dose groups (33.87 ± 3.59%) all displayed a substantial increment in comparison to the model group ($p < 0.01$). These findings indicate that each dosage administration group effectively increased the inclination of mice to explore and remain in the open central area, as opposed to the model group. This trend is further visually exemplified in the group mean heatmap (Figure 3A) and the movement trajectory map (Figure 3B). Figure 3E reveals the aggregate locomotor distance traversed by the mice, with no significant discrepancies observed among the groups. Consequently, it can be inferred that diazepam and CMRC-CDs modulate the exploratory predilection of mice in the open field without affecting the total distance covered.

2.3 Effect of CMRC-CDs on mCPP-treated mice in the EPM test

Figures 4A, B depict the movement of distinct mouse groups in the elevated cross-maze experiment using mean heatmaps and

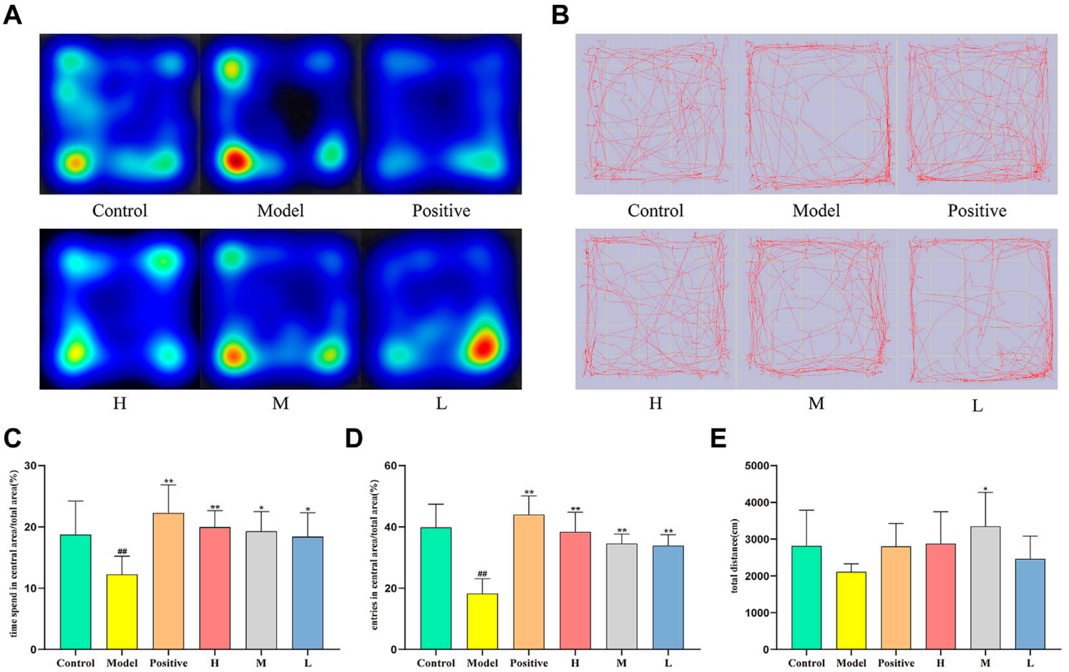

FIGURE 3
Effect of CMRC-CDs on mCPP-treated mice in the OF test. **(A)** Mean heatmap of mice activity in the OF test. **(B)** Path diagram of mice activity in OF test. **(C)** The proportion of time spent in the central zone relative to the total area (%). **(D)** The percentage of entries made into the central area relative to the total area (%). **(E)** Total distance (cm). The data were presented as the mean ± standard deviation (SD). #p < 0.05 and $^{\#\#}p$ < 0.01 vs. control group, *p < 0.05 and **p < 0.01 compared to the model group.

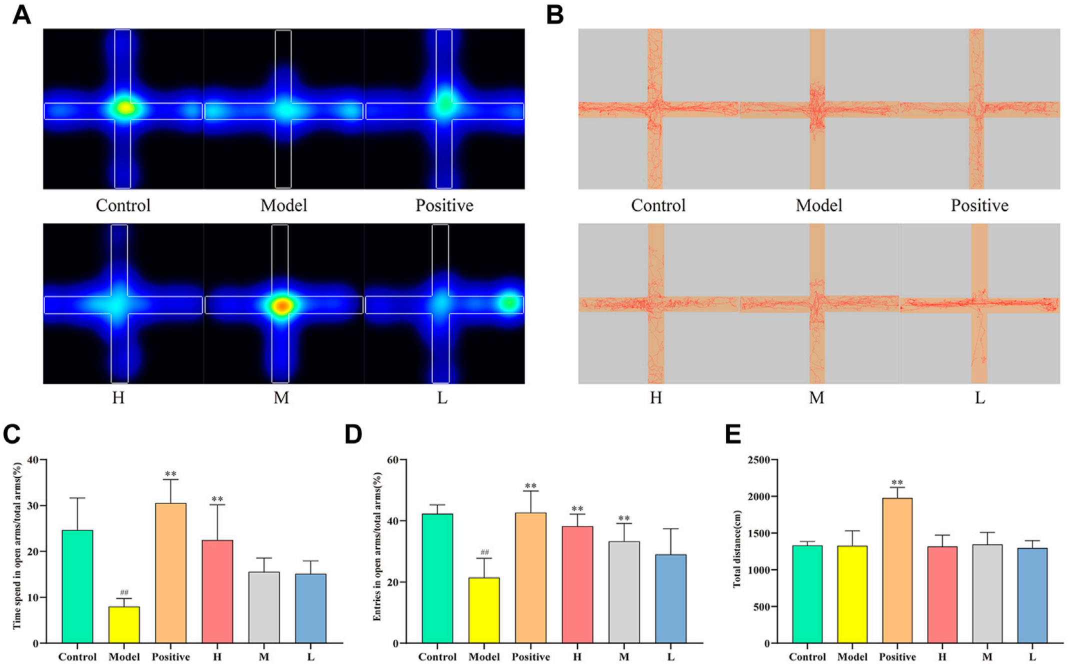

FIGURE 4
Effect of CMRC-CDs on mCPP-treated mice in the EPM test. **(A)** Mean heatmap of mice activity. **(B)** Path diagram of mice activity in EPM test. **(C)** The proportion of time spent in open arms relative to total arms (%). **(D)** The percentage of entries made into open arms relative to total arms (%). **(E)** Total distance (cm). The data were presented as the mean ± standard deviation. #p < 0.05 and ##p < 0.01 compared to control group, *p < 0.05 and **p < 0.01 compared to the model group.

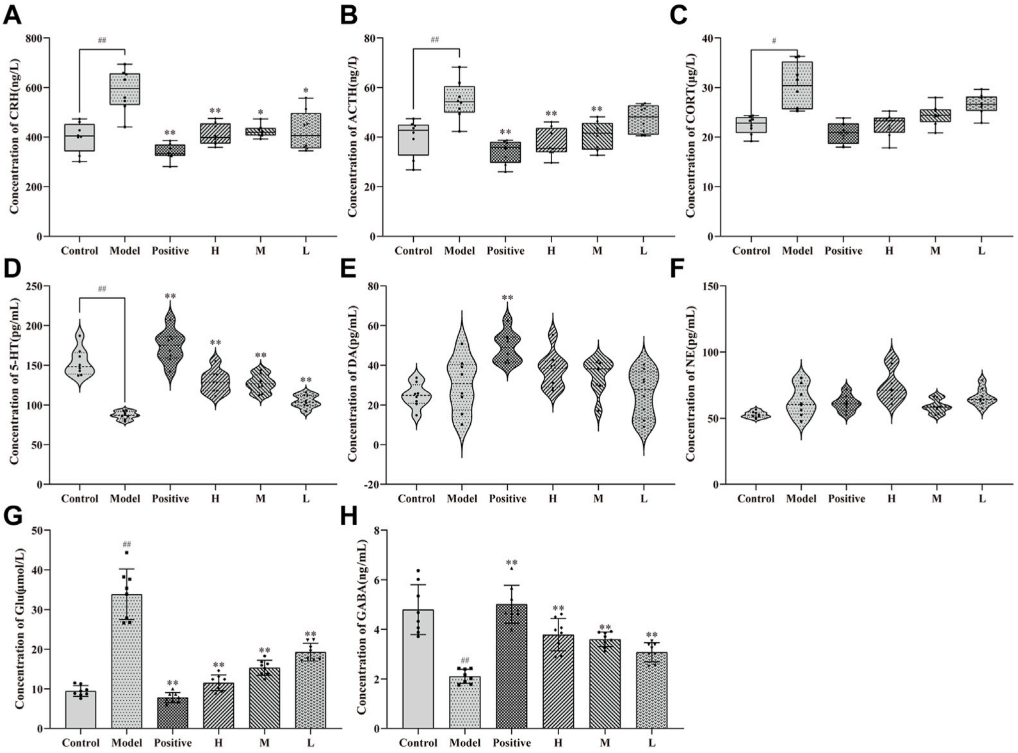

FIGURE 5
Effect of CMRC-CDs on HPA hormone and Neurotransmitter. The serum concentration of **(A)** CRH, **(B)** ACTH, and **(C)** CORT. Brain tissue homogenization concentration of **(D)** 5-HT **(E)** DA, **(F)** NE, **(G)** Glu, and **(H)** GABA. n = 8/group. $^{\#}p < 0.05$ and $^{\#\#}p < 0.01$ compared to the control group, $^{*}p < 0.05$ and $^{**}p < 0.01$ compared to the model group.

roadmaps, respectively. The closed arms are represented horizontally, while the open arms are shown vertically. In Figure 4A, color-coded regions delineate mouse movement, with red, yellow, green, and blue indicating the amount of time spent in descending order. The red line in Figure 4B traces the specific path taken by the mice. As observed, the model group's activity area was considerably smaller compared to the control group, primarily restricted to the closed arms. Conversely, each dosing group broadened their scope of motion and ventured more extensively into open arms. Notably, the positive and high-dose groups demonstrated greater efficacy than the medium- and low-dose groups. Figure 4C reveal that the time spent in open arms was significantly lower in the model group (8.00 ± 1.73%) than in the control group (24.67 ± 6.96%, $p < 0.01$). The positive (30.54 ± 5.09%) and high-dose groups (22.47 ± 7.70%) exhibited significantly higher values than the model group ($p < 0.01$). Although no statistically significant increase was observed in the medium-dose (15.56 ± 3.00%) and low-dose groups (15.13 ± 2.79%) relative to the model group, an upward trend was evident. Figure 4D presents the ratio of open arm entries to total arm entries for each group. The model group (21.47 ± 6.26%) had significantly lower values than the control group (42.31 ± 2.88%, $p < 0.01$). Conversely, the positive (42.66 ± 7.06%), high- (38.25 ± 3.92%), and medium-dose groups (33.29 ± 5.85%) displayed significantly higher values compared to the model group ($p < 0.01$). Despite the lack of statistically significant differences observed between the low-dose group (29.01 ± 8.40%) and the model group, an increasing trend was still apparent. Lastly, Figure 4E illustrates the total distance traveled by each group, with a significant increase observed in the positive group relative to the model group, but no significant differences detected among the remaining groups.

2.4 Effects of CMRC-CDs on HPA axis hormones and neurotransmitters in mCPP-treated mice

After 14 days of treatment with CMRC-CDs followed by 2 days of behavioral testing, alterations in the levels of HPA axis hormones and neurotransmitters in mice were observed, as illustrated in Figure 5. Specifically, changes in HPA axis hormones in mice serum are demonstrated in Figures 5A–C. In comparison to the control group (CRH: 399.32 ± 60.12 ng/L; ACTH: 39.87 ± 7.42 ng/L; CORT: 22.41 ± 1.82 μg/L), the serum concentrations of CRH, ACTH, and CORT were significantly elevated in the mCPP-treated mice (CRH: 588.71 ± 85.07 ng/L, $p < 0.01$; ACTH: 54.77 ± 7.84 ng/L, $p < 0.01$; CORT: 30.30 ± 4.57 μg/L, $p < 0.05$). Nevertheless, each dosing group demonstrated a varied extent of reduction relative to the model group. Notably, the most pronounced decreasing trend was observed in the positive group (CRH: 339.33 ± 32.93 ng/L, $p < 0.01$; ACTH: 173.88 ± 20.17 ng/L, $p < 0.01$; CORT: 20.89 ± 2.15 μg/L, $p < 0.01$). The high-dose group exhibited a smaller reduction (CRH: 410.75 ± 43.02 ng/L, $p < 0.01$; ACTH: 129.56 ± 14.31 ng/L, $p < 0.01$; CORT: 22.50 ± 2.35 μg/L, $p <$

0.05) in comparison to the positive group. Meanwhile, the group administered a medium dosage (CRH: 423.32 ± 24.61 ng/L, $p < 0.05$; ACTH: 127.15 ± 11.23 ng/L, $p < 0.01$; CORT: 24.44 ± 2.10 μg/L, $p > 0.05$) demonstrated a less pronounced reduction compared to the group receiving a high dosage, and the group administered a low dosage (CRH: 423.89 ± 80.81 ng/L, $p < 0.05$; ACTH: 104.68 ± 8.08 ng/L, $p < 0.01$; CORT: 26.61 ± 2.09 μg/L, $p > 0.05$) exhibited a smaller reduction than the medium-dose group. These findings suggest that CMRC-CDs can decrease serum concentrations of CRH, ACTH, and CORT in mice in a dose-dependent manner.

Figure 5D illustrates the disparities in serum 5-HT concentrations among the groups, revealing a notable reduction in the model group (87.04 ± 5.00 pg/mL, $p < 0.01$) in comparison to the control group (153.68 ± 17.28 pg/mL). Furthermore, a marked elevation was observed in the positive (173.88 ± 20.17 pg/mL, $p < 0.01$), high- (129.56 ± 14.31 pg/mL, $p < 0.01$), medium- (127.15 ± 11.23 pg/mL, $p < 0.01$), and low-dose groups (104.68 ± 8.08 pg/mL, $p < 0.01$) when contrasted with the model group. Figure 5E depicts DA concentrations in the serum of each experimental group, exhibiting no significant divergence between the model and control groups or between the distinct CMRC-CDs concentrations and the model group. Nevertheless, a considerable increase was detected in the positive group relative to the model group ($p < 0.01$). Figure 5F demonstrates that the NE concentrations in the serum of mice from each group did not exhibit significant variations, indicating that the intervention strategy employed in this study did not exert a substantial impact on the NE concentrations of the mice.

Figures 5G, H depict the alterations in the concentrations of amino acid neurotransmitters in the brain tissue of mice subjected to various intervention strategies. As illustrated in Figure 5G, the model group exhibited a marked elevation in Glu concentrations (33.85 ± 6.36 μmol/L, $p < 0.01$) compared to the control group (9.45 ± 1.35 μmol/L). Conversely, the positive (7.79 ± 1.27 μmol/L, $p < 0.01$), high- (11.52 ± 1.98 μmol/L, $p < 0.01$), medium- (15.32 ± 1.89 μmol/L, $p < 0.01$), and low-dose groups (19.27 ± 2.23 μmol/L, $p < 0.01$) all demonstrated significantly diminished Glu concentrations relative to the model group. Figure 5H presents an inverse trend for GABA concentrations. Relative to the control group (4.80 ± 1.00 ng/L), the model group displayed a significant reduction in GABA concentrations (2.11 ± 0.29 ng/L, $p < 0.01$). In contrast, the positive (5.01 ± 0.76 ng/L, $p < 0.01$), high- (3.78 ± 0.65 ng/L, $p < 0.01$), medium- (3.60 ± 0.29 ng/L, $p < 0.01$), and low-dose groups (3.08 ± 0.39 ng/L, $p < 0.01$) all exhibited significantly elevated GABA concentrations when compared to the model group. These findings suggest that CMRC-CDs can modulate Glu and GABA concentrations in a dose-dependent manner, resulting in decreased Glu levels and increased GABA levels in the brain tissue of mice. Figure 6 briefly illustrates the entire experimental procedure.

2.5 Cytotoxicity of CMRC-CDs

In order to assess the cytotoxicity of CMRC-CDs, we employed the murine mononuclear macrophage cell line, RAW 264.7. The cell survival rate was measured after 24 h of exposure to various concentrations of CMRC-CDs, ranging from 19.53 to 1,250 μg/mL, as depicted in Figure 7. Our findings revealed a marked decrease in cell viability at concentrations between 312.5 and 1,250 μg/mL in comparison to the control group ($p < 0.01$), suggesting that CMRC-CDs exert an inhibitory effect on cell proliferation within this concentration range. Interestingly, at a concentration of 156.25 μg/mL, no significant difference in cell viability was observed in relation to the control. Furthermore, cell viability demonstrated a significant enhancement at concentrations between 19.53 and 78.13 μg/mL when compared to the control ($p < 0.01$). Taken together, these results suggest that CMRC-CDs exhibit low cytotoxicity at concentrations below 156.25 μg/mL, indicating their potential biocompatibility for various applications.

3 Discussion

Anxiety disorders, representing a predominant health issue in the 21st century, are governed by intricate mechanisms that are not yet fully comprehended. Current understanding implicates neurotransmitters and HPA axis-related hormones in the development of anxiety. Upon HPA axis activation, the hypothalamic paraventricular nucleus synthesizes CRH, which enters the hypophyseal portal blood, subsequently reaching the anterior pituitary to stimulate ACTH synthesis. ACTH, released into the bloodstream, reaches the adrenal cortex and promotes glucocorticoid biosynthesis and release, including corticosterone (Tafet and Nemeroff, 2020). A notable proportion of individuals identified as having chronic anxiety disorders demonstrate heightened activity in the HPA axis (G. E. Tafet et al., 2001; Risbrough and Stein, 2006), suggesting a strong association between elevated HPA axis-related hormones and anxiety (Arborelius et al., 1999; Kinlein et al., 2019), particularly in children experiencing stress-induced events (Faravelli, 2012; Liu and Wang, 2020). Several studies have demonstrated that a variety of anxiolytic drugs, such as tricyclic antidepressants (TCAs), selective serotonin reuptake inhibitors (SSRIs), and benzodiazepines (BZDs), possess the capacity to modulate the hypothalamic-pituitary-adrenal (HPA) axis (Barden et al., 1995; L S Brady et al., 1991; Brady et al., 1992), such as escitalopram's inhibitory effect on CRH and cortisol (Lenze et al., 2011; Flandreau et al., 2013; Benatti et al., 2018).

Neurotransmitters, another group of substances intimately linked to anxiety production, primarily encompass Glu, GABA, 5-HT, DA, and NE. Glu and GABA, quintessential neurotransmitters within the Central Nervous System (CNS), respectively govern excitatory and inhibitory neurotransmission. Disruptions in excitatory/inhibitory (E/I) balance underpin numerous neuropsychiatric disorders, including anxiety disorders (Prager et al., 2016; Yu et al., 2020). As one of the most phylogenetically ancient neurotransmitters, 5-HT is abundant in the cerebral cortex and synapses, regulating a wide array of brain activities, such as mood modulation (Wirth et al., 2017). Alterations in serotonin 5-HT levels have been shown to substantially impact anxiety-related behaviors (Riedel et al., 2002; Pobbe et al., 2011; Zangrossi and Graeff, 2014), while SSRIs have emerged as first-line therapy for anxiety (H. J. Lee and Stein, 2023). SNRIs, also employed as first-line clinical agents, imply an effect of NE on mood. Hyperactivity of the central noradrenaline system can potentially result in a range of symptoms, such as insomnia, emotional

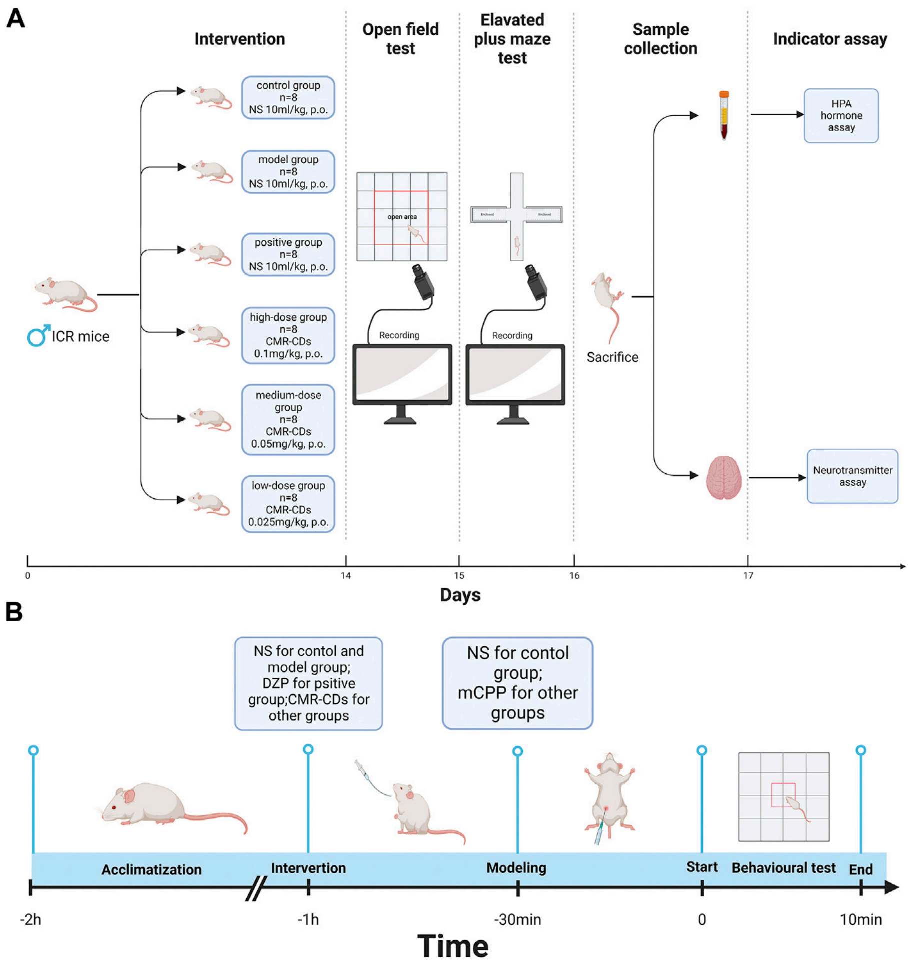

FIGURE 6
Diagram of the experimental procedure. **(A)** Intervention methods, behavioral testing methods, sample collection, and indicator testing. **(B)** Behavioral testing day process, including site adaptation, gavage intervention, modelling, and behavioral test (Created with BioRender.com).

instability, irritability, and anxiety (Yamamoto et al., 2014). According to an expanding corpus of evidence from human brain imaging and preclinical animal research, the mesocorticolimbic dopaminergic system is also suggested to be involved in anxiety disorders (Wee et al., 2008; Zweifel et al., 2011; Russo and Nestler, 2013; Berry et al., 2019).

Due to the complexity and incomplete understanding of anxiety disorder pathogenesis, treating these disorders presents numerous challenges. Current first-line clinical drugs, such as TCAs, SSRIs, and BZDs, are associated with unstable efficacy, significant side effects, or addiction. Consequently, the pursuit of novel anti-anxiety medications remains ongoing. Nanomaterials, characterized by distinct physicochemical properties, have demonstrated promising biological implications in the field of psychiatric disorders (Xue et al., 2016; Ran and Xue, 2018). Furthermore, nanoparticles can traverse the blood-brain barrier (BBB) via receptor-mediated endocytosis, and functionalization or modification facilitates a variety of nanoparticles to cross the BBB through protein and protein-associated receptor interactions (Ran and Xue, 2018). As such, nanoparticles can also serve as drug carriers (Wang et al., 2017). This suggests that nanomedicines may represent potential candidates for the next-generation of anti-anxiety therapeutics.

Traditional herbal medicine, usually derived from natural plants and characterized by its accessibility and lower potential for addiction, represents another promising research avenue. Various herbal medicines have been demonstrated the capacity to ameliorate mood disorders through a range of mechanisms. For instance, Hypericum perforatum exhibits antidepressant properties akin to those of TCAs and SSRIs(Zirak et al., 2019), while Radix rehmanniae extract may exert anxiolytic effects by modulating brain neurotransmitters and neurotrophic proteins (Zhou et al., 2019). Moreover, a specific decoction has been shown to significantly improve cognitive and mood disorders by regulating the GABA/Glu pathway (Xu et al., 2022).

Utilizing various characterization techniques, such as high-resolution electron microscopy, FTIR spectroscopy, and XPS spectroscopy, this study uncovers the presence of carbon dots in Chrysanthemum morifolium Ramat Carbonisata - an herb that has been traditionally used for over 400 years to treat mental illness. The 1.4–4.0 nm diameter of the CMRC-CDs and the abundance of functional groups on their surface suggest their potential as

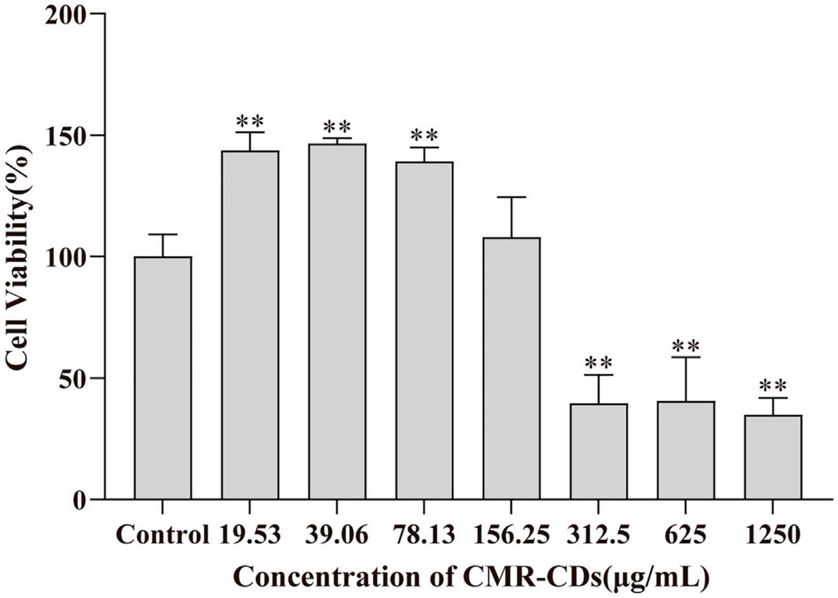

FIGURE 7
Cell viability for 24 h by CCK-8 method. *$p < 0.05$ and **$p < 0.01$ compared to the control group.

biologically active nanomaterials. Moreover, considering the novelty of these nanoparticles, addressing safety concerns is of paramount importance. CCK-8 assay results demonstrate that CMRC-CDs exhibit negligible toxicity at concentrations below 156.25 μg/mL.

mCPP, a metabolite of trazodone and nefazodone, functions as an agonist for the 5-HT receptor (Pigott et al., 1993; Barbhaiya et al., 1995; Eriksson, 1999). Empirical evidence demonstrates that mCPP injections can modulate the performance of mice in behavioral experiments, and induce anxiety in humans (N. Zhang et al., 2018; Pigott et al., 1993). The OF test is a widely employed paradigm in animal psychology, where subjects are positioned in the center or near the perimeter of the apparatus. In such settings, rodents innately exhibit a preference for navigating the periphery, rather than the central region of the open field. Anxiolytic effects are signified by prolonged time allocation within the central zone and an increased ratio of central area/total activity (Prut and Belzung, 2003). In the present investigation, the square field was subdivided into smaller 5 × 5 squares, designating the central nine squares as the central region. The trajectory of mice within the open field over a 5-min interval was monitored and assessed via video recording. Subsequent calculations were made for the proportion of time spent in the central area relative to the total area, the ratio of entries into the central area to the total area, and the cumulative distance traversed. Our findings reveal that CMRC-CDs substantially enhanced the frequency of mice entering the central region and the proportion of time allocated within this designated area.

In the EPM test, an apparatus comprising four elevated arms arranged in a cross-shaped configuration is utilized to assess anxiety-related behaviors in rodents. The EPM consists of two opposing enclosed arms with walls and two opposing open arms, devoid of any barriers. In the test, experimental mice are placed in the central area of the maze and allowed to explore for a defined short period of time. Given their innate aversion to open or elevated spaces, mice displaying lower anxiety levels will exhibit a higher frequency of open arms visits (Kraeuter, Guest, and Sarnyai, 2019). Our findings demonstrate that the administration of CMRC-CDs results in a significant increase in the proportion of entries to open arms and the duration of time spent in the open arms. Importantly, this effect is dose-dependent, as the observed increase in open arms' exploration becomes more pronounced with escalating doses of CMRC-CDs. The consistency of the outcomes from both behavioral tests provides strong evidence that CMRC-CDs may ameliorate mCPP-induced anxiety-like behavior in a dose-dependent manner. Notably, there was no substantial difference in the total distance traversed by the mice in either test, implying that CMRC-CDs selectively influence behavioral tendencies without affecting locomotor capabilities. This observation further underscores the potential of CMRC-CDs as a targeted intervention for anxiety-like behaviors in mice.

To elucidate the potential mechanisms underpinning the anxiolytic properties of CMRC-CDs, we quantified the concentrations of HPA axis hormones in serum and neurotransmitters in murine brain tissue. Our data demonstrated a dose-dependent decline in the serum concentrations of all three HPA axis hormones in mice pre-treated with CMRC-CDs. Moreover, compared with the model group, CRH concentrations exhibited significant differences in all three dosage groups, while ACTH levels were significantly different between the high- and medium-dose groups, and CORT levels were significantly different exclusively in the high-dose group. This suggests that the modulatory capacity of CMRC-CDs on HPA axis activity may diminish as their synthesis progresses. Our findings indicate that CMRC-CDs may exert anxiolytic effects by reducing HPA axis hormone concentrations, with the principal site of regulation potentially being the CRH synthesis in the hypothalamus.

Investigations into neurotransmitter concentrations revealed a decline in Glu levels alongside a concurrent elevation in GABA concentrations within cerebral tissues of the mice administered with CMRC-CDs. A noteworthy influence was observed across all three dosages. These findings suggest that CMRC-CDs may contribute to the alleviation of mood disorders by modulating the Glu/GABA pathway. Considering that GABA can be synthesized via the decarboxylation of Glu (Sarasa et al., 2020), a plausible hypothesis is that CMRC-CDs may facilitate this decarboxylation process, thus promoting the reestablishment of E/I homeostasis.

In a comparative analysis of the three primary monoamine neurotransmitters, CMRC-CDs exhibited a significant increase in 5-HT concentrations in relation to the model group. This elevation was statistically significant across all three administered dosages. In contrast, the administration of various CMRC-CDs doses did not produce significant effects on DA and NE concentrations. Considering that DA is posited to maintain a close relationship with exercise capacity (Meeusen and De Meirleir, 1995; Dohnalová et al., 2022), these findings are consistent with the results of the behavioral experiments, wherein no significant differences were observed in the total distance traversed.

4 Conclusion

In summary, we have successfully synthesized carbon dots derived from Chrysanthemum morifolium Ramat (CMRC-CDs) that exhibit exceptional fluorescence properties and a surface abundant in functional groups. Our thorough behavioral investigations demonstrated that CMRC-CDs effectively ameliorate mCPP-induced anxiety-like behavior in murine models in a dose-responsive manner. This therapeutic effect is primarily mediated through the modulation of HPA axis hormone levels, amino acid neurotransmitter concentrations, and serotonin 5-HT levels. Owing to their environmentally benign nature, cost-effectiveness, and facile preparation, CMRC-CDs hold immense potential as novel nanomedicines for the management of anxiety disorders. Furthermore, our findings offer valuable insights into the therapeutic prospects of traditional Chinese herbal medicine for treating mood disorders, which could inspire further investigations in this field.

5 Materials and methods

5.1 Chemicals

CMR was purchased from Beijing Qiancao Herbal Pieces Co., Ltd. (Beijing, China). Diazepam (DZP) tablets were obtained from Beijing Yimin Pharmaceutical Factory (Beijing, China). Dialysis membranes with 1,000 Da molecular weight cutoff (MWCO) were provided by Beijing Ruida Henghui Technology Development Co., Ltd. (Beijing, China). ELISA kits for measuring neurotransmitter and HPA hormone concentrations were purchased from Jiangsu Kete Biotechnology Co., Ltd. (Jiangsu, China). The cell counting kit-8 (CCK-8) was acquired from Dojindo Molecular Technologies, Inc. (Kumamoto, Japan). Dulbecco's Modified Eagle's Medium (DMEM), fetal bovine serum (FBS), and antibiotics were sourced from Gibco BRL (Gaithersburg, MD, United States). Deionized water (DW) was used in all experiments.

5.2 Animals and cells

All mice were maintained under standardized conditions, including *ad libitum* access to food and water, an ambient temperature of 25.0°C ± 1.0°C, a relative humidity ranging from 55%–65%, and a diurnal rhythm of 12 h light and 12 h darkness. Behavioral experiments were carried out in a tranquil laboratory environment between the hours of 09:00 and 15:00. RAW 264.7 cells were employed in cell viability assays due to their ease of culture and expansion, as well as their ability to maintain high proliferation capacity and *in vitro* cell viability. Furthermore, RAW 264.7 cells exhibit pronounced sensitivity to stimulating substances and promptly respond to external stimuli, eliciting diverse biological effects.

5.3 Preparation of CMRC-CDs

The synthesis of CMRC-CDs was achieved utilizing CMR as the carbon source. In the initial stage, CMR was situated in hermetically sealed porcelain crucibles and subjected to carbonization at a temperature of 350°C for a duration of 1 h, utilizing a muffle furnace. After cooling down to ambient temperature, the resulting CMRC was pulverized into fine fragments using a micro mill. The fine CMRC powder was subsequently dispersed in deionized water at a 1:30 ratio and heated to 100°C for three 1-h boiling sessions. The mixture was then filtered through a 0.22 μm microfiltration membrane. Following this, the solution was dialyzed against deionized water for 7 days using a dialysis membrane with a 1,000 Da molecular weight cut-off, changing the dialysis solution every 8 h. Afterward, the CMRC-CDs solution was placed in a refrigerator at 4°C so that it could be utilized in the future. Figure 8 illustrates a schematic diagram outlining the preparation process.

5.4 Characterization of CMRC-CDs

The physical structure and morphology of CMRC-CDs were meticulously investigated and quantified using transmission electron microscopy (TEM) and high-resolution TEM (HRTEM) at an accelerating voltage of 200 kV. The X-ray Diffractometer was employed to acquire X-ray diffraction (XRD) patterns. The photoluminescence characteristics of CMRC-CDs were scrutinized utilizing a fluorescence spectrophotometer, while the ultraviolet-visible (UV-vis) absorption spectra were probed with a UV-vis spectrometer. In the range of 400–4,000 cm^{-1}, Fourier transform infrared (FTIR) spectroscopy was employed to analyze the organic functional groups present in the CMRC-CDs. Additionally, X-ray photoelectron spectroscopy (XPS) was utilized to determine elemental characterization of the CMRC-CDs.

5.5 Open-field (OF) test

The OF test was employed to assess the autonomous behavior, exploratory tendencies, and anxiety levels of experimental animals when introduced to a novel environment. The open-field apparatus consists of a reaction chamber measuring 30 cm in height, featuring

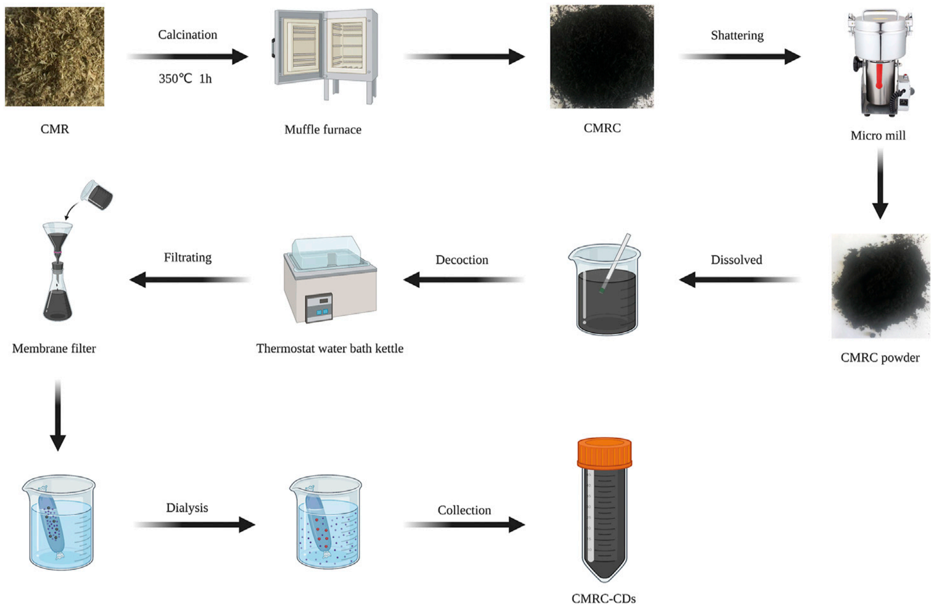

FIGURE 8
A procedural schematic represents the synthesis of carbon dots obtained from Chrysanthemum morifolium Ramat (CMRC-CDs) (Created with BioRender.com).

a square base with dimensions of 50 cm × 50 cm, a black interior, and a floor partitioned evenly into 25 smaller squares. The experiments are meticulously documented using a high-resolution camera positioned directly above the experimental apparatus. This camera is operated by a sophisticated computer program, ensuring accuracy and consistency in data capture. The peripheral area comprised 16 zones situated adjacent to the walls; the central area consisted of the remaining nine central zones. In the experimental setup, every mouse was carefully positioned at the center of the container and subsequently granted a 10-min period for exploration. Prior to testing, animals were acclimated to the experimental environment for 60 min. To mitigate the potential confounding influence of olfactory cues from prior experimental subjects, the apparatus underwent a rigorous cleaning procedure with a 75% ethanol solution following each trial, aimed at eliminating residual odors. This measure was taken to minimize the risk of contamination and reduce the possibility of spurious experimental outcomes stemming from olfactory stimuli.

Anxiety levels and exploratory behavior were assessed by quantifying the proportion of time spent in the central area, the proportion of entries in the central area, and the total distance traveled, respectively (Carola et al., 2002; Saitoh et al., 2004).

5.6 Elevated plus maze (EPM) test

The primary components of the Elevated plus maze (EPM) apparatus consist of two opposing closed arms (30 cm × 5 cm) and two opposing non-transparent open arms (30 cm × 5 cm × 25 cm), arranged in a cross-shaped configuration. The apparatus is elevated to a height of 50 cm from the ground, with the arms connected to a central platform measuring 5 cm × 5 cm. The experiments are meticulously documented using a high-resolution camera positioned directly above the experimental apparatus. This camera is operated by a sophisticated computer program, ensuring accuracy and consistency in data capture. Every murine subject is delicately situated at the core of the apparatus, oriented towards an open arm, and meticulously monitored for an interval of 10 min. Prior to testing, animals are acclimated to the experimental environment for a period of 2 h. To mitigate potential bias from olfactory cues left by previous subjects, the apparatus is thoroughly cleaned with a 75% ethanol solution after each trial (Guo et al., 2011).

Parameters indicative of anxiolytic-like behavior, such as the percentage of time spent in open arms [(open arm duration/total duration) × 100] and the proportion of open arm entries [(open arms entries/total entries) × 100], are assessed through analysis of the recorded video footage. To gauge alterations in exploratory activity, the total distance traversed by the subjects is calculated. Any mouse that inadvertently falls out of the maze is excluded from the experiment.

5.7 Sample collection

Mice were granted a 24-h recovery period following the behavioral assessments before blood collection commenced. Blood samples were procured employing serum collection tubes, subsequently permitting coagulation for a duration of 2 h at room temperature. Following this, samples were subjected to centrifugation at 3,000 revolutions per minute and 4°C for a 10-min interval, resulting in the isolation of the serum component. Subsequent to the blood sampling, the mice, under anesthesia, were euthanized via decapitation. Their brains were then delicately excised on ice, with rigorous care taken to mitigate any potential tissue damage. For subsequent analysis of the relevant variables, samples were preserved at −80°C.

5.8 Quantification of neurotransmitter

Neurotransmitter concentrations, encompassing 5-HT, NE, DA, GABA, and Glu, were ascertained from brain tissue samples through the implementation of ELISA. Murine ELISA kits were employed in strict adherence to the guidelines provided by the manufacturer. The samples were measured for optical density (OD) with a wavelength of 450 nm, utilizing a microplate spectrophotometer (Biotek, VT, United States). Subsequently, neurotransmitter concentrations were denoted in units of either ng/mL or pg/mL, as appropriate.

5.9 Quantification of HPA hormone

ELISA was employed for the quantification of HPA axis hormones, including CRH, ACTH, and CORT, in serum samples. Adherence to the manufacturer's guidelines for the utilization of murine ELISA kits was ensured. Optical density (OD) measurements were performed at 450 nm.

5.10 Cell viability assay of CMRC-CDs

In this investigation, RAW 264.7 cells were propagated in DMEM with 10% FBS, 100 mg/mL streptomycin, and 100 IU/mL penicillin, followed by an incubation period at 37°C within a humidified environment containing 5% CO_2. The cytotoxic effects of CMRC-CDs on RAW 264.7 cells were evaluated employing the CCK-8 assay (Jia et al., 2017). Cells were cultured in 96-well plates at a density of 1×10^5 cells/mL employing serum-free media, followed by a 24-h incubation period under standard conditions. Next, the cells were treated with various concentrations of CMRC-CDs (1,250, 625, 312.5, 156.25, 78.13, and 39.06 μg/mL) by adding 100 μL of the solution to the corresponding wells, followed by a 24-h incubation period. Upon the elimination of the culture media and subsequent dual rinsing with PBS, each well was supplemented with 10 μL of CCK-8 solution, followed by incubation of the cells for an additional 4 h. The OD of each well was measured at a 450 nm wavelength utilizing a microplate reader. The relative cell viability was determined by calculating the percentage relative to the control group using the following formula:

$$\text{Cell viability (\% of control)} = \frac{A_e - A_b}{A_c - A_b} \times 100 \qquad (1)$$

The absorbance values for the experimental, blank, and control groups are denoted as Ae, Ab, and Ac, respectively.

5.11 Experimental procedure

A total of 48 male ICR mice were randomly and equally divided into six groups. After 3 days of acclimatization, the intervention protocol for each group began as follows: control group, model group, and positive group (normal saline [NS] 10 mL/kg, i.g.), high-dose pretreatment group (CMRC-CDs 0.1 mg/kg, i.g.), medium-dose pretreatment group (CMRC-CDs 0.05 mg/kg, i.g.), and low-dose pretreatment group (CMRC-CDs 0.025 mg/kg, i.g.). The intervention was performed for 14 consecutive days.

The OF test was conducted on day 15 and the EPM test was conducted on day 16, respectively. The mice were brought to the experimental site 2 h before the start of the experiment for acclimatization. One hour before the experiment began, each group received the following interventions: control group (NS 10 mL/kg, i.g.), model group (NS 10 mL/kg, i.g.), positive group (DZP, 2 mg/kg, i.g.), high-dose pretreatment group (CMRC-CDs 0.1 mg/kg, i.g.), medium-dose pretreatment group (CMRC-CDs 0.05 mg/kg, i.g.), and low-dose pretreatment group (CMRC-CDs 0.025 mg/kg, i.g.). Anxiety models were established 30 min before the experiment using the following protocols: control group (NS 10 mL/kg, i.p.), other groups (mCPP 2 mg/kg, i.p.) (N. Zhang et al., 2018).

After the EPM test, mice were fasted for 24 h with *ad libitum* access to water. Samples were collected on day 17. Mice received the intervention 1 h after arriving at the experimental site. Anxiety models were established 30 min later. Following an additional 30-min period, the mice were humanely euthanized via decapitation, after which blood samples and brain tissue were systematically collected. The intervention methods and anxiety model establishment were the same as during the behavioral experiments.

Following sample collection, HPA axis hormone concentrations in serum and neurotransmitter concentrations in brain tissue were determined using ELISA. Video analysis software was used to observe and extract data from videos of the mouse behavioral experiments. For the OF test, observations included time spent in the central area, the number of entries into the central area, the total number of entries into all areas, and the total distance traveled. For the EPM test, the metrics observed included dwell time in open arms, total dwell time in the open and closed arms, number of entries into open arms, the total number of entries into the open and closed arms, and total distance traveled.

5.12 Statistical analysis

Statistical analyses were performed using SPSS 20.0. For data adhering to normal distribution with equal variances, means and standard deviations were computed. Multiple comparisons were carried out using one-way analysis of variance (ANOVA). Non-normally distributed data were presented as the median (interquartile range). A non-parametric test was employed for within-group comparisons of such data, whereas between-group differences were examined with the Kruskal–Wallis test. A p-value of less than 0.05 was deemed to indicate statistical significance.

Data availability statement

The original contributions presented in the study are included in the article/Supplementary Material, further inquiries can be directed to the corresponding authors.

Ethics statement

The animal study was reviewed and approved by the Ethics Committee of Animal Experimentation, Beijing University of Chinese Medicine, Beijing, China.

Author contributions

The study was conceived and the experimental approach designed by HQ, HK, and YZ; they also supervised the project, provided expert insights and guidance on the subject matter, and received support funding. Research was conducted by LC, QZ, YZ, and ML. TL and JY ensured the accuracy and integrity of the research data; ZW contributed to the literature review. LC wrote the initial draft of the manuscript and YZ offered critical revisions to the manuscript. All authors contributed to the article and approved the submitted version.

Funding

This work was supported by the Special Funds for Fundamental Research Expenses of Central Universities (China) and Grant for Qihuang Scholars of the State Administration of Traditional Chinese Medicine.

Acknowledgments

We extend our deepest appreciation to the invaluable collaboration provided by the Classical Prescription Basic Research Team at Beijing University of Chinese Medicine, in conjunction with the Key Laboratory of Behavioral Tests, situated within the Center of Scientific Experiment, affiliated with the School of Basic Medical Sciences.

Conflict of interest

Author QZ was employed by Qingdao Zhonghengneng Environmental Science Engineering Research Institute Co., Ltd.

The remaining authors declare that the research was conducted in the absence of any commercial or financial relationships that could be construed as a potential conflict of interest.

Publisher's note

References

Alawdi, S. H., El-Denshary, E. S., Safar, M. M., Eidi, H., David, M. O., and MosaadAbdel-Wahhab, A. (2017). Neuroprotective effect of nanodiamond in alzheimer's disease rat model: A pivotal role for modulating NF-?b and STAT3 signaling. *Mol. Neurobiol.* 54 (3), 1906–1918. doi:10.1007/s12035-016-9762-0

Arborelius, L., Owens, M., Plotsky, P., and Nemeroff, C. (1999). The role of corticotropin-releasing factor in depression and anxiety disorders. *J. Endocrinol.* 160 (1), 1–12. doi:10.1677/joe.0.1600001

Ashrafizadeh, M., Mohammadinejad, R., Kumar Kailasa, S., Ahmadi, Z., Elham Ghasemipour, A., and Pardakhty, A. (2020). Carbon dots as versatile nanoarchitectures for the treatment of neurological disorders and their theranostic applications: A review. *Adv. Colloid Interface Sci.* 278, 102123. doi:10.1016/j.cis.2020.102123

Atchudan, R., Thomas Nesakumar, J. I. E., Mani, S., Perumal, S., Vinodh, R., Thirunavukkarasu, S., et al. (2020). Facile synthesis of a novel nitrogen-doped carbon dot adorned zinc oxide composite for photodegradation of methylene blue. *Dalton Trans.* 49 (48), 17725–17736. doi:10.1039/D0DT02756A

Bala, Areeg, Hoang Minh, T. N., Wayne, J., and Hellstrom, G. (2018). Post-SSRI sexual dysfunction: A literature review. *Sex. Med. Rev.* 6 (1), 29–34. doi:10.1016/j.sxmr.2017.07.002

Barbhaiya, R. H., Shukla, U. A., Natarajan, C. S., Behr, D. A., Greene, D. S., and Sainati, S. M. (1995). Single- and multiple-dose pharmacokinetics of nefazodone in patients with hepatic cirrhosis. *Clin. Pharmacol. Ther.* 58 (4), 390–398. doi:10.1016/0009-9236(95)90051-9

Barden, N., Reul, J. M. H. M., and Holsboer, F. (1995). Do antidepressants stabilize mood through actions on the hypothalamic-pituitary-adrenocortical system? *Trends Neurosci.* 18 (1), 6–11. doi:10.1016/0166-2236(95)93942-Q

Benatti, C., Alboni, S., Blom, J. M. C., Mendlewicz, J., Tascedda, F., and Brunello, N. (2018). Molecular changes associated with escitalopram response in a stress-based model of depression. *Psychoneuroendocrinology* 87, 74–82. doi:10.1016/j.psyneuen.2017.10.011

Berry, A. S., White, R. L., Furman, D. J., Naskolnakorn, J. R., Shah, V. D., Esposito, M. D., et al. (2019). Dopaminergic mechanisms underlying normal variation in trait anxiety. *J. Neurosci.* 39 (14), 2735–2744. doi:10.1523/JNEUROSCI.2382-18.2019

Brady, L. S., Whitfield, H. J., Fox, R. J., Gold, P. W., and Herkenham, M. (1991). Long-term antidepressant administration alters corticotropin-releasing hormone, tyrosine hydroxylase, and mineralocorticoid receptor gene expression in rat brain. Therapeutic implications. *J. Clin. Investigation* 87 (3), 831–837. doi:10.1172/JCI115086

Brady, L. S., Gold, P. W., Herkenham, M., Lynn, A. B., and Whitfield, H. J. (1992). The antidepressants fluoxetine, idazoxan and phenelzine alter corticotropin-releasing hormone and tyrosine hydroxylase MRNA levels in rat brain: Therapeutic implications. *Brain Res.* 572 (1–2), 117–125. doi:10.1016/0006-8993(92)90459-M

Carola, V., D'Olimpio, F., Brunamonti, E., Mangia, F., and Renzi, P. (2002). Evaluation of the elevated plus-maze and open-field tests for the assessment of anxiety-related behaviour in inbred mice. *Behav. Brain Res.* 134 (1–2), 49–57. doi:10.1016/S0166-4328(01)00452-1

Chen, Z., Ye, S. Y., Yang, Y., and Li, Z. Y. (2019). A review on charred traditional Chinese herbs: Carbonization to yield a haemostatic effect. *Pharm. Biol.* 57 (1), 498–506. doi:10.1080/13880209.2019.1645700

Chu, F., Li, K., Li, X., Xu, L., Huang, J., and Yang, Z. (2021). Graphene oxide ameliorates the cognitive impairment through inhibiting PI3K/akt/MTOR pathway to induce autophagy in AD mouse model. *Neurochem. Res.* 46 (2), 309–325. doi:10.1007/s11064-020-03167-z

Cui, L., Ren, X., Sun, M., Liu, H., and Xia, L. (2021). Carbon dots: Synthesis, properties and applications. *Nanomaterials* 11 (12), 3419. doi:10.3390/nano11123419

Delpino, F. M., Nascimento da Silva, C., Santos Jerônimo, J., Stark Mulling, E., Leal da Cunha, L., Krause Weymar, M., et al. (2022). Prevalence of anxiety during the COVID-19 pandemic: A systematic review and meta-analysis of over 2 million people. *J. Affect. Disord.* 318 272–282. doi:10.1016/j.jad.2022.09.003

Dohnalová, L., Lundgren, P., JamieCarty, R. E., Goldstein, N., Wenski, S. L., Nanudorn, P., et al. (2022). A microbiome-dependent gut–brain pathway regulates motivation for exercise. *Nature* 612 (7941), 739–747. doi:10.1038/s41586-022-05525-z

Durán, N., Simões, M. B., de Moraes, A. C. M., Fávaro, W. J., and Seabra, A. B. (2016). Nanobiotechnology of carbon dots: A review. *J. Biomed. Nanotechnol.* 12 (7), 1323–1347. doi:10.1166/jbn.2016.2225

Eriksson, E., Engberg, G., Bing, O., and Nissbrandt, H. (1999). Effects of MCPP on the extracellular concentrations of serotonin and dopamine in rat brain. *Neuropsychopharmacology* 20 (3), 287–296. doi:10.1016/S0893-133X(98)00070-0

Faravelli, C., Lo Sauro, C., Godini, L., Lelli, L., Benni, L., Pietrini, F., et al. (2012). Childhood stressful events, HPA Axis and anxiety disorders. *World J. Psychiatry* 2 (1), 13–25. doi:10.5498/wjp.v2.i1.13

Flandreau, E. I., Chase, H., Bourke, K. J. R., Vale, W. W., Nemeroff, C. B., Owens, M. J., and Owens, M. J. (2013). Escitalopram alters gene expression and HPA Axis reactivity in rats following chronic overexpression of corticotropin-releasing factor from the central amygdala. *Psychoneuroendocrinology* 38 (8), 1349–1361. doi:10.1016/j.psyneuen.2012.11.020

GBD 2019 Mental Disorders Collaborators (2022). Global, regional, and national burden of 12 mental disorders in 204 Countries and Territories, 1990–2019: A systematic analysis for the global burden of disease study 2019. *Lancet Psychiatry* 9 (2), 137–150. doi:10.1016/S2215-0366(21)00395-3

Godavarthi, S., Mohan Kumar, K., Vázquez Vélez, E., Hernandez-Eligio, A., Mahendhiran, M., Hernandez-Como, N., et al. (2017). Nitrogen doped carbon dots derived from sargassum fluitans as fluorophore for DNA detection. *J. Photochem. Photobiol. B Biol.* 172 36–41. doi:10.1016/j.jphotobiol.2017.05.014

Guo, J. Y., Yuan, X. Y., Sui, F., Zhang, W. C., Wang, J. Y., Luo, F., et al. (2011). Placebo analgesia affects the behavioral despair tests and hormonal secretions in mice. *Psychopharmacology* 217 (1), 83–90. doi:10.1007/s00213-011-2259-7

Henna, T. K., Raphey, V. R., Sankar, Renu, Shirin, V. K. A., Gangadharappa, H. V., and Pramod, K. (2020). Carbon nanostructures: The drug and the delivery system for brain disorders. *Int. J. Pharm.* 587 119701. doi:10.1016/j.ijpharm.2020.119701

Horowitz, M. A., and Taylor, D. (2019). Tapering of SSRI treatment to mitigate withdrawal symptoms. *Lancet Psychiatry* 6 (6), 538–546. doi:10.1016/S2215-0366(19)30032-X

Jacobson, Lauren (2014). Hypothalamic-pituitary-adrenocortical Axis: Neuropsychiatric aspects. *Compr. Physiol.* 4, 715–738. doi:10.1002/cphy.c130036

Jaleel, J. A., and Pramod, K. (2018). Artful and multifaceted applications of carbon dot in biomedicine. *J. Control. Release* 269 302–321. doi:10.1016/j.jconrel.2017.11.027

Jia, P., Yu, L., Tao, C., Guo, D., Zhang, Z., and Liu, S. (2017). Chitosan oligosaccharides protect nucleus pulposus cells from hydrogen peroxide-induced apoptosis in a rat experimental model. *Biomed. Pharmacother.* 93 807–815. doi:10.1016/j.biopha.2017.06.101

Khayal, A., Dawane, V., Amin, M. A., Tirth, V., Yadav, V. K., et al. (2021). "Advances in the methods for the synthesis of carbon dots and their emerging applications." *Polymers* 13 (18): 3190. doi:10.3390/polym13183190

Kinlein, S. A., Phillips, D. J., Keller, C. R., and Karatsoreos, I. N. (2019). Role of corticosterone in altered neurobehavioral responses to acute stress in a model of compromised hypothalamic-pituitary-adrenal Axis function. *Psychoneuroendocrinology* 102 248–255. doi:10.1016/j.psyneuen.2018.12.010

Kraeuter, A. K., Guest, P. C., and Sarnyai, Z. (2019). "The elevated plus maze test for measuring anxiety-like behavior in rodents," in *Pre-clinical models. Methods in molecular biology*. Editor Paul C. Guest (New York, NY: Springer New York), 69–74. doi:10.1007/978-1-4939-8994-2_4

Lee, H. J., and Stein, M. B. (2023). Update on treatments for anxiety-related disorders. *Curr. Opin. Psychiatry* 36 (2), 140–145. doi:10.1097/YCO.0000000000000841

Lee, S., and Rhee, D. K. (2017). Effects of ginseng on stress-related depression, anxiety, and the hypothalamic–pituitary–adrenal Axis. *J. Ginseng Res.* 41 (4), 589–594. doi:10.1016/j.jgr.2017.01.010

Lenze, E. J., Mantella, R. C., Shi, P., Goate, A. M., Nowotny, P., Butters, M. A., et al. (2011). Elevated cortisol in older adults with generalized anxiety disorder is reduced by treatment: A placebo-controlled evaluation of escitalopram. *Am. J. Geriatric Psychiatry* 19 (5): 482–490. doi:10.1097/JGP.0b013e3181ec806c

Li, D., Xu, K.Y., Zhao, W. P., Liu, M. F., Feng, R., De-qiang, L., et al. (2022). Chinese medicinal herb-derived carbon dots for common diseases: Efficacies and potential mechanisms. *Front. Pharmacol.* 13 815479. doi:10.3389/fphar.2022.815479

Li, D., Na, X., Zhou, W., Wang, C., Li, Y., Zhu, B. W., et al. (2019). Adverse effects of fluorescent carbon dots from canned yellow croaker on cellular respiration and glycolysis. *Food & Funct.* 10 (2), 1123–1131. doi:10.1039/C8FO02602E

Liu, L., and Wang, M. (2020). Parental corporal punishment and child anxiety in China: The moderating role of HPA-Axis activity. *J. Affect. Disord.* 273 500–507. doi:10.1016/j.jad.2020.04.055

Liu, L., Liu, C., Wang, Y., Wang, P., Li, Y., and Bingjin, L. (2015). Herbal medicine for anxiety, depression and insomnia. *Curr. Neuropharmacol.* 13 (4), 481–493. doi:10.2174/1570159x1304150831122734

Luo, W. K., Zhang, L. L., Yang, Z. Y., Guo, X. H., Wu, Y., Zhang, W., et al. (2021). Herbal medicine derived carbon dots: Synthesis and applications in therapeutics, bioimaging and sensing. *J. Nanobiotechnology* 19 (1), 320. doi:10.1186/s12951-021-01072-3

Mancuso, C. E., Tanzi, M. G., and Gabay, M. (2004). Paradoxical reactions to benzodiazepines: Literature review and treatment options. *Pharmacotherapy* 24 (9), 1177–1185. doi:10.1592/phco.24.13.1177.38089

Mansuriya, B. D., and Zeynep, A. (2021). Carbon dots: Classification, properties, synthesis, characterization, and applications in health care—an updated review (2018–2021). *Nanomaterials* 11 (10), 2525. doi:10.3390/nano11102525

Meeusen, R., and De Meirleir, K. (1995). Exercise and brain neurotransmission. *Sports Med.* 20 (3), 160–188. doi:10.2165/00007256-199520030-00004

Meldrum, B. S. (2000). Glutamate as a neurotransmitter in the brain: Review of physiology and pathology. *J. Nutr.* 130 (4), 1007S–1015S. doi:10.1093/jn/130.4.1007S

Muhammad, W., Ullah, N., Haroon, M., and Abbasi, B. H. (2019). Optical, morphological and biological analysis of zinc oxide nanoparticles (ZnO NPs) using *papaver somniferum* L. *RSC Adv.* 9 (51), 29541–29548. doi:10.1039/C9RA04424H

Olivier, J. D. A., and Olivier., B. (2020). "Translational studies in the complex role of neurotransmitter systems in anxiety and anxiety disorders," in *Anxiety disorders. Advances in experimental medicine and biology*. Editor K. Yong-Ku (Singapore: Springer Singapore), 1191, 121–140. doi:10.1007/978-981-32-9705-0_8

Panossian, A., Wikman, G., and Sarris, J. (2010). Rosenroot (Rhodiola rosea): Traditional use, chemical composition, pharmacology and clinical efficacy. *Phytomedicine* 17 (7), 481–493. doi:10.1016/j.phymed.2010.02.002

Petursson, H. (1994). The benzodiazepine withdrawal syndrome. *Addiction* 89 (11), 1455–1459. doi:10.1111/j.1360-0443.1994.tb03743.x

Pigott, T. A., James, L., Hill, T. A. G., L'Heureux, F., Bernstein, S., Rubenstein, C. S., et al. (1993). A comparison of the behavioral effects of oral versus intravenous MCPP administration in OCD patients and the effect of metergoline prior to IV MCPP. *Biol. Psychiatry* 33 (1), 3–14. doi:10.1016/0006-3223(93)90272-F

Pobbe, R. L. H., Zangrossi, H., Caroline Blanchard, D., and Blanchard, R. J. (2011). Involvement of dorsal raphe nucleus and dorsal periaqueductal gray 5-HT receptors in the modulation of mouse defensive behaviors. *Eur. Neuropsychopharmacol.* 21 (4), 306–315. doi:10.1016/j.euroneuro.2010.05.004

Prager, E. M., Hadley, C., Bergstrom, G. H. W., and MariaBraga, F. M. (2016). The basolateral amygdala γ-aminobutyric acidergic system in health and disease: BLA GABAergic system in health and disease. *J. Neurosci. Res.* 94 (6), 548–567. doi:10.1002/jnr.23690

Prut, L., and Belzung, C. (2003). The open field as a paradigm to measure the effects of drugs on anxiety-like behaviors: A review. *Eur. J. Pharmacol.* 463 (1–3), 3–33. doi:10.1016/S0014-2999(03)01272-X

Ran, W., and Xue, X. (2018). Theranostical application of nanomedicine for treating central nervous system disorders. *Sci. China Life Sci.* 61 (4), 392–399. doi:10.1007/s11427-017-9292-7

Ren, C., Hu, X., and Zhou, Q. (2018). Graphene oxide quantum dots reduce oxidative stress and inhibit neurotoxicity *in vitro* and *in vivo* through catalase-like activity and metabolic regulation. *Adv. Sci.* 5 (5), 1700595. doi:10.1002/advs.201700595

Riedel, W. J., Klaassen, T., Griez, E., Honig, A., Menheere, P. P., and Van Praag, H. M. (2002). Dissociable hormonal, cognitive and mood responses to neuroendocrine challenge: Evidence for receptor-specific serotonergic dysregulation in depressed mood. *Neuropsychopharmacology* 26 (3), 358–367. doi:10.1016/S0893-133X(01)00361-X

Risbrough, V. B., and Stein, M. B. (2006). Role of corticotropin releasing factor in anxiety disorders: A translational research perspective. *Hormones Behav.* 50 (4), 550–561. doi:10.1016/j.yhbeh.2006.06.019

Ross, S., Wu, R. S., Wei, S. C., Ross, G. M., and Chang, H. T. (2020). The analytical and biomedical applications of carbon dots and their future theranostic potential: A review. *J. Food Drug Analysis* 28 (4), 677–695. doi:10.38212/2224-6614.1154

Russo, S. J., and Nestler, E. J. (2013). The brain reward circuitry in mood disorders. *Nat. Rev. Neurosci.* 14 (9), 609–625. doi:10.1038/nrn3381

Saitoh, A., Kimura, Y., Suzuki, T., Kawai, K., Nagase, H., and Kamei, J. (2004). Potential anxiolytic and antidepressant-like activities of SNC80, a selective δ-opioid agonist, in behavioral models in rodents. *J. Pharmacol. Sci.* 95 (3), 374–380. doi:10.1254/jphs.fpj04014x

Santomauro, D. F., AnaHerrera, M. M., Shadid, J., Zheng, P., Ashbaugh, C., Pigott, D. M., et al. (2021). Global prevalence and burden of depressive and anxiety disorders in 204 Countries and Territories in 2020 due to the COVID-19 pandemic. *Lancet* 398 (10312), 1700–1712. doi:10.1016/S0140-6736(21)02143-7

Sarasa, S. B., Mahendran, R., Muthusamy, G., Thankappan, B., Femil Selta, D. R., and Jayaraman, A. (2020). A brief review on the non-protein amino acid, gamma-amino butyric acid (GABA): Its production and role in microbes. *Curr. Microbiol.* 77 (4), 534–544. doi:10.1007/s00284-019-01839-w

Singh, I., Arora, R., Dhiman, H., and Pahwa, R. (2018). Carbon quantum dots: Synthesis, characterization and biomedical applications. *Turkish J. Pharm. Sci.* 15 (2), 219–230. doi:10.4274/tjps.63497

Tafet, G. E., Idoyaga-Vargas, V. P., Abulafia, D. P., Calandria, J. M., Roffman, S. S., Chiovetta, A., et al. (2001). Correlation between cortisol level and serotonin uptake in patients with chronic stress and depression. *Cognitive, Affect. Behav. Neurosci.* 1 (4), 388–393. doi:10.3758/CABN.1.4.388

Tafet, G. E., and Nemeroff, C. B. (2020). Pharmacological treatment of anxiety disorders: The role of the HPA Axis. *Front. Psychiatry* 11 443. doi:10.3389/fpsyt.2020.00443

Wang, Y. F., Liu, L., Xue, X., and Liang, X. J. (2017). Nanoparticle-based drug delivery systems: What can they really do *in vivo*? *F1000Research* 6 681. doi:10.12688/f1000research.9690.1

Wee, N. J. v. d., Frederieke van Veen, J., Stevens, H., Irenevan Vliet, M., Petervan Rijk, P., and Westenberg, H. G. (2008). Increased serotonin and dopamine transporter binding in psychotropic medication–naïve patients with generalized social anxiety disorder shown by ^{123} I-β-(4-Iodophenyl)-Tropane SPECT. *J. Nucl. Med.* 49 (5), 757–763. doi:10.2967/jnumed.107.045518

Wei, X., Li, L., Liu, J., Yu, L., Li, H., Cheng, F., et al. (2019). Green synthesis of fluorescent carbon dots from gynostemma for bioimaging and antioxidant in zebrafish. *ACS Appl. Mater. Interfaces* 11 (10), 9832–9840. doi:10.1021/acsami.9b00074

Wirth, A., Holst, K., and Ponimaskin, E. (2017). How serotonin receptors regulate morphogenic signalling in neurons. *Prog. Neurobiol.* 151 35–56. doi:10.1016/j.pneurobio.2016.03.007

Xiao, S., Zhou, D., Luan, P., Gu, B., Feng, L., Fan, S., et al. (2016). Graphene quantum dots conjugated neuroprotective peptide improve learning and memory capability. *Biomaterials* 106 98–110. doi:10.1016/j.biomaterials.2016.08.021

Xie, W., Meng, X., Zhai, Y., Zhou, P., Ye, T., Wang, Z., et al. (2018). Panax notoginseng saponins: A review of its mechanisms of antidepressant or anxiolytic effects and network analysis on phytochemistry and pharmacology. *Molecules* 23 (4), 940. doi:10.3390/molecules23040940

Xu, Y., Lian, Y., Li, J., Zhang, Y., Liu, Y., Wang, X., et al. (2022). KangPiLao decoction modulates cognitive and emotional disorders in rats with central fatigue through the GABA/Glu pathway. *Front. Pharmacol.* 13 939169. doi:10.3389/fphar.2022.939169

Xue, X., Yang, J. Y., Yi, H., Wang, L. R., Liu, P., Li-Sha, Y., et al. (2016). Aggregated single-walled carbon nanotubes attenuate the behavioural and neurochemical effects of methamphetamine in mice. *Nat. Nanotechnol.* 11 (7), 613–620. doi:10.1038/nnano.2016.23

Yamamoto, K. I., Shinba, T., and Yoshii, M. (2014). Psychiatric symptoms of noradrenergic dysfunction: A pathophysiological view. *Psychiatry Clin. Neurosci.* 68 (1), 1–20. doi:10.1111/pcn.12126

Yu, W., Wang, L., Yang, L., Li, Y. J., Wang, M., Qiu, C., et al. (2020). Activation of LXRβ signaling in the amygdala confers anxiolytic effects through rebalancing excitatory and inhibitory neurotransmission upon acute stress. *Neurotherapeutics* 17 (3), 1253–1270. doi:10.1007/s13311-020-00857-y

Zangrossi, H., and Graeff, F. G. (2014). Serotonin in anxiety and panic: Contributions of the elevated T-maze. *Neurosci. Biobehav. Rev.* 46 397–406. doi:10.1016/j.neubiorev.2014.03.007

Zhang, N., Zhang, L., Feng, L., and Yao, L. (2018). Cananga odorata essential oil reverses the anxiety induced by 1-(3-chlorophenyl) piperazine through regulating the MAPK pathway and serotonin system in mice. *J. Ethnopharmacol.* 219 23–30. doi:10.1016/j.jep.2018.03.013

Zhang, Y., Wang, S., Lu, F., Zhang, M., Kong, H., Cheng, J., et al. (2021). The neuroprotective effect of pretreatment with carbon dots from crinis carbonisatus (carbonized human hair) against cerebral ischemia reperfusion injury. *J. Nanobiotechnology* 19 (1), 257. doi:10.1186/s12951-021-00908-2

Zhou, X. D., Shi, D. D., and Zhang, Z. J. (2019). Ameliorative effects of Radix rehmanniae extract on the anxiety- and depression-like symptoms in ovariectomized mice: A behavioral and molecular study. *Phytomedicine* 63 153012. doi:10.1016/j.phymed.2019.153012

Zirak, N., Shafiee, M., Soltani, G., Mirzaei, M., and Sahebkar, A. (2019). *Hypericum perforatum* in the treatment of psychiatric and neurodegenerative disorders: Current evidence and potential mechanisms of action. *J. Cell. Physiology* 234 (6), 8496–8508. doi:10.1002/jcp.27781

Zweifel, L. S., Fadok, J. P., Argilli, E., Garelick, M. G., Jones, G. L., TavisDickerson, M. K., et al. (2011). Activation of dopamine neurons is critical for aversive conditioning and prevention of generalized anxiety. *Nat. Neurosci.* 14 (5), 620–626. doi:10.1038/nn.2808

frontiers | Frontiers in Molecular Biosciences

TYPE Original Research
PUBLISHED 30 August 2023
DOI 10.3389/fmolb.2023.1253195

Protective effect of carbon dots derived from scrambled *Coptidis Rhizoma* against ulcerative colitis in mice

Yanfang Mou[1†], Xue Bai[1,2†], Huagen Ma[1†], Tingjie Li[3], Yafang Zhao[1], Tong Wu[3], Yue Zhang[4], Huihua Qu[5], Hui Kong[1*], Xueqian Wang[1*] and Yan Zhao[1*]

[1]School of Traditional Chinese Medicine, Beijing University of Chinese Medicine, Beijing, China, [2]Henan University of Chinese Medicine, Zhengzhou, China, [3]School of Chinese Materia Medica, Beijing University of Chinese Medicine, Beijing, China, [4]School of Life Sciences, Beijing University of Chinese Medicine, Beijing, China, [5]Center of Scientific Experiment, Beijing University of Chinese Medicine, Beijing, China

Introduction: Ulcerative colitis (UC) is a chronic and progressive inflammatory disease of the intestines. The primary symptoms, such as bloody diarrhea, can result in weight loss and significantly diminish the patient's quality of life. Despite considerable research endeavors, this disease remains incurable. The scrambled *Coptidis Rhizoma* (SCR) has a rich historical background in traditional Chinese medicine as a remedy for UC. Drawing from a wealth of substantial clinical practices, this study is focused on investigating the protective effects and underlying mechanisms of the active component of SCR, namely SCR-based carbon dots (SCR-CDs), in the treatment of UC.

Methods: SCR-CDs were extracted and isolated from the decoction of SCR, followed by a comprehensive characterization of their morphological structure and functional groups. Subsequently, we investigated the effects of SCR-CDs on parameters such as colonic length, disease activity index, and histopathological architecture using the dextran sulfate sodium (DSS)-induced colitis mice model. Furthermore, we delved into the assessment of key aspects, including the expression of intestinal tight junction (TJ) proteins, inflammatory cytokines, oxidative stress markers, and gut microbial composition, to unravel the intricate mechanisms underpinning their therapeutic effects.

Results: SCR-CDs displayed a consistent spherical morphology, featuring uniform dispersion and diameters ranging from 1.2 to 2.8 nm. These SCR-CDs also exhibited a diverse array of surface chemical functional groups. Importantly, the administration of SCR-CDs, particularly at higher dosage levels, exerted a noteworthy preventive influence on colonic shortening, elevation of the disease activity index and colonic tissue impairment caused by DSS. These observed effects may be closely associated with the hygroscopic capability and hemostatic bioactivity inherent to SCR-CDs. Concurrently, the application of SCR-CDs manifested an augmenting impact on the expression of intestinal TJ proteins, concomitantly leading to a significant reduction in inflammatory cell infiltration and amelioration of oxidative stress. Additionally, SCR-CDs treatment facilitated the restoration of perturbed gut microbial composition, potentially serving as a fundamental mechanism underlying their observed protective effects.

Check for updates

OPEN ACCESS

EDITED BY
Gopinath Packirisamy,
Indian Institute of Technology Roorkee, India

REVIEWED BY
Mingzhen Zhang,
Xi'an Jiaotong University, China
Shrey Kanvinde,
BioMarin, United States

*CORRESPONDENCE
Hui Kong,
✉ doris7629@126.com
Xueqian Wang,
✉ shirlyding@163.com
Yan Zhao,
✉ zhaoyandr@163.com

†These authors have contributed equally to this work and share first authorship

RECEIVED 05 July 2023
ACCEPTED 17 August 2023
PUBLISHED 30 August 2023

CITATION
Mou Y, Bai X, Ma H, Li T, Zhao Y, Wu T, Zhang Y, Qu H, Kong H, Wang X and Zhao Y (2023), Protective effect of carbon dots derived from scrambled *Coptidis Rhizoma* against ulcerative colitis in mice. *Front. Mol. Biosci.* 10:1253195.
doi: 10.3389/fmolb.2023.1253195

Conclusion: This study demonstrates the significant therapeutic potential of SCR-CDs in UC and provides elucidation on some of their mechanisms. Furthermore, these findings hold paramount importance in guiding innovative drug discovery for anti-UC agents.

KEYWORDS

scrambled *Coptidis Rhizoma*, carbon dots, ulcerative colitis, intestinal tight junction proteins, inflammatory cytokines, oxidative stress, gut microbiota

1 Introduction

Ulcerative colitis (UC) is a nonspecific and immune-mediated inflammatory gastrointestinal disease, classified as one of the subtypes of inflammatory bowel disease (IBD). UC and Crohn's disease (CD) are significant global health issues, impacting several million individuals, with their incidence and prevalence continuing to rise worldwide (Ashton et al., 2022; Huang J. G. et al., 2022). Moreover, these conditions impose a substantial economic burden on patients and severely affect their quality of life (Sachar, 2015).

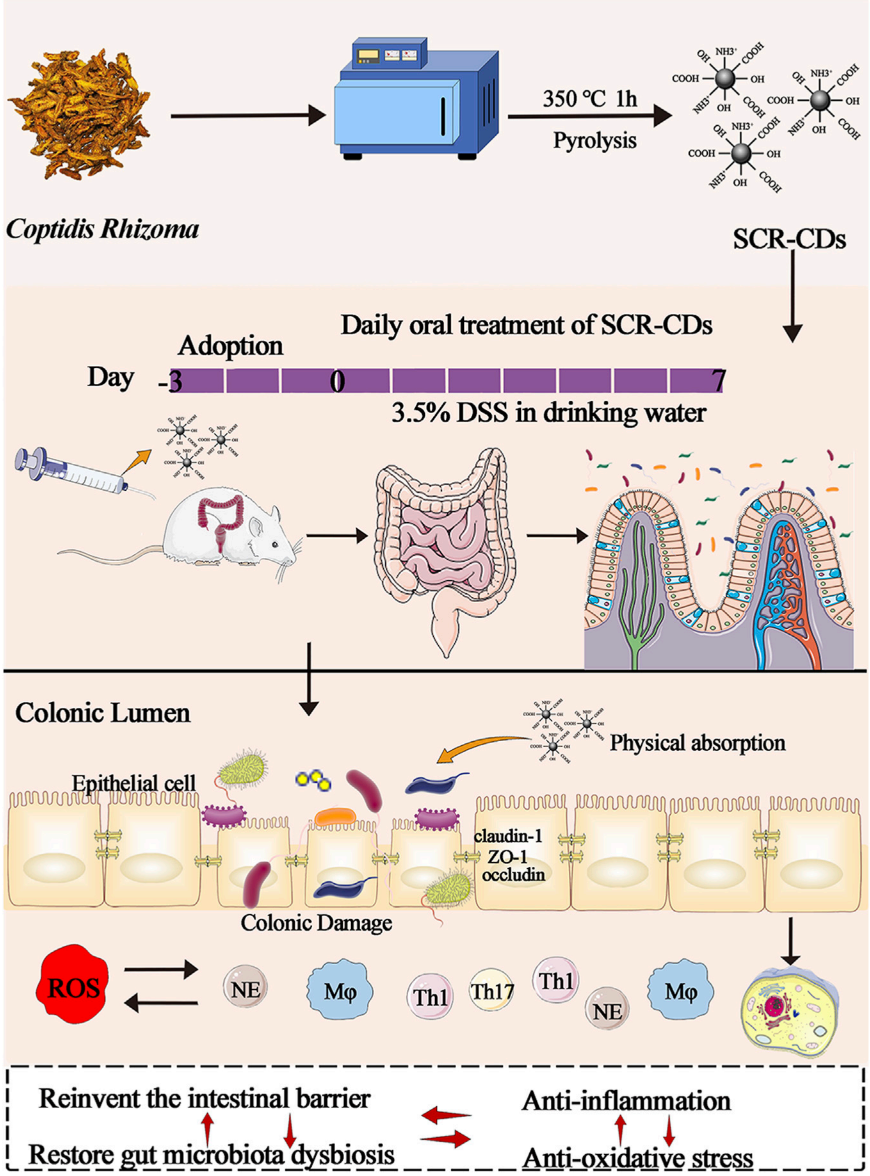

GRAPHICAL ABSTRACT
Schematic diagram of the synthesis of SCR-CDs and diagram of the experimental protocol.

Furthermore, individuals with these conditions are at an elevated risk of developing colorectal cancer (Piovani et al., 2022). Currently, no curative treatment exists for UC, and the management primarily revolves around symptomatic pharmacotherapy (Ferretti et al., 2022). Despite the success of several monotherapies or combination therapies in achieving short-term and long-term remission and maintaining it, a substantial proportion of patients experience a loss of response to available treatments (Rowan et al., 2020). Even with the advent of new biological agents, the remission rate of UC continues to encounter a plateau in terms of achieving clinical targets. Consequently, there is an urgent demand to explore additional therapies that can complement conventional treatments.

The precise etiology of UC remains obscure and is likely to be multifactorial. In the initiation and progression of UC, disruption of the intestinal epithelial barrier increases the risk of bacterial invasion and translocation (Zou et al., 2020). The dysregulated immune response against commensal microflora was orchestrated by the mucosal immune system, leading to an alteration in the balance of the luminal microecological environmental homeostasis. Pathogens and translocated materials can induce the production of potent inflammatory cytokines and other chemical mediators in the colon (Zou et al., 2020). Subsequently, the excessive production of reactive oxygen species (ROS) and continuous oxidative stress can lead to tissue injury. Given that the gastrointestinal tract is the primary source of ROS, IBD has been characterized as an "oxyradical overload" disease (Chiba et al., 2012).

Fortunately, Traditional Chinese Medicine (TCM) has been providing medical assistance to patients for centuries and is often considered a potential treatment strategy. Among the various classic Chinese herbs available, *Coptidis Rhizoma* (CR) has been extensively utilized in clinical settings to alleviate gastrointestinal symptoms, including diarrhea, hematochezia, and stomachache. *Berberine* (BER) is a well-known main bioactive substance of CR. Numerous studies have reported that BER exhibits various beneficial properties, including anti-inflammatory effects (Zou et al., 2017), anti-oxidative activities (Liu et al., 2020), and anti-bacterial properties (Habtemariam, 2020). Despite its advantages, BER suffers from poor aqueous solubility, limited gastrointestinal tract absorption, and low bioavailability (approximately 5%). Consequently, high concentrations of BER must be administered to attain efficacy. This has also led to an elevated risk of adverse drug reactions, thereby restricting its clinical applicability (Dong et al., 2022).

In ancient Chinese medicine, physicians commonly employed the stir-frying method to reduce the toxicity of herbs, enhance their efficacy, and ensure their safe use in meeting clinical requirements. The application of SCR in gastrointestinal disorders has been established in healthcare practice for over two thousand years and continues to be widely accepted in China to this day. For now, the *Pharmacopoeia of the People's Republic of China (2020)* remained recorded SCR processed by the stir-frying method. However, the pyrolysis inherent in the stir-frying process inevitably results in the degradation of specific BER components, leading to a reduction in the biological activity of CR. Therefore, it is reasonable to inquire whether SCR can continue to effectively ameliorate colitis and explore other biologically active ingredients, in addition to BER, that may exert its pharmacological effects.

Fortuitously, our team has previously uncovered that CDs obtained through the pyrolysis of Chinese medicine exhibit analgesic, antioxidant, antibacterial, and anti-inflammatory properties (Zhang M. et al., 2021; Zhang Y. et al., 2021). CDs are a novel class of zero-dimensional carbon nanomaterials with dimensions below 10 nm. Owing to their remarkable biological activity and ultra-low toxicity, CDs have found extensive applications in biomedicine. They serve as targeted nanocarriers, enhancing the efficacy of chemotherapeutic agents through their biocompatible properties. Additionally, CDs have shown promise in providing pharmacological therapy for the treatment of refractory diseases (Jin et al., 2022; Wang et al., 2022; Hsieh et al., 2023). Additionally, it is noteworthy to mention that semi-carbonized nanodots derived from charred *Atractylodes Macrocephala* demonstrated significant biological effects in maintaining the intestinal flora homeostasis of stress-induced gastric ulcer models (Lu et al., 2021). Hence, we postulate that the interaction with microorganisms could potentially serve as a mechanism underlying one aspect of the therapeutic effects of SCR-CDs derived from SCR in the treatment of UC.

Based on these clues, We investigated the protective effects of SCR-CDs against DSS-induced colitis mice model, and further elucidated the mechanisms of SCR-CDs in treating UC by examining the expression of intestinal TJ proteins, inflammatory cytokines, oxidative stress markers, and gut microbial composition. These findings provide further theoretical support for the application of SCR-CDs in the field of medical treatment.

2 Materials and methods

2.1 Materials

Coptidis Rhizoma (CR) was purchased from Beijing Qiancao Herbal Pieces Co., Ltd. (Beijing, China). Dialysis membranes (MWCO: 1000 Da) were purchased from Beijing Ruida Henghui Technology Development Co., Ltd. (Beijing, China). DSS (Molecular weight 36–50 kDa) was purchased from MP Biomedicals, Inc. (Irvine, CA, Uunited States). O-toluidine was purchased from the Beijing John Lunda Technology Development Co., Ltd. (Beijing, China). Haemocoagulase (HC) for injection was purchased from Jinzou Ahon Pharmaceutical Co., Ltd. (Liaoning, China). Enzyme-linked immunosorbent assay (ELISA) kits for mouse Tumor necrosis factor (TNF)-α, Interleukin (IL)-1β, IL-6, IL-17A, IL-22, IL-23, Granulocyte-macrophage colony-stimulating factor (GM-CSF), and Interferon (IFN)-γ were purchased from Jiangsu Kete Biotechnology Co., Ltd. (Jiangsu, China). Myeloperoxidase (MPO), Superoxide dismutase (SOD), Glutathione (GSH), Malondialdehyde (MDA), and Nitric oxide (NO) were purchased from the Nanjing Jiancheng Bioengineering Institute (Nanjing, China). Proteinase, phosphatase inhibitors and the BCA assay kit were purchased from Shanghai Beyotime Biotechnology Co., Ltd. (Shanghai, China).

2.2 Animals

Forty-eight male BALB/c mice and forty male Kunming mice were purchased from SiPeiFu Biotechnology Co., Ltd. (Beijing, China). The mice were reared in a clean-grade animal room (indoor temperature of 24°C ± 1°C and humidity of 50% ± 10%, under 12 h dark/light cycles). All animals were provided *ad libitum* access to food and water. All experimental procedures and animal care were performed according to the guidelines of the Care and Use of Laboratory Animals that were approved by the Ethics Committee of Animal Experimentation of Beijing University of Chinese Medicine.

2.3 Preparation of SCR-CDs

Initially, CR was loaded into a crucible with a lid and subjected to pyrolysis at 350 °C for 1 h in a muffle furnace (TL06112; Beijing ZhongKeAobo Technology Co., Ltd., Beijing, China). Subsequently, the SCR was decocted twice in deionized water (DW) at 100°C for 1 h each time. Following evaporation and concentration, the sample solution was filtered through a microporous membrane (Pore size 0.2 μm, Millipore). The solution was collected after 1 week in DW using a dialysis membrane to obtain the final purified sample containing SCR-CDs for later use. The schematic diagram of the experimental protocol for the preparation of SCR-CDs is exhibited in Supplementary Figure S1.

2.4 Characterization of SCR-CDs

The particle size and microscopic morphology of SCR-CDs were observed using a transmission electron microscope (TEM; Tecnai G2 20; FEI Company, Hillsboro, OR, United States). The atomic lattice spacing of SCR-CDs was uncovered utilizing a high-resolution TEM (JEN-1230; Japan Electron Optics Laboratory, Tokyo, Japan). The ultraviolet-visible (UV-vis) absorption spectra and photoluminescence characteristics of SCR-CDs were determined using a UV-vis spectrometer (CECIL, Cambridge, United Kingdom) and a fluorescence (FL) spectrophotometer (F-4500, Tokyo, Japan), respectively. Moreover, the functional groups and proportioning of chemical elements in SCR-CDs were characterized using Fourier transform infrared (FTIR) spectroscopy (Thermo Fisher, Fremont, CA, United States) and X-ray photoelectron spectroscopy (XPS; ESCALAB 250Xi, Thermo Fisher Scientific, Fremont, CA, United States), respectively. The zeta potential values and hydrodynamic diameter were determined using a Malvern Zetasizer Nano ZS90 (Malvern Instruments). The main components in the solutions of CR and SCR-CDs were identified using high-performance liquid chromatography (HPLC; Agilent 1260) with a ultraviolet detector at 265 nm.

2.5 Models of DSS-induced colitis model in mice and drug treatment

BALB/c mice were administered either regular DW or 3.5% DSS drinking water (with a new DSS solution provided every 2 days) following a 7 days acclimatization period. All animals were randomly divided into 6 groups, with 8 mice per group: 1) vehicle group (equal volume of DW); 2) DSS model group (DSS); 3) Sulfasalazine (SASP) administered group (500 mg/kg, DSS + SASP); 4) High-dose treatment group (0.96 mg/kg, DSS + H-SCR-CDs); 5) Medium-dose treatment group (0.48 mg/kg, DSS + M-SCR-CDs); 6) Low-dose treatment group (0.24 mg/kg, DSS + L-SCR-CDs). All animals received oral administration once daily for a duration of 7 days.

2.6 Disease activity index (DAI)

In this study, we investigated the protective effect of SCR-CDs against DSS-induced colitis in mice by evaluating DAI scores, a widely-used parameter for assessing the severity of colitis in animal models (Jeon et al., 2020). During the administration period, daily records were meticulously maintained for crucial parameters, including body weight, stool condition, as well as the presence of occult or gross bleeding in the mice. The DAI was calculated as the mean of the individual scores for the aforementioned parameters (Table 1), represented by the formula: DAI = (Weight loss + Stool condition + Occult or gross bleeding)/3.

2.7 Sample collection and preparation

Upon conclusion of the experiment, the mice were expediently and humanely euthanized using cervical dislocation. Subsequently, a thorough rinse with phosphate-buffered saline (PBS) was performed, followed by precise measurement and division of the entire colon into two distinct segments. A designated section of the colon was allocated for the meticulous assessment of biochemical indicators. Concurrently, the remaining colon sections alongside pivotal major organs were meticulously immersed in a 4% neutral paraformaldehyde solution for fixation. Subsequent histological evaluation entailed staining with hematoxylin-eosin (H&E) to facilitate a comprehensive assessment of tissue morphology and structure.

2.8 Moisture absorption analysis

The moisture absorption of SCR-CDs was measured gravimetrically, following the methodology previously reported in the literature (Xu et al., 2020). During the sample preparation process, the material was first subjected to drying treatment by heating in an oven at 120 °C for 24 h until a constant weight was achieved. At the conclusion of the drying cycle, the spontaneously cooled sample was placed in a constant temperature and humidity chamber to achieve a stable condition (60% relative humidity at 25 °C room temperature) by absorbing water. During water vapor diffusion at a constant temperature, an analytical balance was used to weigh and record the real-time weight of the material. The percentage moisture absorption was calculated using Equation 1.

$$\text{Percentage moisture absorption} = \frac{w_t - w_i}{w_i} \times 100\% \qquad (1)$$

Where w_t and w_i are the weight of the sample at time “t” and the “initial weight” (g), respectively.

TABLE 1 Parameters, grades, and scores of DAI.

Weight loss (%)	Stool condition	Occult or gross bleeding	Score
None	Normal	Negative	0
1–5		+	1
5–10	Loose stools	++	2
10–15		+++	3
˃15	Diarrhea	Gross bleeding	4

2.9 Hemostasis bioactivity evaluation

The tail-tip amputation and liver scratch models were established following previously published protocols (Sun et al., 2018; Zhang et al., 2018). Specifically, Kunming mice were randomly divided into 5 groups, with 8 mice per group: 1) vehicle group (equal volume of DW); 2) positive treatment group (0.67 Ku/kg, Haemocoagulase, HC); 3) SCR-CDs at different doses administered groups (0.96, 0.48, 0.24 mg/kg for the high-, medium-, low-dose groups). The animals were anesthetized, and a 1 cm segment was excised from the tip of the tail using small scissors. In addition, the trauma-hemorrhage model was established using a 1 mL syringe needle mimicking liver injury. The bleeding condition was monitored at 30 s intervals using filter paper, and the time was recorded until the Hemostatic endpoint was reached. Subsequently, all animals were humanely sacrificed by cervical dislocation.

2.10 Histological evaluation of colitis severity

The histological score, based on Cooper's method, was determined by assessing inflammation severity, inflammation extent, and crypt damage (Cooper et al., 1993). In brief, the histopathological sections of the colon were scored based on the assessment of the following criteria: mucosa was normal and without inflammation, scored 0; mucosal goblet cell loss with mild inflammatory infiltration, scored 1; mucosal goblet cells were largely lost and moderate inflammatory infiltration was present, scored 2; mucosal crypt absence, extensive inflammatory infiltration, and mucosal edema thickening, scored 3; a large area of crypt loss and inflammatory infiltration of the submucosa, scored 4.

2.11 Immunofluorescence staining

Immunofluorescence was performed to determine the levels of ZO-1. For the immunofluorescence staining, the dewaxed sections were first blocked with 10% normal goat serum for 30 min at room temperature. Subsequently, the sections were incubated overnight with primary antibodies against ZO-1 (1:400; GB111981; Servicebio) at 4°C. Following this, the slices were washed and incubated with ZO-1-conjugated goat anti-rabbit secondary antibodies at 37°C for 50 min in the dark. After PBS washing, the sections were counterstained with DAPI for 10 min and sealed with 50% glycerol. Finally, the protein expression levels of ZO-1 were observed using a fluorescent microscope.

2.12 Western blot analysis

The protein concentration was quantified using a bicinchoninic acid (BCA) protein assay kit, and the samples were supplemented with loading buffer for western blot analysis. The proteins were separated by SDS-PAGE and subsequently transferred to PVDF membranes. After 1 h of blocking, the membranes were then incubated overnight at 4°C with specific primary antibodies, including anti-Claudin-1 (1:500; Ab15098; Abcam), anti-Occludin (1:1,000; Df7504; Affinity), ZO-1 (1:1000; Af5145; Affinity), and anti-β-actin (BM0627). Then the samples were incubated with the appropriate secondary antibody at room temperature for 1 h. Following the removal of the secondary antibody by washing, the protein bands were visualized using an ECL hypersensitive luminescent solution (Thermo Fisher, United States).

2.13 Determination of relevant biochemical indicators

The colon tissue was homogenized in normal saline to prepare 10% colon homogenate, which was subsequently centrifuged at 3,000 rpm for 10 min at 4°C to obtain the supernatant. The MPO activity and levels of inflammatory cytokines, including TNF-α, IL-1β, IL-6, IL-17A, IL-22, IL-23, GM-CSF, and IFN-γ, in the colon tissue were determined using commercial ELISA kits. Additionally, the oxidative stress indicators, including SOD, GSH, MDA, and NO levels, were measured following the manufacturer's instructions.

2.14 16S rDNA gene high-throughput sequencing

Fecal samples and cecal contents were collected into sterile tubes and promptly stored at −80°C for preservation. Microbial genomic DNA was then extracted from the fecal samples using standard procedures. The final quantity and quality of DNA were assessed using Nanodrop spectrophotometry and 1.2% agarose gel electrophoresis, respectively. The V3-V4 hypervariable regions of the rRNA genes were amplified using a specific primer with a barcode. PCR amplification was performed using TransStart FastPfu DNA Polymerase (TransGen, Beijing, China). Fluorescence quantification of PCR amplification recovery products was performed using the Quant-iT PicoGreen dsDNA Assay Kit. Sequencing libraries were generated with TruSeq Nano DNA LT Library Prep Kit for Illumina. The library was sequenced by the MiSeq platform in the double-ended sequencing mode. Sequencing was completed by Shanghai Bioprofile Technology Company Ltd. (Shanghai, China). The statistical tests within the microbiome datasets were calculated using the Quantitative Insights Into Microbial Ecology (QIIME) pipeline.

2.15 Cell culture

GES-1 cells (human gastric epithelial cells) and RAW264.7 cells (mouse monocyte-macrophage leukemia cells) were cultured in 4.5 g/L D-glucose Dulbecco's modified Eagle medium (DMEM) supplemented with 20% fetal bovine serum (FBS) and 1% penicillin-streptomycin (PS) solution at 37°C with 5% CO_2.

2.16 Cell viability assay

GES-1 cells and RAW264.7 cells were seeded in a 96-well plate with 100 μL of culture media. The culture media were then replaced with different concentrations of SCR-CDs (SCR-CDs powder after freeze-drying, diluted with the culture medium), and the cells were incubated for an additional 24 h after they had fully adhered. Subsequently, the plates were incubated with 10% cells counting kit-8 solution (CCK-8) for 1 h at 37°C with 5% CO_2. The optical density (OD) was measured at 450 nm using a microplate reader.

2.17 Blood biochemical indicators

At the conclusion of the experiment, blood was collected from the animals following a 12 h fasting period. The animals were swiftly euthanized by cervical dislocation, and the serum was subsequently separated through centrifugation for further biochemical analysis. The hematological parameters, including ALT (Alanine aminotransferase), AST (Aspartate aminotransferase), BUN (Blood urea nitrogen), CRE (Blood creatinine) were obtained using a Beckman Coulter CX4 Pro automatic biochemical analyzer (Beckman Coulter, Brea, CA, United States).

2.18 Statistical analysis

Statistical analysis was conducted using IBM SPSS Statistics software (version 20). The comparison of statistical differences between the two groups was performed using one-way analysis of variance (ANOVA), followed by LSD post-hoc tests. The results are presented as mean ± SD (standard deviations).

3 Results and discussion

3.1 Synthesis and characterization of SCR-CDs

TCM possesses the unique advantage of being multi-targeted, safe, and effective in the treatment of UC (Liu et al., 2022). SCR has long been recognized as one of the vital traditional herbs extensively employed in the treatment of gastrointestinal diseases in China. Its application has been documented in ancient medical literature, and its efficacy has been substantiated through numerous clinical practices. In this study, we utilized a muffle furnace with customized time and temperature parameters to control the degree of pyrolysis during the preparation of SCR. We successfully synthesized SCR-CDs through a simple and eco-friendly calcination method at 350°C for 1 h, avoiding the complexity and instability often associated with other synthesis methods (Supplementary Figure S1). To investigate the ultrastructure and morphology of SCR-CDs, we utilized TEM measurements. The obtained results revealed that SCR-CDs exhibited a roughly spherical structure (Figure 1A). The diameter of SCR-CDs ranged from 1.2 nm to 2.8 nm, with an average particle size of 2.0 nm (Figure 1B). High-resolution TEM enables the characterization of sample morphology with exceptional precision and provides detailed insights into microscopic physical properties. In the Figure 1C, two solid lines delineate distinct crystallographic planes of the matrix. Notably, the core of the nanowire exhibits well-resolved lattice fringes, revealing a lattice spacing of d = 0.201 nm. Moreover, SCR-CDs exhibited a positive zeta potential of + 0.0808 mV (Figure 1D). The observation of the Tyndall phenomenon, as depicted in Supplementary Figure S2, further supports the notion that SCR-CDs form a stable colloidal system in water. Furthermore, the SCR-CDs exhibited ultraviolet absorption properties, as confirmed by UV-vis spectral analysis (Figure 1E). Additionally, fluorescence characterization of the SCR-CDs revealed that the optimal excitation and maximum emission wavelengths were 321 nm and 420 nm, respectively (Figure 1F).

The FTIR spectra were analyzed to discern the surface functional groups of the SCR-CDs (Figure 2A). FTIR analysis depicted the peak at 3,438 cm^{-1} that belonged to the overlapping peaks of -OH (Ţucureanu et al., 2016) and -NH (Jafari et al., 2022) in the sample. A peak at 2,922 cm^{-1} was observed, which was assigned to the stretching C-H mode (Qambrani et al., 2022). Additionally, the FTIR spectrum showed the presence of stretching C=O modes at 1636 cm^{-1} (Feng et al., 2022). Furthermore, a peak at 1384 cm^{-1} was identified, corresponding to the C-O and N-O stretching in the carbohydrate, which may have resulted from dehydration during pyrolysis (Jalali et al., 2021). Based on these characterizations, it can be inferred that SCR-CDs with nanoscale dimensions exhibit optical properties of photoluminescence and fluorescence. To further assess the surface chemical composition and elemental status, we utilized XPS techniques to characterize the surface chemistry. Figure 2B showed the wide-range XPS spectra of the sample. The elemental composition of C, O, and N were determined to be 58.62%, 34.13%, and 4.51%, respectively. Three peaks were fitted to the C 1s spectrum of the region, further assigned to C-C (284.57 eV) (Zhao et al., 2022), C-O (285.79 eV) (Luo et al., 2022), and C=O (288.30 eV) (Noli et al., 2022) (Figure 2C). Due to the overlapping of peaks in the O 1s spectrum, we fitted two peaks corresponding to C-O (529.8 eV) (Zhu et al., 2022) and C=O (531.0 eV) (Shu et al., 2022) (Figure 2D). For the N 1s spectra, two peaks at 400.00 eV and 402.59 eV were observed, which could be attributed to the N-H (Shu et al., 2022) and C-N (Shaikh et al., 2022) bonds, respectively (Figure 2E). The accuracy of surface element identification was enhanced by considering the consistent information from both XPS and FTIR spectra.

The HPLC results revealed the presence of several compounds in the CR solution, including palmatine and BER (Figure 2F).

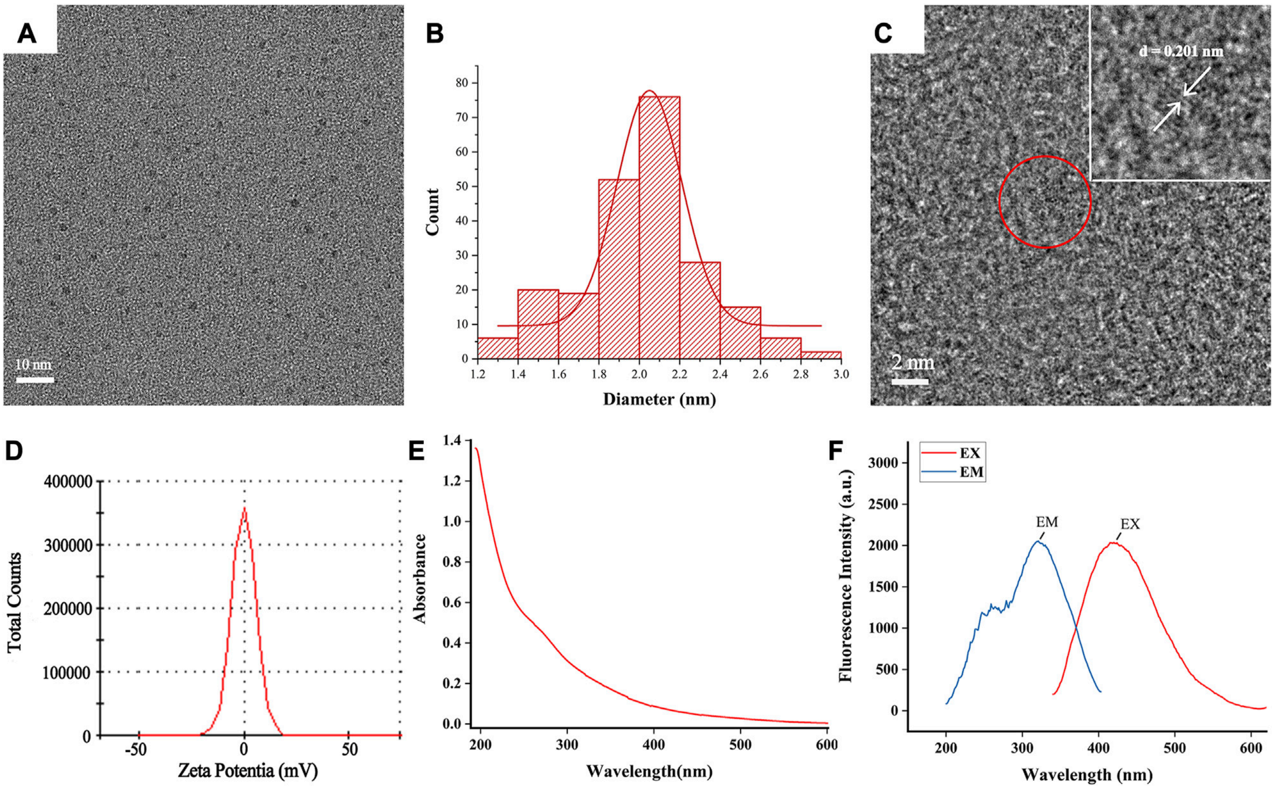

FIGURE 1
Ultrastructure characterization and optical properties of SCR-CDs. **(A)** Transmission electron microscopy (TEM) images of SCR-CDs displaying ultra-small particles. **(B)** Particle size distribution histogram of SCR-CDs. **(C)** High-resolution TEM image of individual SCR-CDs. **(D)** Zeta potential. **(E)** Ultraviolet–visible spectrum. **(F)** Fluorescence spectra.

However, as depicted in Figure 2G, the characteristic peak of the major component from CR was absent in the aqueous SCR-CDs after pyrolysis, isolation, and purification. This finding provides further evidence that active small molecule compounds were not present in SCR-CDs.

3.2 SCR-CDs alleviated the clinical symptoms in DSS-induced mice

The effectiveness of SCR-CDs on colitis symptoms in mice subjected to 3.5% DSS in drinking water for 7 days post-induction were illustrated in Figure 3A. In addition to the body weight of normal mice increasing over time, DSS-exposed mice experienced marked weight loss due to colonic inflammation. Remarkably, varying degrees of body weight recovery were observed in the different doses of the SCR-CDs-treated group (Figure 3B).

Furthermore, a progressive increase in DAI scores was not only associated with the severity of weight loss but also related to the incidence of diarrhea and rectal bleeding. Based on these, DAI was a reliable indicator to evaluate colon inflammation and damage. The DSS group exhibited a higher likelihood of hematochezia and colon shortening compared to the vehicle group. In each of the other groups, the DAI increased with time in comparison to the vehicle group. However, the group treated with DSS individually showed the most significant increase in DAI (Figure 3C). Interestingly, the treatment with SCR-CDs significantly reduced the DAI and ameliorated colon length shortening (Figure 3D) in the experimental colitis mice. Notably, mice in the high-dose SCR-CDs group exhibited greater improvement compared to the other administration groups.

The moisture absorption curves of SCR-CDs demonstrated an extremely rapid initial rate of moisture uptake (Figure 3E). As water vapor gradually penetrated the sample, its mass increased with time, reaching moisture sorption equilibrium after 1 h. The hygroscopicity of SCR-CDs can be attributed to the presence of hydrophilic groups, such as -NH_2, which readily form hydrogen bonds with water molecules. This hypothesis was further confirmed by the XPS results. In contrast to BER, SCR-CDs exhibit enhanced absorptive capacity and contribute to the alleviation of diarrhea symptoms. The physical property similar to activated carbons was also related to other medicinal effects in disease models (Hu et al., 2021; Lu et al., 2021; Luo et al., 2021).

Interestingly, we made a further discovery that SCR-CDs shortened the tail bleeding time (Figure 3F) and liver bleeding time (Figure 3G) in untreated mice, indicating that SCR-CDs enhanced the physiological hemostasis process. This effect could be attributed to formation of a protein corona with serum proteins after CDs were absorbed into the bloodstream, which might further impact the coagulation pathway (Fleischer and Payne, 2014). The symptomatic resolution is a primary clinical endpoint in treating UC

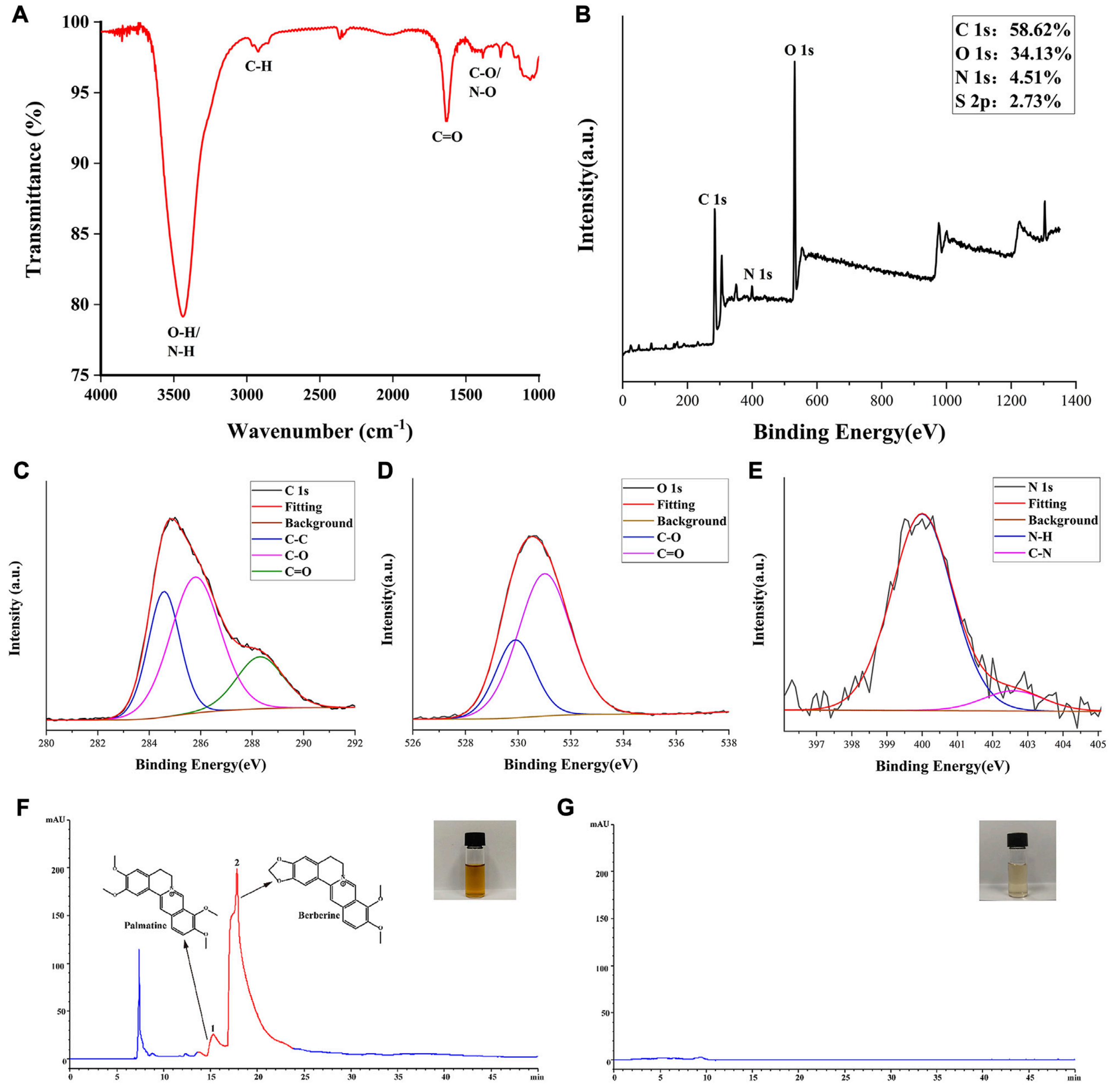

FIGURE 2
Elemental composition, functional group and main constituents of SCR-CDs. **(A)** Fourier transform infrared spectrum of SCR-CDs. **(B)** Full survey spectrum of X-ray photoelectron spectroscopy (XPS). High-resolution survey spectra of **(C)** C1s, **(D)** O1s and **(E)** N1s by XPS. The high-performance liquid chromatography fingerprint spectra of CR **(F)** and SCR-CDs **(G)**.

with complicated pathogenesis at present. Consequently, the hemostasis effect of SCR-CDs may show therapeutic potential in relieving the clinical symptom of UC, especially bloody stool.

In this section, the nanosized SCR-CDs after purification of SCR had hygroscopic and hemostatic bioactivities that BER did not. It is noteworthy that positively charged SCR-CDs are expected to be readily taken up, given that epithelial cells typically display a net negative surface charge (Bannunah et al., 2014). Thus, SCR-CDs were administered in much lower doses than BER, establishing a prerequisite for the safety of SCR-CDs upon entry into the biological environment. These effect of SCR-CDs served as a motivation to further explore their underlying mechanisms in the treatment of different subtypes of IBD.

3.3 SCR-CDs ameliorated the infiltration of inflammatory cells and restored the mucosal barrier in DSS-induced mice

To quantify the extent of colonic inflammatory injury in each group of mice, we observed H&E staining sections (Figure 4A) and calculated a pathological histological score (Figure 4B). In normal

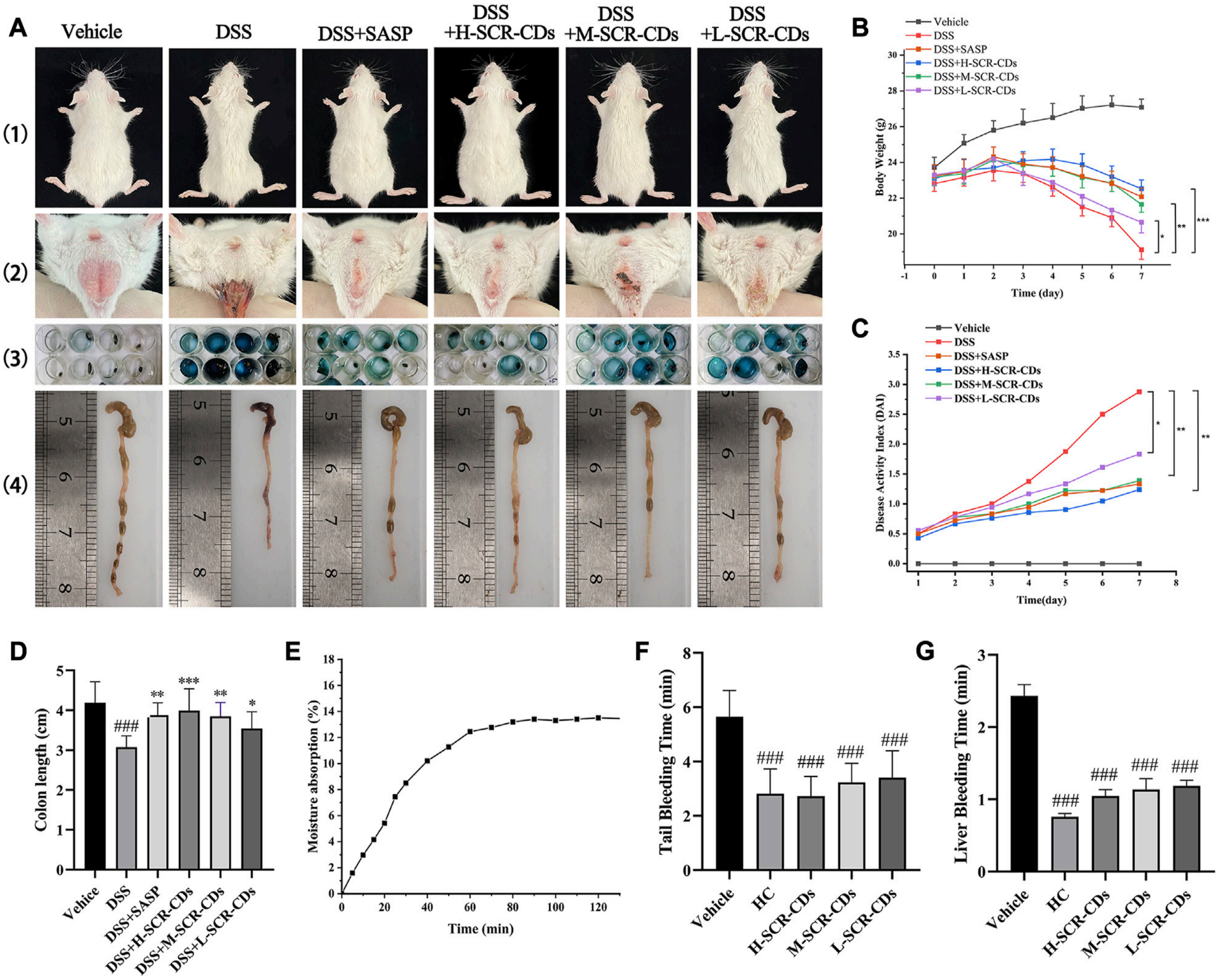

FIGURE 3
Effects of SCR-CDs on clinical symptoms in DSS-induced colitis mice and evaluation of SCR-CDs' hygroscopic and hemostatic bioactivities. **(A)** 1) Presentation of gross body size of animals; 2) Soiled perianal region and accumulation of excreta at the anal; 3) Representative photograph of fecal occult blood test (blue corresponds to positive); 4) Macroscopic appearances of the colon. **(B)** Body weight changes in each group of mice. **(C)** DAI in each group of mice. **(D)** Histogram of colon length. **(E)** Moisture absorption analysis of SCR-CDs. **(F)** Tail amputation and **(G)** liver scratch models were treated with DW, HC, and different concentrations of SCR-CDs. Data are expressed as mean ± SD ($n = 8$). $^{###}p < 0.001$ versus vehicle group; $^{*}p < 0.05$, $^{**}p < 0.01$ and $^{***}p < 0.001$ versus DSS group.

mice, colonic sections exhibited a clear texture of the wrinkled wall, smooth mucosa, intact epithelium, absence of inflammatory cell infiltration, and no signs of congestion, edema, or ulcers in the submucosal layer. However, in DSS-treated mice, we observed focal epithelial necrosis, exfoliation of colonocytes and goblet cells, crypt disappearance, and submucosal edema with abundant neutrophil infiltration. Remarkably, the administration of SCR-CDs exhibited significant protective effects against DSS-induced colon damage. Microscopic manifestations showed the regeneration of the mucosal epithelium, restoration of tissue integrity, increased presence of colonocytes and goblet cells, reduced neutrophil infiltration, and efficient alleviation of congestion in the submucosa. Based on the inflammatory cell infiltration observed in the pathological sections, we further assessed neutrophil infiltration in the intestinal tissue through measurement of MPO activity. Neutrophil infiltration is the marker of intestinal inflammation in experimental IBD (Wu et al., 2023). MPO, as its characteristic enzyme, can induce damage to intestinal mucosal cells, inciting inflammatory responses, and exhibits a direct positive correlation with the severity of the disease (Wang et al., 2023). As depicted in Figure 4C, the MPO activity significantly increased to 10.91 U/g following DSS induction compared to the vehicle group (4.62 U/g). In contrast, the high-dose SCR-CDs treated group exhibited a modest elevation in MPO activity, reaching only 5.60 U/g. Based on the aforementioned results, SCR-CDs exhibited protective effects against colitis, including reduced mucosal erosions and decreased inflammatory infiltrations.

The tightly intact intestinal barrier is essential for segregating the appropriate microbial population and maintaining the homeostasis of multicellular organisms (Wells et al., 2022). The TJ proteins play a crucial role in preventing or regulating the invasion by microorganisms and are considered the primary structural

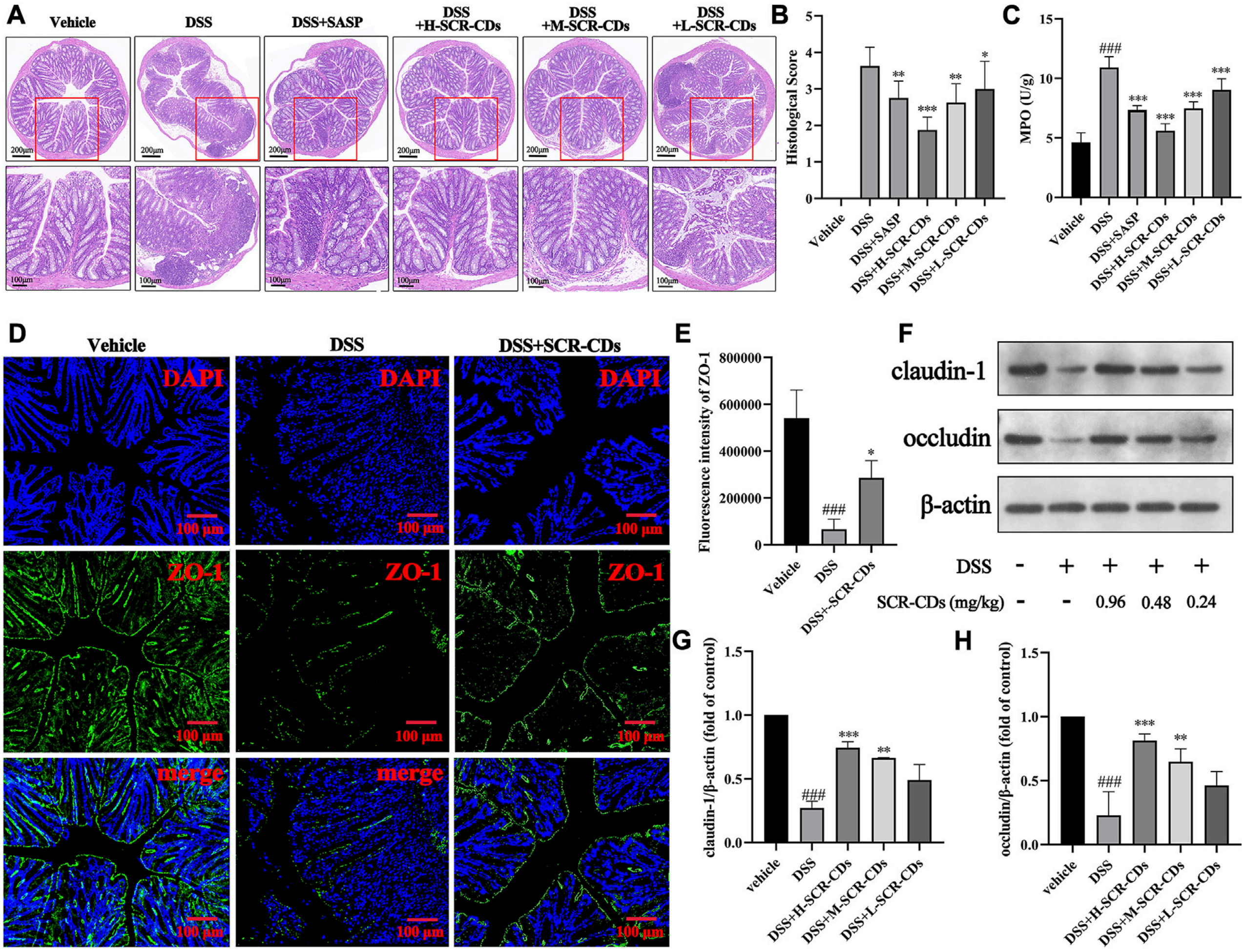

FIGURE 4
The effects of SCR-CDs on colonic inflammatory injury and the expression of intestinal tight junction proteins in DSS-induced mice. **(A)** Representative light microscopy image of H&E staining colon tissue sections (×100 magnification, Scar bar = 200 μm; ×200 magnification, Scar bar = 100 μm). **(B)** Statistical analysis of the pathological histological scores. **(C)** MPO activity in the colon homogenates. **(D–E)** Immunofluorescence for ZO-1 in colonic tissue and its quantified results (×100 magnification, Scar bar = 200 μm). **(F)** Immunoblot for claudin-1 and occludin in colonic tissue. **(G–H)** Immunoblot analysis of the protein density of claudin-1 and occludin in colonic tissue. Data are expressed as mean ± SD ($n = 8$). $^{###}p < 0.001$ versus vehicle group; $^{*}p < 0.05$, $^{**}p < 0.01$ and $^{***}p < 0.001$ versus DSS group.

component controlling paracellular permeability (Zuo et al., 2020). Numerous studies have indicated that upon entering a biological environment, especially in the presence of proteins, the surface of CDs rapidly gets coated with a layer of biomolecules (Nel et al., 2009; Mahmoudi et al., 2011). The protein corona on the surface of CDs undergoes dynamic changes over time as different proteins compete and replace each other. Upon entry into the colonic environment, the positively charged SCR-CDs might adhere to the intestinal epithelial cells (IECs) and become coated with a protein corona containing TJ proteins, which may contribute to the remodeling of the intestinal barrier. To validate this hypothesis, we performed immunofluorescence staining and western blot analysis to detect the expression of intestinal TJ proteins, and the results obtained were consistent with previous research findings (Ye et al., 2022). In Figures 4D–H, Supplementary Figure S3, it was observed that the protein levels of ZO-1, claudin-1, and occludin were significantly downregulated after the DSS induction ($p < 0.05$). The decrease in the expression of these three intestinal TJ proteins and the compromised integrity of the gut barrier in DSS-induced mice were consistent with previous studies (Li et al., 2022). Remarkably, following the administration of SCR-CDs, a notable increase in the levels of intestinal TJ proteins was observed. Among the groups treated with SCR-CDs, the high-dose group exhibited the most pronounced effect in enhancing the positive expression of these metrics. Taken together, these findings indicate that SCR-CDs play a substantial role in maintaining the integrity of the epithelial barrier and augmenting the expression of intestinal TJ proteins.

3.4 SCR-CDs effectively regulated the intestinal microecological environment in DSS-induced mice

The disruption of the epithelial barrier and disassembly of intestinal TJ proteins facilitated the exposure to gut bacteria and subsequent pro-inflammatory stimulation (Figures 5A–H). The

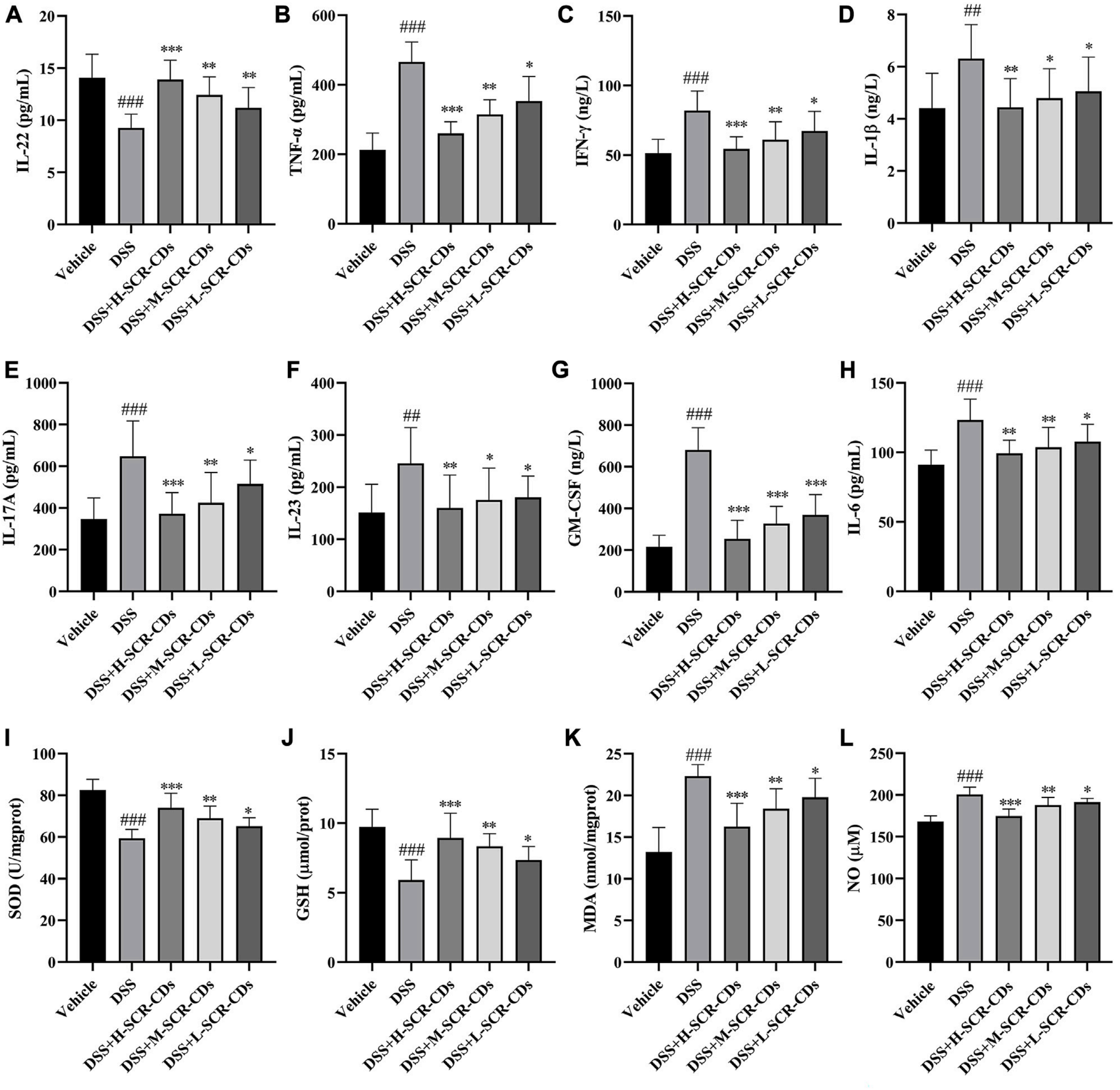

FIGURE 5
Effects of SCR-CDs on inflammatory cytokines and oxidative stress indicators associated with the mucosal microecological environment in DSS-induced mice. The detection of inflammatory cytokines IL-22 **(A)**, TNF-α **(B)**, IFN-γ **(C)**, IL-1β **(D)**, IL-17A **(E)**, IL-23 **(F)**, GM-CSF **(G)** and IL-6 **(H)**. The detection of oxidative stress indicators SOD **(I)**, GSH **(J)**, MDA **(K)** and NO **(L)**. Data are expressed as mean ± SD ($n = 8$). $^{###}p < 0.001$ versus vehicle group; $^{*}p < 0.05$, $^{**}p < 0.01$ and $^{***}p < 0.001$ versus DSS group.

structural and functional disruption of the barrier in UC also led to the absence of IECs. To maintain intestinal homeostasis, further differentiation of IECs is necessary to restore the integrity of the mucosal barrier and epithelial function. The phase was facilitated by regulatory proteins, including IL-22, which represents one of the key cytokines regulated by IL-23 (Neurath and Travis, 2012). In addition to preserving the integrity of the enteric epithelium, IL-22 has the capacity to influence the composition of the microbiota and prevent bacterial translocation (Renga et al., 2022). This study, consistent with the literature reported, demonstrated that the levels of IL-22 were downregulated in DSS-induced colitis. Thus, it was conceivable that elevation of IL-22 and TJ levels after SCR-CDs treatment could maintain paracellular permeability of the intestinal epithelium and block the process of microbiota invasion in colonic tissue.

The infiltration of activated immune cells promotes the abnormal expression of relevant inflammatory cytokines during the perturbation of this mucosal barrier (Ban et al., 2022). IL-23 enhances the effector function of both innate and adaptive lymphocytes, leading to the production of IL-17A and GM-CSF. Furthermore, the IL-23/granulocyte-macrophage colony-stimulating factor (GM-CSF) axis plays a crucial role in driving neutrophil recruitment and exacerbating intestinal inflammation

(Griseri et al., 2012). During the inflammatory response, monocytes migrate from the bloodstream into infected tissues and eventually differentiate into mature macrophages in the presence of GM-CSF. After activation, macrophages secrete pro-inflammatory cytokines such as TNF-α, IL-1β, and IL-6, which enhance leukocyte recruitment to the inflammatory foci. In comparison to the vehicle group, the DSS-treated group exhibited a significant increase in the levels of TNF-α, IFN-γ, IL-1β, IL-17A, IL-23, GM-CSF, and IL-6. However, each group treated with SCR-CDs exhibited a varying degree of mitigation of these changes. Collectively, these data indicate that SCR-CDs exert an anti-colitis effect, as evidenced by the reduction of inflammatory cell infiltration and the regulation of cytokines in DSS-induced mice.

The oxidative stress also accompanies the pathological processes involved in the occurrence and development of UC. SOD and GSH are indispensable antioxidant substances in the body, crucial for mitigating the generation of free radicals during intense inflammation (Duan et al., 2023). MDA is a product of lipid peroxidation in the body, and its quantification provides insight into the extent of lipid peroxidation (Huang J. Q. et al., 2022). Dysregulated expression of NO also contributes to elevated oxidative stress levels (Amirshahrokhi and Imani, 2023). A previous report has proposed that CDs can protect cells from oxidative stress. This protective mechanism is associated with intracellular ROS elimination and the intracellular SOD production (Xu et al., 2015). Consistently, the results of this study demonstrated that the activities of SOD and GSH in the DSS group were significantly lower than those in the vehicle group, while the content of MDA and NO was increased, indicating that the mice after DSS induction were experiencing peroxidative stress. However, compared to the DSS group, upon administration of SCR-CDs, the activities of SOD and GSH were increased, and the levels of MDA and NO were decreased, suggesting that SCR-CDs had a protective effect against oxidative stress injury in the UC model mice (Figure 5I, L).

According to the results, SCR-CDs exerted the anti-colitis effect as evidenced by preventing activation of the inflammatory cascade and inhibiting oxidative stress in DSS-induced mice, and thus the homeostasis of the intestinal microbiological environment.

3.5 SCR-CDs modulated the gut microbiota of DSS-induced mice

The intestinal microbial imbalance in IBD has been extensively reported, and this imbalance can exacerbate the inflammatory process. To elucidate the impact of SCR-CDs on the gut microbiota in DSS-induced mice, we conducted 16 S rDNA profiling. Additionally, we investigated the effect of SCR-CDs on the intestinal microbiome structure by analyzing the distribution of gut microbiota species and their relative abundance among the three groups.

In the comparison between the vehicle group and the DSS group, 467 overlapping Operational Taxonomic Units (OTUs) were identified, representing 1.29% of the total OTUs. Similarly, the DSS group and the SCR-CDs group exhibited 1356 overlapping OTUs, accounting for 3.75% of the total OTUs. Notably, the DSS-treated mice exhibited a lower number of OTUs compared to the vehicle or SCR-CDs-treated mice (Figure 6A). As depicted in Figures 6B–E, the assessment of alpha diversity through the Chao1 index, Observed index, Shannon index, and Simpson index indicated a notable reduction in microbial richness and community diversity in the DSS-treated groups. However, the administration of SCR-CDs effectively restored the alpha diversity of gut microbiota. Moreover, based on OTU abundance, the principal coordinates analysis (PCoA) revealed that the microbiota of the SCR-CDs group exhibited greater similarity with that of the vehicle group, as compared to the DSS-treated group (Figure 6F). The above results indicate that the treatment with SCR-CDs could partially reverse the dysbiosis of gut microbiota in DSS-induced colitis mice.

Linear discriminant analysis effect size (LEfSe) identified the characteristic microorganisms within each group, and the taxonomic hierarchy of these characteristic microorganisms was shown in Figure 6G. Compared to the vehicle group, the DSS-induced colitis group exhibited an abundance of *Proteobacteria*, *Blautia*, and *Mucispirillum* in the intestine. After oral administration of SCR-CDs, an increase in beneficial bacteria, including *Bacteroidales*, was detected. To further investigate the relationship between SCR-CDs-regulated gut microbiota and UC, a significant change in abundance was analyzed. As shown in Figure 6H, N, the abundance of *Muribaculaceae, Lactobacillus, Ruminococcaceae,* and *Bacteroides* significantly decreased while the abundance of *Proteobacteria*, *Akkermansia*, and *Mucispirillum* significantly increased after the DSS treatment in genus level. However, after the administration of SCR-CDs, the overall gut microbiota distributions converged to be similar to those of the untreated group. These results indicated that SCR-CDs could help to restore the gut microbiota structure in mice with DSS-induced colitis.

Literature research has shown that intestinal epithelial damage and disruption results in the translocation of commensal bacteria in the bowel wall, which played a pivotal role in the pathogenesis of UC (Glassner et al., 2020). Typically, in healthy individuals, *Firmicutes* and *Bacteroidetes* constitute approximately 90% of the gut microbiota (Lee and Chang, 2021). The imbalance of the *Bacteroidetes/Firmicutes* ratio has been implicated in predisposition to IBD (Stojanov et al., 2020). Although the flora communities of individuals were not identical to those of animals, our study revealed that the DSS model exhibited intestinal injury accompanied by a decrease in microbiota abundance and an imbalance between probiotics and harmful bacteria. Our study observed marked increases in *Bacteroidetes* after oral administration of SCR-CDs. Previous researchers have demonstrated that *Lactobacillus* could suppress TNF-α expression, improved antioxidant capacity, and directly compete with pathogenic bacteria, thus contributing to ameliorated body weight loss (Hu et al., 2018; Chen et al., 2019). Remarkably, the administration of SCR-CDs in mice protected against the substantial depletion of beneficial microorganisms, such as *Lactobacillus*, *Ruminococcaceae*, and *Muribaculaceae* (Hao et al., 2021). Conversely, an increase in harmful bacteria, such as *Proteobacteria*, which contains many potential pathogens, has been proposed as a diagnostic marker for dysbiosis and an increased risk of disease in the colon (Shin et al., 2015). Therefore, we hypothesized that SCR-CDs could impact the

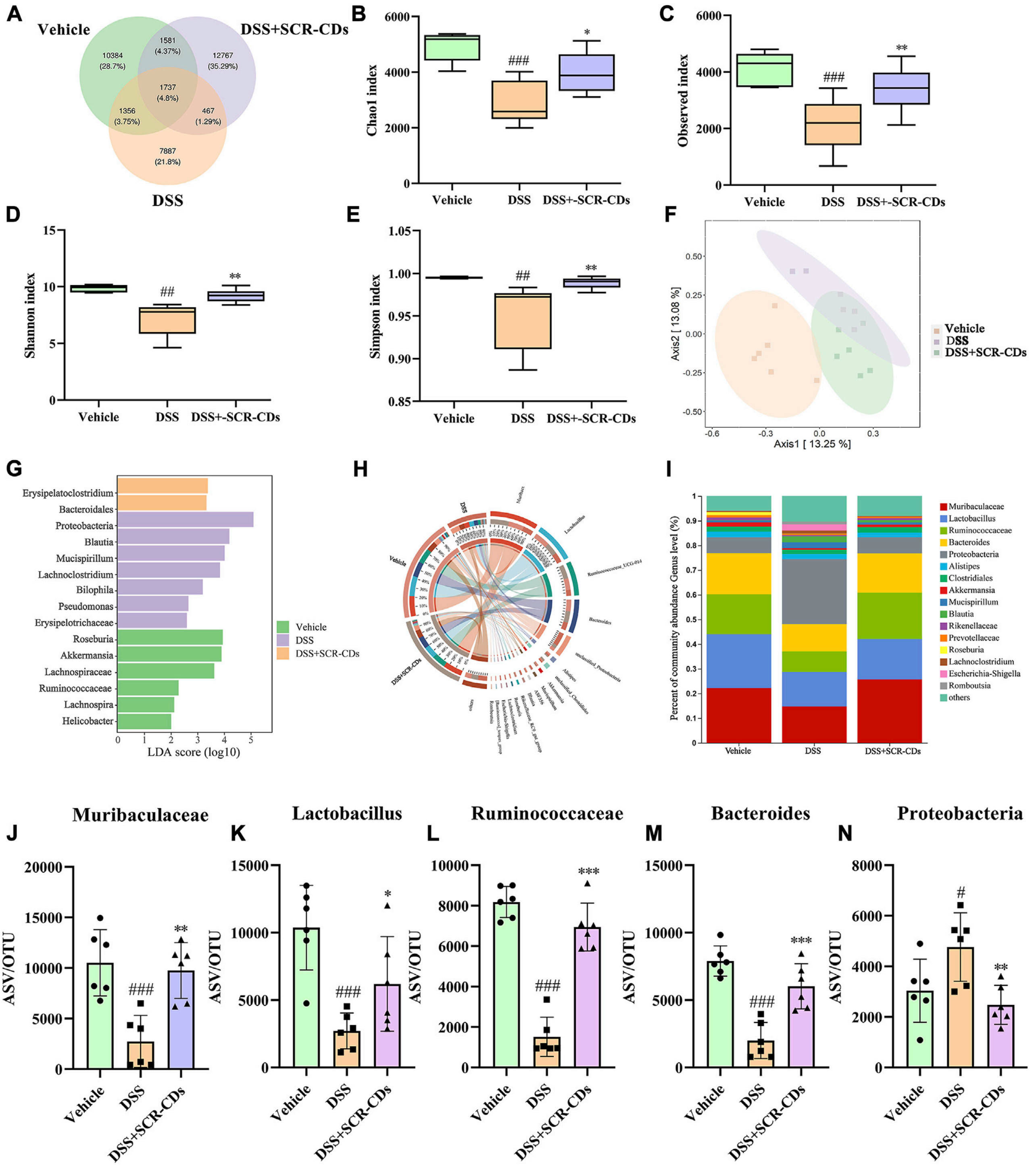

FIGURE 6
Regulatory effect of SCR-CDs on gut microbiota disturbance induced by DSS in colitis mice. **(A)** Venn diagram displaying common or unique species among the three groups. **(B–E)** Alpha diversity indexes were evaluated according to the OTU numbers of each group. $^{\#\#}p < 0.01$, $^{\#\#\#}p < 0.001$ versus vehicle group; $^{*}p < 0.05$, $^{**}p < 0.01$ and $^{***}p < 0.001$ versus DSS group. **(F)** Multiple sample principal coordinates analysis (PCoA) on the bacterial flora in feces. **(G)** Differentially enriched gut microbiota in each group of mice at the genus level by linear discriminant analysis (LDA). LDA score higher than 2 indicates a higher relative abundance in the corresponding group than that in other groups. **(H)** Circos plot showing the distribution of genus level between the different treatment groups. **(I)** The column chart of the relative distribution of each group at the genus level. **(J-N)** Significantly different bacteria at the genus level in the fecal microbiota.

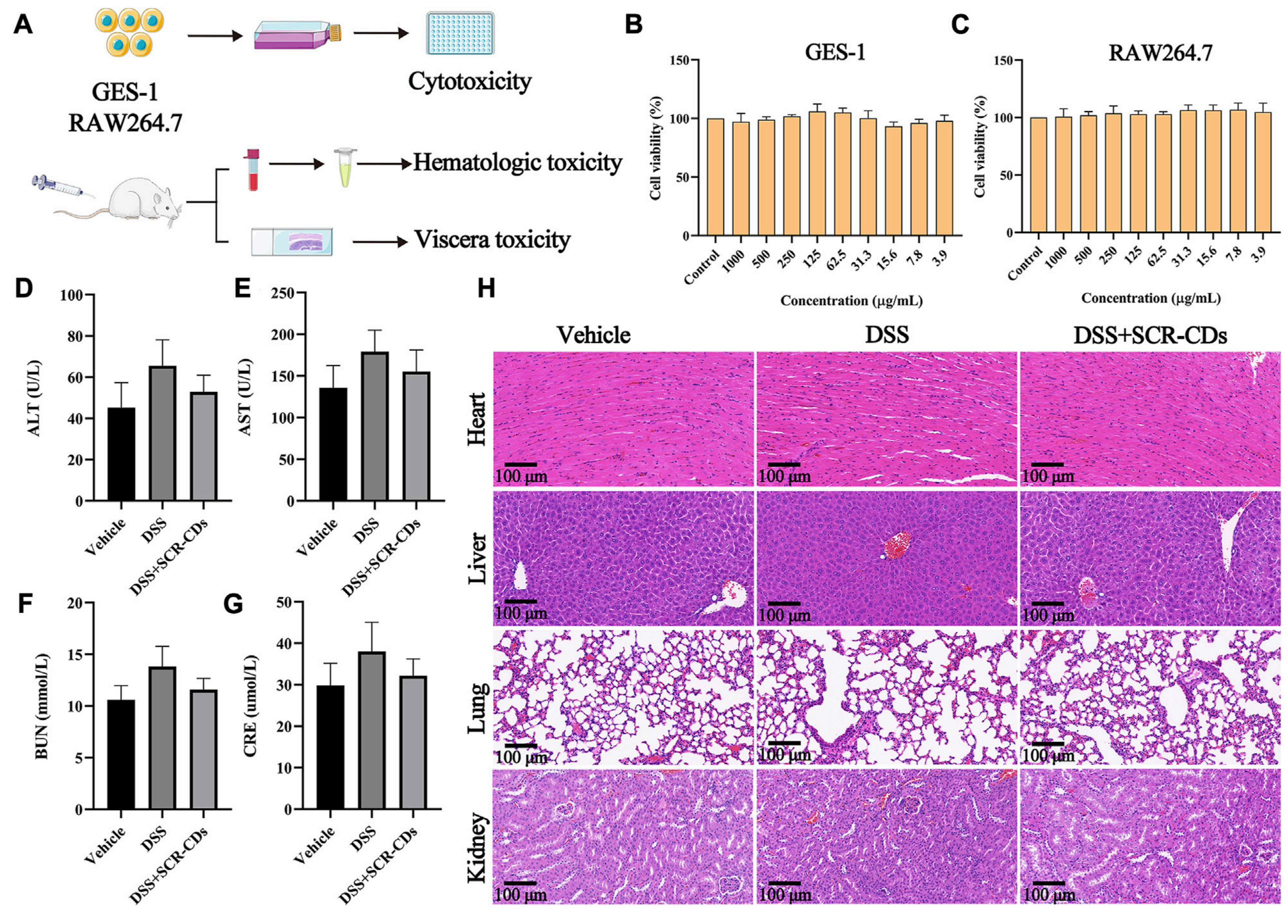

FIGURE 7
In vitro and *in vivo* biosafety evaluation of SCR-CDs. **(A)** Experimental scheme for toxicity detection. CCK-8 analysis was performed with GES-1 cells **(B)** and RAW264.7 cells **(C)** in various concentrations of SCR-CDs for 24 h. Blood was analyzed for ALT **(D)**, AST **(E)**, BUN **(F)** and CRE **(G)**. **(H)** Histological evaluation of four major organs of mice in different groups (×200 magnification, Scar bar = 100 μm). Data are expressed as mean ± SD (*n* = 8).

abundance of dominant bacteria in the intestine. The main bacterial flora and associated pathological states were described in detail in Supplementary Table S1. Our study revealed that SCR-CDs increased the diversity of the intestinal microbiota and restored the balance between beneficial and pathogenic bacteria. These findings demonstrate that the protective effect of SCR-CDs on colitis might be attributed to its regulation of gut microbiota correlated with inflammation.

3.6 Biotoxicity analysis of SCR-CDs *in vitro* and *in vivo*

CDs had great potential for therapeutic applications with the majority of nanoparticles approved for healthcare applications being carbon-based (Truskewycz et al., 2022). Despite the publication of encouraging results regarding the suitability of CDs for biomedical applications, it is essential to evaluate their biosafety from various perspectives before including them in clinical studies (Rennick et al., 2021). Consequently, after the administration of SCR-CDs, we conducted the CCK-8 assay to assess its cytotoxic effect and observed changes in blood biochemical markers and histological sections of major organs (Figure 7A). At the cellular level, we investigated the cytotoxicity of SCR-CDs against GES-1 cells and RAW 264.7 cells at different dose concentrations. Interestingly, no significant effect on the survival rates of GES-1 cells and RAW 264.7 cells was observed under the present experimental conditions (Figure 7B, C). Moreover, the viabilities of GES-1 cells and RAW 264.7 cells remained above 90% across a wide dosing range (ranging from 3.9 to 1,000 μg/mL), indicating that SCR-CDs had no adverse impact on cell growth. It is worth mentioning that SCR-CDs showed no toxicity towards GES-1 cells, providing safety data regarding the oral administration of SCR-CDs.

Satisfactorily, blood chemical examinations, including ALT, AST, BUN, and CRE levels, in mice orally administered with SCR-CDs, showed no noticeable abnormalities (Figures 7D–G). Furthermore, we conducted a evaluation of potential toxicity towards multiple organs *in vivo*. Histological analysis and H&E staining demonstrated that no morphological or pathological abnormalities were detected in any of the treatment groups, indicating that SCR-CDs intervention had little impact on the major organs of mice (Figure 7H, Supplementary Figure S4). Based on the results, SCR-CDs exhibited excellent biocompatibility and biosafety in both *in vitro* and *in vivo* settings.

4 Conclusion

In this study, we conducted a comprehensive characterization of the morphological structure and functional groups of SCR-CDs, which were isolated from SCR. Moreover, we evaluated the protective effect of SCR-CDs against UC using a widely accepted DSS-induced disease model in mice. The hygroscopic capacity and hemostatic bioactivity displayed by SCR-CDs were found to be beneficial in ameliorating the main manifestations of UC, particularly bloody diarrhea. Furthermore, the treatment with SCR-CDs led to an improvement in the intestinal microecological environment by restoring the gut barrier and regulating the microflora, thereby modulating the hyperimmune status. This study offers novel insights into the carbonization process of pure plants in the preparation of carbon dots. We believe that the environmentally friendly, cost-effective, and safer SCR-CDs hold great potential to augment therapeutic strategies for UC.

Data availability statement

The original contributions presented in the study are included in the article/Supplementary Material, further inquiries can be directed to the corresponding authors.

Ethics statement

The animal study was approved by Ethics Committee of Animal Experimentation of Beijing University of Chinese Medicine. The study was conducted in accordance with the local legislation and institutional requirements.

Author contributions

The conception and experimental design of this study were carried out collaboratively by HK, XW, and YnZ. They also supervised the entire project, providing professional insights and guidance on the subject matter, and received financial support. YM, XB, and HM conducted the research experiments. TL and YfZ ensured the accuracy and integrity of the research data, while TW and HQ participated in the literature review. YM and XB drafted the initial manuscript, and HM and YeZ made significant revisions to the manuscript. All authors contributed to the article and approved the submitted version.

Funding

This research was funded by Grant for Qihuang Scholars of the State Administration of Traditional Chinese Medicine, grant number 90020163320012.

Acknowledgments

We greatly appreciate the support of Classical Prescription Basic Research Team of the Beijing University of Chinese Medicine.

Conflict of interest

The authors declare that the research was conducted in the absence of any commercial or financial relationships that could be construed as a potential conflict of interest.

Publisher's note

Supplementary material

The Supplementary Material for this article can be found online at: https://www.frontiersin.org/articles/10.3389/fmolb.2023.1253195/full#supplementary-material

References

Amirshahrokhi, K., and Imani, M. (2023). Levetiracetam attenuates experimental ulcerative colitis through promoting Nrf2/HO-1 antioxidant and inhibiting NF-κB, proinflammatory cytokines and iNOS/NO pathways. *Int. Immunopharmacol.* 119, 110165. doi:10.1016/j.intimp.2023.110165

Ashton, J. J., Barakat, F. M., Barnes, C., Coelho, T. A., Batra, A., Afzal, N. A., et al. (2022). Incidence and prevalence of paediatric inflammatory bowel disease continues to increase in the south of England. *J. Pediatr. Gastroenterol. Nutr.* 75 (2), e20–e24. doi:10.1097/MPG.0000000000003511

Ban, Q. Y., Liu, M., Ding, N., Chen, Y., Lin, Q., Zha, J. M., et al. (2022). Nutraceuticals for the treatment of IBD: current progress and future directions. *Front. Nutr.* 9, 794169. doi:10.3389/fnut.2022.794169

Bannunah, A. M., Vllasaliu, D., Lord, J., and Stolnik, S. (2014). Mechanisms of nanoparticle internalization and transport across an intestinal epithelial cell model: effect of size and surface charge. *Mol. Pharm.* 11 (12), 4363–4373. doi:10.1021/mp500439c

Chen, C. L., Hsu, P. Y., and Pan, T. M. (2019). Therapeutic effects of Lactobacillus paracasei subsp. paracasei NTU 101 powder on dextran sulfate sodium-induced colitis in mice. *J. Food Drug Anal.* 27 (1), 83–92. doi:10.1016/j.jfda.2018.05.004

Chiba, T., Marusawa, H., and Ushijima, T. (2012). Inflammation-associated cancer development in digestive organs: mechanisms and roles for genetic and epigenetic modulation. *Gastroenterology* 143 (3), 550–563. doi:10.1053/j.gastro.2012.07.009

Cooper, H. S., Murthy, S. N., Shah, R. S., and Sedergran, D. J. (1993). Clinicopathologic study of dextran sulfate sodium experimental murine colitis. *Lab. Invest.* 69 (2), 238–249.

Dong, Y., Fan, H., Zhang, Z., Jiang, F., Li, M., Zhou, H., et al. (2022). Berberine ameliorates DSS-induced intestinal mucosal barrier dysfunction through microbiota-dependence and Wnt/β-catenin pathway. *Int. J. Biol. Sci.* 18 (4), 1381–1397. doi:10.7150/ijbs.65476

Duan, S., Wang, H., Gao, Y., Wang, X., Lyu, L., and Wang, Y. (2023). Oral intake of titanium dioxide nanoparticles affect the course and prognosis of ulcerative colitis in mice: involvement of the ROS-TXNIP-NLRP3 inflammasome pathway. *Part Fibre Toxicol.* 20 (1), 24. doi:10.1186/s12989-023-00535-9

Feng, F., Hong, H., Gao, X., Ren, T., Ma, Y., and Feng, P. (2022). Effectiveness of oxygen during sintering of silver thin films derived by nanoparticle ink. *Nanomater. (Basel)* 12 (11), 1908. doi:10.3390/nano12111908

Ferretti, F., Cannatelli, R., Monico, M. C., Maconi, G., and Ardizzone, S. (2022). An update on current pharmacotherapeutic options for the treatment of ulcerative colitis. *J. Clin. Med.* 11 (9), 2302. doi:10.3390/jcm11092302

Fleischer, C. C., and Payne, C. K. (2014). Nanoparticle-cell interactions: molecular structure of the protein corona and cellular outcomes. *Acc. Chem. Res.* 47 (8), 2651–2659. doi:10.1021/ar500190q

Glassner, K. L., Abraham, B. P., and Quigley, E. M. M. (2020). The microbiome and inflammatory bowel disease. *J. Allergy Clin. Immunol.* 145 (1), 16–27. doi:10.1016/j.jaci.2019.11.003

Griseri, T., McKenzie, B. S., Schiering, C., and Powrie, F. (2012). Dysregulated hematopoietic stem and progenitor cell activity promotes interleukin-23-driven chronic intestinal inflammation. *Immunity* 37 (6), 1116–1129. doi:10.1016/j.immuni.2012.08.025

Habtemariam, S. (2020). Berberine pharmacology and the gut microbiota: a hidden therapeutic link. *Pharmacol. Res.* 155, 104722. doi:10.1016/j.phrs.2020.104722

Hao, H., Zhang, X., Tong, L., Liu, Q., Liang, X., Bu, Y., et al. (2021). Effect of extracellular vesicles derived from Lactobacillus plantarum Q7 on gut microbiota and ulcerative colitis in mice. *Front. Immunol.* 12, 777147. doi:10.3389/fimmu.2021.777147

Hsieh, C. T., Gu, S., Gandomi, Y. A., Fu, C. C., Sung, P. Y., Juang, R. S., et al. (2023). Employing functionalized graphene quantum dots to combat coronavirus and enterovirus. *J. Colloid Interface Sci.* 630 (Pt B), 1–10. doi:10.1016/j.jcis.2022.10.082

Hu, J., Luo, J., Zhang, M., Wu, J., Zhang, Y., Kong, H., et al. (2021). Protective effects of radix sophorae flavescentis carbonisata-based carbon dots against ethanol-induced acute gastric ulcer in rats: anti-Inflammatory and antioxidant activities. *Int. J. Nanomedicine* 16, 2461–2475. doi:10.2147/IJN.S289515

Hu, J., Ma, L., Nie, Y., Chen, J., Zheng, W., Wang, X., et al. (2018). A microbiota-derived bacteriocin targets the host to confer diarrhea resistance in early-weaned piglets. *Cell Host Microbe* 24 (6), 817–832. doi:10.1016/j.chom.2018.11.006

Huang, J. G., Wong, Y. K. Y., Chew, K. S., Tanpowpong, P., Calixto Mercado, K. S., Reodica, A., et al. (2022). Epidemiological characteristics of asian children with inflammatory bowel disease at diagnosis: insights from an asian-pacific multi-centre registry network. *World J. Gastroenterol.* 28 (17), 1830–1844. doi:10.3748/wjg.v28.i17.1830

Huang, J. Q., Wei, S. Y., Cheng, N., Zhong, Y. B., Yu, F. H., Li, M. D., et al. (2022). Chimonanthus nitens oliv. Leaf granule ameliorates DSS-induced acute colitis through treg cell improvement, oxidative stress reduction, and gut microflora modulation. *Front. Cell Infect. Microbiol.* 12, 907813. doi:10.3389/fcimb.2022.907813

Jafari, A., Rashidipour, M., Kamarehi, B., Alipour, S., and Ghaderpoori, M. (2022). Toxicity of green synthesized TiO_2 nanoparticles (TiO_2 NPs) on zebra fish. *Environ. Res.* 212 (Pt E), 113542. doi:10.1016/j.envres.2022.113542

Jalali, S., Ardjmand, M., Ramavandi, B., and Nosratinia, F. (2021). Removal of amoxicillin from wastewater in the presence of H_2O_2 using modified zeolite Y-MgO catalyst: an optimization study. *Chemosphere* 274, 129844. doi:10.1016/j.chemosphere.2021.129844

Jeon, Y. D., Lee, J. H., Lee, Y. M., and Kim, D. K. (2020). Puerarin inhibits inflammation and oxidative stress in dextran sulfate sodium-induced colitis mice model. *Biomed. Pharmacother.* 124, 109847. doi:10.1016/j.biopha.2020.109847

Jin, Y., Zhang, Q., Qin, X., Liu, Z., Li, Z., Zhong, X., et al. (2022). Carbon dots derived from folic acid attenuates osteoarthritis by protecting chondrocytes through NF-κB/MAPK pathway and reprogramming macrophages. *J. Nanobiotechnology* 20 (1), 469. doi:10.1186/s12951-022-01681-6

Lee, M., and Chang, E. B. (2021). Inflammatory bowel diseases (IBD) and the microbiome-searching the crime scene for clues. *Gastroenterology* 160 (2), 524–537. doi:10.1053/j.gastro.2020.09.056

Li, Q., Wu, W., Fang, X., Chen, H., Han, Y., Liu, R., et al. (2022). Structural characterization of a polysaccharide from bamboo (Phyllostachys edulis) shoot and its prevention effect on colitis mouse. *Food Chem.* 387, 132807. doi:10.1016/j.foodchem.2022.132807

Liu, H., You, L., Wu, J., Zhao, M., Guo, R., Zhang, H., et al. (2020). Berberine suppresses influenza virus-triggered NLRP3 inflammasome activation in macrophages by inducing mitophagy and decreasing mitochondrial ROS. *J. Leukoc. Biol.* 108 (1), 253–266. doi:10.1002/JLB.3MA0320-358RR

Liu, Y., Li, B. G., Su, Y. H., Zhao, R. X., Song, P., Li, H., et al. (2022). Potential activity of traditional Chinese medicine against ulcerative colitis a review. *J. Ethnopharmacol.* 289, 115084. doi:10.1016/j.jep.2022.115084

Lu, F., Ma, Y., Huang, H., Zhang, Y., Kong, H., Zhao, Y., et al. (2021). Edible and highly biocompatible nanodots from natural plants for the treatment of stress gastric ulcers. *Nanoscale* 13 (14), 6809–6818. doi:10.1039/d1nr01099a

Luo, J., Hu, J., Zhang, M., Zhang, Y., Wu, J., Cheng, J., et al. (2021). Gastroprotective effects of Nelumbinis Rhizomatis Nodus-derived carbon dots on ethanol-induced gastric ulcers in rats. *Nanomedicine (Lond)* 16 (19), 1657–1671. doi:10.2217/nnm-2020-0472

Luo, T., Wang, R., Chai, F., Jiang, L., Rao, P., Yan, L., et al. (2022). Arsenite (III) removal via manganese-decoration on cellulose nanocrystal -grafted polyethyleneimine nanocomposite. *Chemosphere* 303 (Pt 1), 134925. doi:10.1016/j.chemosphere.2022.134925

Mahmoudi, M., Lynch, I., Ejtehadi, M. R., Monopoli, M. P., Bombelli, F. B., and Laurent, S. (2011). Protein-nanoparticle interactions: opportunities and challenges. *Chem. Rev.* 111 (9), 5610–5637. doi:10.1021/cr100440g

Nel, A. E., Mädler, L., Velegol, D., Xia, T., Hoek, E. M., Somasundaran, P., et al. (2009). Understanding biophysicochemical interactions at the nano-bio interface. *Nat. Mater* 8 (7), 543–557. doi:10.1038/nmat2442

Neurath, M. F., and Travis, S. P. (2012). Mucosal healing in inflammatory bowel diseases: A systematic review. *Gut* 61 (11), 1619–1635. doi:10.1136/gutjnl-2012-302830

Noli, F., Dafnomili, A., Sarafidis, G., Dendrinou-Samara, C., Pliatsikas, N., and Kapnisti, M. (2022). Uranium and Thorium water decontamination via novel coated Cu-based nanoparticles, the role of chemistry and environmental implications. *Sci. Total Environ.* 838 (Pt 2), 156050. doi:10.1016/j.scitotenv.2022.156050

Piovani, D., Hassan, C., Repici, A., Rimassa, L., Carlo-Stella, C., Nikolopoulos, G. K., et al. (2022). Risk of cancer in inflammatory bowel diseases: Umbrella review and reanalysis of meta-analyses. *Gastroenterology* 163 (3), 671–684. doi:10.1053/j.gastro.2022.05.038

Qambrani, N., Buledi, J. A., Khand, N. H., Solangi, A. R., Ameen, S., Jalbani, N. S., et al. (2022). Facile Synthesis of NiO/ZnO nanocomposite as an effective platform for electrochemical determination of carbamazepine. *Chemosphere* 303 (Pt 3), 135270. doi:10.1016/j.chemosphere.2022.135270

Renga, G., Nunzi, E., Pariano, M., Puccetti, M., Bellet, M. M., Pieraccini, G., et al. (2022). Optimizing therapeutic outcomes of immune checkpoint blockade by a microbial tryptophan metabolite. *J. Immunother. Cancer* 10 (3), e003725. doi:10.1136/jitc-2021-003725

Rennick, J. J., Johnston, A. P. R., and Parton, R. G. (2021). Key principles and methods for studying the endocytosis of biological and nanoparticle therapeutics. *Nat. Nanotechnol.* 16 (3), 266–276. doi:10.1038/s41565-021-00858-8

Rowan, C. R., Boland, K., and Harewood, G. C. (2020). Ustekinumab as induction and maintenance therapy for ulcerative colitis. *N. Engl. J. Med.* 382 (1), 91. doi:10.1056/NEJMc1915042

Sachar, D. B. (2015). Ulcerative colitis: Dead or alive. *Ann. Intern Med.* 163 (4), 316–317. doi:10.7326/M15-1190

Shaikh, W. A., Kumar, A., Chakraborty, S., Islam, R. U., Bhattacharya, T., and Biswas, J. K. (2022). Biochar-based nanocomposite from waste tea leaf for toxic dye removal: From facile fabrication to functional fitness. *Chemosphere* 291 (Pt 2), 132788. doi:10.1016/j.chemosphere.2021.132788

Shin, N. R., Whon, T. W., and Bae, J. W. (2015). Proteobacteria: microbial signature of dysbiosis in gut microbiota. *Trends Biotechnol.* 33 (9), 496–503. doi:10.1016/j.tibtech.2015.06.011

Shu, Y., Ye, Q., Dai, T., Guan, J., Ji, Z., Xu, Q., et al. (2022). Incorporation of perovskite nanocrystals into lanthanide metal-organic frameworks with enhanced stability for ratiometric and visual sensing of mercury in aqueous solution. *J. Hazard Mater* 430, 128360. doi:10.1016/j.jhazmat.2022.128360

Stojanov, S., Berlec, A., and Štrukelj, B. (2020). The influence of probiotics on the firmicutes/bacteroidetes ratio in the treatment of obesity and inflammatory bowel disease. *Microorganisms* 8 (11), 1715. doi:10.3390/microorganisms8111715

Sun, Z., Lu, F., Cheng, J., Zhang, M., Zhang, Y., Xiong, W., et al. (2018). Haemostatic bioactivity of novel Schizonepetae Spica Carbonisata-derived carbon dots via platelet counts elevation. *Artif. Cells Nanomed Biotechnol.* 46 (Suppl. 3), S308-S317–s317. doi:10.1080/21691401.2018.1492419

Truskewycz, A., Yin, H., Halberg, N., Lai, D. T. H., Ball, A. S., Truong, V. K., et al. (2022). Carbon dot therapeutic platforms: Administration, distribution, metabolism, excretion, toxicity, and therapeutic potential. *Small* 18 (16), e2106342. doi:10.1002/smll.202106342

Ţucureanu, V., Matei, A., and Avram, A. M. (2016). FTIR spectroscopy for carbon family study. *Crit. Rev. Anal. Chem.* 46 (6), 502–520. doi:10.1080/10408347.2016.1157013

Wang, K., Qin, L., Cao, J., Zhang, L., Liu, M., Qu, C., et al. (2023). κ-Selenocarrageenan oligosaccharides prepared by deep-sea enzyme alleviate inflammatory responses and modulate gut microbiota in ulcerative colitis mice. *Int. J. Mol. Sci.* 24 (5), 4672. doi:10.3390/ijms24054672

Wang, L., Gu, D., Su, Y., Ji, D., Yang, Y., Chen, K., et al. (2022). Easy synthesis and characterization of novel carbon dots using the one-pot green method for cancer therapy. *Pharmaceutics* 14 (11), 2423. doi:10.3390/pharmaceutics14112423

Wells, J. M., Gao, Y., de Groot, N., Vonk, M. M., Ulfman, L., and van Neerven, R. J. J. (2022). Babies, bugs, and barriers: dietary modulation of intestinal barrier function in early life. *Annu. Rev. Nutr.* 42, 165–200. doi:10.1146/annurev-nutr-122221-103916

Wu, A., Gao, Y., Kan, R., Ren, P., Xue, C., Kong, B., et al. (2023). Alginate oligosaccharides prevent dextran-sulfate-sodium-induced ulcerative colitis via enhancing intestinal barrier function and modulating gut microbiota. *Foods* 12 (1), 220. doi:10.3390/foods12010220

Xu, J., Li, T., Chao, J., Wu, S., Yan, T., Li, W., et al. (2020). Efficient solar-driven water harvesting from arid air with metal-organic frameworks modified by hygroscopic salt. *Angew. Chem. Int. Ed. Engl.* 59 (13), 5202–5210. doi:10.1002/anie.201915170

Xu, Z. Q., Lan, J. Y., Jin, J. C., Dong, P., Jiang, F. L., and Liu, Y. (2015). Highly photoluminescent nitrogen-doped carbon nanodots and their protective effects against oxidative stress on cells. *ACS Appl. Mater Interfaces* 7 (51), 28346–28352. doi:10.1021/acsami.5b08945

Ye, Z., Zhu, Y., Tang, N., Zhao, X., Jiang, J., Ma, J., et al. (2022). α7 nicotinic acetylcholine receptor agonist GTS-21 attenuates DSS-induced intestinal colitis by improving intestinal mucosal barrier function. *Mol. Med.* 28 (1), 59. doi:10.1186/s10020-022-00485-6

Zhang, M., Cheng, J., Hu, J., Luo, J., Zhang, Y., Lu, F., et al. (2021). Green Phellodendri Chinensis Cortex-based carbon dots for ameliorating imiquimod-induced psoriasis-like inflammation in mice. *J. Nanobiotechnology* 19 (1), 105. doi:10.1186/s12951-021-00847-y

Zhang, M., Zhao, Y., Cheng, J., Liu, X., Wang, Y., Yan, X., et al. (2018). Novel carbon dots derived from Schizonepetae Herba Carbonisata and investigation of their haemostatic efficacy. *Artif. Cells Nanomed Biotechnol.* 46 (8), 1562–1571. doi:10.1080/21691401.2017.1379015

Zhang, Y., Wang, S., Lu, F., Zhang, M., Kong, H., Cheng, J., et al. (2021). The neuroprotective effect of pretreatment with carbon dots from Crinis Carbonisatus (carbonized human hair) against cerebral ischemia reperfusion injury. *J. Nanobiotechnology* 19 (1), 257. doi:10.1186/s12951-021-00908-2

Zhao, Y., Li, B., Li, Y., Fan, X., Zhang, F., Zhang, G., et al. (2022). Synergistic activation of peroxymonosulfate between Co and MnO for bisphenol A degradation with enhanced activity and stability. *J. Colloid Interface Sci.* 623, 775–786. doi:10.1016/j.jcis.2022.05.105

Zhu, S., Xiao, P., Wang, X., Liu, Y., Yi, X., and Zhou, H. (2022). Efficient peroxymonosulfate (PMS) activation by visible-light-driven formation of polymorphic amorphous manganese oxides. *J. Hazard Mater* 427, 127938. doi:10.1016/j.jhazmat.2021.127938

Zou, D., Pei, J., Lan, J., Sang, H., Chen, H., Yuan, H., et al. (2020). A SNP of bacterial blc disturbs gut lysophospholipid homeostasis and induces inflammation through epithelial barrier disruption. *EBioMedicine* 52, 102652. doi:10.1016/j.ebiom.2020.102652

Zou, K., Li, Z., Zhang, Y., Zhang, H. Y., Li, B., Zhu, W. L., et al. (2017). Advances in the study of berberine and its derivatives: a focus on anti-inflammatory and anti-tumor effects in the digestive system. *Acta Pharmacol. Sin.* 38 (2), 157–167. doi:10.1038/aps.2016.125

Zuo, L., Kuo, W. T., and Turner, J. R. (2020). Tight junctions as targets and effectors of mucosal immune homeostasis. *Cell Mol. Gastroenterol. Hepatol.* 10 (2), 327–340. doi:10.1016/j.jcmgh.2020.04.001

frontiers | Frontiers in Molecular Biosciences

TYPE Original Research
PUBLISHED 02 November 2023
DOI 10.3389/fmolb.2023.1284599

OPEN ACCESS

EDITED BY
Md Palashuddin Sk,
Aligarh Muslim University, India

REVIEWED BY
Atikur Hassan,
Indian Institute of Technology Patna, India
Somnath Mondal,
The Pennsylvania State University, United States
Nemany A. N. Hanafy,
Kafrelsheikh University, Egypt

*CORRESPONDENCE
Hui Kong,
✉ doris7629@126.com
Yue Zhang,
✉ 201801024@bucm.edu.cn
Huihua Qu,
✉ quhuihuadr@163.com

RECEIVED 28 August 2023
ACCEPTED 12 October 2023
PUBLISHED 02 November 2023

CITATION
Wu T, Li M, Li T, Zhao Y, Yuan J, Zhao Y, Tian X, Kong R, Zhao Y, Kong H, Zhang Y and Qu H (2023), Natural biomass-derived carbon dots as a potent solubilizer with high biocompatibility and enhanced antioxidant activity.
Front. Mol. Biosci. 10:1284599.
doi: 10.3389/fmolb.2023.1284599

Natural biomass-derived carbon dots as a potent solubilizer with high biocompatibility and enhanced antioxidant activity

Tong Wu[1], Menghan Li[2], Tingjie Li[1], Yafang Zhao[2], Jinye Yuan[2], Yusheng Zhao[2], Xingrong Tian[2], Ruolan Kong[2], Yan Zhao[2], Hui Kong[2]*, Yue Zhang[3]* and Huihua Qu[2,4]*

[1]School of Chinese Materia Medica, Beijing University of Chinese Medicine, Beijing, China, [2]School of Traditional Chinese Medicine, Beijing University of Chinese Medicine, Beijing, China, [3]School of Life Science, Beijing University of Chinese Medicine, Beijing, China, [4]Centre of Scientific Experiment, Beijing University of Chinese Medicine, Beijing, China

Numerous natural compounds exhibit low bioavailability due to suboptimal water solubility. The solubilization methods of the modern pharmaceutical industry in contemporary pharmaceutical research are restricted by low efficiency, sophisticated technological requirements, and latent adverse effects. There is a pressing need to elucidate and implement a novel solubilizer to ameliorate these challenges. This study identified natural biomass-derived carbon dots as a promising candidate. We report on natural fluorescent carbon dots derived from *Aurantia Fructus Immatures* (AFI-CDs), which have exhibited a remarkable solubilization effect, augmenting naringin (NA) solubility by a factor of 216.72. Subsequent analyses suggest that the solubilization mechanism is potentially contingent upon the oration of a nanostructured complex (NA-AFI-CDs) between AFI-CDs and NA, mediated by intermolecular non-covalent bonds. Concomitantly, the synthesized NA-AFI-CDs demonstrated high biocompatibility, exceptional stability, and dispersion. In addition, NA-AFI-CDs manifested superior free radical scavenging capacity. This research contributes foundational insights into the solubilization mechanism of naringin-utilizing AFI-CDs and proffers a novel strategy that circumvents the challenges associated with the low aqueous solubility of water-insoluble drugs in the field of modern pharmaceutical science.

KEYWORDS
carbon dots, solubilization, biomass, antioxidant, nanocomplex

1 Introduction

In pharmaceutical development, over 40% of newly synthesized candidate therapeutics fall under BCS II or BCS IV, categories notorious for their poor water solubility (Charalabidis et al., 2019), particularly compounds originating from natural plants. These plant-derived derivatives (e.g., paclitaxel, resveratrol, and curcumin) have demonstrated a plethora of functional diversity and therapeutic potential, finding applications in the food industry, biopharmaceuticals, and adjacent sectors (Li and Vederas, 2009; Kundu et al., 2021; Cruz-Hernández et al., 2022). Nevertheless, these compounds all exhibit poor bioavailability due to their low aqueous solubility. Water remains the predominant solvent, and the aqueous solubility of these compounds constitutes a crucial determinant influencing their efficacy, which in turn constrains their subsequent advancement. Recently, a myriad of solubilization strategies have been employed to enhance aqueous solubility, such as the modification of hydrophobic groups, augmentation of the glycosidic proportion, encapsulation via amphiphilic molecules, and incorporation of surfactants (Kometani et al., 1996; Jambhekar and Breen, 2016; Liang X. et al., 2023; Wang X. et al., 2023). However, these methodologies have yielded suboptimal solubilization outcomes and the unintended release of noxious chemical agents, potentially culminating in toxicity.

Naringin (NA), a ubiquitous therapeutic employed in the food and pharmaceutical sectors, is comprised of 4′,5,7-hydroxyflavone (saccharide ligand) and rhamnose-β-1,2-glucose and is one of the most abundant bioflavonoids in citrus fruits (Ghanbari-Movahed et al., 2021; Jiang et al., 2023). Regarded as a critical therapeutic agent with a broad spectrum of physiological effects, NA not only exhibits potent bioactivities in anti-inflammatory (Bharti et al., 2014), anti-osteoporosis (Gan et al., 2023b), and anticancer modalities (Farhan, 2022), but also amplifies the absorption of other therapeutics (Choi and Shin, 2005). As a common compound in BCS II, NA possesses poor water solubility, which is measured at 81.1 μM (4.71×10^{-2} g/L) at 25°C in the pH range of 1–7.6. This escalates formulation costs and impacts drug absorption in the intestine (Rao et al., 2017; Xiang et al., 2021). Numerous solubilization techniques exist to enhance its solubility, including structural modification, liposome formation, and polymeric micelle encapsulation (Ravetti et al., 2023). Nevertheless, these approaches often entail intricate experimental conditions and hazardous reagents with prohibitive costs and stringent synthetic constraints; furthermore, commonly synthesized complexes exhibit low encapsulation efficiency and compromised stability (Jat et al., 2022; Secerli et al., 2023). Thus, this body of evidence has catalyzed our pursuit to conceive a novel strategy to address these limitations.

Carbon dots (CDs), recognized as emerging zero-dimensional carbonaceous materials, are spherical nanodots comprising an sp^2 or sp^3 carbon core and complex surface oxygen-containing groups (Nair et al., 2020; Wareing et al., 2021; Gan et al., 2023a). CDs manifest an ultrasmall size, high biocompatibility, chemical robustness, and notable bioactivities, rendering them promising candidate biomaterials for biotherapy (Wang L. et al., 2023; Kalluri et al., 2023; Singh et al., 2023). Previous studies have corroborated that CDs possess considerable potential for development and utilization in the field of solubilization. CDs can not only adsorb compounds via complex porous surfaces (Cutrim et al., 2021), but also bind small molecules through surface functional groups and charge accumulation via non-covalent interactions (e.g., electrostatic interactions, hydrogen bonding, and coordinate bonds) (Arcudi and Đorđević, 2023). Concomitantly, these complexes engendered by CDs and drugs exhibit low biotoxicity, high drug-loading efficiency, and sustained release profiles (Kaurav et al., 2023; Veerapandian et al., 2023). However, the synthesis of many CDs typically involves chemical precursor materials and noxious reagents, which could impede their further biomedical applications. Propitiously, a considerable array of CDs utilizing low-cost and readily available green materials as precursors have been synthesized via environmentally benign processes, while retaining many of the functional groups of the precursor and sufficient bioactivities (Nair et al., 2020; Luo et al., 2021). It is noteworthy that herbal medicine, classified as a potent green precursor, is increasingly garnering attention due to its high yield, abundant active components, and verified pharmacological activities among natural biomass precursors (Luo et al., 2022; Qiang et al., 2023). Simultaneously, some herbal medicine-derived CDs have demonstrated excellent solubilization effects (Luo et al., 2019; Zhang et al., 2021b), and these mechanisms remain largely unexplored.

Thus, motivated by processing technology from Traditional Chinese Medicine (TCM), we synthesized a green natural CD (named AFI-CDs) derived from *Aurantia Fructus Immatures* (an immature fruit from citrus) via a simple one-step pyrolysis method (Figure 1A). We then ascertained its superior solubilization effect on NA compared with other herb-derived CDs (Supplementary Table S1). Subsequently, we devised and optimized a preparation method using AFI-CDs to enhance the solubility of NA and postulated that the solubilization mechanism likely hinges upon the formation of a nanostructured complex (NA-AFI-CDs) between AFI-CDs and NA. Predicated on a series of characterization and property tests, NA-AFI-CDs were revealed to engage in specific structural assembly mediated by intermolecular non-covalent forces. Additionally, AFI-CDs and NA-AFI-CDs both exhibited marked biocompatibility and antioxidant capacities. This study harbors the potential to facilitate the development of an innovative solubilizer for NA and contribute to the foundational theory of solubilization via herb-derived CDs.

2 Results and discussion

2.1 Synthesis and characterization of AFI-CDs

As illustrated in (Supplementary Figure S1), AFI-CDs synthesized via a one-step pyrolysis method underwent a green synthesis process and incorporated no additional pharmaceutical ingredients, thereby ameliorating the complications associated with convoluted operations and unstable efficacy in synthesis. Following dialysis, we procured transparent brown stock solutions, and their freeze-dried powders exhibited remarkable water solubility. The outcome of the high-performance liquid chromatography (HPLC) analysis concerning raw AFI and AFI-CDs demonstrated that no small molecules (such as naringin or hesperidin) remained in the AFI-CDs solution, thereby eliminating interference from uncarbonized natural compounds (Supplementary Figure S2).

Utilizing transmission electron microscopy (TEM), AFI-CDs manifested uniformly spherical nanoscale dots with excellent dispersibility (Figures 1B, C). The majority exhibited a narrow particle size distribution of 1–5 nm with an average diameter of approximately 2.75 ± 0.6 nm, as ascertained through quantitative analysis and statistical methods employing ImageJ software (Figure 1E). The micrograph in high-resolution TEM verified a graphite-like crystalline structure with a lattice spacing of 0.241 nm (Figure 1D), congruent with the common lattice spacing of carbon skeletons in CDs derived from other natural products (Zhai et al., 2023). In accordance with the recombination of radiation on the surface functional groups, numerous CDs possess distinctive optical characteristics and luminescence (Liu et al., 2022; Tao et al., 2023). Spectral analyses of AFI-CDs revealed weak π-π* electronic

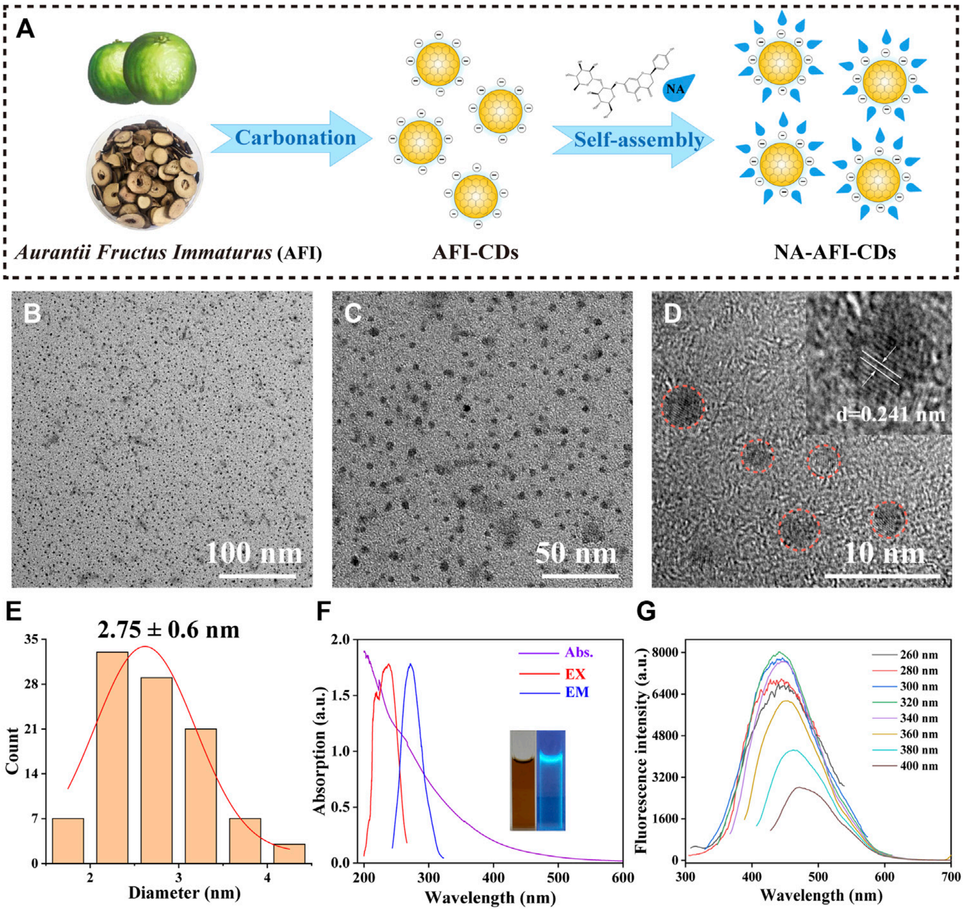

FIGURE 1
Synthesis and characterization of AFI-CDs. **(A)** Schematic diagram of AFI-CDs and NA-AFI-CDs. **(B, C)** TEM images of AFI-CDs at 100 and 50 nm. **(D)** High-resolution TEM image of AFI-CDs (inset, lattice space of AFI-CDs). **(E)** Diameter distribution of AFI-CDs measured by ImageJ. **(F)** UV-vis and FL spectra (inset, AFI-CDs solution in light and UV light). **(G)** Fluorescence spectra of AFI-CDs with different excitation wavelengths. a.u., arbitrary units.

transitions in the sp^2 domains at approximately 280 nm in the UV-vis spectrum (Lu et al., 2021), and their maximal emission and excitation were observed at 320 nm and 440 nm, respectively, in fluorescence spectra (Figure 1F). Simultaneously, the aqueous solution of AFI-CDs (depicted in the inset image in Figure 1F) emitted a light blue-green fluorescence under UV light at 365 nm. Additionally, AFI-CDs displayed excitation-dependent emission behaviors as the excitation wavelength varied from 260 to 400 nm at 20 nm intervals (Figure 1G). Collectively, these indicators substantiate that AFI-CDs are ultrasmall (<5 nm) CDs with fluorescence.

2.2 Solubilization effects of AFI-CDs

The HPLC chromatograms of NA and AFI-CDs indicated that the selectivity of the established HPLC method exhibited commendable performance for subsequent investigation (Figure 2A). The residual standard deviations (RSDs) of precision, repeatability, and stability amounted to 0.64%, 0.60%, and 0.94%, respectively. The linear regression equation of the standard curve was formulated as: $Y = 7020.2X+233.25$, $R^2 = 0.9999$, where Y and X denote the HPLC map peak area and concentration of NA (mg/mL). The linear range of NA spanned from 9.9275 mg/mL to 0.019 mg/mL, and all analytical parameters fell within the methodological requirements.

Previously ascertained process parameters exerted a substantial influence on the solubilization of small molecular compounds (You et al., 2021; Tian et al., 2022). Our study concentrated on augmenting the value of NA through interaction with AFI-CDs. As the concentration of AFI-CDs escalated from 7.8125 to 500 μg/mL, the solubility of NA experienced a pronounced increase from 0.01631 mg/mL to 6.3449 mg/mL, subsequently declining at 750 μg/mL (Figure 2B), a phenomenon consistent with previous studies on the solubilization of CDs (Chen et al., 2023). The dosage of NA was an integral determinant influencing the stability of the NA-AFI-CDs. As the dosage of NA increased from 2 to 12 mg, the solubility of NA initially proliferated up to 8 mg, then diminished (Figure 2C). The temperature of the aqueous solution constituted an important factor in NA-AFI-CDs; as illustrated in Figure 2D, the solubilization of NA correlated positively with temperature and amounted to 2.42, 4.70, and 6.34 mg at temperatures of 40, 60, and 80°C, respectively. No discernible differences in solubility were observed from 100°C to 140°C, and all registered lower concentrations of NA than the procedure conducted at 80°C. Concomitantly, we investigated

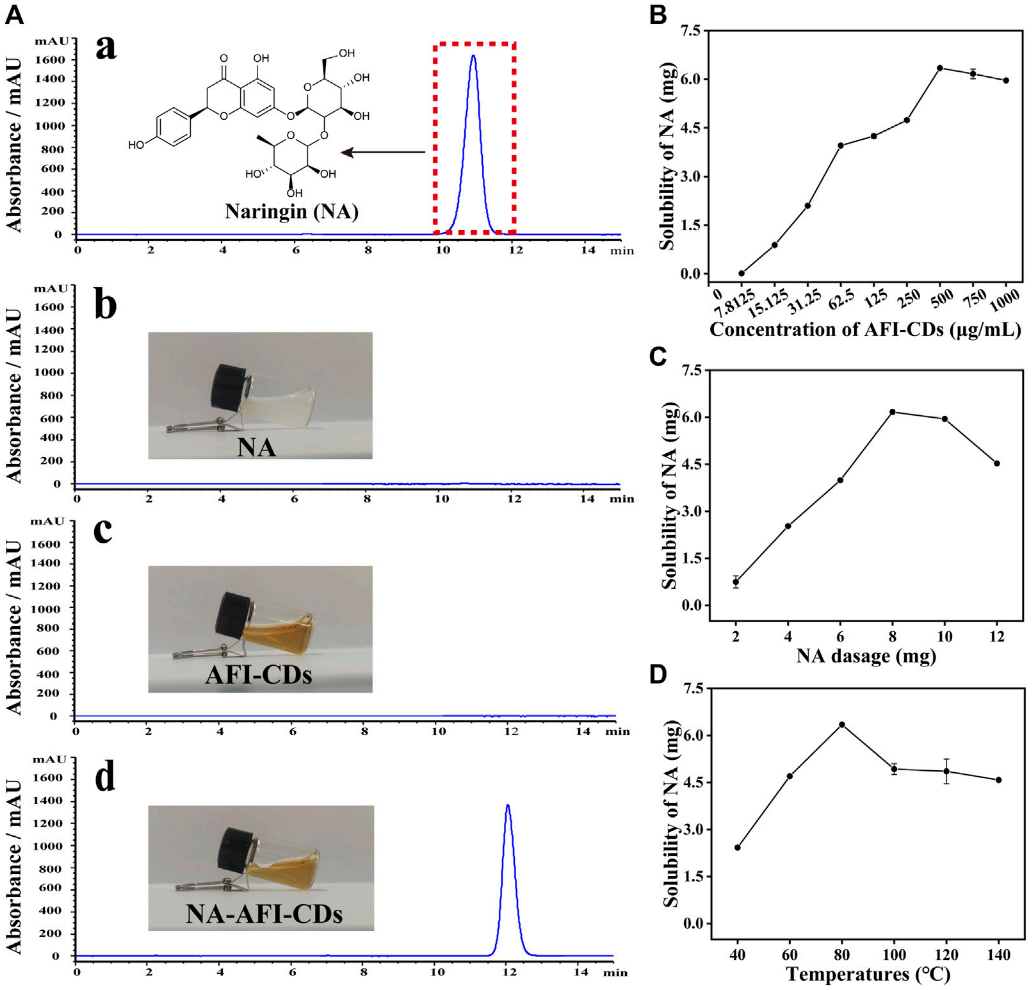

FIGURE 2
Solubilization tests of AFI-CDs. **(A)** HPLC chromatograms of **(a)** NA in methanol; **(b)** NA in water; **(c)** AFI-CDs; and **(d)** NA-AFI-CDs. **(B–D)** The effect of the concentration of AFI-CDs, NA dosage, and temperature. Each set of experiments was repeated three times.

variations in solubility attributable to heating duration; minimal fluctuations were evident with heating from 4 to 10 h. Thus, the optimal heating duration for the solubilization of AFI-CDs transpired to be 6 h in the aqueous solution (Supplementary Figure S3). Additionally, we examined the impact of varying oscillation durations on the solubilization of NA. As oscillation time extended, the solubilization of NA escalated from 3.31 to 6.34 mg and manifested a notable decrease at 160 min, suggesting that protracted oscillations may compromise the stabilization of NA-AFI-CDs (Supplementary Figure S4). Simultaneously, we analyzed and compiled DLE and SE of NA-AFI-CDs under various conditions and observed a congruent trend with the solubility of NA (Supplementary Tables S2–S6). In accordance with the empirical findings, the optimal preparation conditions for NA-AFI-CDs were ascertained: 8 mg of NA (13.73 μmol) was amalgamated with 500 μg/mL of AFI-CDs in a vial, a mix that was subjected to agitation for 80 min at room temperature; subsequently, the procured solution underwent heating at 80°C for 4 h in the dark. The optimal method was deemed applicable for ensuing research endeavors.

2.3 Solubilization mechanism of AFI-CDs

2.3.1 Morphology of NA-AFI-CDs

As depicted in the inset image in Figure 2A, the aqueous solution of AFI-CDs manifested as a lucid and transparent solution with a pH of 6.7, whereas NA constituted a milky suspension in water, evidencing weak solubility in water. Conversely, the solution of NA-AFI-CDs exhibited a pellucid brown hue, akin to the AFI-CDs solution, implying that insoluble NA may transmute into an amorphous state during interaction with AFI-CDs. Figure 3A, acquired through TEM and HRTEM, reveals that NA-AFI-CDs comprised agglomerated spherical nanodots devoid of discernible lattice space. Figure 3B indicates that NA-AFI-CDs possessed a homogeneous shape with an augmented mean particle size of 4.49 ± 1.2 nm, ranging from 2 to 10 nm, when compared with the AFI-CDs solution. Simultaneously, in comparison with NA suspension, the Tyndall phenomenon of NA-AFI-CDs manifested as a narrow bright singular light path, corroborating the colloidal nature of the solution (Figure 3A and Supplementary Figure S5). Moreover, dynamic light scattering (DLS) ascertained that the

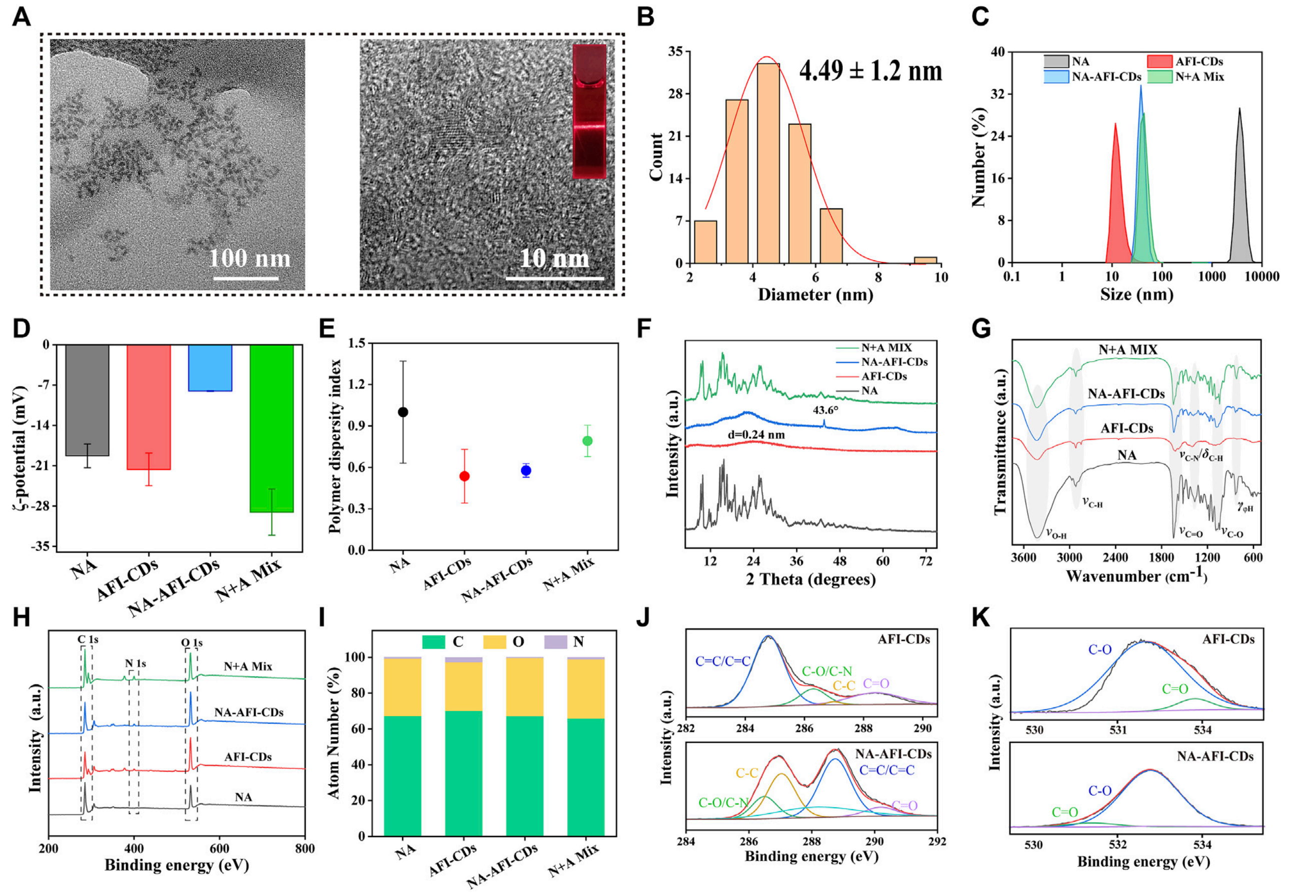

FIGURE 3
Morphology and characterization of NA-AFI-CDs. **(A)** TEM and HRTEM of NA-AFI-CDs (inset, Tyndall phenomenon of AFI-CDs). **(B)** Diameter distribution of NA-AFI-CDs. **(C)** DLS assay. **(D)** ζ-potentials evaluation. **(E)** PDI assay. **(F)** XRD spectra. **(G)** FT-IR spectra. **(H)** XPS spectra. **(I)** Elemental composition. **(J)** C 1s high-resolution XPS spectra. **(K)** O 1s high-resolution XPS spectra. a.u., arbitrary units.

NA suspension exhibited poor distribution (PDI = 1) and an approximate hydrodynamic size of 3,000 nm, attributable to its low water solubility. Contrastingly, both AFI-CDs and NA-AFI-CDs displayed uniform distribution in water, with hydrodynamic diameters of 11.7 and 38.8 nm, respectively; their uniform PDI indicated optimal distribution in the water dispersion system (Figures 3C, E). The ζ-potentials of NA, AFI-CDs, NA-AFI-CDs, and the physical mixture were measured as −19.3 ± 2.07, −21.6 ± 2.81, −8.0 ± 0.05, and −29.1 ± 4.01 mV, respectively (Figure 3D). The negative charge was correlated with abundant oxygen-containing groups, and the enhanced charge of NA-AFI-CDs was ascribed to electrostatic adsorption (Ghanbari et al., 2021).

2.3.2 Optical nature of NA-AFI-CDs

To elucidate the altered optical characteristics of the nanostructure, the synthesized AFI-CDs and NA-AFI-CDs samples were characterized via UV-vis absorption spectrophotometer and fluorescence (FL) spectroscopy, respectively. UV-vis absorption spectrophotometer further validated the interaction of NA-AFI-CDs (Supplementary Figure S6A). Peaks at 223.46 and 282.9 nm were identifiable as the characteristic peaks of NA, and the UV spectrum of NA-AFI-CDs paralleled that of NA. The absorbance of NA-AFI-CDs underwent a blue shift from 224.6 to 223.4 nm, suggesting that small molecules and CDs may amalgamate to form a complex. Intriguingly, NA-AFI-CDs exhibited diminished blue-green fluorescence relative to AFI-CDs and the physical mixture of AFI-CDs and NA (Supplementary Figure S6B). Concurrently, FL spectra discerned that NA-AFI-CDs emanated weaker emission fluorescence with a redshift from 438 to 449 nm (Supplementary Figure S6C). These phenomena imply that NA-AFI-CDs are not a mere mixture of AFI-CDs and NA but rather a complex composite of the two.

2.3.3 Characterization of NA-AFI-CDs

The elucidation of the formulation mechanism of NA-AFI-CDs was predicated upon a series of spectroscopic characterizations. As depicted in Figure 3F, the X-ray diffraction patterns (XRD) of the NA exhibited multiple sharp diffraction peaks with a well-defined crystal structure. The integral amorphous state of AFI-CDs was preserved due to its elevated aqueous solubility. Concurrently, the reflection planes at approximately 26.603° were attributed to highly disordered carbon structures corresponding to the (002) plane of the graphitic framework (Xu et al., 2022). Furthermore, NA-AFI-CDs manifested a high-energy amorphous state, obliterating the characteristic peaks and introducing sharp peaks related to the correlation with the amorphization of the NA. The physical mixture exhibited a hybrid characterization between NA and

AFI-CDs, corroborating that the novel nanostructure was successfully synthesized rather than being a mere physical mixture.

Subsequently, Fourier Transform Infrared Spectrometry (FT-IR) validated the formation of NA-AFI-CDs (Figure 3G). NA-AFI-CDs possessed analogous chemical signatures to those of NA and AFI-CDs, such as γ-C-OH (3,420 cm^{-1}) of AFI-CDs and γ-C=O (1,618 cm^{-1}) and γ-C-O (1,100 cm^{-1}) of NA, as well as NA-AFI-CDs exhibiting a predominant spectrum closely resembling AFI-CDs. In contradistinction, the physical mixture of NA and AFI-CDs comprised solely the sample superposition of monomer materials. This evidence substantiates that NA and AFI-CDs were successfully amalgamated. Moreover, the absorption peaks such as γ-C-N (from 1,404 to 1,385 cm^{-1}) and γ-C-O (from 1,088 to 1,081 cm^{-1}) exhibited slight shifts to lower wavenumbers with attenuated peak intensities, compared with those of AFI-CDs and NA, respectively. This phenomenon is attributable to electrostatic interaction and intermolecular hydrogen bonding between NA and AFI-CDs, resulting in the weakening of the chemical bond force constant and delocalization of the electron cloud (Pinilla-Peñalver et al., 2022).

Subsequent X-ray Photoelectron Spectroscopy (XPS) was undertaken to augment the structural assessment, and the resultant spectra of each element were documented (Figure 3H). The elemental composition in Figure 3I and Supplementary Table S7 revealed that NA-AFI-CDs contain a higher proportion of O (32.47%) and a diminished proportion of N (0.2%) compared with NA (O, 32.01%; N, 0.59%) and AFI-CDs (O, 27.27%; N, 0.2%), signifying that oxygen elements play an integral role in the assembly of NA-AFI-CDs. The XPS survey energy spectrum furnished additional corroborative evidence of bonding (Figures 3J, K, Supplementary Figures S7, S8). The C 1s spectrum of AFI-CDs consisted of three surface components manifesting at 284.80, 286.30, 281.02, and 288.39 eV, corresponding to C=C/C≡C, C-O/C-N, C=C, and C=O, respectively (Tong et al., 2020). The distinctive binding energy spectrum of C=C/C≡C and C-C indicated the amorphous character of AFI-CDs with a carbon core comprising both sp^2 and sp^3 C orbitals (Li et al., 2023). The core level spectrum of O 1s in the top exhibited two components with binding energies at 532.73 and 533.87 eV, attributed to C=O and C-OH bonds (Liang P. et al., 2023). Pertaining to NA-AFI-CDs, the XPS survey spectrum of NA-AFI-CDs displayed similar characteristic peaks for C, O, and N elements as observed in the unmodified AFI-CDs and NA, and altered binding energies of distinct chemical bonds indicated interactions between the two materials. For instance, the XPS spectrum of the C=C bond of C 1s exhibited an elevated value in NA-AFI-CDs compared with NA and AFI-CDs, which may be correlated with amorphous NA interacting with AFI-CDs through a series of processes. All the characterization results revealed that the solubilization mechanism is primarily attributed to the formation of cluster-like amorphous nanocomplexes between NA and AFI-CDs; concurrently, non-covalent forces (e.g., electrostatic adsorption and intermolecular hydrogen bonding) play a pivotal role in the interlacing of the two materials.

2.3.4 The interaction between NA and AFI-CDs

Although the aforementioned evidence affords sufficient insight to substantiate structural alterations and crystal transition, it lacks direct corroboration to further elucidate intricate aspects of the interaction between NA and AFI-CDs. The *in vitro* release profile constitutes a classical methodological approach for ascertaining the binding state and delivery capacity of the complex. In Figure 4A, a saturated NA solution, employed as a control group, attained its cumulative drug release in 1,440 min at 43.69%. By contrast, the cumulative drug release from NA-AFI-CDs not only reached 91.96% within the same identical release timeframe but also exhibited a lower dissolution rate than the control group. These outcomes indubitably substantiate that the solubilization capability of AFI-CDs possesses substantial potential for drug release and affirms that the interaction between NA and AFI-CDs is primarily governed by non-covalent forces rather than covalent bonds. Subsequently, isothermal titration calorimetry (ITC) was used to explore the presence of non-covalent forces between NA and AFI-CDs. An AFI-CDs solution was titrated with an NA suspension at room temperature (25°C), manifesting a positive energy change between the two constituents, thereby suggesting an exothermic reaction propelled by an enthalpy change (Figure 4B). Concomitantly, the negative ΔH and -TΔS signified the spontaneity and stability of this reaction (Figure 4C) (Zhao et al., 2020). These findings corroborate that non-covalent forces facilitate aggregation and self-assembly between NA and AFI-CDs.

Moreover, the solubilization efficacy of AFI-CDs on naringenin, NA, and narirutin was assessed. The data demonstrated that AFI-CDs augmented the solubilization efficacy of naringenin eight-fold compared with its solubility in water, thereby corroborating that the interaction of the glycosidic fraction of NA with AFI-CDs has a pronounced impact on its solubilization capability (Figures 4D, E). Pertaining to narirutin, an isomer of NA with the identical glycoside, AFI-CDs exhibited no significant solubilization effect (Figure 4F), implying that AFI-CDs may achieve enhanced solubilization through the recognition and binding to corresponding glycosidic structures. To validate this hypothesis, the solubilization efficacy of AFI-CDs on hesperidin and neohesperidin (isomers with identical glycosides) was assessed; the findings indicated a stronger solubilization effect for neohesperidin than for hesperidin (Figure 4G). The neohesperidin possesses a comparable disaccharide structure and binding site with NA, indicating that AFI-CDs principally recognize these disaccharides and self-assemble into complexes to enhance solubility. This molecular recognition phenomenon may be facilitated by non-covalent forces generated between these AFI-CDs and NA (Figure 4H). Extant literature confirms that CDs significantly inhibit the conformational change of isomers through self-recognition (Liang et al., 2022; Jv et al., 2023), and our data elucidate that such recognition also amplifies molecular interactions and facilitates assembly into complexes. Owing to limited techniques, AFI-CDs lack a well-defined chemical structure for identification. Our analyses have thus far scrutinized the principal nanostructure of NA-AFI-CDs and partially assessed interactions between molecules, necessitating further verification through robust research methodologies in the future.

2.4 Physicochemical properties of NA-AFI-CDs

To assess the thermal stability of NA-AFI-CDs, TG (thermogravimetry) and DSC (differential scanning calorimetry)

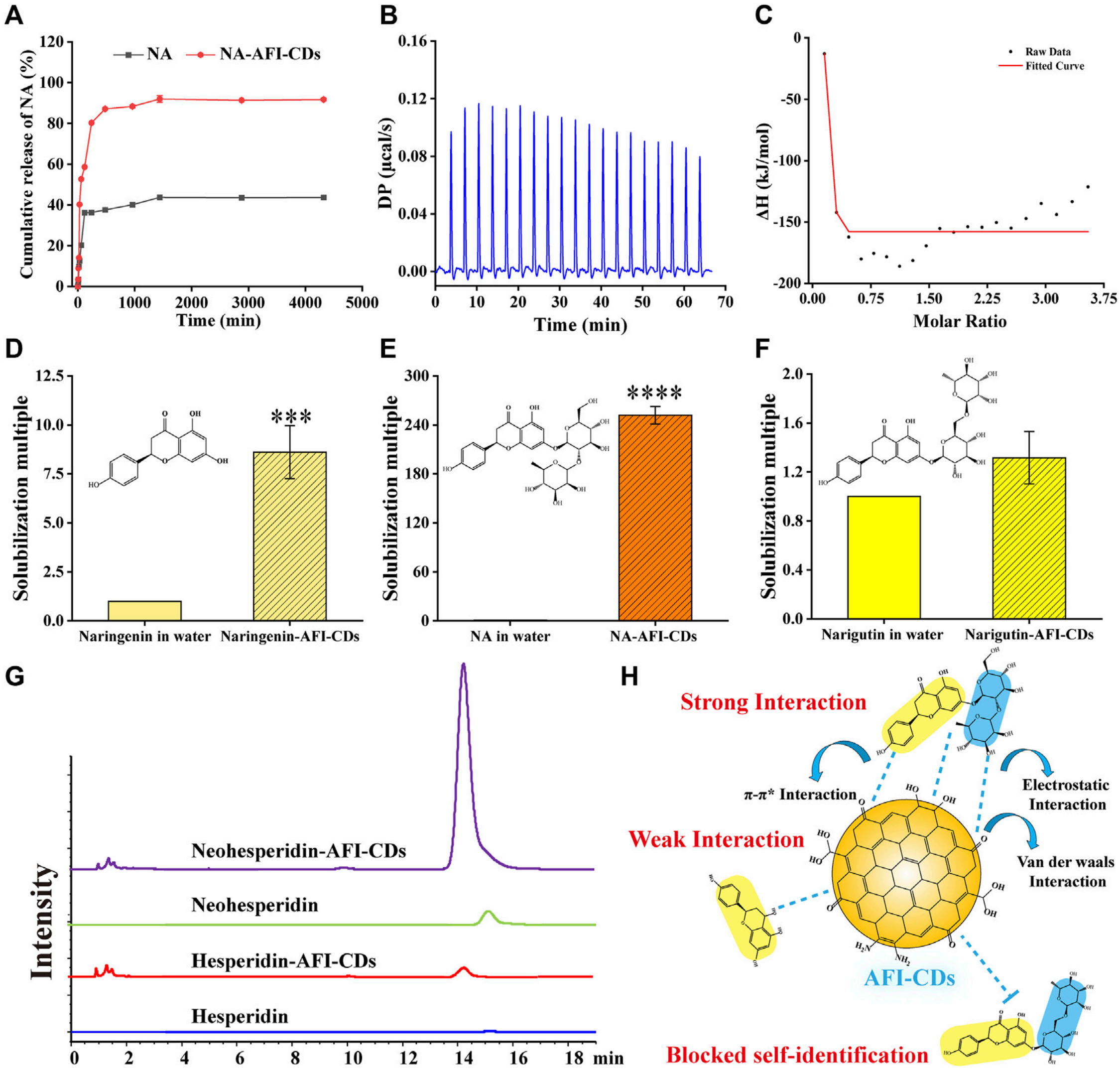

FIGURE 4
The interaction evaluation and solubilization mechanism of NA-AFI-CDs. **(A)** *In vitro* release profile of NA and NA-AFI-CDs. **(B)** The calorimetric titration. **(C)** Binding isotherm. **(D–F)** The solubilization effect assays to naringenin, naringin, and narirutin. **(G)** HPLC chromatograms of hesperidin and neohesperidin mixed with water or AFI-CDs. **(H)** Schematic diagram of the solubilization mechanism.

analyses were conducted under an N_2 atmosphere. As illustrated in Figure 5A, the initial phase of pure NA in TG revealed a weight loss of 5.65% from 50°C to 135°C, attributed to the loss of adsorbed water and crystalline water. In the second phase, a substantial weight loss (37.38%) from 248°C to 350°C was observed, attributable to the thermal degradation of NA. In the DSC curve, NA manifested a distinct endothermic enthalpy commencing at 248°C, correlated with the structural decomposition induced by the melting of NA crystals. AFI-CDs exhibited only a singular weight loss zone (27%) from 50°C to approximately 350 °C, correlated with water evaporation (Figure 5B). In the DSC curve for AFI-CDs, a pronounced broad exothermic peak at 82.1°C suggested the decomposition of crystalline water in the carbon dots during the heating process. The data for NA-AFI-CDs indicated relative stability between 50°C and 225°C, accompanied by a gradual weight loss of 34.57% from 225°C to 350°C (Figure 5C). For NA-AFI-CDs, the DSC thermogram revealed the characteristics of both NA and AFI-CDs, with the characteristic peak of NA shifting to 230°C, indicating the formation of a novel structure between NA and AFI-CDs. TG and DSC thermograms of the physical mixture yielded similar mass loss and residual mass relative to NA, suggesting that the simple physical mixture exerted no significant influence on thermogravimetric alterations (Figure 5D). The TG curves disclosed that the four samples possessed 55.29%, 73.66%, 57.25%, and 56.17% thermal decomposition residues, corresponding to NA, AFI-CDs, NA-AFI-CDs, and the physical mixture, respectively. The expanded pyrolysis temperature range and higher proportion of residual substances implied that NA-AFI-CDs boasted superior thermal stability.

Furthermore, the solvent stability of NA-AFI-CDs was evaluated. The aqueous solution of NA-AFI-CDs presented a clear brown fluid with a narrow light path characteristic of the Tyndall phenomenon and retained its clarity without sedimentation even after 7 days at room temperature (Figure 5E). Concurrently, the

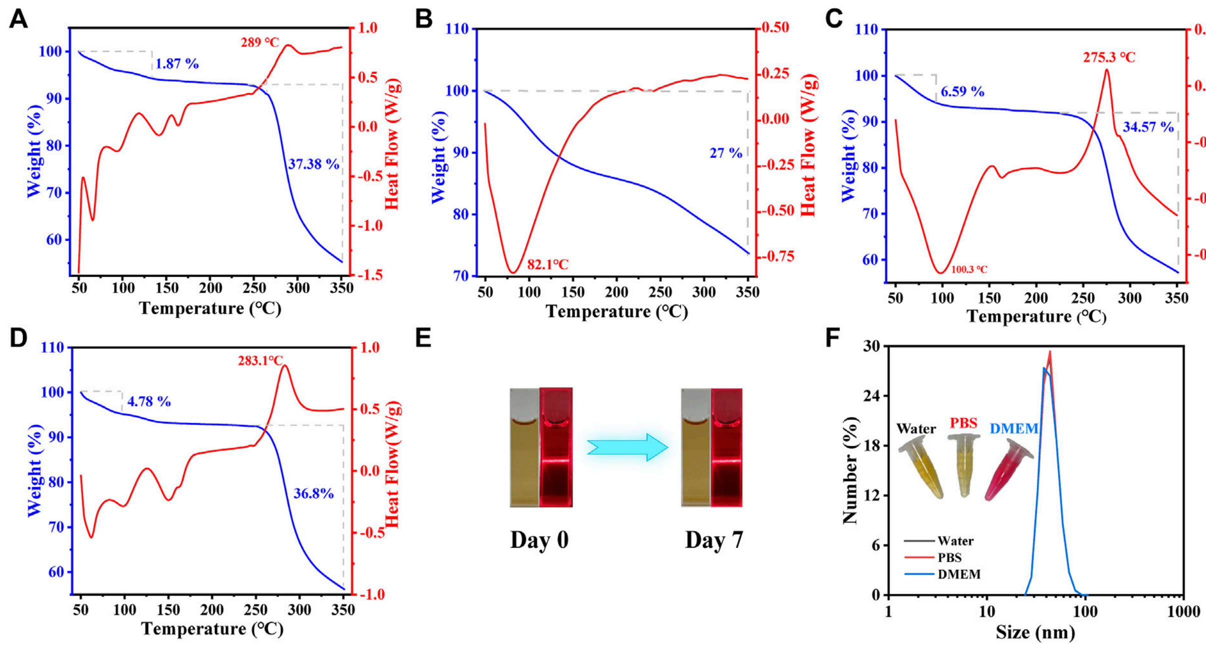

FIGURE 5
Physicochemical properties of AFI-CDs. The thermal assay by TG (blue line) and DSC (red line) on NA **(A)**, AFI-CDs **(B)**, NA-AFI-CDs **(C)** and physical mixture **(D)**. The stability of NA-AFI-CDs were investigated at room temperature **(E)** and with different solvents (water, PBS, and DMEM) **(F)**.

hydrodynamic size demonstrated exceptional stability over a 7-day period in water, phosphate-buffered saline (PBS), and cell culture medium (Dulbecco's Modified Eagle's Medium or DMEM) (Figure 5F). Collectively, these data substantiate that NA-AFI-CDs exhibit exceptional stability.

2.5 Biocompatibility of AFI-CDs and NA-AFI-CDs

Numerous solubilizers exhibit varying degrees of toxicity and potential side effects. Despite the eco-friendly synthesis process of AFI-CDs and NA-AFI-CDs, it is imperative to consider the potential biotoxicity arising from possible interactions with biological systems (Domingues et al., 2000; Zhang et al., 2022). A hemolysis assay, cell cytotoxicity test, and biosafety evaluations were conducted *in vitro* and *in vivo*, respectively. The hemolysis assay results showed that even at concentrations of AFI-CDs and NA-AFI-CDs as high as 1,000 μg/mL, there was negligible hemolytic activity in rat red blood cells (Figure 6A). The solutions of all groups were clear, and the chromatic attributes of NA-AFI-CDs were all comparable with that of the PBS group. The solutions of all groups were clear, and the chromatic attributes of the NA-AFI-CDs solution were all comparable with that of the PBS group. Concomitantly, the hemolysis rates of AFI-CDs were significantly lower than internationally recognized standards (5%), indicating their well biocompatibility (Jia et al., 2022). The cytotoxicity of AFI-CDs and NA-AFI-CDs was assessed in L02 and 293T cells, respectively. When the concentration of AFI-CDs increased to 1,000 μg/mL, cell viability for both L02 and 293T cells remained above 80%, corroborating the low cytotoxicity of CDs as previously documented (Zhang et al., 2021a). For NA-AFI-CDs, the survival rates of L02 cells exceeded 100% from concentrations ranging from 1,000 μg/mL to 7.8125 μg/mL (Figure 6B), suggesting that NA-AFI-CDs may facilitate L02 growth due to the enrichment of hepatocytes by nanoparticles. Simultaneously, all concentrations of NA-AFI-CDs manifested negligible toxicity on 293T cells (Figure 6C). As previously reported (Li et al., 2022), a myriad of CDs derived from carbonized plants exhibited negligible cytotoxicity across most concentrations, and NA-AFI-CDs, a composite of CDs and NA, maintained low cytotoxicity. These aforementioned results imply that AFI-CDs and NA-AFI-CDs possess very low biotoxicity and could be amenable to further *in vivo* evaluations.

Additionally, further assessments concerning potential toxicity toward biochemical indices and multiple organs *in vivo* were undertaken. After administration of AFI-CDs and NA-AFI-CDs for 7 days, there were no appreciable weight changes compared with the control group (Figure 6D). Concurrently, nanoparticles might accumulate and potentially occlude the liver or kidneys through metabolic and excretory processes, yielding alterations in biochemical indices (Vilas-Boas and Vinken, 2021). As depicted in Figure 6E, biochemical indices related to liver and kidney function (ALT, AST, BUN, CRE, and O/P) exhibited no significant changes upon administration with AFI-CDs or NA-AFI-CDs, mirroring *in vitro* cellular experiments. Given that CDs might induce inflammation in major organs and gastrointestinal injuries (Zhang et al., 2023), toxicity assessments for five major organs (heart, liver, spleen, lung, and kidney) and digestive organs (stomach and intestine) were also conducted. Nanoscale carbon materials have been suspected to cause reproductive toxicity or brain injury

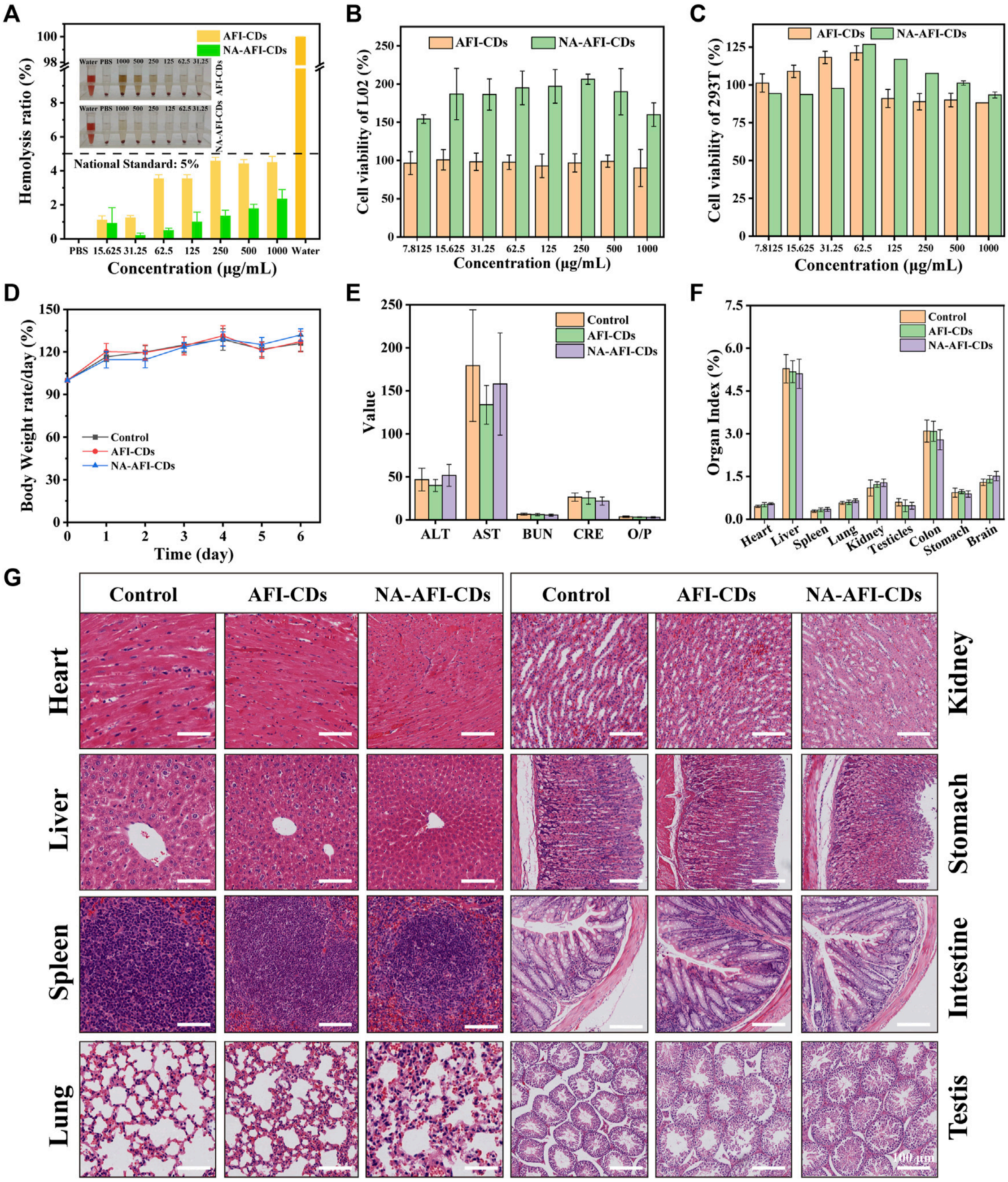

FIGURE 6
Biosafety evaluation of AFI-CDs and NA-AFI-CDs. **(A)** The hemocompatibility test of NA-AFI-CDs at different concentrations. **(B, C)** Cell viability of L02 and 293T cells with AFI-CDs and NA-AFI-CDs, respectively ($n = 6$). **(D)** Body weight change in the control, AFI-CDs, and NA-AFI-CDs groups ($n = 6$). **(E)** Biochemical data. **(F)** Organ index. **(G)** Histological evaluation of eight major organs of mice in different groups on day 7. Scale bars: 100 μm. Data are mean ± SD. $^*p < 0.05$.

(Hansen and Lennquist, 2020; Kang et al., 2023); thus, our study also observed pathological changes in the testes and brain. As illustrated in Figures 6F, G and Supplementary Figure S9, no appreciable organ index changes between the control and administration groups were detected, nor were any significant morphological or pathological abnormalities. In summary, according to these results, AFI-CDs and NA-AFI-CDs demonstrated high levels of biocompatibility and biosafety *in vitro* and *in vivo*.

2.6 Antioxidant ability of AFI-CDs and NA-AFI-CDs

Numerous studies have ascertained the formation between CDs and polyphenols (such as lutein and naringenin) can significantly enhance antioxidant efficacy (Pérez-Gálvez et al., 2020) (Figure 7A). In the present study, 1,1-diphenyl-2-picrylhydrazyl (DPPH, a stable nitrogen-centered free radical) and 2,2′-azinobis-(3-

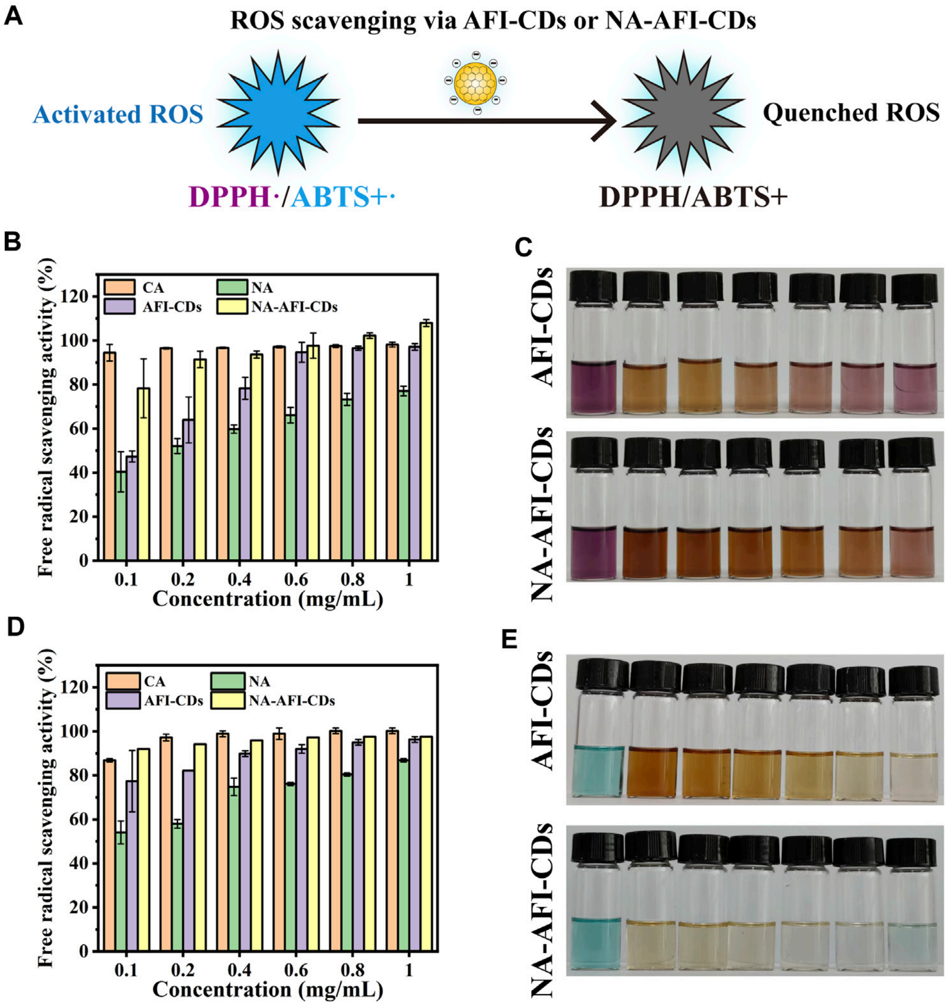

FIGURE 7
Antioxidant assays of AFI-CDs and NA-AFI-CDs. **(A)** Schematic illustration of the ROS scavenging process. **(B)** DPPH radical scavenging ability of CA, NA, AFI-CDs, and NA-AFI-CDs. **(C)** A photograph of the reaction systems featured in **(B)**. **(D)** ABTS+● radical scavenging ability of CA, NA, AFI-CDs, and NA-AFI-CDs. **(E)** A photograph of the reaction systems featured in **(D)**.

ethylbenzthiazoline-6-sulphonate) (ABTS) were used to investigate the oxidative resistance of these nanomaterials (Liu et al., 2021; Han et al., 2023). Citric acid (CA) was employed as a control group to evaluate antioxidative capabilities. As illustrated in Figure 7B, the results for AFI-CDs and NA-AFI-CDs manifested dose-dependency and enhanced DPPH● scavenging activities compared with pure NA. Ranging from 0.1 to 0.6 mg/mL, the DPPH● scavenging rate of AFI-CDs incrementally augmented, while the free radical scavenging rate remained analogous to that of CA beyond that concentration. The NA-AFI-CDs exhibited robust antioxidant potency, comparable with CA at low concentrations (0.4 mg/mL) and surpassing it at elevated concentrations ($p < 0.01$). As paramagnetic entities with solitary electrons, DPPH● free radicals accept an electron from a free radical scavenger to synthesize a stable DPPH-H compound (Zhu et al., 2004), inducing a colorimetric transition from dark purple to the respective solution color. After incubation, AFI-CDs and NA-AFI-CDs both manifested efficacious clearance effects, as depicted in Figure 7C.

Moreover, ABTS can be oxidized by $K_2S_20_8$ to yield the cationic radical ABTS+, a solution with a blue-green hue; the presence of antioxidants reverts them back to their original ABTS form. Upon interaction with AFI-CDs or NA-AFI-CDs, the chromaticity of the ABTS+● solution progressively attenuated to either colorless or the inherent hue of the nanomaterial solution; these changes were concomitantly observed with increasing concentrations of AFI-CDs or NA-AFI-CDs (Figure 7E). Relative to radical scavenging proficiency, AFI-CDs virtually obliterated ABTS+● at 1 mg/mL, and NA-AFI-CDs achieved a commensurate scavenging impact at 0.6 mg/mL (Figure 7D). However, CA possessed a superior clearance rate of approximately 100% at 0.8 mg/mL. The putative antioxidant mechanism underlying the augmentation of antioxidant capabilities in NA-AFI-CDs consisted of the complexation between NA and AFI-CDs, which facilitated electron or hydrogen atom transfer and contributed additional electron donors to neutralize free radicals (Chae et al., 2021). With the increment in NA-AFI-CDs, the antioxidant efficacy markedly amplified, which could be attributed to the combinatorial synergistic interplay between NA and AFI-CDs.

3 Materials and methods

3.1 Materials

Naringenin, naringin, narirutin, hesperidin, neohesperidin, and citric acid were procured from Chengdu Herbpurify Biotechnology Co., Ltd (Chengdu, China), and the purity of these compounds exceeded 98%. The sample of AFI (Batch No: 220708002) was acquired from Beijing Qiancao Traditional Chinese Medicine Co., Ltd (Beijing, China), and AFIC (*Aurantii fructus immaturus* carbonisata) was synthesized in our laboratory. HPLC-grade methanol was procured from Honeywell (New York, USA). The remaining analytical-grade chemical reagents were sourced from Sinopharm Chemical Reagents Beijing (Beijing, China). Fetal bovine serum (FBS), Dulbecco's modified Eagle's medium (DMEM), and cell counting kit (CCK-8) were acquired from Beijing BioDee Biotechnology Co., Ltd (Beijing, China). All experiments were conducted using deionized water (DW).

3.2 Animals

Male Kunming (KM) mice (SPF-group, 8-week-old, 25.0 ± 2.0 g) were procured from SIBEIFU Biotechnology Co., Ltd. (Beijing, China). All animals were accommodated in a temperature-controlled environment (20°C–25°C) with a relative humidity of 50%–60% and a 12 h light/dark cycle. We adhered to all guidelines of the laboratory animal center. All animal procedures in this study complied with the Guide for the Care and Use of Laboratory Animals and were endorsed by the Animal Ethical Committee of Beijing University of Chinese Medicine.

3.3 Synthesis of AFI-CDs and NA-AFI-CDs

AFI-CDs were synthesized via a modified one-step pyrolysis method (Wang et al., 2019). Concisely, 200 g of dry AFI was placed in crucibles, and encased with aluminum foil. Subsequently, the crucibles were sustained at a temperature of 350°C for 1 h for additional carbonization in a muffle furnace (TL0612, Beijing Zhong Ke Aobo Technology Co., Ltd.; Beijing, China). Post-pyrolysis, the prepared AFIC was ground into powder and subjected to a water bath at 100°C twice for 1 h each. The resultant mixture dispersions were filtered using a 0.22 μm cellulose acetate membrane. Thereafter, the filtered brown dispersions were subsequently concentrated and dialyzed using DW for 72 h. Ultimately, AFI-CDs were freeze-dried in a freeze dryer (TGL-16G, Beijing Restorative Centrifuge Manufacturing Plant, Beijing, China) for 3 days. The prepared AFI-CDs were redispersed in DW to achieve solutions of varying concentrations. NA was incorporated into the AFI-CDs solution. The resultant mixture was homogenized on the shaker and continuously heated at a constant temperature. To mitigate interference from residual NA, the synthesized solution, after cooling to ambient temperature, was centrifuged (4,000 rpm) for 10 min. The supernatant was isolated and freeze-dried to yield dry pure powder (named NA-AFI-CDs). Equivalent quantities of AFI-CDs and NA were co-mingled to fabricate the physical mixture, serving as the control. All samples were preserved at 4°C for subsequent utilization.

3.4 Characterization of AFI-CDs and NA-AFI-CDs

Morphology, size distribution, and thickness were assessed via Transmission Electron Microscopy (TEM, Tecnai G220) and high-resolution TEM (HRTEM, JEN-1230) at 220 kV. The UV-vis absorption spectra were acquired on a UV-vis spectrophotometer (CECIL, United Kingdom), and the FL spectra were scrutinized via a fluorescence spectrophotometer (F-4500, Japan). The DLS and ζ-potential were ascertained by Malvern Zetasizer Nano ZS (Zetasizer Nano ZS 90, United Kingdom) at 25°C. FT-IR spectra were recorded on a Fourier transform infrared spectrophotometer (Thermo Fisher, United States) to ascertain surface structure. X-ray diffraction patterns (XRD, D8-Advanced, Germany) with Cu Kα radiation (λ = 1.5418 Å) were used to assess crystalline alterations. X-ray photoelectron spectroscopy (XPS, Thermo Fisher Scientific, United States) and elemental composition were executed with a monochromatic Al Kα X-ray source. The thermal characteristics of the samples were assessed via thermogravimetry (TG) and differential scanning calorimetry (DSC). TG curves were concurrently acquired using an SDT-Q600 thermal analyzer from room temperature to 350°C. A METTLER TOLEDO thermal analyzer was employed for deriving DSC curves with respect to time. These analyses were conducted under a nitrogen atmosphere (20 mL/min) at a heating rate of 10°C min^{-1}.

3.5 Solubilization experiment

3.5.1 Naringin determination

The anhydrous NA standard was accurately weighed and aliquoted into methanol to fabricate a stock solution with a concentration of 9.9275 mg/mL. Subsequently, a spectrum of dilutions was prepared to yield solutions ranging from 0.019 to 9.9275 mg/mL. The quantification of NA was performed via HPLC (Agilent LC-1260, Waldbronn, Germany) employing a C-18 column (250 mm × 4.6 mm × 0.5 μm, ZORBAX SB-C18, United States). The mobile phase comprised pure water (A) and methanol (B), and isocratic elution was instituted with a constituent ratio of 65% phase A from 0 to 20 min. The injection volume, flow rate, column temperature, and detection wavelength were 10 μL, 1 mL/min, 30°C, and 284 nm, respectively. Additional methodological validation was performed in accordance with repeatability, precision, and stability. Moreover, all samples were filtrated through a 0.22 μm cellulose membrane for purification and analyzed in triplicate. The solubility of NA, drug loading efficiency (DLE), and solubilization effect (SE) were employed to gauge solubilization efficacy, and DLE and SE were calculated using the ensuing equations:

$$\boldsymbol{DLE}\ (\%) = \frac{\boldsymbol{Loaded\ NA\ dosage\ (mg)}}{\boldsymbol{Total\ NA\ dosage\ (mg)}} \times \mathbf{100}$$

$$\boldsymbol{SE}\ (fold) = \frac{\boldsymbol{Peak\ area\ of\ simples}}{\boldsymbol{Peak\ area\ of\ NA\ in\ water}}$$

3.5.2 Solubilization test

To examine the influence of disparate process conditions, a suite of experiments was conducted employing a single-variable approach, encompassing variables such as the concentration of AFI-CDs, dosage of NA, oscillation time, heating duration, and heating temperature. The synthesis was executed in darkness to ensure that the samples were devoid of photonic interference. Each batch of sample was consistently positioned throughout the process.

3.5.3 *In Vitro* release profile of NA

Release profiles utilizing dialysis methods were executed to assess solubilization behavior *in vitro*. Concisely, NA-AFI-CDs (5 mL) and saturated NA suspension (5 mL, comprising 8 mg NA) were independently loaded into dialysis bags (MW = 1,000 Da), after immersion in freshly prepared PBS solution (pH = 6.8) containing 0.1% Tween 80, and magnetically stirred at 180 rpm and 37°C ± 2°C for 72 h. Thereafter, an equivalent volume of sample was replaced at designated sampling intervals (5, 10, 20, 30, 60, 120, 240, 480, 960, 1,440, 2,880, and 4,320 min), and all samples were triply analyzed after filtration through a 0.22 μm filter membrane.

3.5.4 The interaction assay by ITC

In accordance with preceding investigations concerning nanocomplexes, isothermal titration calorimetry (ITC) analysis curves were generated to substantiate non-covalent interactions between compounds (Pi et al., 2023). An AFI-CDs suspension (8 mg NA dispersed in 3 mL DW) was introduced into the sample cell; concomitantly, an NA suspension was allocated to the injection syringe and the reference cell contained deionized water. To circumvent bubble formation during titration, all samples were meticulously degassed for 30 min. All ITC experiments were conducted at room temperature. The NA suspension was titrated into the sample cell in 20 individual injections, each comprising 2.5 μL. Each injection yielded a singular peak in the isotherm. The angular velocity of the injection syringe was 250 rpm.

3.6 Biosafety evaluation

3.6.1 Cytotoxicity assays

The CCK-8 assay was performed on L02 cells (normal hepatocyte) and 293T (human renal epithelial cell) to measure the cytotoxicity of AFI-CDs and NA-AFI-CDs. Briefly, cells were cultured on a 96-well plate at 37°C and 5% CO_2, which spread to 1×10^4 per well for 24 h. Then, 100-μL aliquots of medium containing different concentrations of nanoparticles (1,000, 500, 250, 125, 62.5, 31.25, 15.63, and 7.81 μg/mL) were added to each well for 24 h, and 10% CCK-8 solution was added to each well for an additional 2 h after cleaning three times with PBS. The absorbance of each well was recorded using a microplate reader (BioTek, Vermont, United States). The cell viability was calculated according to the following formula:

$$\boldsymbol{Cell\ viability}\ (\%) = \frac{\boldsymbol{A_e - A_c}}{\boldsymbol{A_b - A_c}} \times \mathbf{100},$$

where Ae, Ab, and Ac represent the absorbance of the experimental, control, and blank (no cells) groups at 450 nm, respectively.

3.6.2 Hemocompatibility *in vitro*

Red blood cells, isolated from fresh rat blood, were used to fabricate a 10% erythrocyte suspension in PBS. A microplate reader was employed to quantify the absorbance of materials, measured at 570 nm and averaged over three calculations. The positive control comprised DW and the negative control consisted of PBS. The following formula was employed to compute the hemolysis rate:

$$\boldsymbol{Hemolysis\ rate}\ (\%) = \frac{\boldsymbol{D_a - D_b}}{\boldsymbol{D_c - D_b}} \times \mathbf{100},$$

where Da is the hemolysis absorbance of the experimental group, Db is the hemolysis absorbance of the negative control group, and Dc is the hemolysis absorbance of the positive control group.

3.6.3 Biosafety evaluation *in vivo*

After administering AFI-CDs and NA-AFI-CDs intragastrically at a dosage of 30 g/kg for 7 days, peripheral blood samples were harvested into centrifuge tubes via ocular extraction and were employed to ascertain hematological parameters using an automated biochemical analyzer (AU-480, Beckman Kurt Co., Ltd., Brea, CA, United States). Simultaneously, the principal organs were weighed and subjected to histological examination with H&E staining in accordance with standard procedures.

3.7 Antioxidant study

The free radical scavenging abilities of DPPH• and ABTS+• were the important indices to evaluate the antioxidant activity of nanoparticles. Simultaneously, ABTS+• solution was synthesized by amalgamating 0.8 mL ABTS (4 mg/mL) and 1 mL potassium persulfate ($K_2S_2O_8$, 1 mg/mL) and allowing them to incubate overnight in the dark. Likewise, a DPPH• solution (0.04 g/L) was formulated in an anhydrous ethanol medium under dark conditions. Typically, dried powders of CA, NA, AFI-CDs, and NA-AFI-CDs were diluted to various concentrations (0.1, 0.2, 0.4, 0.6, 0.8, and 1 mg/mL). Subsequently, 1 mL of each sample was admixed with 1 mL of DPPH• or ABTS+• anhydrous ethanol (constituting the experimental cohort). The resultant solution was sequestered in darkness for 30 min. A mixture of DPPH• or ABTS+• ethanol solution with 1 mL of DW served as the blank control, and the comparative control group was constituted by samples to which an equal volume of anhydrous ethanol had been added. The inhibition percentage and free radical scavenging efficacy were calculated employing relevant equations.

$$\boldsymbol{Radical\ scavenging\ activity}\ (\%) = \mathbf{1} - \frac{\boldsymbol{A_0 - A_1}}{\boldsymbol{A_2}} \times \mathbf{100},$$

where A_0 is the absorbance of the experimental group, A_1 is the absorption of the control group, and A_2 is the absorbance of the blank group.

3.8 Statistical analysis

Results are presented as mean ± SD. Student's t-test or one-way analysis of variance (ANOVA) were used to analyze statistical significance between two or multiple groups, respectively. Differences were considered to be statistically significant when $p < 0.05$.

4 Conclusion

In summation, AFI-CDs, unique green multifunctional CDs synthesized from AFI, were successfully fabricated and demonstrated excellent solubilization efficacy for naringin (216.72-fold) by assembling into NA-AFI-CD complexes without the utilization of any auxiliary agents for the first time. The procured NA-AFI-CDs were elucidated by TEM images, DLS analysis, ζ-potential measurements, UV-vis spectra, PLFL spectra, FT-IR spectra, XRD spectra, and XPS spectra, and these results revealed that the composition of NA-AFI-CDs predominantly hinges on intermolecular non-covalent bonds. Simultaneously, these forces drive AFI-CDs to more readily recognize specific glycoside structures. The procured NA-AFI-CDs exhibited exceptional stability and dispersibility, as well as manifested high biocompatibility *in vitro* and *in vivo*. The antioxidant assays substantiated that NA-AFI-CDs outperformed in free radical scavenging capacity when compared with pure NA and AFI-CDs, signifying a synergistic effect engendered by interactions between NA and AFI-CDs. This utilization of AFI-CDs may pave the way for a novel solubilization strategy pertaining to naringin in food or pharmaceutical domains. Future studies shall concentrate on the synthesis of additional herbal-derived CDs to function as solubilizers and further elucidate details in bio-delivery systems.

Data availability statement

The original contributions presented in the study are included in the article/Supplementary Material, further inquiries can be directed to the corresponding authors.

Ethics statement

The animal study was approved by the Ethics Committee of Animal Experimentation, Beijing University of Chinese Medicine, Beijing, China. The study was conducted in accordance with the local legislation and institutional requirements.

Author contributions

TW: Writing–review and editing, Data curation, Methodology, Visualization, Writing–original draft, Software, Validation. ML: Data curation, Methodology, Writing–review and editing. TL: Methodology, Writing–review and editing, Data curation. YZ: Data curation, Writing–review and editing, Methodology. JY: Data curation, Writing–review and editing, Methodology. YZ: Formal Analysis, Writing–review and editing, Validation. XT: Writing–review and editing, Formal Analysis, Validation. RK: Writing–review and editing, Formal Analysis, Validation. YZ: Funding acquisition, Project administration, Writing–review and editing. HK: Funding acquisition, Project administration, Writing–review and editing, Conceptualization. YZ: Conceptualization, Funding acquisition, Project administration, Writing–review and editing. HQ: Conceptualization, Funding acquisition, Project administration, Writing–review and editing.

Funding

The author(s) declare financial support was received for the research, authorship, and/or publication of this article. This study was supported by Grant for Qihuang Scholars of the State Administration of Traditional Chinese Medicine (China, 90020163320012).

Conflict of interest

The authors declare that the research was conducted in the absence of any commercial or financial relationships that could be construed as a potential conflict of interest.

Publisher's note

Supplementary material

The Supplementary Material for this article can be found online at: https://www.frontiersin.org/articles/10.3389/fmolb.2023.1284599/full#supplementary-material

References

Arcudi, F., and Đorđević, L. (2023). Supramolecular chemistry of carbon-based dots offers widespread opportunities. *Small* 19 (31), e2300906. doi:10.1002/smll.202300906

Bharti, S., Rani, N., Krishnamurthy, B., and Arya, D. S. (2014). Preclinical evidence for the pharmacological actions of naringin: a review. *Planta Med.* 80 (6), 437–451. doi:10.1055/s-0034-1368351

Chae, S. Y., Shin, M. C., Jeon, S., Kang, M. S., Han, D. W., and Hong, S. W. (2021). A simple route to the complexation of lutein with reduced graphene oxide nanocarriers and antioxidant protection against blue light. *Int. J. Nanomedicine* 16, 6843–6860. doi:10.2147/ijn.S320790

Charalabidis, A., Sfouni, M., Bergström, C., and Macheras, P. (2019). The biopharmaceutics classification system (BCS) and the biopharmaceutics drug disposition classification system (BDDCS): beyond guidelines. *Int. J. Pharm.* 566, 264–281. doi:10.1016/j.ijpharm.2019.05.041

Chen, Q., Wu, C., Wang, S., Wang, Q., Wu, P., Wang, L., et al. (2023). Glycyrrhizic acid modified Poria cocos polyscaccharide carbon dots dissolving microneedles for methotrexate delivery to treat rheumatoid arthritis. *Front. Chem.* 11, 1181159. doi:10.3389/fchem.2023.1181159

Choi, J. S., and Shin, S. C. (2005). Enhanced paclitaxel bioavailability after oral coadministration of paclitaxel prodrug with naringin to rats. *Int. J. Pharm.* 292 (1-2), 149–156. doi:10.1016/j.ijpharm.2004.11.031

Cruz-Hernández, C., García-Espinosa, D. A., and Guadarrama, P. (2022). Click synthesis of novel dendronized curcumin and analogs. Strengthening of physicochemical properties toward biological applications. *Org. Biomol. Chem.* 20 (13), 2643–2650. doi:10.1039/d2ob00284a

Cutrim, E. S. M., Vale, A. A. M., Manzani, D., Barud, H. S., Rodríguez-Castellón, E., Santos, A., et al. (2021). Preparation, characterization and *in vitro* anticancer performance of nanoconjugate based on carbon quantum dots and 5-Fluorouracil. *Mater Sci. Eng. C Mater Biol. Appl.* 120, 111781. doi:10.1016/j.msec.2020.111781

Domingues, F. C., Queiroz, J. A., Cabral, J. M., and Fonseca, L. P. (2000). The influence of culture conditions on mycelial structure and cellulase production by Trichoderma reesei Rut C-30. *Enzyme Microb. Technol.* 26 (5-6), 394–401. doi:10.1016/s0141-0229(99)00166-0

Farhan, M. (2022). Naringin's prooxidant effect on tumor cells: copper's role and therapeutic implications. *Pharm. (Basel)* 15 (11), 1431. doi:10.3390/ph15111431

Gan, J., Chen, L., Chen, Z., Zhang, J., Yu, W., Huang, C., et al. (2023a). Lignocellulosic biomass-based carbon dots: synthesis processes, properties, and applications. *Small*, e2304066. doi:10.1002/smll.202304066

Gan, J., Deng, X., Le, Y., Lai, J., and Liao, X. (2023b). The development of naringin for use against bone and cartilage disorders. *Molecules* 28 (9), 3716. doi:10.3390/molecules28093716

Ghanbari, N., Salehi, Z., Khodadadi, A. A., Shokrgozar, M. A., and Saboury, A. A. (2021). Glucosamine-conjugated graphene quantum dots as versatile and pH-sensitive nanocarriers for enhanced delivery of curcumin targeting to breast cancer. *Mater Sci. Eng. C Mater Biol. Appl* 121, 111809. doi:10.1016/j.msec.2020.111809

Ghanbari-Movahed, M., Jackson, G., Farzaei, M. H., and Bishayee, A. (2021). A systematic review of the preventive and therapeutic effects of naringin against human malignancies. *Front. Pharmacol.* 12, 639840. doi:10.3389/fphar.2021.639840

Han, Z., Gao, X., Wang, Y., Cheng, S., Zhong, X., Xu, Y., et al. (2023). Ultrasmall iron-quercetin metal natural product nanocomplex with antioxidant and macrophage regulation in rheumatoid arthritis. *Acta Pharm. Sin. B* 13 (4), 1726–1739. doi:10.1016/j.apsb.2022.11.020

Hansen, S. F., and Lennquist, A. (2020). Carbon nanotubes added to the SIN list as a nanomaterial of very high concern. *Nat. Nanotechnol.* 15 (1), 3–4. doi:10.1038/s41565-019-0613-9

Jambhekar, S. S., and Breen, P. (2016). Cyclodextrins in pharmaceutical formulations II: solubilization, binding constant, and complexation efficiency. *Drug Discov. Today* 21 (2), 363–368. doi:10.1016/j.drudis.2015.11.016

Jat, S., Bhatt, M., Roychowdhury, S., Dixit, V. A., Pawar, S. D., Kulhari, H., et al. (2022). Preparation and characterization of amoxapine- and naringin-loaded solid lipid nanoparticles: drug-release and molecular-docking studies. *Nanomedicine (Lond)* 17 (28), 2133–2144. doi:10.2217/nnm-2022-0167

Jia, X., Yuan, Z., Yang, Y., Huang, X., Han, N., Liu, X., et al. (2022). Multi-functional self-assembly nanoparticles originating from small molecule natural product for oral insulin delivery through modulating tight junctions. *J. Nanobiotechnology* 20 (1), 116. doi:10.1186/s12951-022-01260-9

Jiang, H., Zhang, M., Lin, X., Zheng, X., Qi, H., Chen, J., et al. (2023). Biological activities and solubilization methodologies of naringin. *Foods* 12 (12), 2327. doi:10.3390/foods12122327

Jv, D. J., Ji, T. H., Xu, Z., Li, A., and Chen, Z. Y. (2023). The remarkable enhancement of photo-stability and antioxidant protection of lutein coupled with carbon-dot. *Food Chem.* 405, 134551. doi:10.1016/j.foodchem.2022.134551

Kalluri, A., Dharmadhikari, B., Debnath, D., Patra, P., and Kumar, C. V. (2023). Advances in structural modifications and properties of graphene quantum dots for biomedical applications. *ACS Omega* 8 (24), 21358–21376. doi:10.1021/acsomega.2c08183

Kang, H., Zhang, W., Jing, J., Huang, D., Zhang, L., Wang, J., et al. (2023). The gut-brain axis involved in polystyrene nanoplastics-induced neurotoxicity via reprogramming the circadian rhythm-related pathways. *J. Hazard Mater* 458, 131949. doi:10.1016/j.jhazmat.2023.131949

Kaurav, H., Verma, D., Bansal, A., Kapoor, D. N., and Sheth, S. (2023). Progress in drug delivery and diagnostic applications of carbon dots: a systematic review. *Front. Chem.* 11, 1227843. doi:10.3389/fchem.2023.1227843

Kometani, T., Nishimura, T., Nakae, T., Takii, H., and Okada, S. (1996). Synthesis of neohesperidin glycosides and naringin glycosides by cyclodextrin glucanotransferase from an alkalophilic Bacillus species. *Biosci. Biotechnol. Biochem.* 60 (4), 645–649. doi:10.1271/bbb.60.645

Kundu, M., Majumder, R., Das, C. K., and Mandal, M. (2021). Natural products based nanoformulations for cancer treatment: current evolution in Indian research. *Biomed. Mater* 16 (4), 044101. doi:10.1088/1748-605X/abe8f2

Li, C., Han, P., Mao, H., Lv, C., Huang, K., and Jin, M. (2023). Glycyrrhizic acid-based carbonized dots boost antiviral activity against influenza A virus via multisite inhibition mechanisms. *ACS Appl. Mater Interfaces* 15 (8), 10441–10451. doi:10.1021/acsami.2c21319

Li, D., Xu, K. Y., Zhao, W. P., Liu, M. F., Feng, R., and Li, D. Q. (2022). Chinese medicinal herb derived carbon dots for common diseases: efficacies and potential mechanisms. *Front Pharmacol.* 22 (13), 815479. doi:10.3389/fphar.2022.815479

Li, J. W., and Vederas, J. C. (2009). Drug discovery and natural products: end of an era or an endless frontier? *Science* 325 (5937), 161–165. doi:10.1126/science.1168243

Liang, P., Bi, T., Zhou, Y., Wang, C., Ma, Y., Xu, H., et al. (2023a). Carbonized platycladus orientalis derived carbon dots accelerate hemostasis through activation of platelets and coagulation pathways. *Small*, e2303498. doi:10.1002/smll.202303498

Liang, X., Chen, L., McClements, D. J., Peng, X., Xu, Z., Meng, M., et al. (2023b). Bioactive delivery systems based on starch and its derivatives: assembly and application at different structural levels. *Food Chem.* 432, 137184. doi:10.1016/j.foodchem.2023.137184

Liang, Y., Hou, D., Ni, Z., Cao, M., and Cai, L. (2022). Preparation, characterization of naringenin, β-cyclodextrin and carbon quantum dot antioxidant nanocomposites. *Food Chem.* 375, 131646. doi:10.1016/j.foodchem.2021.131646

Liu, H., Li, Y., Sun, S., Xin, Q., Liu, S., Mu, X., et al. (2021). Catalytically potent and selective clusterzymes for modulation of neuroinflammation through single-atom substitutions. *Nat. Commun.* 12 (1), 114. doi:10.1038/s41467-020-20275-0

Liu, J., Kong, T., and Xiong, H. M. (2022). Mulberry-leaves-derived red-emissive carbon dots for feeding silkworms to produce brightly fluorescent silk. *Adv. Mater* 34 (16), e2200152. doi:10.1002/adma.202200152

Lu, F., Ma, Y. R., Wang, H. B., Zhang, M. L., Wang, B., Zhang, Y., et al. (2021). Water-solvable carbon dots derived from curcumin and citric acid with enhanced broad-spectrum antibacterial and antibiofilm activity. *Mater. Today Commun.* 26, 102000. doi:10.1016/j.mtcomm.2020.102000

Luo, J., Kong, H., Zhang, M., Cheng, J., Sun, Z., Xiong, W., et al. (2019). Novel carbon dots-derived from radix puerariae carbonisata significantly improve the solubility and bioavailability of baicalin. *J. Biomed. Nanotechnol.* 15 (1), 151–161. doi:10.1166/jbn.2019.2675

Luo, W. K., Zhang, L. L., Li, X. X., Zheng, J., Chen, Q., Yang, Z. Y., et al. (2022). Green functional carbon dots derived from herbal medicine ameliorate blood-brain barrier permeability following traumatic brain injury. *Nano Res.* 15 (10), 9274–9285. doi:10.1007/s12274-022-4616-8

Luo, W. K., Zhang, L. L., Yang, Z. Y., Guo, X. H., Wu, Y., Zhang, W., et al. (2021). Herbal medicine derived carbon dots: synthesis and applications in therapeutics, bioimaging and sensing. *J. Nanobiotechnology* 19 (1), 320. doi:10.1186/s12951-021-01072-3

Nair, A., Haponiuk, J. T., Thomas, S., and Gopi, S. (2020). Natural carbon-based quantum dots and their applications in drug delivery: a review. *Biomed. Pharmacother.* 132, 110834. doi:10.1016/j.biopha.2020.110834

Pérez-Gálvez, A., Viera, I., and Roca, M. (2020). Carotenoids and chlorophylls as antioxidants. *Antioxidants (Basel)* 9 (6), 505. doi:10.3390/antiox9060505

Pi, W., Wu, L., Lu, J., Lin, X., Huang, X., Wang, Z., et al. (2023). A metal ions-mediated natural small molecules carrier-free injectable hydrogel achieving laser-mediated photo-Fenton-like anticancer therapy by synergy apoptosis/cuproptosis/anti-inflammation. *Bioact. Mater* 29, 98–115. doi:10.1016/j.bioactmat.2023.06.018

Pinilla-Peñalver, E., García-Béjar, B., Contento, A. M., and Ríos, Á. (2022). Graphene quantum dots an efficient nanomaterial for enhancing the photostability of trans-resveratrol in food samples. *Food Chem.* 386, 132766. doi:10.1016/j.foodchem.2022.132766

Qiang, R., Huang, H., Chen, J., Shi, X., Fan, Z., Xu, G., et al. (2023). Carbon quantum dots derived from herbal medicine as therapeutic nanoagents for rheumatoid arthritis with ultrahigh lubrication and anti-inflammation. *ACS Appl. Mater Interfaces* 15 (32), 38653–38664. doi:10.1021/acsami.3c06188

Rao, K., Imran, M., Jabri, T., Ali, I., Perveen, S., Shafiullah, et al. (2017). Gum tragacanth stabilized green gold nanoparticles as cargos for Naringin loading: a morphological investigation through AFM. *Carbohydr. Polym.* 174, 243–252. doi:10.1016/j.carbpol.2017.06.071

Ravetti, S., Garro, A. G., Gaitán, A., Murature, M., Galiano, M., Brignone, S. G., et al. (2023). Naringin: nanotechnological strategies for potential pharmaceutical applications. *Pharmaceutics* 15 (3), 863. doi:10.3390/pharmaceutics15030863

Secerli, J., Adatepe, Ş., Altuntas, S., Topal, G. R., Erdem, O., and Bacanlı, M. (2023). *In vitro* toxicity of naringin and berberine alone, and encapsulated within PMMA nanoparticles. *Toxicol Vitro* 89, 105580. doi:10.1016/j.tiv.2023.105580

Singh, P., Kumar, K., Kumar, S., Kumar, P., Kataria, N., Bhankar, V., et al. (2023). Assessment of biomass-derived carbon dots as highly sensitive and selective templates for the sensing of hazardous ions. *Nanoscale*. doi:10.1039/d3nr01966g

Tao, Y., Wan, R., Wang, J., Liu, Q., Tian, M., Wang, L., et al. (2023). Carbonized human hair derived carbon dots for detection of clozapine. *Spectrochim. Acta A Mol. Biomol. Spectrosc.* 298, 122803. doi:10.1016/j.saa.2023.122803

Tian, Y., Tang, G., Gao, Y., Chen, X., Zhou, Z., Li, Y., et al. (2022). Carrier-free small molecular self-assembly based on berberine and curcumin incorporated in submicron particles for improving antimicrobial activity. *ACS Appl. Mater Interfaces* 14 (8), 10055–10067. doi:10.1021/acsami.1c22900

Tong, T., Hu, H., Zhou, J., Deng, S., Zhang, X., Tang, W., et al. (2020). Glycyrrhizic-acid-Based carbon dots with high antiviral activity by multisite inhibition mechanisms. *Small* 16 (13), e1906206. doi:10.1002/smll.201906206

Veerapandian, M., Ramasundaram, S., Jerome, P., Chellasamy, G., Govindaraju, S., Yun, K., et al. (2023). Drug delivery application of functional nanomaterials synthesized using natural sources. *J. Funct. Biomater.* 14 (8), 426. doi:10.3390/jfb14080426

Vilas-Boas, V., and Vinken, M. (2021). Hepatotoxicity induced by nanomaterials: mechanisms and *in vitro* models. *Arch. Toxicol.* 95 (1), 27–52. doi:10.1007/s00204-020-02940-x

Wang, L., Weng, S., Su, S., and Wang, W. (2023a). Progress on the luminescence mechanism and application of carbon quantum dots based on biomass synthesis. *RSC Adv.* 13 (28), 19173–19194. doi:10.1039/d3ra02519e

Wang, S., Zhang, Y., Kong, H., Zhang, M., Cheng, J., Wang, X., et al. (2019). Antihyperuricemic and anti-gouty arthritis activities of Aurantii fructus immaturus carbonisata-derived carbon dots. *Nanomedicine (Lond)* 14 (22), 2925–2939. doi:10.2217/nnm-2019-0255

Wang, X., Liu, Y., Wu, T., Gu, B., Sun, H., He, H., et al. (2023b). A win-win scenario for antibacterial activity and skin mildness of cationic surfactants based on the modulation of host-guest supramolecular conformation. *Bioorg Chem.* 134, 106448. doi:10.1016/j.bioorg.2023.106448

Wareing, T. C., Gentile, P., and Phan, A. N. (2021). Biomass-Based carbon dots: current development and future perspectives. *ACS Nano* 15 (10), 15471–15501. doi:10.1021/acsnano.1c03886

Xiang, L., Lu, S., Quek, S. Y., Liu, Z., Wang, L., Zheng, M., et al. (2021). Exploring the effect of OSA-esterified waxy corn starch on naringin solubility and the interactions in their self-assembled aggregates. *Food Chem.* 342, 128226. doi:10.1016/j.foodchem.2020.128226

Xu, Y., Wang, B., Zhang, M., Zhang, J., Li, Y., Jia, P., et al. (2022). Carbon dots as a potential therapeutic agent for the treatment of cancer-related anemia. *Adv. Mater* 34 (19), e2200905. doi:10.1002/adma.202200905

You, G., Feng, T., Zhang, G., Chen, M., Liu, F., Sun, L., et al. (2021). Preparation, optimization, characterization and *in vitro* release of baicalein-solubilizing glycyrrhizic acid nano-micelles. *Int. J. Pharm.* 601, 120546. doi:10.1016/j.ijpharm.2021.120546

Zhai, C., Lu, F., Du, X., Zhang, M., Zhang, Y., Ma, Y., et al. (2023). Green carbon dots derived from Atractylodes macrocephala: a potential nanodrug for treating alcoholic gastric ulcer. *Colloids Surf. B Biointerfaces* 230, 113492. doi:10.1016/j.colsurfb.2023.113492

Zhang, B., Fan, X., Du, H., Zhao, M., Zhang, Z., Zhu, R., et al. (2023). Foodborne carbon dot exposure induces insulin resistance through gut microbiota dysbiosis and damaged intestinal mucus layer. *ACS Nano* 17 (6), 6081–6094. doi:10.1021/acsnano.3c01005

Zhang, M., Cheng, J., Hu, J., Luo, J., Zhang, Y., Lu, F., et al. (2021a). Green Phellodendri Chinensis Cortex-based carbon dots for ameliorating imiquimod-induced psoriasis-like inflammation in mice. *J. Nanobiotechnology* 19 (1), 105. doi:10.1186/s12951-021-00847-y

Zhang, M., Cheng, J., Luo, J., Hu, J., Zhang, Y., Sun, Z., et al. (2021b). Development of ecofriendly carbon dots for improving solubility and antinociceptive activity of glycyrrhizic acid. *J. Biomed. Nanotechnol.* 17 (4), 640–651. doi:10.1166/jbn.2021.3058

Zhang, W., Kandel, N., Zhou, Y., Smith, N., Ferreira, C. L. B. F., Perez, M., et al. (2022). Drug delivery of memantine with carbon dots for Alzheimer's disease: blood-brain barrier penetration and inhibition of tau aggregation. *J. Colloid Interface Sci.* 617, 20–31. doi:10.1016/j.jcis.2022.02.124

Zhao, Y., Wan, P., Wang, J., Li, P., Hu, Q., and Zhao, R. (2020). Polysaccharide from vinegar baked radix bupleuri as efficient solubilizer for water-insoluble drugs of Chinese medicine. *Carbohydr. Polym.* 229, 115473. doi:10.1016/j.carbpol.2019.115473

Zhu, Y. Z., Huang, S. H., Tan, B. K., Sun, J., Whiteman, M., and Zhu, Y. C. (2004). Antioxidants in Chinese herbal medicines: a biochemical perspective. *Nat. Prod. Rep.* 21 (4), 478–489. doi:10.1039/b304821g

Frontiers in Molecular Biosciences

TYPE Original Research
PUBLISHED 04 December 2023
DOI 10.3389/fmolb.2023.1282929

OPEN ACCESS

EDITED BY
Md Palashuddin Sk,
Aligarh Muslim University, India

REVIEWED BY
Upashi Goswami,
Indian Institute of Science (IISc), India
Hifzur R. Siddique,
Aligarh Muslim University, India
Neha Arora,
University of Texas Health Science Center at Houston, United States

*CORRESPONDENCE
Hui Kong,
doris7629@126.com
Yan Zhao,
zhaoyandr@163.com
Huihua Qu,
quhuihuadr@163.com

†These authors have contributedequally to this work

RECEIVED 25 August 2023
ACCEPTED 27 October 2023
PUBLISHED 04 December 2023

CITATION
Zhao Y, Dai E, Dong L, Yuan J, Zhao Y, Wu T, Kong R, Li M, Wang S, Zhou L, Yang Y, Kong H, Zhao Y and Qu H (2023), Available and novel plant-based carbon dots derived from Vaccaria Semen carbonisata alleviates liver fibrosis. *Front. Mol. Biosci.* 10:1282929. doi: 10.3389/fmolb.2023.1282929

Available and novel plant-based carbon dots derived from Vaccaria Semen carbonisata alleviates liver fibrosis

Yafang Zhao[1], Ertong Dai[2†], Liyang Dong[1], Jinye Yuan[1], Yusheng Zhao[1], Tong Wu[3], Ruolan Kong[1], Menghan Li[1], Shuxian Wang[1], Long Zhou[1], Yingxin Yang[1], Hui Kong[1]*, Yan Zhao[1]* and Huihua Qu[4]*

[1]School of Traditional Chinese Medicine, Beijing University of Chinese Medicine, Beijing, China, [2]Qingdao Eighth People's Hospital, Qingdao, Shandong, China, [3]School of Chinese Materia Medica, Beijing University of Chinese Medicine, Beijing, China, [4]Center of Scientific Experiment, Beijing University of Chinese Medicine, Beijing, China

Background: Liver fibrosis represents an intermediate stage in the progression of liver disease, and as of now, there exists no established clinical therapy for effective antifibrotic treatment.

Purpose: Our aim is to explore the impact of Carbon dots derived from *Vaccaria Semen* Carbonisata (VSC-CDs) on carbon tetrachloride-induced liver fibrosis in mice.

Methods: VSC-CDs were synthesized employing a modified pyrolysis process. Comprehensive characterization was performed utilizing various techniques, including transmission electron microscopy (TEM), multiple spectroscopies, X-ray photoelectron spectroscopy (XPS), and high-performance liquid chromatography (HPLC). A hepatic fibrosis model induced by carbon tetrachloride was utilized to evaluate the anti-hepatic fibrosis effects of VSC-CDs.

Results: VSC-CDs, exhibiting a quantum yield (QY) of approximately 2.08%, were nearly spherical with diameters ranging from 1.0 to 5.5 nm. The VSC-CDs prepared in this study featured a negative charge and abundant chemical functional groups. Furthermore, these particles demonstrated outstanding dispersibility in the aqueous phase and high biocompatibility. Moreover, VSC-CDs not only enhanced liver function and alleviated liver damage in pathomorphology but also mitigated the extent of liver fibrosis. Additionally, this study marks the inaugural demonstration of the pronounced activity of VSC-CDs in inhibiting inflammatory reactions, reducing oxidative damage, and modulating the TGF-β/Smad signaling pathway.

Conclusion: VSC-CDs exerted significant potential for application in nanodrugs aimed at treating liver fibrosis.

KEYWORDS

carbon dots, Vaccaria Semen, antifibrotic, anti-inflammatory, antioxidant

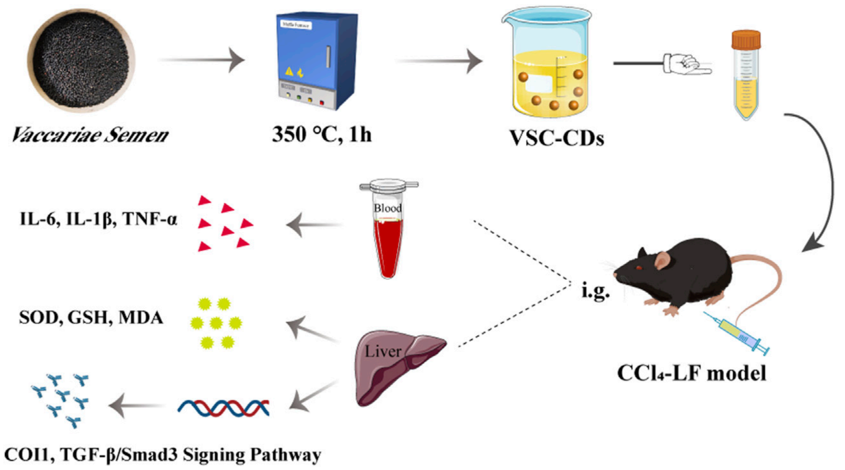

GRAPHICAL ABSTRACT

Introduction

Liver fibrosis (LF), as a wound-healing response, is caused by various chronic persistent liver injury (Cheng et al., 2021; Seitz and Hellerbrand, 2021) including viral hepatitis, alcoholic liver disease (Yang et al., 2021), and non-alcoholic fatty liver disease and has garnered considerable attention (Kumar et al., 2021). Liver fibrosis, including subsequent inflammatory responses and oxidative stress following liver injury, is characterized by the excessive deposition and accumulation of extracellular matrix proteins (Bataller and Brenner, 2005). If it is not promptly prevented and treated, continued progression of liver fibrosis can eventually lead to cirrhosis and even hepatocellular carcinoma. Some research attributes this to the removal or elimination of chronic liver injury resulting from various factors (Huang et al., 2023; Pellicano et al., 2023; You et al., 2023; Zhang et al., 2023) (suppression of extracellular matrix accumulation, anti-inflammatory, and anti-oxidative stress). However, no approved therapy for LF was used in clinical trials, which is in contrast with the robust effects of many anti-LF candidate drugs exhibited in experimental animal models. To date, methods of effective treatment remain unclear except for liver transplant surgery (Deng et al., 2022), which plagues clinical workers and scientific researchers. Therefore, finding innovative pharmacotherapeutic methods to relieve symptoms and arrest the course of liver fibrosis is urgently needed.

Carbon dots (CDs) with ultrafine sizes less than 10 nm are an emerging carbon nanomaterial that has aroused many medical researchers' interest owing to their diverse physicochemical properties, such as having superior biocompatibility (Belza et al., 2021), photostabilities (Kumar et al., 2022), low cytotoxicitiesties (Mu et al., 2021), and excellent water dispersion (Cai et al., 2021). Additionally, CDs are simple to functionalize due to the multitude of functional groups on their surfaces. Of note, these advantageous properties contributed to the biomedical application of CDs (Liu et al., 2019; Luo et al., 2021; Mansuriya and Altintas, 2021; Wang et al., 2022). Moreover, the development of CDs with inherent bioactivity impelled the progress and innovation of nanotechnology, especially nanomedicine. It is noteworthy that exploration of several medical bioactivities concerning CDs (antitumor (Cai et al., 2021), anti-inflammatory (Hu et al., 2016), anti-oxidant (Wei et al., 2019), hemostasis (Yan et al., 2017)) remarkably exhibited potential strategies for unsolved clinical conundrums like liver fibrosis.

Several studies have focused on exploring the antifibrotic effect of nanodrugs and CDs (Boey et al., 2021; Ren et al., 2021; Xu et al., 2022). Furthermore, the emerging nanotherapeutics could remodel the hepatic fibrotic microenvironment (Zhao et al., 2023), and nanoparticles have served targeted drug delivery of synthetic molecules for management of liver fibrosis based on inflammation and oxidative stress (Singh et al., 2023; Vyas and Patel, 2023). It follows that carbon-based nanoparticles play a crucial role in the treatment of liver diseases. Traditional Chinese medicine (TCM) is economical, shows lower biotoxicity, easily available, and widely used. Our research team have discovered that *Paeoniae Radix Alba carbonisata*-derived carbon dots exhibit a prominent hepatoprotective effect (Zhao et al., 2020). In addition, novel CDs derived from *Junci Medulla Carbonisata* perform hepatoprotective bioactivity (Cheng et al., 2019). Accordingly, functional carbon dots synthesized from green precursors possess unique advantages and extensive potential for exploitation and utilization for LF.

As a traditional Chinese medicine, *Vaccariae Semen* (VS) has a long clinical application history. VS, the dried mature seeds of *Vaccaria Segetalis (Neck) Garcke,* is named after 'Wangbuliuxing' in Chinese and recorded in the ancient Chinese classic medical book "the *Synopsis of the Golden Chamber*" by Zhang Zhongjing in the Eastern Han Dynasty: Incinerate VS into ashes without excessive burning. Originally utilized in the treatment of metal knife wounds, through the accumulation of medical experience, processed (fried) VS has been integrated into traditional Chinese medicine formulations for the treatment of liver diseases. We found that in patents related to traditional Chinese medicine formulations for liver diseases (hepatitis, cirrhosis), the use of VS or stir-fried VS is also indicated. Following these clues, we have learned that VS is applied in traditional Chinese medicine formulations for chronic hepatitis B liver fibrosis. From a contemporary pharmacological

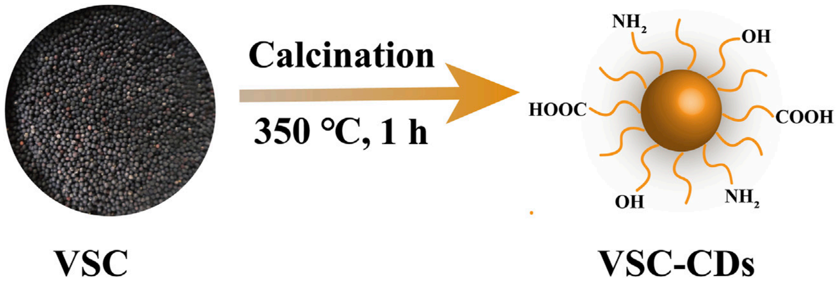

FIGURE 1
Illustration for as-prepared *Vaccaria Semen* Carbonisatum-based carbon dots (VSC-CDs) by one-step calcination method.

perspective, certain active ingredients in VS exhibit a variety of properties, such as anti-inflammation (Sun et al., 2017; Gong et al., 2019) and antioxidant effects (Yuan et al., 2014). Therefore, it is reasonable to persist in exploring the therapeutic effects of *Vaccaria Semen* Carbonisatum (VSC), the product of prepared VS on LF. Moreover, we explore the material basis and mechanism of action of VSC.

In this study, we identified and synthesized a novel nano-component named *Vaccaria Semen* Carbonisatum-derived Carbon dots (VSC-CDs) utilizing a green and one-step pyrolysis method (Figure 1). Besides, based on identification of their physicochemical characteristics (e.g., morphology, optical properties, functional groups and carried negative charges), we evaluated the alleviation effect of VSC-CDs on LF induced by the carbon tetrachloride (CCl_4) as well as the cytotoxicity of RAW264.7 cells and blood compatibility. Our study, to the best of our knowledge, focused on inflammation (IL-6, IL-1β, TNF-α), oxidative stress (SOD, GSH, MDA) in the process of CCl_4-induced LF, and the preliminary mechanism of the alleviation effect of VSC-CDs by detecting the contents of collagen1 (COI1), transforming growth factor-β1 (TGF-β1), Smad3, and α-smooth muscle actin (α-SMA). The results indicate that VSC-CDs exhibit the ability to reduce inflammation levels, enhance antioxidant capacity, facilitate the restoration of impaired liver function in mice, and alleviate liver fibrosis. Our findings hold promise for the development of a novel, environmentally friendly, and effective nanomedicine, offering a potential therapeutic strategy for mitigating liver fibrosis in clinical applications.

Material and methods

Chemicals

VS was purchased from Beijing Qiancao Herbal Pieces Co., Ltd. (Beijing, China), and the VSC was prepared in a muffle furnace in our research facility. A dialysis membrane of 1,000 Da molecular weight cut-off was purchased from Beijing Ruida Henghui Technology Development Co., Ltd. (Beijing, China). The Cell Counting Kit-8 (CCK-8) was obtained from Dojindo Molecular Technologies, Inc. (Kumamoto, Japan), and Silybin was purchased from Tianjin Tasly Sants Pharmaceutical Co., Ltd. (Tianjin, China). Carbon Tetrachloride (CCl_4) was obtained from Beijing InnoChem Science & Technology Co., Ltd. (Beijing, China). Other analytical-grade chemical reagents were acquired from Sinopharm Chemical Reagents Beijing (Beijing, China). Mouse IL-6, IL-1β, and TNF-α enzyme-linked immunosorbent assay (ELISA) kits were brought from Cloud-Clone Crop. (Wuhan, China). SOD, GSH, and MDA kits were from Nanjing Jiancheng Bioengineering Institute (Nanjing, China). Mouse monocyte-macrophage RAW264.7 cells were purchased with Peking Union Cell Bank (Beijing, China). Deionized water was available in all experiments.

Animals

Adult male C57BL/6J mice (weighing 20.0 ± 2.0 g) were purchased from SiPeiFu Biotechnology Co., Ltd. (Beijing, China) with a Laboratory Animal Certificate of Conformity and raised in a controlled laboratory environment with a well-ventilated room, suitable temperature (24.0°C ± 1.0°C), and relative humidity (45.0%–55.0%) under a 12 h light/dark cycle. The animals were provided with plenty of food and water throughout the experiment. The execution of experimental protocols was strictly in accordance with the Guidelines for Care and Use of Laboratory Animals and approved by the Ethics Review Committee of Animal Experimentation of the Beijing University of Traditional Chinese Medicine.

Preparation and characterization of VSC-CDs

Preparation of VSC-CDs

Previously weighed VS dried herbs were placed in a crucible and covered with aluminum foil, which was put into a muffle furnace for high-temperature calcination at 350°C for 1 h (TL0612, Beijing Zhong Ke Aobo Technology Co., Ltd., Beijing, China). The carbonized product, *Vaccaria Semen* Carbonisatum (VSC), was ground into fine powder after it had naturally cooled to 30 °C. Then, 30-fold deionized water (DW) was added to 30 g of VSC powder, and the VSC was boiled twice at 100°C for 1 h each time. The aqueous decoction was subjected to filtration through a 0.22 μm microfiltration membrane, followed by consolidation and concentration of the resulting filtrates utilizing a rotary evaporator. To further remove small molecules and non-carbonaceous impurities, the solution was dialyzed against DW through a dialysis membrane (MWCO = 1,000) for 72 h, which was stored at 4°C for further use.

Characterization of VSC-CDs

The morphological features and particle size distribution of the VSC-CDs were observed using transmission electron microscopy (TEM; Tecnai G220, FEI Company, Hillsboro, OR, United States). Meanwhile, atomic lattice fringes and structural details were examined by high-resolution transmission electron microscope (HRTEM; JEN-1230, Japan Electron Optics Laboratory, Tokyo, Japan). The fluorescent performances and ultraviolet-visible (UV-vis) absorption spectra of the VSC-CDs were measured via a performing fluorescence spectrophotometer (FL; F-4500, Tokyo, Japan) and an ultraviolet spectrophotometer (CECIL, Cambridge, United Kingdom), respectively. Fourier transform infra-red (FTIR) spectrum (Thermo Fisher, California, United States) data were collected to identify functional groups in VSC-CDs, and the zeta potential values were calculated using a malvern zetasizer nano ZS90 (Malvern Instruments, United Kingdom). X-ray photoelectron spectroscopy (XPS; ESCALAB 250Xi, Thermo Fisher Scientific, Fremont, CA) was used to record the surface composition and chemical elements of VSC-CDs with a mono X-ray source Al Kα excitation (1,486.6 eV).

Quantum yield of VSC-CDs

We chose Quinine sulfate (quantum yield [QY]: 54%, 0.1 M sulfuric acid [H_2SO_4]) as the reference sample to measure the comparative QY of VSC-CDs. To minimize the reabsorption effect, the absorbance of the CDs and the R were kept under 0.05. QY of VSC-CDs was calculated by the following Formula 1:

$$QY_{CDs} = QY_R \times \frac{I_{CDs}}{I_R} \times \frac{A_R}{A_{CDs}} \times \frac{\eta^2_{CDs}}{\eta^2_R} \quad (1)$$

where QY is fluorescence quantum yield, *I* represent an integrated area of emission intensity, and *A* and η indicate the absorption value at 371 nm wavelength and the refractive index of the solvent, respectively. The CDs and the R denote VSC-CDs and the reference sample, respectively.

Fingerprint analysis of VSC and VSC-CDs by high-performance liquid chromatography

The individual components determination of VSC and VSC-CDs was detected by HPLC (Agilent LC-1260, Waldbronn, Germany) with a C-18 column (250 mm × 4.6 mm × 0.5 μm, ZORBAX SB-C18, United States). The mobile phase consisted of methanol (A) and 0.3% phosphoric acid (B). The gradient elution procedure was as follows: 35%–35% A at 0–3 min; 35%–40% A at 3–5 min; 40%–45% A at 5–10 min; 45%–40% A at 10–20 min. The flow rate of the mobile phase was 1 mL/min, the column temperature was 30°C, the detection wavelength was 254 nm, and the injection volume was 5 μL. Furthermore, all samples were purified by filtration through a 0.22 μm cellulose membrane and analyzed in triplicate.

In vitro assay

Cytotoxicity and hemocompatibility assay of VSC-CDs

RAW 264.7 cells were used to measure the cytotoxicity of VSC-CDs using a CCK-8 assay *in vitro*. Firstly, RAW 264.7 cells were cultured in Dulbecco's modified Eagle's medium (DMEM) supplemented with 20% fetal bovine serum at 37°C in a humidified 5% CO_2. Then the cells were seeded in a 96-well plate at a density of 1×10^4 cells per well and incubated for 24 h. After disposing of the original medium in each well, different concentrations of VSC-CDs were added (1,000, 500, 250, 125, 62.5, 31.25, 15.62, and 7.81 μg/mL) to the designated wells. Another 24 h later, the medium containing VSC-CDs was discarded and the cells were washed with phosphate-buffered saline (PBS) twice. Subsequently, we added 10 μL CCK-8 solution and incubated for 4 h. The absorbance of each well was detected by a microplate reader (Bitoke, VT, USA) at a wavelength of 450 nm, and cell viability was calculated according to the following Formula 2:

$$\text{Cell Viability (\% of control)} = \frac{A_e\text{-}A_b}{A_c\text{-}A_b} \times 100 \quad (2)$$

Ae, Ab, and Ac represent the experimental, blank, and control groups, respectively, at 450 nm.

Hemolysis assay of VSC-CDs was carried out according to the method described by previous report. The red blood cells (RBCs) were centrifugated at 3,500 rpm for 15 min in a constant temperature centrifuge at 4°C and were washed three times with PBS (pH = 7.2–7.5). The sample was added into a 2 mL EP tube with 500 μL 10% RBC suspension and mixed with different concentration VSC-CDs solution (1,000, 800, 400, 200, and 100 μg/mL) in the same volume at room temperature. Subsequently, this sample was incubated at 37°C for 2 h and 4 h. The hemolysis ratio was calculated according to the following Formula 3:

$$\text{Hemolysis (\%)} = \frac{A_{Sample}\text{-}A_{PBS}}{A_{Water}\text{-}A_{PBS}} \times 100 \quad (3)$$

When the hemolysis ratio was lower than the internationally recognized standard (5%), we believed that the medicine had high blood compatibility.

In vivo experiments

Models of hepatic fibrosis and drug treatment

Male C57BL/6J mice were randomly allocated into six groups (*n* = 7) as follows: control group (normal saline [NS] 10 mL/kg, p.o.), model group (CCl_4 10 mL/kg, p.o.), positive group (silybin

10 mL/kg, p.o.), and the high-, medium-, and low-dose VSC-CDs groups (3.63, 1.81, and 0.91 mg/kg, respectively, intraperitoneally). All groups were injected intraperitoneally with the prepared carbon tetrachloride oil solution (10 mL/kg) for 8 weeks, two times per week, with a 3-day interval, apart from the control group, where mice were given an intraperitoneal injection of an equal volume of corn oil. Then, we performed oral administration for mice in the VSC-CDs groups. The mice of the control group and the model group were given an equivalent volume to normal saline positive group. The mice of the positive group were given silybin. Body weight was recorded daily at a regular time until the end of the experiment to count and analyze the weight difference. A total of 12 h after the final administration, all mice were sacrificed. The liver was isolated and weighted to gain the weight ratio of liver to body (liver/body wt%) and photographed for observing morphological changes.

Histopathological observation

After removing liver tissue rapidly and rinsing it with ice-cold saline, a small piece of liver tissue was cut and fixed in 4% paraformaldehyde, dehydrated, and embedded in paraffin. Then 4 μm thick sections were prepared for H&E, Masson staining, and Sirius red staining. Morphological changes were observed with an optical microscope to compare the severity of liver injuries and the fibrosis status among various treatment groups.

Detection of biochemical indexs

All mice were anaesthetized with 4% chloral hydrate (0.40 g/kg), and retro-orbital blood samples were collected into an Eppendorf tube to clot overnight at 4°C, centrifuged at 750 × g for 15 min, and then the blood serums were separated from whole blood. One part of the sera samples was determined to analyze the changes in alanine transaminase (ALT) and aspartate aminotransferase (AST) activity and the levels of total bile acid (TBA), total bilirubin (TBIL), and cholesterol (TC) by an automatic biochemical analyzer (XI-800, Sismecon Co., Ltd, Japan). Other part of those sera samples was used to examine the contents of tumor necrosis factor-α (TNF-α), interleukin (IL)- 6, and interleukin (IL)- 1β in serum detected using corresponding kits (Nanjing Jiancheng Biochemical Reagent Co., Nanjing, China) according to the manufacturer's instructions. What is more, after taking out the liver tissues from the different groups stored at −80°C, those tissue samples were cut into small pieces, homogenized with PBS on ice, and then centrifuged at 750 × g for 15 min. The gained supernatants were collected to determine levels of SOD, GSH, and MDA using respective kits.

Western blot analysis

Total protein extracted from liver tissue in a RIPA buffer (Beyotime Institute of Biotechnology, Shanghai, China) was used for Western blot analysis. The BCA Protein Assay Kit was applied to quantitate protein content following the manufacturer's protocol. Proteins were separated by gel electrophoresis and transferred to membranes, followed by blocking in 1× TBST (5% *w*/*v* skim milk) for 2 h at room temperature and probing overnight with primary antibodies against COI1 (1:3000), TGF-β1 (1:4000), Smad3 (1:4000), α-SMA (1:5000), and GAPDH (1:8000) at 4°C. After washing membranes and incubating with horseradish peroxidase-conjugated secondary antibodies (1:8000) for 1 h, the films were scanned densitometrically. By considering the GAPDH density as an internal control, the gray densities of the protein bands were normalized and quantified using ImageJ software.

Statistical analysis

All statistical analysis was carried out and analyzed using IBM SPSS statistics software, version 20.0. data, with normal distribution, and uniform variance were shown as means ± standard deviation (SD). One-way analysis of variance (ANOVA) was performed to compare statistically significant differences with the least significant difference (LSD) test used for multiple comparisons. Data with non-normal distribution non-normally distributed data were analyzed using non-parametric statistics using the Kruskal–Wallis test and a *post hoc* test; $p < 0.05$ and $p < 0.01$ were taken as statistically significant differences.

Results

Characterization of VSC-CDs

The TEM image showed the morphology and size distribution of as-prepared VSC-CDs. As depicted in Figure 2, the CDs were almost spherical with favorable homogeneous dispersibility and the particle size distribution of VSC-CDs ranged primarily from 1.0–5.5 nm based on factual examination and calculation of hundred particles (Figure 2A). The HRTEM image (Figure 2B) revealed that the distinct lattice spacing was 0.23 nm. Furthermore, the zeta potential of VSC-CDs dissolved in aqueous solution was −26.6 ± 2.65 mV (Figure 2C), indicating VSC-CDs attained a state of moderate stability. The surface of VCS-CDs contains numerous oxygen-containing functional groups, making it susceptible to releasing hydrogen ions and rendering the solution negatively charged. Comparatively, carbon dots with negative charge exhibit lower toxicity (Havrdova et al., 2016; Yan et al., 2018), and the negative potential of nanoparticles contributes to their *in vivo* dispersibility and stability (Tang et al., 2023) and diminishes aggregation of the particles in the solution (Hou et al., 2023).

The spectral properties were exhibited next. The fluorescence emission spectra demonstrated a maximum emission at 460 nm and maximum excitation at 371 nm in the emission and excitation spectrum (Figure 2D). The aqueous solution of VSC-CDs was brown in the room light, giving off blue fluorescence under 365 nm ultraviolet lamp. The UV-Vis absorption spectra of VSC-CDs indicated a weak absorption peak at 260 nm, which was attributed to the conjugated C=C bonds π–π* electron transition of VSC-CDs (Figure 2E). Meanwhile, the QY of VSC-CDs was calculated to be 2.08% using quinine sulphate as a reference. The aforementioned results indicate that VSC-CDs manifest photoluminescent properties.

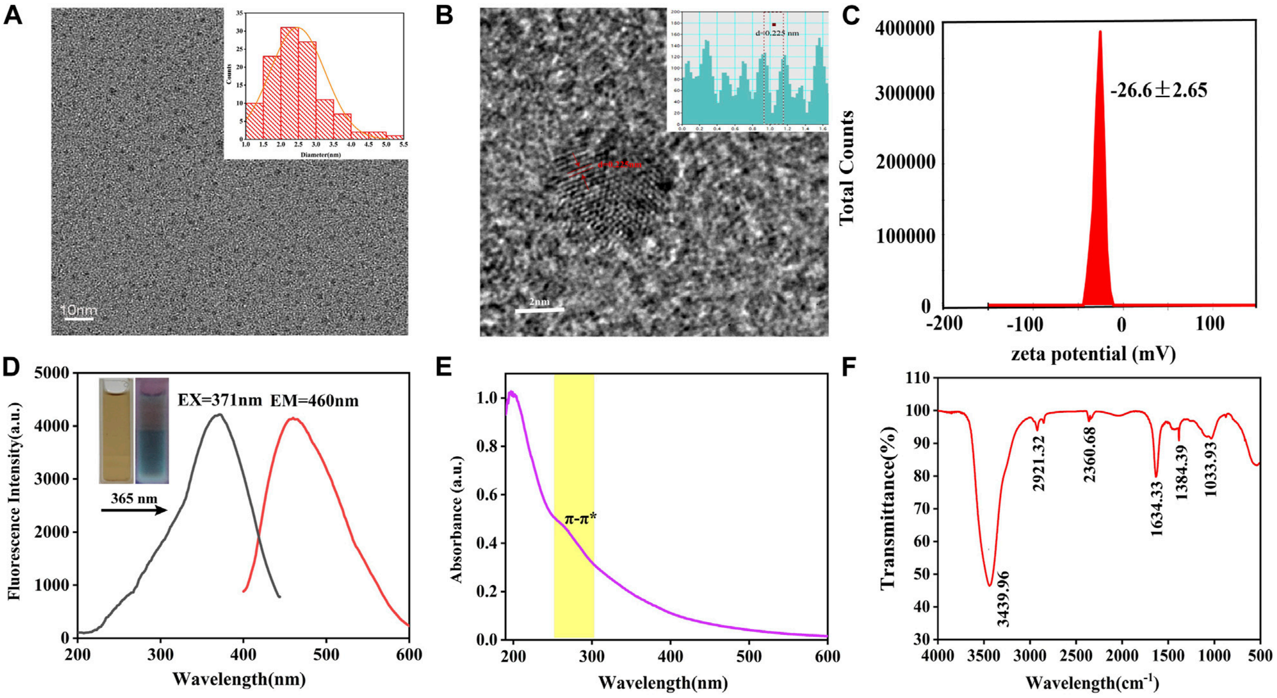

FIGURE 2
TEM images of VSC-CDs and histogram depicting the **(A)** particle size distribution, **(B)** HR-TEM image, **(C)** zeta potential, **(D)** excitation and emission spectrum, **(E)** ultraviolet-visible spectrum, and **(F)** FTIR spectrum.

In terms of surface functional groups and chemical characteristics of the VSC-CDs, FTIR spectra (Figure 2F) displayed a strong characteristic peak at 3,439 cm^{-1} attributed to the absorption bands of O–H. The absorption peak located at 2,921 cm^{-1} was assigned to -C-H stretching vibration, suggesting the existence of $-CH_3$ and $-CH_2$ groups in VSC-CDs. Moreover, the peak at 2,360 cm^{-1} showed the presence of the -C≡N bond. The peak observed at 1,634 cm^{-1} was associated with -C=O stretching vibration. Both peaks appearing at 1,384 cm^{-1} and 1,033 cm^{-1} were corresponding to -C-N and -C-O-C bonds separately. The above-mentioned results indicate that the surface of VSC-CDs features multifunctional groups, including carbonyl, carboxyl, and hydroxyl moieties, those organic functional groups enhanced water-solubility on VSC-CDs.

XPS further disclosed the element composition and allocation information of VSC-CDs (Zhao et al., 2021). As shown in Figure 3A, three peaks were evident at 284.94, 399.67, and 531.8 eV, which indicated the purified CDs were mainly composed of C (65.31%), O (30.67%), and a small amount of N (4.02%). The C 1s spectrum (Figure 3B) deconvoluted into three peaks at 284.28, 285.85, and 287.61 eV and was related to the C-C/C=C, C-N, C=O groups (Han et al., 2019; Wang et al., 2020; Zhang et al., 2020). In the high-resolution O 1s spectrum (Figure 3C), the O 1s peak consisted of two subpeaks at 530.83 eV (C-O) (Zhang et al., 2020) and 532.28 eV (C=O) (Wang et al., 2020). Two peaks at 399.24 and 399.75 eV were presented in the high-resolution N 1s spectrum (Figure 3D), representing the presence of C-N-C and C=N bonds. The XPS spectra substantiated the presence of diverse functional groups, encompassing carbonyl, carboxyl, and hydroxyl on the surface of VSC-CDs. All the above results were in line with FTIR analysis.

The high-performance liquid chromatogram results of the VSC and VSC-CDs are shown in Figure 4. Chlorogenic acid is the main small molecule in VSC, while the corresponding characteristic peaks disappeared in VSC-CDs, which indicated no active small-molecule compounds in VSC-CDs.

Cytotoxicity evaluation and hemocompatibility

To investigate the cytotoxicity of VSC-CDs, a CCK-8 assay was carried out. RAW264.7 cells were cultured to different concentrations of VSC-CDs (7.81–1,000 μg/mL) for 24 h. Figure 5A illustrated that the viability of RAW264.7 cells treated with VSC-CDs was all over 100% compared with the control cells. Cell viability increased steadily between 7.81 μg/mL and 125 μg/mL, reaching as high as 195% when the concentration of VSC-CDs was up to 125 μg/mL. The proliferation effect gradually got weaken at values of ranging from 125 to 1,000 μg/mL. In conclusion, VSC-CDs possessed scarce biotoxicity and good biocompatibility, which means VSC-CDs have a good application prospect for drugs.

Hemolysis assay is typically used in biocompatibility testing to evaluate the blood safety of materials. Intuitively, as Figures 5B,C show, all doses of VSC-CDs did not cause significant hemolysis of red blood cells. Moreover, this property of VSC-CDs does not change as the incubation time changes (for 2 h and 4 h). Accordingly, VSC-CDs are highly hemocompatible.

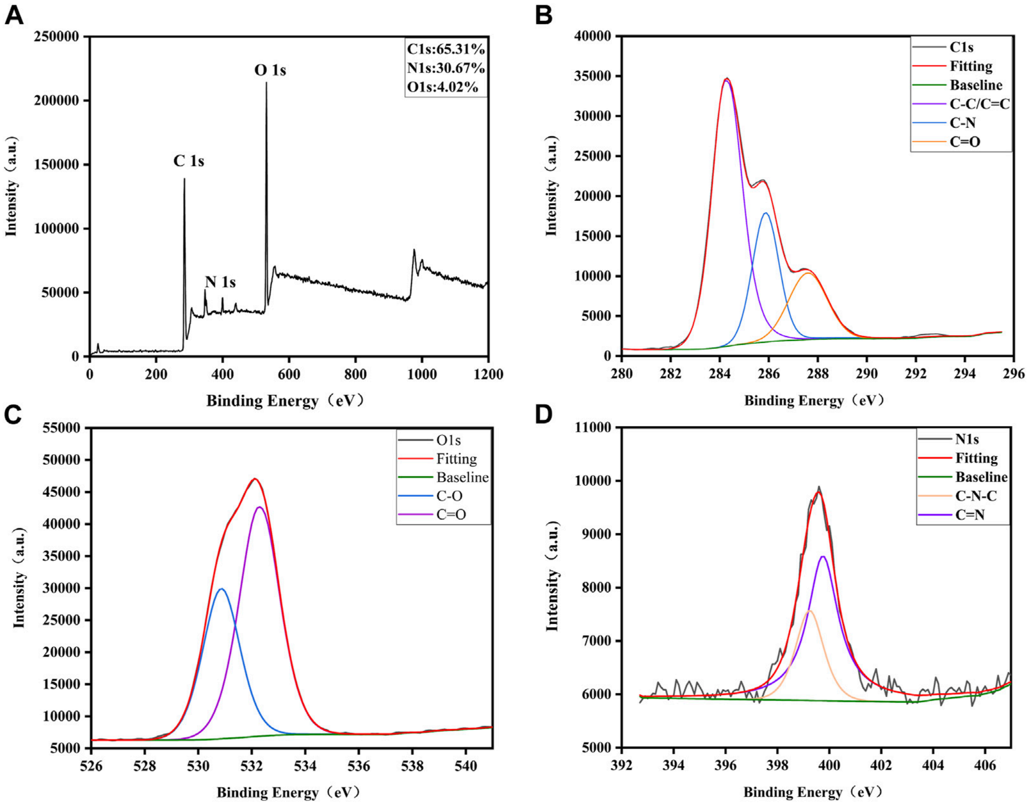

FIGURE 3
Surface composition and elemental analysis of VSC-CDs by XPS. **(A)** XPS spectra of VSC-CDs, **(B)** C 1s, **(C)** O 1s, and **(D)** N 1s.

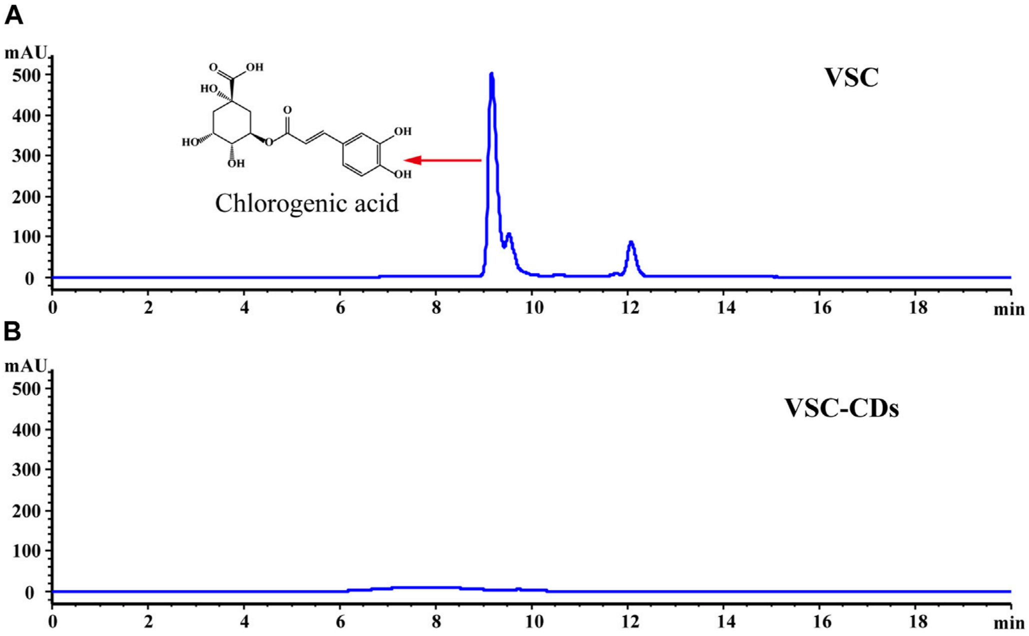

FIGURE 4
High-performance liquid chromatogram of **(A)** VSC and **(B)** VSC-CDs.

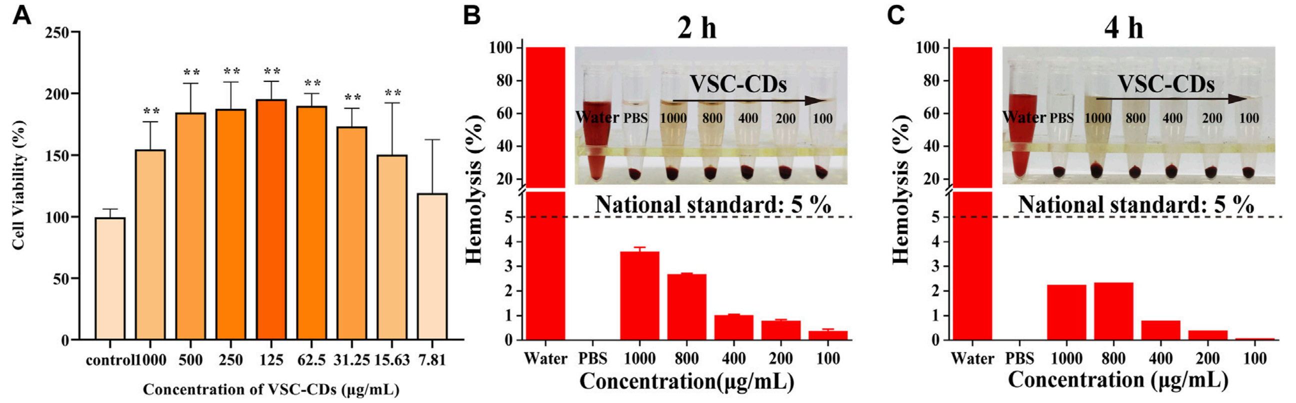

FIGURE 5
(A) Effect of different concentrations of VSC-CDs on cell viability of the RAW264.7 macrophage; **(B,C)** hemolytic assay of VSC-CDs for 2 h and 4 h.

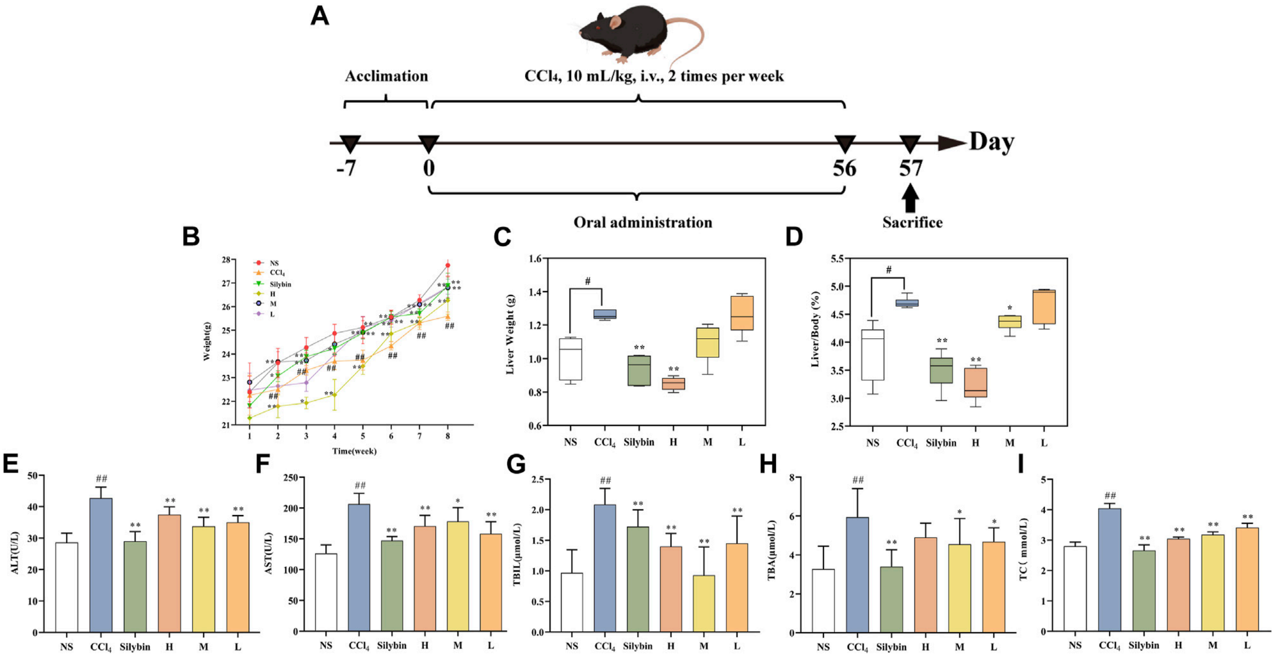

FIGURE 6
(A) schemes of RM-AKI model **(B–D)** the effect of VSC-CD$_S$ on the body weight, liver weight, and liver index of mice with liver fibrosis **(E–I)** biomarker measurements including ALT, AST, TBIL, TBA, and TC vs. control group #$p < 0.05$ and ##$p < 0.01$, vs. Model group *$p < 0.05$ and **$p < 0.01$. **(H)** High dose; L: Low dose; M: Medium dose; NS: Normal saline.

The VSC-CDs mitigated CCl$_4$-induced LF model

Effect of VSC-CDs on body weight and liver/body wt%

In Figure 6A, after almost 2 months of molding and drug administration, the mice were then sacrificed. We recorded the weight every week (Figure 6B); in the second week, the weight profile showed that in contrast to the control group, body weight of the CCl$_4$-induced group mice was decreased ($p < 0.01$), while VSC-CDs of the high- and medium-dose groups remarkably counteracted ($p < 0.01$) weight loss in mice. In the next week, the body weight of the positive group was also significantly elevated ($p < 0.01$). Similar observations were made about the mice in the high-, medium-, and low-dose groups treated with VSC-CDs as well as the silybin group for 5–8 weeks. Moreover, the control group displayed a tendency for weight gain throughout the experiment. These results manifested that VSC-CDs could reduce the loss of the body weight by CCl$_4$ injection.

The severity of liver disease may be partially reflected by the liver/body weight ratio (Figures 6C,D). To investigate the effects of prolonged exposure to CCl_4 on organ weight, the weights of the liver samples were assessed and used to determine the liver/body weight ratio. Liver/body wt% and liver weight in the model group were significantly higher ($p < 0.05$) compared with the control group. After the consequent application of VSC-CDs for 8 weeks, liver/body wt% and weight showed a prominent decrease in high-dose ($p < 0.01$) and medium-dose groups ($p < 0.05$) of VSC-CDs. The decreasing trend of liver weight existed also in high-dose of VSC-CDs ($p < 0.01$).

VSC-CDs inhibited expression of biochemical parameters

As shown in Figures 6E–I, several biochemical markers (ALT, AST, TBIL, TBA, TC) were determined to evaluate hepatocyte injury in serum levels. Figure 6 showed the content of ALT, AST, TBIL, TBA, and TC in the model group were significantly higher than the normal saline group ($p < 0.01$). In contrast with the model group, the serum ALT, TBIL, and TC activity of mice was significantly decreased in the positive group and high-, medium-, and low-dose groups of VSC-CDs ($p < 0.01$). As for the serum content of AST, the model group was higher than the control group, and the medium-dose of VSC-CDs significantly downregulated its levels ($p < 0.05$) compared with the model group. More specifically, the serum content of AST ($p < 0.01$) was substantially suppressed by high and low doses of VSC-CDs and silybin treatment. The medium- and low-dose groups (in both groups: $p < 0.05$) of VSC-CDs exhibited a pronounced reduction as compared to the model group, showing similar results for TBA levels. The results of liver function indicator testing suggest that VSC-CDs can mitigate liver damage induced by CCl_4.

VSC-CDs ameliorated CCl_4-induced histopathology and morphology

CCl_4 administration for 8 weeks triggered morphological changes of liver tissue, as evidenced by the roughened surface attached to a granular substance, dull luster, and edge passivation (Figure 7A). Nonetheless, treatment with VSC-CDs mitigated the pathological alterations in liver. Along with the measurement of morphological observation, we performed a histopathological examination of liver tissues. Liver sections of the control group (Figure 7B) stained with H&E showed normal hepatic architecture; liver cells were arranged in plates or cords and radiated from the central venue regions without hepatic steatosis or necrosis. It was worth noting that the liver structure was destroyed and the boundary blurred, accompanied by massive necrosis of liver cells, and infiltration of inflammatory, diffuse microvesicular steatosis lesions by the injection of CCl_4. In contrast, VSC-CDs treatment significantly attenuated the liver injury and lesions as mentioned in the CCl_4-administrated group. In addition, Masson staining (Figure 7C) and Sirius red staining (Figure 7D) were employed to detect collagen deposition. We could distinctly observe excessive accumulation and fibrotic septa in the CCl_4-treated fibrotic liver, while CCl_4-induced elevation evidently was alleviated by VSC-CDs treatment. Taken together, the observed alterations in pathological slices directly demonstrate that VSC-CDs can inhibit CCl_4-induced liver fibrosis.

Effect of VSC-CDs on inflammatory cytokines in serum

Inflammatory mediators play a crucial role in the induction, initiation, progression, and aggravation of liver fibrosis (Zhang et al., 2016a). The levels of TNF-α, IL-6, and IL-1β in liver tissue were determined to determine the anti-inflammatory effect of VSC-CDs. As Figures 8A–C show, in comparison to that in the control group, serum concentrations of TNF-α were dramatically upregulated in the model group ($p < 0.01$). In sharp contrast, silybin and VSC-CDs (high-, medium-, low-dose) inhibited CCl_4-induced elevated content of TNF-α relative to the model group ($p < 0.01$). The contents of IL-6 and IL-1β were similar to those for TNF-α. Based on the results, VSC-CDs in various dosage groups significantly diminish the levels of TNF-α, IL-6, and IL-1β, signifying that VSC-CDs inhibit the inflammatory response and thereby alleviate liver fibrosis.

Effect of VSC-CDs on antioxidant levels

Oxidative stress is one of the underlying mechanisms in CCl_4-induced liver fibrosis; reactive oxygen species can trigger the initiation of the inflammatory cascade to further accelerate the progression of liver fibrosis (Xu et al., 2022). Antioxidant markers (SOD, GSH) and peroxidation product (MDA) (Figures 8D–F) were measured to evaluate the alterations of the redox status.

When it comes to SOD in liver tissue, a significant difference ($p < 0.01$) was seen: the activity of SOD in the model group was visibly restrained compared with the control group. More remarkably, VSC-CDs treatment improved the levels of SOD to a large degree. Otherwise, injection of CCl_4 resulted in a significant decrease in the activities of GSH compared to the control group, and, as expected, silybin and the different dosages of VSC-CDs also accomplished elevation of GSH levels ($p < 0.01$).

On the contrary, MDA, one of lipid metabolites, must be scavenged in a timely manner to protect hepatocytes from oxidative damage. The assay results indicated that, owing to the intervention of CCl_4, the contents of MDA inevitably were increased in comparison to in the control group ($p < 0.01$). Of note, the increase was evidently attenuated by VSC-CDs and silybin treatment ($p < 0.01$). Collectively, VSC-CDs could improve the antioxidant capacity of the liver and scavenge oxygen-free radicals to balance the redox system.

According to the results, under the intervention of VSC-CDs, oxidative stress levels decrease, contributing to the mitigation of liver fibrosis along with a reduction in the inflammatory response.

Effect of related proteins on TGF-β/Smad signaling pathway

The TGF-β/Smad signaling pathway is one of representative signaling pathways in liver fibrosis. We conducted a preliminary

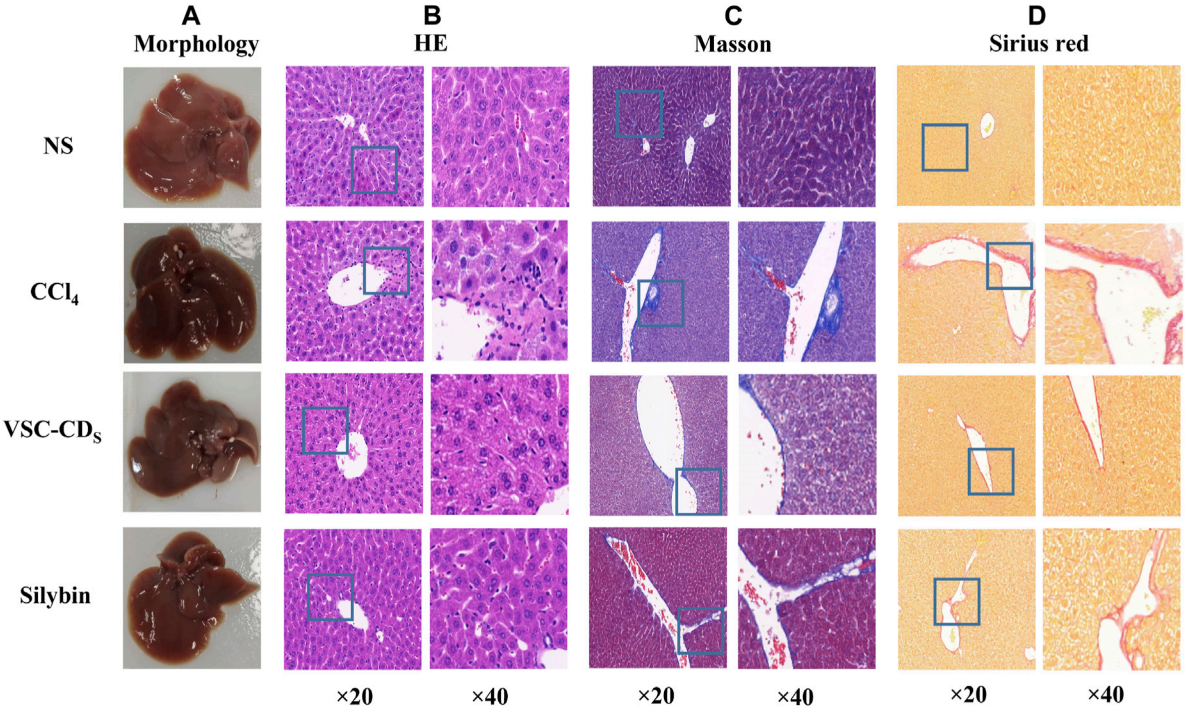

FIGURE 7
Effects of VSC-CDs on the appearance and pathological changes of liver tissue in CCl_4-induced liver fibrosis model mice. **(A)** the appearance of liver tissue, **(B)** H&E staining, **(C)** Masson staining, and **(D)** Sirius red staining.

investigation on TGF-β/Smad signaling pathway to elucidate tentatively the potential mechanism of action. The results of semi-quantitative analysis (Figures 8G–K) showed the expressions of the COI1 and TGF-β1 proteins was highly elevated compared with the control group ($p < 0.01$), the three VSC-CDs doses (H, M and L: $p < 0.01$) significantly inhibited the levels of TGF-β1, while the expressions of COI1 was notably lessened by M and L-doses ($p < 0.01$) $VSC\text{-}CD_S$. In addition, the concentrations of Smad3 proteins markedly reduced in silybin ($p < 0.05$) and VSC-CDs groups (H: $p < 0.05$, M and L: $p < 0.01$). α-SMA is considered a marker of Hepatic stellate cell (HSC) activation with CCl_4 -stimulation, and the expression levels of α-SMA in the model group ($p < 0.05$) was increased distinctively, which indicated CCl_4 induced the activation of HSCs. Inhibition of the expression of α-SMA was found in VSC-CDs treated groups (M: $p < 0.01$, L: $p < 0.05$) compared to the model group. These findings suggest that the favorable effects of VSC-CDs on the improvement of liver fibrosis may be linked to the modulation of the TGF-β/Smad signaling pathway.

Discussion

CDs seen as a newly carbon nanomaterial joined latest the carbon family, which gained tremendous concern and research by virtue of its unique biological properties, such as excellent absorbance and optical photoluminescence. Noteworthy, uptake, biodistribution, and excretion of nanoparticles (NPs) are closely linked to many organs, especially the liver. Most of the NPs are taken up by non-parenchymal cells of the liver, then phagocytosed, and delivered to the lysosome by kupffer cells for enzymatic digestion (Zhang et al., 2016b; Cornu et al., 2020; Truskewycz et al., 2022). Meanwhile, physicochemical properties including charge, size, surface functionality, zeta potential and chemical composition, can largely influence the uptake, biodistribution, excretion, and even the toxicity of NPs. As previously reported, hepatocyte uptake increases for NPs with positive zeta potential, contrary to macrophages that preferentially take up negatively charged NPs (Wang et al., 2015). On the excretion of NPs, the particles with positive charge were strongly through the kidney, in contrast, the negatively charged through the liver (Liang et al., 2016). And renal excretion is prevented when the NPs size are above 6 nm (Dogra et al., 2018). Thus, physicochemical properties of nanoparticle were merited to be identificated and characterized to explore their bioactivity.

In recent years, renewable sources were used for the preparation of CDs, including apple (Mehta et al., 2015), oolong tea (Shi et al., 2017), guava leaf (Ramanarayanan and Swaminathan, 2020) as well as natural source of carbon dots from part of the plant and its applications (Humaera et al., 2021), which encouraged and enlightened the developments of CDs choosing biomass as the novel precursors, like charcoal drugs. By using low-cost, low energy consumption, simple manipulation, and one-step preparation method as selection of preparation conditions, VSC-CDs were synthesized with high temperature carbonization. Then VSC-CDs were characterized and identified by a range of characterization instruments. Meanwhile, we have proved that VSC-CDs had hepatoprotective effect on the mice induced by alcohol, which laid the groundwork for this study (Zhao et al., 2021).

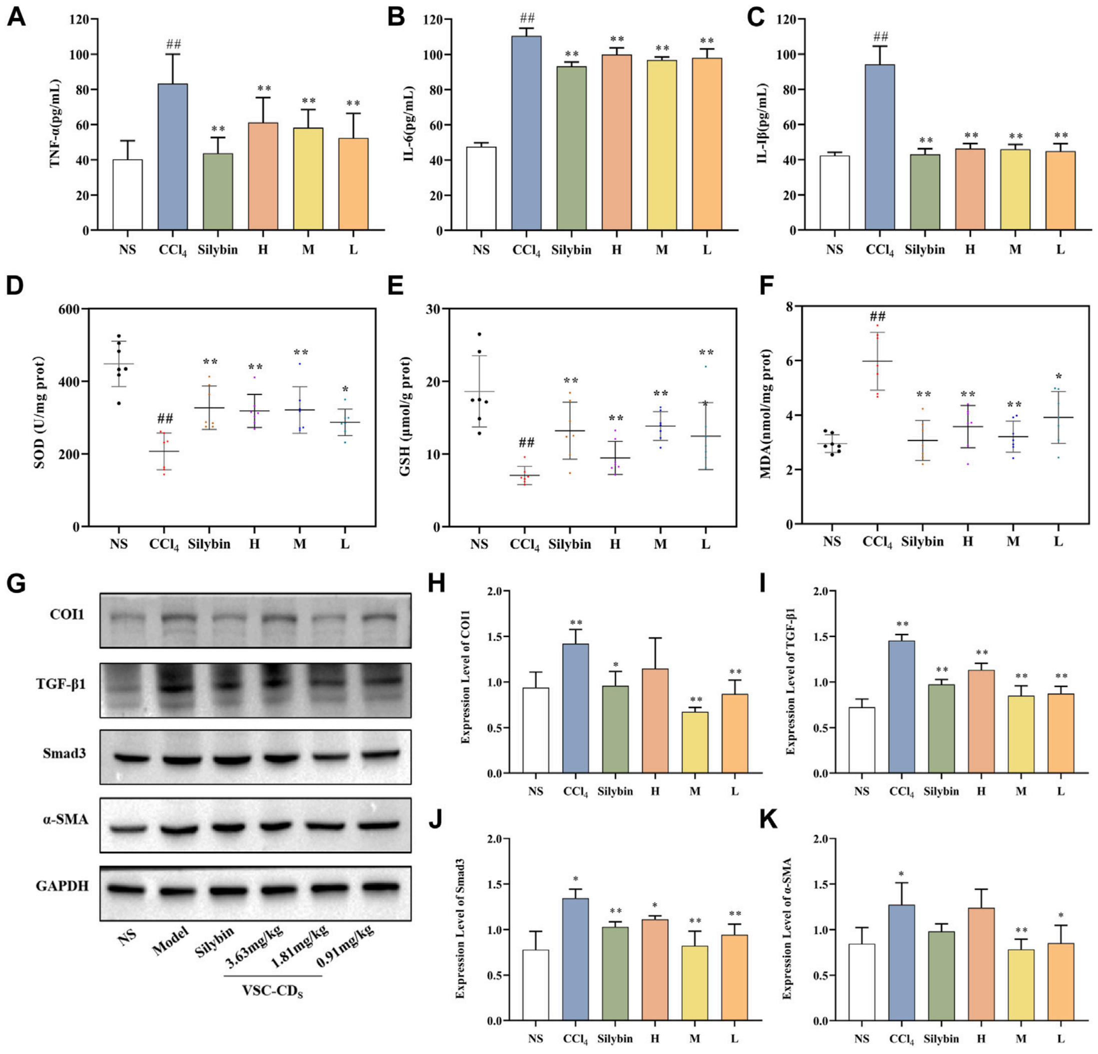

FIGURE 8
Effects of inflammatory cytokines, antioxidant levels and the expression of TGF-β/Smad signaling pathway-related proteins in the liver tissue of CCl_4-induced LF model mice. Content of **(A)** TNF-α, **(B)** IL-6, and **(C)** IL-1β; Effects of **(D)** SOD, **(E)** GSH, and **(F)** MDA; the western blot image **(G)** and the expression level of **(H)** COI1, **(I)** TGF-β1, **(J)** Smad3, and **(K)** α-SMA.H: High dose (3.63 mg/mg); M: Medium dose (1.81 mg/kg); L: Low dose (0.91 mg/kg); NS: Normal saline.

Current researches mostly put eyes on nanoparticles as delivery carriers for liver fibrosis therapy (Wang et al., 2021; Xu et al., 2022), whereas the application of CDs for treating liver fibrosis is in its infancy. In this study, novel carbon dots with tiny size (1.0–5.5 nm), zeta potential (−26.6 ± 2.65 mV), chemical composition (-C≡N, -C=O, C-O-C) and optical properties were developed from *Vaccaria Semen* carbonisata. Based on those, we evaluated the alleviation effect of VSC-CDs by using CCl_4-induced liver fibrosis model in mice and preliminarily explored the underlying mechanism.

Safety is a primary and principal issue in the development of new drugs along of clinical application. In our study, we first assessed the cytotoxicity of VSC-CDs to prepare for the study of follow-up pharmacodynamic effects. VSC-CDs showed no cytotoxicity and exhibited an excellent cell proliferation of RAW264.7 cells, while superior cytocompatibility makes VSC-CDs potential alleviation candidate drug. Hemolysis assay evaluated the blood safety of materials. VSC-CDs did not cause significant haemolysis of red blood cells. Moreover, this high hemocompatiblity of VSC-CDs does not change from 2 h to 4 h), VSC-CDs have excellent blood safety. Undoubtedly, VSC-CDs exhibit high cellular compatibility and excellent blood compatibility. This advantage serves as a prerequisite for their translation into clinical applications.

Herein, we found VSC-CDs extenuated liver injury in LF mice both in macrography and micrography. After administration for 8 consecutive weeks, VSC-CDs exhibited greater efficacy in improving weight and reducing the liver/body ratio compared to treatment with CCl_4 alone. Concurrently, liver morphology changed positively, and the destruction of hepatic cells was partly restored upon morphological and pathological observations, which might be due to VSC-CDs. To the best of our knowledge, LF is characterized by massive accumulation involved in collagens and additional ECM protein (Dinarello, 2006). Masson staining and Sirius red stained sections illustrated the area covered by collagen deposition was lessened. These results definitely attested to impairment of liver deformity and anti-fibrotic activity which matched the previous study (Khalil et al., 2021). The observed alterations in the appearance of liver tissues and pathological slices constitute evidence confirming that VSC-CDs can alleviate CCl_4-induced liver damage and mitigate liver fibrosis.

The liver was harmed by multiple pathogenic agents, which led to hepatic fibrosis. It is well-documented that an inflammatory micro-environment, oxidative stress, and excessive deposition of ECM must be orchestrated to inhibit the progress of liver fibrosis (Liu et al., 2022; Rodríguez et al., 2021). Many other studies confirmed CCl_4 induced a liver fibrosis model (liver cirrhosis), which has applied extensively by a multitude of researchers (Scholten et al., 2015; Cong et al., 2017). In addition, liver function problems, inflammation, and oxidative stress induced by CCl_4 have been identified as closely associated with liver fibrosis. In our investigations, we conducted research specifically addressing these aspects.

Serum parameters of liver function (ALT, AST, TBA, TBIL, TC) were detected. The liver enzymes (ALT, AST) and biliary index (TBA, TBIL, TC) in serum are markers of liver inflammation and necrosis in liver tissue (Mohamed et al., 2015). ALT and AST levels of animals exposed to CCl_4 in serum were significantly improved, which is in agreement with previous studies (Khalil et al., 2021). In this study, treatment with VSC-CDs downregulated the increment of ALT and AST. The metabolism of TBA and TBIL is determined by liver function (Zhao et al., 2020). CCl_4 injection increased the contents of TBA and TBIL in blood serum, which indicated liver function was damaged. Besides, the serum levels of TC were also increased due to abnormal lipid metabolism caused by CCl_4. Our results showed that VSC-CDs suppressed the release of TBA, TBIL, and TC and diminished liver damage by impairing liver function. Indeed, VSC-CDs exerted an alleviated effect on liver injury by chronic CCl_4 injection.

The inflammatory response is involved in multicellular interaction and dynamically regulated by diverse factors covering the chronic irritants of viruses, drugs, and alcohol, which caused damage to hepatocytes. Hepatocyte injury inevitably contributed to the release of inflammatory cytokines from kupffer cells, thereafter activating HSCs. During an inflammatory response, various kinds of cytokines such as TNF-α, IL-1β, and IL-6 resulted in further damage to liver tissue (Li et al., 2015; Krenkel and Tacke, 2017). Serum TNF-α, IL-1β, and IL-6 concentrations in mice with CCl_4-induced liver fibrosis were increased in our study, which coincided with the assay results of inflammatory factors in previous studies (Zhao et al., 2017; Abdelghffar et al., 2022). The role of VSC-CDs inhibited the expression of inflammatory mediators to regulate the inflammatory microenvironment within the liver and resist the activation of HSCs. Altogether, VSC-CDs exhibited anti-inflammation properties and alleviated some effects of chronic hepatic injury.

Oxidative stress is another indispensable factor related to liver fibrosis. In reference to previously discovered results (Brenner et al., 2013; Luedde et al., 2014), CCl_4-induction gives rise to oxidative imbalance and oxidative stress damage. To our knowledge, the liver depends on defense mechanisms (antioxidant systems) to mitigate liver attack from reactive oxygen species (ROS); some antioxidants including SOD and GSH effectively scavenge free radicals (Han et al., 2017). Our results showed redox imbalance and decreased vitality of SOD and GSH occurred in CCl_4-treated groups, which is consistent with similar liver fibrosis model (Zhang et al., 2018; Liu et al., 2021), while VSC-CDs could eliminate oxygen-free radicals to reduce oxidative stress damage. MDA, the product of liver oxidative mutilation and lipid peroxidation, was significantly raised in CCl_4-induced groups, exerting severe damage to an antioxidant defense system. MDA content was greatly reduced after treatment with VSC-CDs. In conclusion, extenuating oxidative stress damage is a potential mechanism of anti-hepatic fibrosis in VSC-CDs treatment.

Exposure to CCl_4 also provoked the activation of the TGF-β/Smad signaling pathway. The production of TGF-β_1, as the main transforming growth factor isoform associated with liver fibrosis, facilitates transcription of Smad target genes (Paz and Shoenfeld, 2010). After the Smad signaling pathway was activated, phosphorylated Smad 2/3 complex binds with $Smad_4$, which was translocated to the nucleus to regulate expression of target genes (Dooley et al., 2001). TGF-β_1 and Smad3 levels were diminished via the modulation of VSC-CDs. Our study also validated VSC-CDs prevented the formation of ECM and aggravation of liver fibrosis. COI1 is one of the primary sources of excessive deposition of extracellular matrix materials, which forms fibrous scar tissues that replaces damaged normal tissue and ultimately compromises normal liver function (Li and Zhu, 2022). Notably, VSC-CDs reduced the production of COI1 in liver tissues. α-SMA, as a specific marker for HSCs activation, could be implicated in the TGF-β/Smad signaling pathway (Mao et al., 2015). α-SMA expressions was obviously upregulated under the stimulus of CCl_4, indicating the activation and proliferation of HSCs, showing reduction after treatment of VSC-CDs. These results implied the inhibition effect of the TGF-β/Smad signaling may be a latent key mechanism in liver fibrosis.

In conclusion, we have developed an eco-friendly and safe carbon dot derived from traditional Chinese medicine that is characterized by an ultra-small particle size, distinctive fluorescence characteristics, and abundant functional groups on the surface. VSC-CDs have demonstrated the ability to partially reverse liver damage, inhibit inflammatory response and oxidative stress, and alleviate liver fibrosis. The potential mechanism involves the modulation of the TGF-β/Smad signaling pathway. These affirmative results suggest that VSC-CDs hold potential for clinical applications and exhibit promising prospects.

Conclusion

In summary, novel fluorescent carbon dots were prepared with a green and eco-friendly method, and we conducted a comprehensive characterization of their morphological structure. They possessed desirable biocompatibility, low cytotoxicity, and high blood safety. Importantly, VSC-CDs demonstrated a mitigating effect on CCl_4-induced liver fibrosis, as evidenced by the reduction in inflammatory cytokines (TNF-α, IL-6, IL-1β), elevation in antioxidant levels (SOD and GSH), and a decrease in lipid metabolites (MDA) to counteract oxidative stress damage. Furthermore, VSC-CDs demonstrated the ability to modulate the TGF-β/Smad signaling pathway and regulate the protein expressions of α-SMA and COI1, thereby inhibiting the progression of liver fibrosis. The above results highlight the underlying mechanism of action against liver fibrosis, laying a foundation for the development and application of carbon-based medicine. We propose that the safer and environmentally friendly VSC-CDs offer a promising avenue for the development of anti-liver fibrosis drugs.

Data availability statement

The original contributions presented in the study are included in the article/Supplementary material, further inquiries can be directed to the corresponding authors.

Ethics statement

The animal study was approved by the Ethics Review Committee of Animal Experimentation of the Beijing University of Traditional Chinese Medicine. The study was conducted in accordance with the local legislation and institutional requirements.

Author contributions

YZ: Conceptualization, Conceptualization, Supervision, Validation, Writing–original draft, Writing–review and editing. ED: Investigation, Project administration, Visualization, Writing–original draft, Writing–review and editing. LD: Data curation, Methodology, Project administration, Visualization. JY: Formal Analysis, Software, Validation, Writing–review and editing. YZ: Investigation, Methodology, Visualization, Writing–review and editing. TW: Resources, Software, Validation, Writing–review and editing. RK: Data curation, Writing–review and editing. ML: Data curation, Project administration, Supervision, Writing–review and editing. SW: Software, Supervision, Writing–review and editing. LZ: Software, Supervision, Validation, Writing–review and editing. YY: Data curation, Methodology, Visualization, Writing–review and editing. HK: Conceptualization, Resources, Supervision, Writing–review and editing. YZ: Conceptualization, Funding acquisition, Resources, Supervision, Writing–review and editing. HQ: Conceptualization, Resources, Validation, Visualization, Writing–review and editing.

Funding

The author(s) declare financial support was received for the research, authorship, and/or publication of this article. This work was supported by the Grant for Qihuang Scholars of the State Administration of Traditional Chinese Medicine, Special Funds for Fundamental Research Expenses of Central Universities (2019-JYB-TD-001). We are extremely grateful to the Classical Prescription Basic Research Team of the Beijing University of Chinese Medicine.

Conflict of interest

The authors declare that the research was conducted in the absence of any commercial or financial relationships that could be construed as a potential conflict of interest.

Publisher’s note

References

Abdelghffar, E. A., Obaid, W. A., Alamoudi, M. O., Mohammedsaleh, Z. M., Annaz, H., Abdelfattah, M. A. O., et al. (2022). Thymus fontanesii attenuates CCl_4-induced oxidative stress and inflammation in mild liver fibrosis. *Biomed. Pharmacother.* 148, 112738. doi:10.1016/j.biopha.2022.112738

Bataller, R., and Brenner, D. A. (2005). Liver fibrosis. *J. Clin. Invest.* 115 (2), 209–218. doi:10.1172/JCI24282

Belza, J., Opletalová, A., and Poláková, K. (2021). Carbon dots for virus detection and therapy. *Mikrochim. Acta* 188 (12), 430. doi:10.1007/s00604-021-05076-6

Boey, A., Leong, S. Q., Bhave, S., and Ho, H. K. (2021). Cerium oxide nanoparticles alleviate hepatic fibrosis phenotypes *in vitro*. *Int. J. Mol. Sci.* 22 (21), 11777. doi:10.3390/ijms222111777

Brenner, C., Galluzzi, L., Kepp, O., and Kroemer, G. (2013). Decoding cell death signals in liver inflammation. *J. Hepatol.* 59 (3), 583–594. doi:10.1016/j.jhep.2013.03.033

Cai, R., Xiao, L., Liu, M., Du, F., and Wang, Z. (2021). Recent advances in functional carbon quantum dots for antitumour. *Int. J. Nanomedicine* 16, 7195–7229. doi:10.2147/IJN.S334012

Cheng, D., Chai, J., Wang, H., Fu, L., Peng, S., and Ni, X. (2021). Hepatic macrophages: key players in the development and progression of liver fibrosis. *Liver Int.* 41 (10), 2279–2294. doi:10.1111/liv.14940

Cheng, J., Zhang, M., Sun, Z., Lu, F., Xiong, W., Luo, J., et al. (2019). Hemostatic and hepatoprotective bioactivity of Junci Medulla carbonisata-derived carbon dots. *Nanomedicine (Lond).* 14 (4), 431–446. doi:10.2217/nnm-2018-0285

Cong, M., Zhao, W., Liu, T., Wang, P., Fan, X., Zhai, Q., et al. (2017). Protective effect of human serum amyloid P on CCl4-induced acute liver injury in mice. *Int. J. Mol. Med.* 40 (2), 454–464. doi:10.3892/ijmm.2017.3028

Cornu, R., Béduneau, A., and Martin, H. (2020). Influence of nanoparticles on liver tissue and hepatic functions: a review. *Toxicology* 430, 152344. doi:10.1016/j.tox.2019.152344

Deng, Y., Xia, B., Chen, Z., Wang, F., Lv, Y., and Chen, G. (2022). Stem cell-based therapy strategy for hepatic fibrosis by targeting intrahepatic cells. *Stem Cell Rev. Rep.* 18 (1), 77–93. doi:10.1007/s12015-021-10286-9

Dinarello, C. A. (2006). Interleukin 1 and interleukin 18 as mediators of inflammation and the aging process. *Am. J. Clin. Nutr.* 83 (2), 447S-455S–455S. doi:10.1093/ajcn/83.2.447S

Dogra, P., Adolphi, N. L., Wang, Z., Lin, Y. S., Butler, K. S., Durfee, P. N., et al. (2018). Establishing the effects of mesoporous silica nanoparticle properties on *in vivo* disposition using imaging-based pharmacokinetics. *Nat. Commun.* 9 (1), 4551. doi:10.1038/s41467-018-06730-z

Dooley, S., Delvoux, B., Streckert, M., Bonzel, L., Stopa, M., ten Dijke, P., et al. (2001). Transforming growth factor beta signal transduction in hepatic stellate cells via Smad2/3 phosphorylation, a pathway that is abrogated during *in vitro* progression to myofibroblasts. TGFbeta signal transduction during transdifferentiation of hepatic stellate cells. *FEBS Lett.* 502 (1-2), 4–10. doi:10.1016/s0014-5793(01)02656-4

Gong, L., Lei, Y., Liu, Y., Tan, F., Li, S., Wang, X., et al. (2019). Vaccarin prevents ox-LDL-induced HUVEC EndMT, inflammation and apoptosis by suppressing ROS/p38 MAPK signaling. *Am. J. Transl. Res.* 11 (4), 2140–2154.

Han, X.-Y., Hu, J.-N., Wang, Z., Wei, S. N., Zheng, S. W., Wang, Y. P., et al. (2017). 5-HMF attenuates liver fibrosis in CCl4-plus-alcohol-induced mice by suppression of oxidative stress. *J. Nutr. Sci. Vitaminol. (Tokyo)* 63 (1), 35–43. doi:10.3177/jnsv.63.35

Han, Y., Chen, Y., Wang, N., and He, Z. (2019). Magnesium doped carbon quantum dots synthesized by mechanical ball milling and displayed Fe3+ sensing. *Mater. Technol.* 34 (6), 336–342. doi:10.1080/10667857.2018.1556469

Havrdova, M., Hola, K., Skopalik, J., Tomankova, K., Zboril, R., Cepe, K., et al. (2016). Toxicity of carbon dots – effect of surface functionalization on the cell viability, reactive oxygen species generation and cell cycle. *Carbon* 99, 238–248. doi:10.1016/j.carbon.2015.12.027

Hou, T., Guo, Y., Han, W., Zhou, Y., Netala, V. R., Li, H., et al. (2023). Exploring the biomedical applications of biosynthesized silver nanoparticles using perilla frutescens flavonoid extract: antibacterial, antioxidant, and cell toxicity properties against colon cancer cells. *Molecules* 28 (17), 6431. doi:10.3390/molecules28176431

Hu, Z., Song, B., Xu, L., Zhong, Y., Peng, F., Ji, X., et al. (2016). Aqueous synthesized quantum dots interfere with the NF-κB pathway and confer anti-tumor, anti-viral and anti-inflammatory effects. *Biomaterials* 108, 187–196. doi:10.1016/j.biomaterials.2016.08.047

Huang, C., Zhou, Y., Cheng, J., Guo, X., Shou, D., Quan, Y., et al. (2023). Pattern recognition receptors in the development of nonalcoholic fatty liver disease and progression to hepatocellular carcinoma: an emerging therapeutic strategy. *Front. Endocrinol. (Lausanne).* 14, 1145392. doi:10.3389/fendo.2023.1145392

Humaera, N. A., Fahri, A. N., Armynah, B., and Tahir, D. (2021). Natural source of carbon dots from part of a plant and its applications: a review. *Luminescence* 36 (6), 1354–1364. doi:10.1002/bio.4084

Khalil, M. R., El-Demerdash, R. S., Elminshawy, H. H., Mehanna, E. T., Mesbah, N. M., and Abo-Elmatty, D. M. (2021). Therapeutic effect of bone marrow mesenchymal stem cells in a rat model of carbon tetrachloride induced liver fibrosis. *Biomed. J.* 44 (5), 598–610. doi:10.1016/j.bj.2020.04.011

Krenkel, O., and Tacke, F. (2017). Liver macrophages in tissue homeostasis and disease. *Nat. Rev. Immunol.* 17 (5), 306–321. doi:10.1038/nri.2017.11

Kumar, P., Dua, S., Kaur, R., Kumar, M., and Bhatt, G. (2022). A review on advancements in carbon quantum dots and their application in photovoltaics. *RSC Adv.* 12, 4714–4759. doi:10.1039/d1ra08452f

Kumar, S., Duan, Q., Wu, R., Harris, E. N., and Su, Q. (2021). Pathophysiological communication between hepatocytes and non-parenchymal cells in liver injury from NAFLD to liver fibrosis. *Adv. Drug Deliv. Rev.* 176, 113869. doi:10.1016/j.addr.2021.113869

Li, L., and Zhu, Z. (2022). Pharmacological modulation of ferroptosis as a therapeutic target for liver fibrosis. *Front. Pharmacol.* 13, 1071844. doi:10.3389/fphar.2022.1071844

Li, Y., Zeng, R., Chen, J., Wu, Y. b., Chou, G. x., Gao, Y., et al. (2015). Pharmacokinetics and metabolism study of isoboldine, a major bioactive component from Radix Linderae in male rats by UPLC-MS/MS. *J. Ethnopharmacol.* 171, 154–160. doi:10.1016/j.jep.2015.05.042

Liang, X., Wang, H., Zhu, Y., Zhang, R., Cogger, V. C., Liu, X., et al. (2016). Short- and long-term tracking of anionic ultrasmall nanoparticles in kidney. *ACS Nano* 10 (1), 387–395. doi:10.1021/acsnano.5b05066

Liu, L., Guo, H.-B., Shao, C.-P., et al. (2022). Shugan Huoxue Huayu Fang attenuates carbon tetrachloride-induced hepatic fibrosis in rats by inhibiting transforming growth factor-β1/Smad signaling. *J. Tradit. Chin. Med.* 42 (1), 65–72. doi:10.19852/j.cnki.jtcm.20210624.001

Liu, M. L., Chen, B. B., Li, C. M., and Huang, C. Z. (2019). Carbon dots: synthesis, formation mechanism, fluorescence origin and sensing applications. *Green Chem.* 21 (3), 449–471. doi:10.1039/c8gc02736f

Liu, X., Liu, W., Ding, C., Zhao, Y., Chen, X., Ling, D., et al. (2021). Taxifolin, extracted from waste *Larix olgensis* roots, attenuates CCl_4-induced liver fibrosis by regulating the PI3K/AKT/mTOR and TGF-β1/smads signaling pathways. *Drug Des. Devel Ther.* 15, 871–887. doi:10.2147/DDDT.S281369

Luedde, T., Kaplowitz, N., and Schwabe, R. F. (2014). Cell death and cell death responses in liver disease: mechanisms and clinical relevance. *Gastroenterology* 147 (4), 765–783. doi:10.1053/j.gastro.2014.07.018

Luo, W.-K., Zhang, L.-L., Yang, Z.-Y., Guo, X. H., Wu, Y., Zhang, W., et al. (2021). Herbal medicine derived carbon dots: synthesis and applications in therapeutics, bioimaging and sensing. *J. Nanobiotechnology* 19 (1), 320. doi:10.1186/s12951-021-01072-3

Mansuriya, B. D., and Altintas, Z. (2021). Carbon dots: classification, properties, synthesis, characterization, and applications in Health care-an updated review (2018-2021). *Nanomater. (Basel)* 11 (10), 2525. doi:10.3390/nano11102525

Mao, Y., Zhang, S., Yu, F., Guo, C., and Fan, X. (2015). Ghrelin attenuates liver fibrosis through regulation of TGF-β1 expression and autophagy. *Int. J. Mol. Sci.* 16 (9), 21911–21930. doi:10.3390/ijms160921911

Mehta, V. N., Jha, S., Basu, H., Singhal, R. K., and Kailasa, S. K. (2015). One-step hydrothermal approach to fabricate carbon dots from apple juice for imaging of mycobacterium and fungal cells. *Sensors Actuators B Chem.* 213, 434–443. doi:10.1016/j.snb.2015.02.104

Mohamed, H., Elswefy, S., Rashed, L. A., et al. (2015). Cholestatic liver fibrosis in a rat model of bile duct ligation: evaluating biochemical versus histopathological changes. *Int. J. Pharm. Pharm. Sci.* 7, 349–354.

Mu, X., Wu, M., Zhang, B., Liu, X., Xu, S., Huang, Y., et al. (2021). A sensitive "off-on" carbon dots-Ag nanoparticles fluorescent probe for cysteamine detection via the inner filter effect. *Talanta* 221, 121463. doi:10.1016/j.talanta.2020.121463

Paz, Z., and Shoenfeld, Y. (2010). Antifibrosis: to reverse the irreversible. *Clin. Rev. Allergy Immunol.* 38 (2-3), 276–286. doi:10.1007/s12016-009-8157-7

Pellicano, R., Ferro, A., Cicerchia, F., Mattivi, S., Fagoonee, S., and Durazzo, M. (2023). Autoimmune hepatitis and fibrosis. *J. Clin. Med.* 12 (5), 1979. doi:10.3390/jcm12051979

Ramanarayanan, R., and Swaminathan, S. (2020). Synthesis and characterisation of green luminescent carbon dots from guava leaf extract. *Mater. Today Proc.* 33, 2223–2227. doi:10.1016/j.matpr.2020.03.805

Ren, L., Li, J., Liu, L., Wu, W., Zhao, D., Zhang, K., et al. (2021). Resolving hepatic fibrosis *via* suppressing oxidative stress and an inflammatory response using a novel hyaluronic acid modified nanocomplex. *Biomater. Sci.* 9 (24), 8259–8269. doi:10.1039/d1bm01499d

Rodríguez, M. J., Sabaj, M., Tolosa, G., Herrera Vielma, F., Zúñiga, M. J., González, D. R., et al. (2021). Maresin-1 prevents liver fibrosis by targeting Nrf2 and NF-κB, reducing oxidative stress and inflammation. *Cells* 10 (12), 3406. doi:10.3390/cells10123406

Scholten, D., Trebicka, J., Liedtke, C., and Weiskirchen, R. (2015). The carbon tetrachloride model in mice. *Lab. Anim.* 49 (1), 4–11. doi:10.1177/0023677215571192

Seitz, T., and Hellerbrand, C. (2021). Role of fibroblast growth factor signalling in hepatic fibrosis. *Liver Int.* 41 (6), 1201–1215. doi:10.1111/liv.14863

Shi, L., Zhao, B., Li, X., Zhang, G., Zhang, Y., Dong, C., et al. (2017). Green-fluorescent nitrogen-doped carbon nanodots for biological imaging and paper-based sensing. *Anal. Methods* 9 (14), 2197–2204. doi:10.1039/c7ay00163k

Singh, S., Sharma, N., Shukla, S., Behl, T., Gupta, S., Anwer, M. K., et al. (2023). Understanding the potential role of nanotechnology in liver fibrosis: a paradigm in therapeutics. *Molecules* 28 (6), 2811. doi:10.3390/molecules28062811

Sun, H., Cai, W., Wang, X., Liu, Y., Hou, B., Zhu, X., et al. (2017). Vaccaria hypaphorine alleviates lipopolysaccharide-induced inflammation via inactivation of NFκB and ERK pathways in Raw 264.7 cells. *BMC Complement. Altern. Med.* 17 (1), 120. doi:10.1186/s12906-017-1635-1

Tang, Z., Li, X., Tian, L., Sun, Y., Zhu, X., and Liu, F. (2023). Mesoporous polydopamine based biominetic nanodrug ameliorates liver fibrosis via antioxidation and TGF-β/SMADS pathway. *Int. J. Biol. Macromol.* 248, 125906. doi:10.1016/j.ijbiomac.2023.125906

Truskewycz, A., Yin, H., Halberg, N., Lai, D. T. H., Ball, A. S., Truong, V. K., et al. (2022). Carbon dot therapeutic platforms: administration, distribution, metabolism, excretion, toxicity, and therapeutic potential. *Small* 18 (16), e2106342. doi:10.1002/smll.202106342

Vyas, K., and Patel, M. M. (2023). Insights on drug and gene delivery systems in liver fibrosis. *Asian J. Pharm. Sci.* 18 (2), 100779. doi:10.1016/j.ajps.2023.100779

Wang, H., Thorling, C. A., Liang, X., Bridle, K. R., Grice, J. E., Zhu, Y., et al. (2015). Diagnostic imaging and therapeutic application of nanoparticles targeting the liver. *J. Mater Chem. B* 3 (6), 939–958. doi:10.1039/c4tb01611d

Wang, N., Li, X., Zhong, Z., Qiu, Y., Liu, S., Wu, H., et al. (2021). 3D hESC exosomes enriched with miR-6766-3p ameliorates liver fibrosis by attenuating activated stellate cells through targeting the TGFβRII-SMADS pathway. *J. Nanobiotechnology* 19 (1), 437. doi:10.1186/s12951-021-01138-2

Wang, X., Zhang, Y., Kong, H., Cheng, J., Zhang, M., Sun, Z., et al. (2020). Novel mulberry silkworm cocoon-derived carbon dots and their anti-inflammatory properties. *Artif. Cells Nanomed Biotechnol.* 48 (1), 68–76. doi:10.1080/21691401.2019.1699810

Wang, Z.-X., Wang, Z., and Wu, F.-G. (2022). Carbon dots as drug delivery vehicles for antimicrobial applications: a minireview. *ChemMedChem* 17 (13), e202200003. doi:10.1002/cmdc.202200003

Wei, X., Li, L., Liu, J., Yu, L., Li, H., Cheng, F., et al. (2019). Green synthesis of fluorescent carbon dots from gynostemma for bioimaging and antioxidant in zebrafish. *ACS Appl. Mater Interfaces* 11 (10), 9832–9840. doi:10.1021/acsami.9b00074

Xu, Y., Chen, J., Jiang, W., Zhao, Y., Yang, C., Wu, Y., et al. (2022). Multiplexing nanodrug ameliorates liver fibrosis via ROS elimination and inflammation suppression. *Small* 18 (3), e2102848. doi:10.1002/smll.202102848

Yan, J., Hou, S., Yu, Y., Qiao, Y., Xiao, T., Mei, Y., et al. (2018). The effect of surface charge on the cytotoxicity and uptake of carbon quantum dots in human umbilical cord derived mesenchymal stem cells. *Colloids Surf. B Biointerfaces* 171, 241–249. doi:10.1016/j.colsurfb.2018.07.034

Yan, X., Zhao, Y., Luo, J., Xiong, W., Liu, X., Cheng, J., et al. (2017). Hemostatic bioactivity of novel Pollen Typhae Carbonisata-derived carbon quantum dots. *J. Nanobiotechnology* 15 (1), 60. doi:10.1186/s12951-017-0296-z

Yang, F., Li, H., Li, Y., Hao, Y., Wang, C., Jia, P., et al. (2021). Crosstalk between hepatic stellate cells and surrounding cells in hepatic fibrosis. *Int. Immunopharmacol.* 99, 108051. doi:10.1016/j.intimp.2021.108051

You, H., Wang, X., Ma, L., Zhang, F., Zhang, H., Wang, Y., et al. (2023). Insights into the impact of hepatitis B virus on hepatic stellate cell activation. *Cell Commun. Signal* 21 (1), 70. doi:10.1186/s12964-023-01091-7

Yuan, X. H., Fu, L. N., Gu, C. B., Zhang, Y. D., and Fu, Y. J. (2014). Microwave-assisted extraction and antioxidant activity of vaccarin from the seeds of Vaccaria segetalis. *Sep. Purif. Technol.* 133, 91–98. doi:10.1016/j.seppur.2014.06.002

Zhang, C.-Y., Liu, S., and Yang, M. (2023). Antioxidant and anti-inflammatory agents in chronic liver diseases: molecular mechanisms and therapy. *World J. Hepatol.* 15 (2), 180–200. doi:10.4254/wjh.v15.i2.180

Zhang, J., Yang, A., Wu, Y., Guan, W., Xiong, B., Peng, X., et al. (2018). Stachydrine ameliorates carbon tetrachloride-induced hepatic fibrosis by inhibiting inflammation, oxidative stress and regulating MMPs/TIMPs system in rats. *Biomed. Pharmacother.* 97, 1586–1594. doi:10.1016/j.biopha.2017.11.117

Zhang, M., Cheng, J., Zhang, Y., Kong, H., Wang, S., Luo, J., et al. (2020). Green synthesis of Zingiberis rhizoma-based carbon dots attenuates chemical and thermal stimulus pain in mice. *Nanomedicine (Lond)* 15 (9), 851–869. doi:10.2217/nnm-2019-0369

Zhang, Y.-N., Poon, W., Tavares, A. J., McGilvray, I. D., and Chan, W. C. W. (2016b). Nanoparticle-liver interactions: cellular uptake and hepatobiliary elimination. *J. Control Release* 240, 332–348. doi:10.1016/j.jconrel.2016.01.020

Zhang, Z., Guo, M., Zhao, S., Shao, J., and Zheng, S. (2016a). ROS-JNK1/2-dependent activation of autophagy is required for the induction of anti-inflammatory effect of dihydroartemisinin in liver fibrosis. *Free Radic. Biol. Med.* 101, 272–283. doi:10.1016/j.freeradbiomed.2016.10.498

Zhao, L., Wu, D., Sang, M., Xu, Y., Liu, Z., and Wu, Q. (2017). Stachydrine ameliorates isoproterenol-induced cardiac hypertrophy and fibrosis by suppressing inflammation and oxidative stress through inhibiting NF-κB and JAK/STAT signaling pathways in rats. *Int. Immunopharmacol.* 48, 102–109. doi:10.1016/j.intimp.2017.05.002

Zhao, X., Amevor, F. K., Xue, X., Wang, C., Cui, Z., Dai, S., et al. (2023). Remodeling the hepatic fibrotic microenvironment with emerging nanotherapeutics: a comprehensive review. *J. Nanobiotechnology* 21 (1), 121. doi:10.1186/s12951-023-01876-5

Zhao, Y., Li, Y., Chen, Y., et al. (2021). Discovery of *Vaccaria Segetalis Carbonisatum* nano-components and their hepatoprotective effect. *Chin. Traditional Herb. Drugs* 52 (22), 6825–6833. doi:10.7501/j.issn.0253-2670.2021.22

Zhao, Y., Zhang, Y., Kong, H., Zhang, M., Cheng, J., Wu, J., et al. (2020). Carbon dots from Paeoniae Radix Alba carbonisata: hepatoprotective effect. *Int. J. Nanomedicine* 15, 9049–9059. doi:10.2147/IJN.S281976

Frontiers in Bioengineering and Biotechnology

TYPE Review
PUBLISHED 14 December 2023
DOI 10.3389/fbioe.2023.1292641

OPEN ACCESS

EDITED BY
Md Palashuddin Sk,
Aligarh Muslim University, India

REVIEWED BY
Sadhucharan Mallick,
Indira Gandhi National Tribal University,
India
Alessandra Quarta,
National Research Council (CNR), Italy
Mohammad Ehtisham Khan,
Jazan University, Saudi Arabia

*CORRESPONDENCE
Ihsan Ullah,
ihsanmtk@uswat.edu.pk,
ihsanmtk@yahoo.com
Muhammad Omer,
omermarwat@hotmail.com

RECEIVED 11 September 2023
ACCEPTED 20 November 2023
PUBLISHED 14 December 2023

CITATION
Ullah I, Suliman H, Alamzeb M, Abid O-U-R, Sohail M, Ullah M, Haleem A and Omer M (2023), An insight into recent developments of copper, silver and gold carbon dots: cancer diagnostics and treatment.
Front. Bioeng. Biotechnol. 11:1292641.
doi: 10.3389/fbioe.2023.1292641

An insight into recent developments of copper, silver and gold carbon dots: cancer diagnostics and treatment

Ihsan Ullah[1]*, Hazrat Suliman[1], Muhammad Alamzeb[2], Obaid-Ur-Rahman Abid[3], Muhammad Sohail[1], Mohib Ullah[4], Abdul Haleem[5] and Muhammad Omer[1]*

[1]Institute of Chemical Sciences, University of Swat, Swat, Pakistan, [2]Department of Chemistry, University of Kotli, Kotli, Pakistan, [3]Department of Chemistry, Hazara University, Mansehra, Pakistan, [4]Department of Chemistry, Balochistan University of Information Technology Engineering and Management Sciences (BUITEMS), Takatu Campus, Quetta, Pakistan, [5]School of Chemistry and Chemical Engineering, Jiangsu University, Zhenjiang, China

Cancer is one of the most fatal diseases globally, however, advancement in the field of nanoscience specifically novel nanomaterials with nano-targeting of cancer cell lines has revolutionized cancer diagnosis and therapy and has thus attracted the attention of researchers of related fields. Carbon Dots (CDs)–C-based nanomaterials–have emerged as highly favorable candidates for simultaneous bioimaging and therapy during cancer nano-theranostics due to their exclusive innate FL and theranostic characteristics exhibited in different preclinical results. Recently, different transition metal-doped CDs have enhanced the effectiveness of CDs manifold in biomedical applications with minimum toxicity. The use of group-11 (Cu, Ag and Au) with CDs in this direction have recently gained the attention of researchers because of their encouraging results. This review summarizes the current developments of group-11 (Cu, Ag and Au) CDs for early diagnosis and therapy of cancer including their nanocomposites, nanohybrids and heterostructures etc. All The manuscript highlights imaging applications (FL, photoacoustic, MRI etc.) and therapeutic applications (phototherapy, photodynamic, multimodal etc.) of Cu-, Ag- and Au-doped CDs reported as nanotheranostic agents for cancer treatment. Sources of CDs and metals alogwith applications to give a comparative analysis have been given in the tabulated form at the end of manuscript. Further, future prospects and challenges have also been discussed.

KEYWORDS

cancer, nanotheranostics, bioimaging, phototherapy, doped carbon dots

---

Abbreviations: CDs, Carbon Dots; NPs, Nanoparticles; NSs, Nanosheets, Nanospheres; NCs, Nanocomposites; FL, Fluorescence; FI, Fluorescence Imaging; PA, Photoacoustic; PT, Phototherapy, Photothermal; CT, Chemotherapy; PTT, Photothermal Therapy; PDT, Photodynamic Therapy; CDT, Chemo dynamic Therapy; PTA, Photothermal ablation, Photothermal agent; AAS, Atomic absorption spectroscopy; NIR, Near infrared; GSH, glutathione; CBQD, Chlorophyll rich biomass quantum dots; PGA, poly glutamic acid; Cys, Cysteamine, Cysteine; LOD, Limit of Detection; ECL, Electrochemiluminescence; PEG, polyethylene glycol; MCs, multicellular spheroids; ROS, Reactive Oxygen Specie; EDTA, Ethylene diamine tetraacetic acid; MTT, methyl thiazolyltetrazolium.

1 Introduction

Cancer is the second biggest cause of human deaths after cardiovascular diseases (Bray et al., 2018). Even though significant advancement in cancer treatment has been achieved recently, however, aggressive breast-, lung- and pancreatic tumors with low survival rate suggests many efforts to be undertaken (Leonardi et al., 2018). Millions of people are diagnosed with cancer every year most oftenly in the last stages of this disease. Therefore, for effective cancer treatment timely and correct diagnosis is of crucial importance. Majority of anticancer drugs that are generally recommended for tumor enucleation induce terrible damage not only to the cancer cells, but also to other normal cells (Sunbal et al., 2023). One of the most important areas of cancer research is to improve and enhance the targeting efficacy of anticancer drugs over cancer cell lines. Recently, in this direction novel nanomaterials have aided in targeting cancer cells with overall low dosage, higher efficacy, minimal side effects and improved patients' life quality (Khan et al., 2022; Ullah et al., 2022).

Nowadays, nanotechnology has emerged as a key player in cancer treatment and therefore different nanomaterials are studied for successful and improved imaging, sensing, drug delivery, therapy of cancer cell lines (Nocito et al., 2021; Ali et al., 2022). Like other nanomaterials, C-based quantum NPs have also the ability to refurbish cell fate, prevent or induce mutations, trigger cell–cell communication and revamp cell structure in a fashion required mainly during the phenomena at the bio-nano interface (Naik et al., 2022).

Since their accidental discovery in 2004, CDs have found huge biomedical applications due to their wide choice of precursors, low cost, facile synthesis, exceptional biocompatibility, fairly high shelf life, easy and tunable surface passivation, exclusive physical and optical properties, low or either nontoxicity, up-conversion photoluminescence and excitation wavelength-dependent FL emission in comparison to other carbon nanomaterials (Tejwan et al., 2021). Further, their enhanced photostability and brilliant PL intensity gives them superiority over other available semiconductor quantum dots (Hadad et al., 2021).

CDs can be easily and immediately excreted from the body through urine. With a neutral surface charge and hydrodynamic diameter of less than 5.5 nm carbon dots can efficiently pass through glomerular filtration without any harmful aggregation in spleen or liver (Nie, 2010; Pal et al., 2020). Due to these unique and state-of-the-art features, they are potential candidates in cancer treatment and have been successfully used in bioimaging, as a nano-drug carrier, drug and gene delivery and photothermal and photodynamic therapy etc (Kaurav et al., 2023). It has also been noted that all these properties of CDs are mainly dependent on the sources used, synthesis routes and it has been proved that these properties can be enhanced by surface modification and doping (Fang et al., 2017).

Recently, the development of heteroatom-doped Carbon Dots has gained enormous attention. Several non-metallic heteroatoms (N, S, P, B, F, etc.) as well as metallic heteroatoms (Ag, Au, Cu, Co, Fe, Ga, Gd, Mg, Mo, Ni, Sn, Zn, etc.) as dopants to increase the physicochemical properties of CDs. Some of these metals are essential elements for human body like Fe, Cu and Zn etc. while others like Au, Ag, Ga, La, etc. are eco-friendly and less toxic in nature making them potential dopants for CDs owing to their biomedical usefulness (Khera et al., 2010; Ullah et al., 2011a; Nawaz et al., 2011; Nawaz et al., 2012; Tejwan et al., 2021). These metal-doped carbon dots excrete very rapidly within 10 min post-injection through urine with complete elimination from body within 24 h in mice whether either administered through intramuscular, intravenous and subcutaneous injection routes (Huang et al., 2013).

As metals have larger atomic radius, better electron donation and higher number of unoccupied orbitals than non-metal heteroatoms therefore, metal ions doping could alter the electronic structure of CDs. This changes the HOMO-LUMO energy gap which shifts the FL from blue to red emission that determines the improved photo-optical and physicochemical properties of metal-functionalized doped carbon dots as compared with non-metallic heteroatom doping (Ullah et al., 2009; Ahmad Khera et al., 2010; Ullah et al., 2010a; Ibad et al., 2010; Ullah et al., 2011b; Ali et al., 2013; Hassan et al., 2013; Yue et al., 2023). In comparison to pristine carbon-dots the metal-functionalized CDs show intense optical absorbance in the visible region due to charge-transfer absorbance while enhanced FL is observed due to surface plasmonic resonance (SPR) of metal NPs (Sun et al., 2019).

Metal-doping of CDs generates new emission energy traps that brings about structural changes in carbon dots and better electron-hole purging which results in excellent quantum yield of CDs. As a result, multicolor emission under single excitation wavelength of 365 nm such as deep ultraviolet, blue, blue-green, green, yellow etc. is obtained (Zhai et al., 2018; Arshad and Sk, 2020). Metal doping also enhances the possibility for effective binding with redox species due to better charge distribution and spin density (Kar et al., 2023).

The biological and medicinal importance of group-11 metals (Copper (Safaei and Howell, 2005; Farrer and Sadler, 2008; Ali et al., 2009; Ullah et al., 2010b; Scheiber et al., 2013), Silver (George et al., 1997; Chopra, 2007; Soumya and Hela, 2013) and Gold (El-Sayed et al., 2005; Rosi et al., 2006; Dhar et al., 2009; Raubenheimer and Schmidbaur, 2014)) is well recognized. Apart from their medicinal importance these metals have high electrical conductivity and better electron-donating/accepting potential which makes them useful dopants resulting in comparatively enhanced applications of CDs (Jiao et al., 2022). Although some reviews have reported physical, chemical and biomedical applications of metal/non-metal-doped CDs. However, no such review is available on biomedical applications of Cu-, Ag- and Au-doped/hybrid CDs especially on cancer imaging, diagnosis and therapy. This review highlights imaging applications (FL, PA, MRI etc.) and therapeutic applications (phototherapy, photodynamic, multimodal etc.) of Cu-, Ag- and Au-doped CDs reported as nanotheranostic agents for cancer treatment. Further, future prospects and challenges have also been discussed at the end of manuscript.

2 Biomedical applications

The most encouraging applications of CDs have been reported in biomedicine. With no phenomenal signs of inflammation in rats (Nekoueian et al., 2019), the applications of CDs for cancer treatment has gained momentum in recent days.

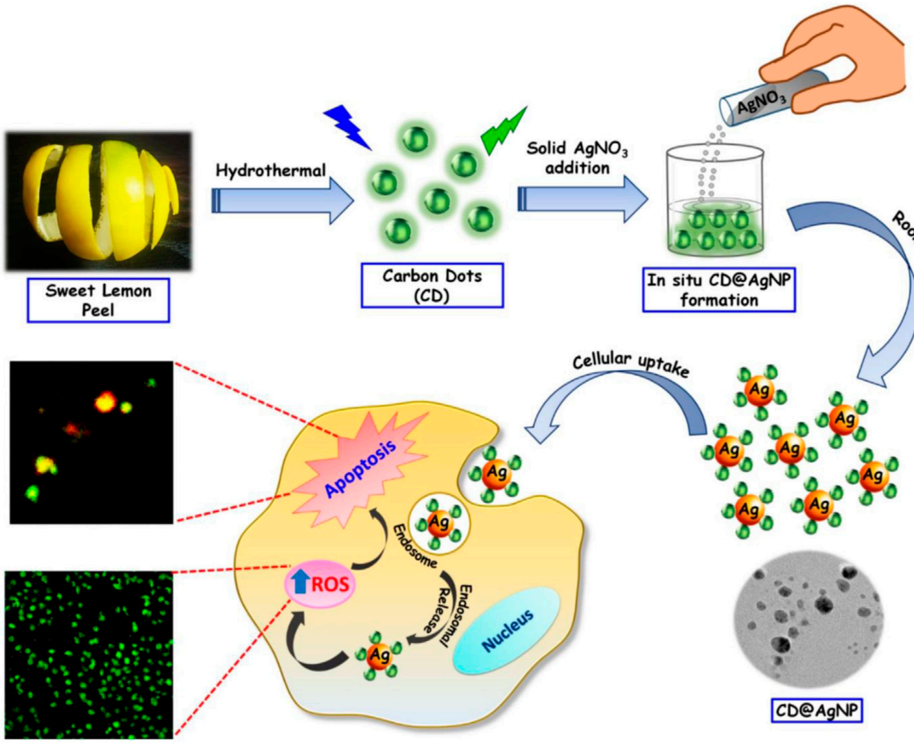

FIGURE 1
Representative Schematic presentation of group-11-CDs nanocomposites indicating stages of synthesis and applications (Ghosal et al., 2020): CD@AgNPs synthesis with their probable cellular activity toward breast cancer cells.

Copper (Cu), Silver (Ag), and Gold (Au) doped Carbon Dots (CDs) nanoparticles and nanocomposites can be synthesized employing a diverse range of preparation techniques, including hydrothermal (as shown in Figure 1), solvothermal, microwave, ultrasonic, laser ablation, carbonization, and pyrolysis. The precursor selection involves the utilization of suitable carbon source such as glucose, plant leaves and fruits, and various acids for CDs synthesis. Various sources of metals can be utilized such as $CuCl_2$, $CuSO_4$, and $CuNO_3$ for Copper doping, while silver doping mainly utilizes $AgNO_3$ as shown in Figure 1 and gold doping utilizes primarily $HAuCl_4$, respectively.

These nanoparticles play a crucial role in multimodal imaging-guided photothermal cancer therapy. Both *in vivo* and *in vitro* studies demonstrate synergistic cancer therapies encompassing photothermal therapy (PTT), photodynamic therapy (PDT), chemotherapy (CT), chemodynamic therapy (CDT), among others. Additionally, they induce apoptosis (cell thermal death) by generating reactive oxygen species (ROS) or singlet oxygen ($^1O_2$) within cancerous cells as shown in Figure 1. Furthermore, the nanoparticles exhibit fluorescence imaging capabilities and facilitate cancer cell detection.

2.1 Bioimaging

Bioimaging is an established and facile technique that can give clear real-time and an unambiguous picture of biological taking use of different types of detectors and probes. There are various bioimaging techniques like B-ultrasound, Computed tomography (CT), Magnetic resonance imaging (MRI), Positron emission computed tomography (PET), X-ray and so on (Li et al., 2021). Among them FI, plays an important role for clinical diagnosis and bioimaging because of its cost-effective simple and convenient instrumentation, easy and long-term observation, high sensitivity and noninvasiveness. Until now, different fluorescent materials have been employed for bioimaging including small organic molecules and nanomaterials. However, typical fluorophores like organic dyes and quantum dots have the disadvantage of low FL performance and toxicity. Therefore, carbon dots have emerged as promising candidates as a replacement for conventional fluorescent probes both for biological *in-vitro* and *in-vivo* imaging with advantages as mentioned earlier (Li et al., 2017). Customarily, CDs can enter quickly into cells and are thus distributed into imaging organelles to study and understand organelle related diseases (Li et al., 2017). In addition, when conjugated with protoporphyrin IX, a nucleus photodynamic therapy capability was obtained to achieve efficient tumor removal after laser irradiation without any toxicity. Taking advantage of the minimal auto-FL and light straggling by tissues, CDs with red/NIR emission or two-/multiphoton photoluminescence have given best results for *in-vivo* FI (Yang et al., 2009). In addition, CDs have been identified to show outstanding multimodal imaging performance with an advantage to increase the efficiency of imaging-guided theranostics by visual information and guidance like circulation in physiological environments and location of agent (Liu et al., 2020; He et al., 2022).

In the following section Cu-, Ag-, and Au-doped CDs are discussed that have been used to achieve *in-vitro* and *in-vivo* bioimaging in the recent past.

2.1.1 Cancer detection and imaging based on Cu-CDs

Bao et al. (2018) have developed CuCDs interconnected nanosheets that exhibit remarkable optical absorption in the NIR region (Entry-1 of Table 1). When modified with PEG, the resulting PEG-CuCDs NSs, which have a size range of 20–30 nm, exhibit good photothermal stability and biocompatibility. These nanosheets were utilized for a combination of imaging techniques and photothermal therapy to target and treat cancer cells effectively, Consisting of *in vivo* PA, Photothermal imaging also FL imaging *in vitro*. The high NIR optical absorption of the modified CuCDs NSs was used to investigate their PA properties, a direct correlation was noticed between the intensity of the PA signal and the concentration of copper, making them suitable for quantitative imaging using photoacoustic technique. Furthermore, after FL labeling and modification with HS-PEG, the CuCDs NSs were effectively reached tumor sites and target it by EPR phenomenon, where FI was used to guide photothermal therapy (PTT). Guo et al. (2018) used copper N-carbon dots both *in vivo* and *in vitro* as a FI probe and thermal imaging probe to render the therapeutic treatment process (Entry-2 of Table 1). The B16 cells were stained with Cu, N-CDs for cellular visualization to determine the Cu, N-CDs presence, within the cells. A bright FL was observed in the cytoplasm of the cell, confirming the entrance of Cu, N-CDs inside cell. Moreover, the fluctuations in tumor temperatures during laser exposure of 808 nm were recorded using an IR thermal camera. This shows that Cu, N-CDs can also be used as type of Infrared thermal imaging probe for monitoring the variations in temperature during PA process. Liu et al. (2019) developed a novel carbon nanostructure known as CBQDs using spinach, which exhibits near-infrared emission (Entry-3 of Table 1). Further binding of Cu ions leads to CBQD-Cu NCs. *In vivo* this NC demonstrated a capability for NIR FI of Biothiol. Since in cancerous cells the level of Biothiol is significantly higher as compare to normal cells, CBQD-Cu NCs have the potential to differentiate between cancerous and normal cells, enabling cancer diagnosis. The study used 7702 and HeLa cells for FI, where Biothiol emitted red FL after incubation with CBQD-Cu NCs and with a laser irradiation of 405 nm. They also validate the lower intensity of red FL exhibited by 7702 cells compared to HeLa cells. These findings indicate the potential of CBQD-Cu NCs for cancer diagnosis. Wang et al. (2019) describes synthesis and characterization of Cu-CDs that are suitable for FI in case of both HeLa and human neuroblastoma cells line (Entry-4 of Table 1). Confocal laser scanning microscopy (CLSM) was employed to capture FI of Cu-CDs in both SH-SY5Y multicellular spheroids (MCs) and HeLa cells. Which showed a 24.4% FL quantum yield. The Cu-CDs displayed favorable solubility, intense FL, and minimal cytotoxicity making them a promising candidate for optical bioimaging applications Ming Zhang, Wentao Wanga et al. synthesized a biodegradable, versatile NP system called γ-PGA @GOx @Mn, Cu-CDs for synergistic cancer therapy and simultaneous multimodal imaging, including FI, MRI, photoacoustic (PA) and ultrasound imaging. Briefly the study showed that the 4T1 tumor had a higher FL intensity compared to other organs. This indicates that the NPs exhibited a preference for accumulation in the tumor tissue. The signal strength within the tumor area on MRI images was also observed to be heightened after the injection of NPs, the photoacoustic (PA) images provided further evidence of NP accumulation within the tumor tissue with maximum accumulation observed after 36 h. Finally, the ultrasound imaging shows the production of oxygen (O_2) within the tumor. The experiment revealed a progressive increase in oxygen (O_2) levels within the tumor following NP injection (Liu et al., 2020) (Entry-5 of Table 1). Jiang et al. (2020) successfully synthesized a versatile nano platform known as CuO@ CNSs-DOX, which combines CuO and CNSs for dual-modal imaging techniques namely, Infrared thermal imaging and photoacoustic imaging to provide the live diagnosis of a diseases (Entry-6 of Table 1). The IR thermal imaging results demonstrated that the application of CuO@CNSs and exposure to an 808-nm laser led to a 20°C rise in the tumor surface temperature. In contrast, the control group exhibited a temperature increase of 10°C. This result suggests that CuO@ CNSs can effectively induce hyperthermia in tumors. The CuO@CNSs have been demonstrated to be a highly effective as a contrast agent in facilitating image-guided cancer diagnosis, particularly in photoacoustic (PA) imaging. *In vitro* studies showed a strong linear relationship between the concentration of CuO@CNSs and PA signal, CuO@CNSs have shown promising potential as a highly effective contrast agent for PA imaging. *In vivo* PA imaging also confirmed the effectiveness of CuO@CNSs as a contrast agent, Prior to injection, the tumor region exhibited weak PA signals, but after intratumoral administration of CuO@ CNSs, strong PA signals were observed in the same area. These results suggest that CuO@CNSs can be an important tool for real-time imaging-guided cancer diagnosis. Sun et al. (2020) developed a nanoassembly called Cu/CC NPs by combining a photosensitizer called (chlorine e6 (Ce6), modified CDs (CDs-Ce6) and Cu^{2+} (Entry-7 of Table 1). These NPs were found to have exceptional capabilities for tumor microenvironment (TME) triggered FI. Confocal laser scanning microscopy (CLSM) was employed *in vitro* to investigate the FI of Cu/CC NPs in relation to three distinct carcinoma cell lines. The results showed that the Cu/CC NPs efficiently penetrated the cells and had a TME-stimuli responsive FL recovery, as evidenced by the bright red emission of the 4T1 cells that could be easily distinguished in the CLSM images. Additionally, nucleus-targeted staining was performed using Hoechst dye, demonstrating the suitability of the nanoassemblies for effective counterstaining. Comparable imaging properties were likewise observed for A549 and MCF-7 cells. The effect of GSH on FI using Cu/CC NPs was also investigated. When 4T1 cancerous cells were pre-cultured with acids known as alpha lipoic acid, which act as promoter for GSH, there was a 1.8-fold increase in FL intensity compared to untreated cells. This result was consistent with FL recovery seen after the GSH introduction. This indicates that in living cells the GSH can enhance the FI performance of the nano-assemblies. *In vivo* imaging the study investigated the effects of Cu/CC NPs, which showed excellent TME-triggered FI at the cellular level. Hemolysis experiments were performed to examine the blood compatibility of

TABLE 1 Summary of anticancer activities of Cu, Ag and Au Carbon Dots covered in this review.

Entry No.	Description	Precursor	Application	Reference
Copper-doped-CDs				
1	Cu-CD NanoSheets	*o*-phenylenediamine and L-cysteine; Cu ions	Multimodal imaging guided Photothermal Cancer Therapy	Bao et al. (2018)
2	Cu,N-CDs nanodots	EDTA.2Na; $CuCl_2$	B16 cell imaging and therapy	Guo et al. (2018)
3	CBQD-Cu NC	Spinach leaves; Copper ions	*In vivo* Biothiol imaging and Enhanced PDT of mice tumor	Liu et al. (2019)
4	Cu-CDs	Poly (acrylic acid); Cu $(NO_3)_2$	HeLa and SH-SY5Y MCs cells FL imaging and inhibition of MCs growth	Wang et al. (2019a)
5	γ-PGA@GOx@Mn, Cu-CDs Nanomaterial	Citric Acid; $CuCl_2$	*In vivo* 4T1 cell imaging and therapy, *In vitro* PTT/PDT therapy of Tumor	Liu et al. (2020b)
6	CuO@CNSs-DOX nanoplatforms	Glucose; $CuCl_{2.}$ $2H_2O$	FL imaging of 4T1 cell, apoptosis via enhanced antitumor efficacy by combined therapies (PTT, CDT, CT)	Jiang et al. (2020)
7	Cu/CC NPs Nanoassembly	n/a	*In vivo*/vitro FL imaging and Synergistic Cancer therapy of A549 and 4T1 cells by (PTT, PDT, CDT)	Sun et al. (2020)
8	CuSCDB@MMT7 NC	Saccharomycetes; $CuCl_2$	Cancer cell Targeting, Enhanced Antitumor. (PTT)	Yu et al. (2020)
9	CQDs/Cu_2O Composite	Glucose; $CuSO_4$	cancer ovarian (SKOV3) cell death and antiangiogenic activity	Chen et al. (2021)
10	CD (HA)/TiO2/Cu2+ NPs biosensor	Mango; $CuCl_2$	HeLa cell detection	Giang et al. (2021)
11	CuO NPs-CNPs colloidal NPs	Graphite pellets; Copper suspension	Antiproliferative Actions against Breast Cancer Cell line (MCF-7)	Mohammed et al. (2022)
12	Cu-CDs	Alcea Leaf; $CuSO_4$	Thermal ablation of 4T1 cancer cells	Najaflu et al. (2022)
Silver-Doped-CDs				
13	CD-Ag@ZnO NC	Acetic Acid; $(AgNO_3)$, $(ZnNO_3)$	FL imaging and apoptosis in MCF-7 and A549 cancer cells.	Sachdev et al. (2015)
14	CyOH–AgNP/CD Nanophotosensitizer	Citric Acid; $AgNO_3$	4T1 cell imaging and antitumor PDT	Liu et al. (2020c)
15	CD@AgNPs NC	Sweet lemon Peels; $AgNO_3$	anticancer activity against MCF7 breast cancer cells	Ghosal et al. (2020)
16	Ag-CDs Colorimetric Sensor	Citric Acid; $AgNO_3$	lactate sensing and imaging in 4T1 breast cancer cells	Park et al. (2021)
17	Ag@CDs Nanoconjugate	Citric acid; $AgNO_3$	Imaging and apoptosis in HeLa cells	Priyadarshini et al. (2022)
Gold-Doped-CDs				
18	Fe3O4@PC-CDs-Au hybrid NP	Acetone; $Fe(C_5H_5)_2$, $HAuCl_4$	B16F10 cell imaging, Drug delivery and high Photothermal conversion efficiency	Wang et al. (2015)
19	C-dots–AuNPs–Cys conjugates	n/a	Detecting tumor in Hela cell using light and electricity	Liu et al. (2015)
20	AuCDs	Glucose; $HAuCl_4$	FL imaging of MCF-7 and UMR-106 cells	Zhang et al. (2016)
21	GCDs NC	Citric Acid; $HAuCl_4$	cytosensing of metals in cancer A549 cells	Abdelhamid et al. (2017)
22	Au/GdC NC	N-acetyl-L-cysteine; $(HAuCl_4)$, $(GdCl_3)$	MRI contrast and PTA therapy agent	Gedda et al. (2017)
23	Au@C/CaP NPs	Polyacrylic acid; $(Ca(OH)_2)$, (Na_2HPO_4)	CT imaging contrast agent, drug delivery and Synergistic chemo-photothermal therapy	Wang et al. (2017)
24	C-dots@Au nanoflowers	Citric Acid; $HAuCl_4$	HeLa cell imaging and Photothermal therapy	Hou et al. (2018)
25	(CQDs/Au) NC	Glucose; $HAuCl_4$	Detection of pancreatic tumor marker (CA 19-9)	Alarfaj et al. (2018)
26	C-dots-Ab AuNPs/PAMAM/aptamer	Histidine; $HAuCl_4$	Immunosensor for detection of breast tumor marker (CA 15-3)	Mohammadi et al. (2018)
27	MitoCAT-g	Citric acid; $HAuCl_4$	Mitochondrial damage and apoptosis in HepG-2 cancer cell	Gong et al. (2019)

(Continued on following page)

TABLE 1 (*Continued*) **Summary of anticancer activities of Cu, Ag and Au Carbon Dots covered in this review.**

Entry No.	Description	Precursor	Application	Reference
28	CD/AuNP	CDs Purchased; $HAuCl_4$	Detection of MUC1 (Tumor Marker)	Wang et al. (2019b)
29	AuNP-peptide-CDs nanobiosensor	Chitosan	Detection of Matrilysin a salivary gland cancer biomarker (MMP-7)	Behi et al. (2020)
30	Au@CDs nanoalloys	Citric Acid; $HAuCl_4$	Detection of MUC1-positive MCF-7 cells in serum	Liu et al. (2020a)
31	AuNP@CDs inorganic nanoflares-DNAzyme, APCD	citric acid; $HAuCl_4$	Detection of exosomal miRNAs miR-133b and miR-135b	Zhang et al. (2022)
32	Au@CDs nanohybrids	Citric acid; $HAuCl_4$	Tumor catalytic therapy, apoptosis in 4T1 cell	Li et al. (2022)

the NPs, which showed no significant damage to red blood cells, indicating their safety for use *in vivo*. The biodistribution of Cu/CC NPs was evaluated by employing an IVIS spectrum imaging system, which demonstrated a remarkable propensity of the nanoassemblies to accumulate efficiently at tumor site. Giang et al. (2021) created wireless biosensing device using CD (HA)/TiO2/Cu^{2+} coated surfaces to detect cancer cells (Entry-10 of Table 1). The biosensor uses carbonized hyaluronic acid CD (HA) as probes and is responsive to pyrophosphates (PPi) and alkaline phosphatase (ALP) concentrations. These substances are found in higher levels in cancer cell lines as compared to normal cells. These CD (HA)/TiO2/Cu^{2+} nanoassemblies has antifouling properties when exposed to visible light, which improves the accuracy of cancer cell detection by preventing unwanted biological materials from interfering. The MDCK cells were cultured on substrates coated with CD (HA)/TiO2/Cu^{2+} and exposed to visible light until the cells completely detached. Interestingly, no notable alterations were observed in the electrochemical properties and FL intensity. Conversely, when the HeLa cells were detached from the surface, there was an observed rise in resistance and FL intensity. This results shows that the CD (HA)/TiO2/Cu^{2+} exhibits great potential for investigating cell-surface interactions and cancer cell detection.

2.1.2 Cancer detection and imaging based on Ag-CDs

Sachdev et al. (2015) successfully synthesized a CD-Ag@ZnO NC that demonstrates promising potential for direct FL monitoring of cellular uptake in both A549 and MCF-7 cancerous cells (Entry-13 of Table 1). The NC allows for the concurrent green FL emission of CDs, thereby eliminating the need for fluorescent organic dyes to track the distribution of CD-Ag@ZnO NC. The technique of FL microscopy and AAS were utilized to evaluate the qualitative/quantitative aspects of cell absorption. Furthermore, they employed FL and SEM to examine distinctive nuclear and morphological alterations during apoptosis. Liu et al. (2020) have developed a highly biocompatible and low-toxicity NC, [CyOH–AgNP/CDs], which acts as a nano-photosensitizer and can be used for targeted tumor imaging (Entry-14 of Table 1). They have also conducted *in vivo* FI studies to investigate the tumor accumulation capacity of CyOH and [CyOH–AgNP/CDs]. The findings demonstrate that the near-infrared FL signals emitted by CyOH showed a progressive increase at the tumor site, peaking at 20 h after injection as shown in (Figures 2A, C). Conversely, in the case of [CyOH–AgNP/CDs], the FL signal at the tumor site reached its max intensity at 24 h following-injection (Figures 2B, D). Furthermore, confocal FL microscopy images showed (Figures 2E) weak FL for CyOH and (Figures 2G) strong FL for [CyOH–AgNP/CDs] in the tumor. This work demonstrates the potential of the [CyOH–AgNP/CDs] NC as highly effective and focused tool for tumor visualization, with low toxicity and high biocompatibility.

Priyadarshini et al. (2022) synthesized Ag@CDs nanoconjugates and investigated their potential use in biomedical applications (Entry-17 of Table 1). They found that the nanoconjugates were taken up by HeLa cells, as demonstrated by blue FL in the cells observed through confocal imaging. In addition, they measured the generation of reactive oxygen species in HeLa cancer cells treated with nanoconjugates using FI with DCFHDA dye. The internalization of CDs and Ag@CDs into cells was assessed by exposing the cells to a concentration of 50 μg/mL. Remarkably, this concentration was found to be only 1/2 of the concentrations that exhibited toxicity towards the cells. Confocal imaging data provided compelling evidence of the internalization of nanoconjugates within HeLa cells, as indicated by the presence of a distinct blue FL signal. Overall, the study demonstrated the potential of Ag@CDs nanoconjugates in various biomedical applications, including live cell imaging.

2.1.3 Cancer detection and imaging based on Au-CDs

Wang et al. (2015) synthesis a type of hybrid NP, Fe3O4@PC-CDs-Au that have very potential uses in drug delivery, cell imaging, and cancer therapy (Entry-18 of Table 1). The efficacy of these NPs was tested on mouse melanoma B16F10 cells, which showed strong FL when exposed to various light wavelengths, attributed to synergistic effect of the FL CDs and Au nano-crystals in the carbon shells. Also, the cellular imaging function of the NPs was evaluated using confocal microscopy, which indicates that the NPs had the capability to penetrate the intracellular space and illuminate the cells with intense FL. The Z-scanning confocal FI of B16F10 cells following incubation with Fe_3O_4@PC-CDs-Au NPs provided additional evidence of the vibrant FL observed in the cytoplasm surrounding the cell nucleus upon excitation with a 488 nm laser. The images obtained from this evaluation demonstrated that

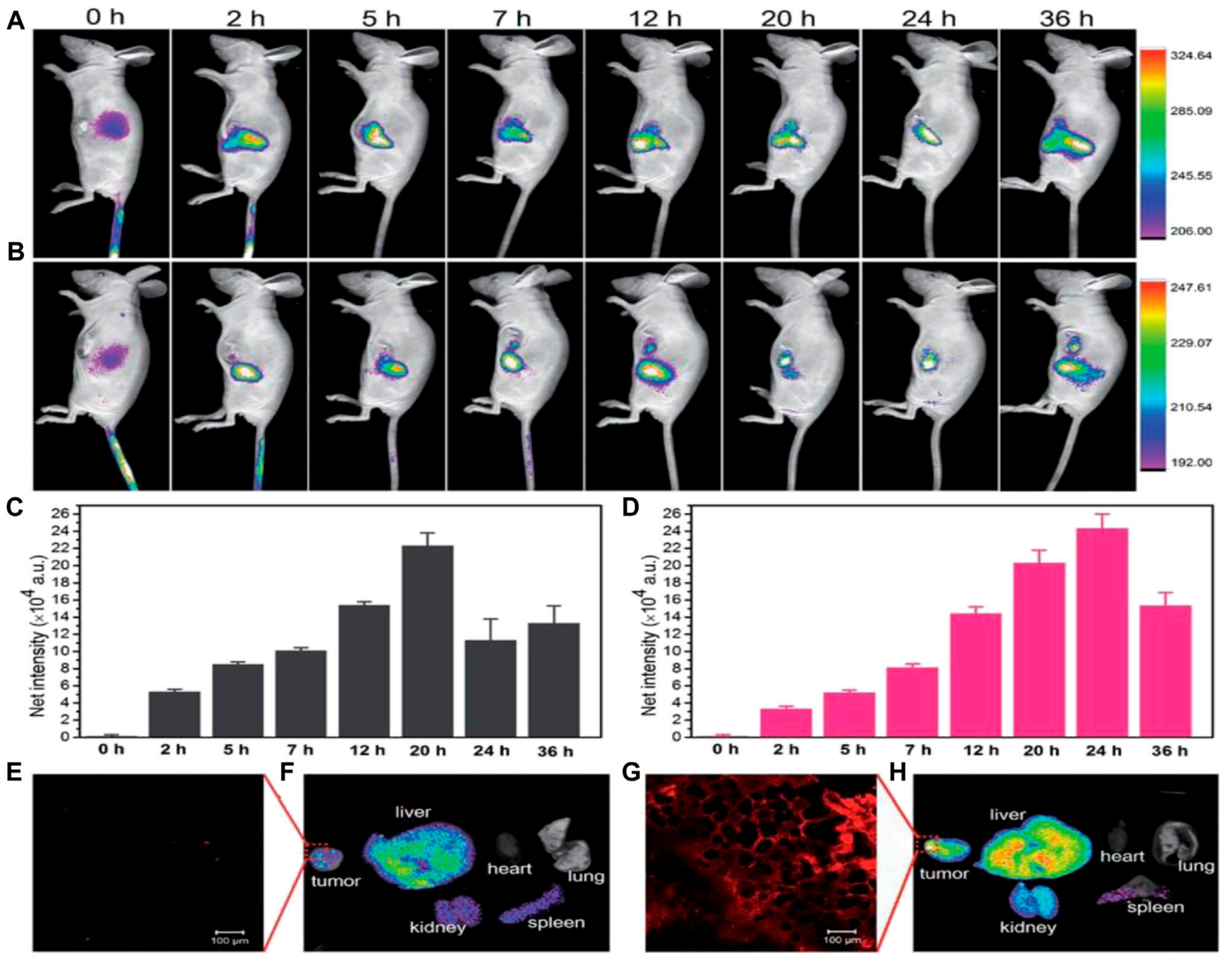

FIGURE 2
In vivo fluorescence images of CyOH **(A)** and CyOH–AgNP/CD **(B)** at different time points after intravenous injection. The fluorescence intensity of tumors with CyOH **(C)** and CyOH–AgNP/CD **(D)** at different time points. Confocal fluorescence microscopy image of tumors after treatment with CyOH **(E)** and CyOH–AgNP/CD **(G)**, lex ¼ 633 nm, and lem ¼ 650–750 nm. Biodistribution of CyOH **(F)** and CyOH–AgNP/CD **(H)** in tumor-bearing mice after 36 h. Reproduced from reference (Liu et al., 2020).

Fe_3O_4@PC-CDs-Au NPs can surpass cell barriers and produce multicolor images of cells under laser excitation. The confocal images also showed that the NPs demonstrated Possessing exceptional photostability as an optical indicator, rendering them well-suited for extended cellular imaging purposes. Liu et al. (2015) design a CDs and cysteamine capped AuNP cytosensing platform (CDs–AuNPs–Cys) which proposes a novel method for detecting tumor cells using light and electricity without any labels or probes with high sensitivity and specificity (Entry-19 of Table 1). HeLa cancerous cells were utilized as the representative analyte model. The method uses CDs and AuNPs that can transfer energy between them when they are attached to different receptors on the cell surface and close to each other via the resonance energy transfer (RET). This energy transfer affects the electric current generated by the CDs when they are exposed to light. By measuring this current, they can tell how many cells are present on the surface of an electrode. The RET also enhances the photoelectrochemical signal of the CDs, which can be measured by a device called a photoelectrochemical Cytosensor. These advancements shows the promise of detection and diagnosis of cancer at early stages. Zhang et al. (2016) developed an Au-CDs composed of CDs and Au nanoclusters (Entry-20 of Table 1). They evaluate the cytotoxicity and cellular imaging capabilities of these Au-CDs. The results revealed that the Au-CDs exhibited biocompatibility and minimal toxicity to both cancerous and normal cells when utilized at concentrations lower than 833 μg/mL. Moreover, the Au-CDs were capable of penetrating live cells within 10 h and producing diverse colored emissions when imaged to a sole 405 nm laser stimulus. The study suggests that Au-CDs hold potential applications as multiplexed bioimaging agents for both cancer and normal cells. Specifically, under single excitation the Au-CDs were able to facilitate dual FL visualization of MCF-7 and UMR-106 cells which are breast cancerous and normal rat osteoblast cells respectively. Abdelhamid et al. (2017) fabricated modified CDs with AuNPs (Entry-21 of Table 1). The NC can be used for cytosensing of biological metals such as Fe and Cu in cancer cells (A549). The NC demonstrated exceptional ultraviolet absorption properties that aligned precisely with the N_2 laser's wavelength, allowing for selective detection of different metals in cancer cells with high sensitivity and accuracy. Mefenamic acid served as both a chelating agent and a co-matrix for mass spectrometry purposes, which further improving the efficiency of metal detection. Gedda et al. (2017) successfully synthesized a NC consisting of AuNPs and Gd-CDs (Entry-22 of Table 1). They further assessed the capabilities of this NC as a contrast agent for MRI. Gd containing NCs are commonly utilized as positive contrast agent in magnetic resonance imaging because they have exceptional magnetic characteristics that enable it to interact with protons in water molecules, resulting in a brighter image. They used an electron paramagnetic resonance (EPR) spectrometer to confirm the presence of Gd in the NC, and then conducted MRI experiments to measure the NCs longitudinal relaxivity (r1), which is a measure of how effectively the NC interacts with water protons to produce a contrast effect in MRI. The results showed that the Au/Gd-CDs NC had a significantly higher r1 value compared to a clinical contrast agent, Magnevist, indicating that it has strong T1 contrast ability. The elevated r1 value observed in the Au/Gd-CDs NC can be attributed to its compact size, leading to enhanced interactions between Hydrogen protons and Gd^{3+} ions. Furthermore, the NCs extensive specific surface area amplifies the dipole-dipole interactions b/w H protons and Gd^{3+} ions. Wang et al. (2017) synthesized the Au@C/CaP NPs, Consisting of an Au-core, C-shell, and Ca-Phosphate coating (Entry-23 of Table 1). The NPs were assessed as a contrast agent for computed tomography imaging, demonstrating an elevated X-ray absorption coefficient compared to conventional iodine agents, indicating a promising alternative for CT imaging. This work demonstrated a strong linear correlation (R2 value of 0.9947) between the Hounsfield units (HU) values and the Au concentration in the Au@C/CaP NPs, indicating their effectiveness as positive CT visualization contrast agents. The effectiveness of CT signals was further confirmed as their intensity increased with higher concentrations of Au. Moreover, the study revealed that the Au@C/CaP NPs did not retain any significant effect on cell viability when used alone or either with laser irradiation, as demonstrated by green FL (indicating live cells). However, when utilized alongside the exposure of an 808 nm laser beam, the Au@C/CaP NPs caused cell death in HeLa cells, as demonstrated by red FL. These findings indicate that Au@C/CaP NPs exhibit a promising and safe contrast agent for CT imaging. Which can help doctors to locate tumors and other disease. (Hou et al. (2018) have developed CDs@Au nanoflowers that exhibit dual-modal imaging capabilities for PA and FL imaging (Entry-24 of Table 1). The researchers conducted experiments on HeLa cells and found that CDs@Au nanoflowers exhibited intracellular red-emissive FL when excited by 543 nm. The results were visualized through confocal imaging and confirmed by DAPI staining technique combined with Z-stack visualization, which showed that CDs@Au nanoflowers were localized inside the cytoplasm. Additionally, they performed PA imaging experiments on an agarose gel phantom filled with CDs@Au nanoflowers at different concentrations, ranging from 50 to 300 μg/mL. The NIR region facilitated efficient absorbance of PA signals, resulting in their strong intensity. Additionally, the concentration-dependent PA curves of CDs@Au nanoflowers exhibited a linear correlation with a coefficient of determination (R2) of (0.92). These results demonstrate the potential of CDs@Au nanoflowers as a simultaneous FL and PA imaging agent for tumor diagnosis. Alarfaj et al. (2018) introduced an innovative approach for the detection of CA 19-9, a biomarker for pancreatic tumors (Entry-25 of Table 1). This method involved the utilization of a NC comprising CDs and Au. The immobilization of NCs was performed by antibody-horseradish peroxidase (Ab–HRP) formed CDs/Au–Ab–HRP. Simply it is a new way to make tiny particles that can glow when they detect a substance called CA 19-9 in blood samples. The method utilized peptide bonds to effectively capture the specific CA 19-9 antigen in human serum. This was achieved through a sandwich capping antibody-antigen-antibody reaction, enabling the immobilization of the antigen within the NC. This new technique could potentially save lives and reduce healthcare costs, by providing a faster and more cost-effective way of diagnosing pancreatic cancer. Mohammadi et al. (2018) have developed a CDs labeled with CA15-3 antibody and AuNP aptamer-based FRET immunoassay CDs-Ab–AuNPs/PAMAM/aptamer for the responsive and efficient tracing of mammary tumor biomarkers CA15-3 in various physiological samples (Entry-26 of Table 1). This method has the potential to replace or enhance existing technologies such as ELISA. When CA15-3 antigen is present in serum or cancer cell, it binds to the antibody-antigen-aptamer complex, which brings the CDs and AuNPs closer together, resulting in decreased FL intensity. The immunoassay has a high sensitivity, capable of detecting CA15-3 at extremely low concentrations of 0.9 μU/mL. Additionally, it is effective in identifying MDA-MB-231 cancerous cells within a concentration range of 1,000 to 40,000 cells, with a detection limit as low as 3 cells per 10 μL. Wang et al. (2019) presents an innovative technique to measure MUC1, a protein found on some cancer cells, using anti-MUC1 aptamers and AuNPs combined with CDs. By using inner filter effect b/w AuNPs and CDs, the method is highly selective to detect MUC1, the CDs brightness is diminished due to the filter effect in the presence of the Au particles (Entry-28 of Table 1). However, upon the addition of MUC1, the aptamers bind to it, separating them from the Au particles with restoring the CDs brightness. By quantifying the CDs brightness, the amount of MUC1 present can be calculated. This innovative method has promising potential for cancer diagnosis. Behi et al. (2020) have successfully designed nanosensing platform (Nanobiosensor) AuNPs-peptide-CDs for the rapid, sensitive and highly precise method for detecting matrilysin, a biomarker associated with salivary gland cancer (Entry-29 of Table 1). The detection platform utilizes peptides that can be digested by matrilysin, connecting AuNPs and CDs. The nanobiosensor demonstrates an impressive capability to detect minute amounts with high sensitivity, detecting particles as small as 39 nm. Additionally, it boasts a remarkably fast response time of approximately 30 s. These features make it an encouraging candidate for the noninvasive identification of tumors in their initial stages, offering great potential in the field of early tumor detection. The AuNPs-peptide-CDs complex exhibits excellent optical properties, showcasing significant FL quenching effects. When the peptide is cleaved by matrilysin, the CDs detach from the surface of the AuNPs. This leads to the rapid generation of detectable violet and visible FL signals. These results are a major step forward in developing advanced biosensors for early-stage tumor detection, with significant potential for cancer diagnosis. Liu et al. (2020a) have synthesized a new type of nanoalloy, namely Au@CDs, which exhibits exceptional electrochemiluminescence (ECL) efficiency (Entry-30 of Table 1). In order to enhance the identification of

MUC1-positive MCF-7 cancerous cells, which are a type of circulating tumor cells frequently present in the bloodstream of cancer patients, they also utilized a technique involving the attachment of MUC1 aptamer, a human mucin1 protein, onto the surface of Au-coated CDs. This work investigated the ECL Cytosensor performance under optimal conditions, testing its ability to detect different levels of MCF-7 cell concentrations accurately. During their observations, it was noticed that the (ECL) signal showed a gradual decrease as the concentration of cells increased. Additionally, they observed a positive linear correlation between the ECL signal and the logarithm of MCF-7 cell concentration. Specifically, within the concentration range of 100-10,000 cells/mL. Importantly, the calculated limit of detection (LOD) for MCF-7 cell concentration was found to be 34 cells/mL, which are lower than many previous studies. These findings demonstrate the remarkable sensitivity of the Cytosensor in detecting MCF-7 cells at an extremely low concentration level. Potentially enabling earlier detection and treatment of cancer patients. Notably, this approach is comparatively straightforward and does not require separation or labeling procedures, making it an attractive option for CTCs detection. Zhang et al. (2022) developed a cutting-edge technique for detecting bladder cancer-related exosomal miRNAs simultaneously (Entry-31 of Table 1). Their method combines inorganic nanoflares with DNAzyme walkers, enabling the precise and accurate detection of miRNAs in urine samples with high sensitivity and specificity from bladder cancer patients. Specifically, the inorganic nanoflares consist of AuNPs modified with CDs labeled substrates and DNAzyme strands (AuNPs@CDs inorganic nanoflares-DNAzyme APCD). By integrating these components into a single assay, they successfully attained an impressive sensitivity level for detecting a solitary miRNA, reaching the femtomolar range. Moreover, they established a broad linear detection range spanning from 50 fM to 10 nM. This innovative technique has the potential to revolutionize the early detection of bladder cancer.

2.2 Phototherapy

Phototherapy whether PDT or PTT, is a type of noninvasive therapy (not invading adjacent healthy cells, tissues and blood vessels) which changes the irradiating light into a variety of ROS (e.g., O_2 •−, •OH etc.), heat with the aid of photosensitizers and induces local apoptosis of cancer cell lines. CDs have attained enormous attraction as brilliant phototherapeutic agents because of their exclusive optical characteristics, enhanced photostability and high water-solubility. The therapeutic effects of CDs can be dangerously blocked in oxygen-dependent PDT due to rapid oxygen consumption and hypoxic (low oxygen) tumor microenvironment. This may result in inevitable drug resistance or tumor metastasis. To tackle this problem NCs for light-driven water splitting have been developed to improve the intra-tumoral oxygen level and finally reverse the hypoxia-triggered PDT resistance and tumor metastasis (Zheng et al., 2016). Apart from anticancer phototherapies, drug delivery efficiency with advantage of therapy can be achieved by combining imaging tools with drugs or genes to in the form of imaging-guided nanohybrids (Liu et al., 2020). Carrying medicine to a specified location and then its release in uninterrupted fashion is the key to efficient safe treatment. Therefore, this is a crucial step to enhance the localized therapy with minimum side effects to healthy and non-cancerous cells. CDs with aid of their excellent fluorescent properties during efficient therapy can rapidly visualize drug accumulation and activities in the cancer cell lines (Gao et al., 2020). CDs have exhibited potential clinical imaging and drug delivery applications during brain cancer and CNS diseases (Shao et al., 2017).

In the following section, Cu-, Ag-, and Au-doped CDs are summarized which have been reported to apply during drug delivery and cancer therapy treatments.

2.2.1 Cancer therapy based on Cu-CDs

Bao et al. (2018) have developed Cu/CDs-crosslinked NSs (Entry-1 of Table 1). These NSs demonstrate exceptional optical absorption in the NIR range and an impressive photothermal conversion efficiency of 41.3% at 808 nm after modification with PEG. This high conversion efficiency enables it to convert NIR light energy to hyperthermia rapidly and efficiently, which can be used to kill cancerous cells. In this study, the cell toxicity of the CuCD NSs was evaluated using various cells, including MCF-7, HepG2, AT II, A549 and L02 cells. The results showed that the cellular survival rates exceed 80% even when exposed to Cu concentration of 30 μg/mL, indicating low toxicity. Additionally, no hemolysis was observed when RBCs were treated with various concentrations of Cu^{2+}. Therefore, *in vivo* and *in vitro* the PEG-modified CuCD NSs are suitable for PTT. The NSs were also found to enhanced therapeutic effectiveness through laser-induced delivery into the cytosol, escape from the lysosomes, and targeting of the nucleus like properties. Guo et al. (2018) investigated the potential use of Cu,N-CDs for cancer treatment, examining their effectiveness in both *in vivo* and vitro (Entry-2 of Table 1). The study focused on evaluating the ability of these CDs to serve as a therapeutic agent against cancer, using melanoma B16 cells. The Cu,N-CDs possess NIR absorption properties that generate heat and ROS necessary for PTT and PDT. The production of ROS, particularly $^1O_2$, is crucial for PDT promoting cancer cell apoptosis. To determine the ROS production capacity of Cu,N-CDs, the chemical trapping agent 1,3-diphenylbenzofuran (DPBF) was used, and the results indicated, Cu,N-CDs generate ROS efficiently when exposed to laser irradiation of 800 nm. The phototherapeutic effect of Cu,N-CDs was evaluated *in vitro* by incubating B16 cells with varying concentrations of Cu,N-CDs and subjecting them to laser exposure of 800 nm for 10 min. The results demonstrated a concentration-dependent reduction in cell viability, from 88% to 20%, proposing toxicity arising from both the thermally-induced photothermal effects and the generation of ROS triggering photodynamic effects. Overall, the study suggests that Cu,N-CDs can inhibit melanoma tumors in mice through synergistic PT and PDT, providing a promising therapeutic approach for cancer therapy. Liu et al. (2019) prepared "chlorophyll-inrich biomass QDs" and formed CBQD-Cu NCs by adding Cu (Entry-3 of Table 1). The CBQD-Cu have emerged as an exceptionally potent form of nanomedicine utilized for the identification and therapy of tumors. *In vivo* study demonstrated that these CBQD-Cu NCs exhibit dual enhanced PDT of tumors. When tested on mice with tumors, the NCs successfully treated the tumors, with no detectable infected tissues found after 12 days of complete treatment, as observed through optical microscopy. The attachment of chlorophyll and Cu^{2+} on the surface of the CBQDs also played a crucial role in enhancing PDT. This binding reduced difference in energy level of the chlorophyll molecules, which led to an increase of ROS under NIR irradiation. This increase in ROS production ultimately resulted in enhanced PDT, making these CBQD-Cu NCs a promising new nanomedicine for PDT of tumors. Wang et al. (2019) reports that the Cu-CDs synthesized in this study exhibited a higher quantum yield 36% of $^1O_2$ and inhibition the growth of 3D multicellular spheroid (Entry-4 of Table 1). Indicating their potential to promise visualizing-guided PDT agent. They used EPR spectroscopy to validate the effectiveness of PDT by detecting the presence of singlet oxygen ($^1O_2$). The EPR analysis revealed an enhancement in the signal of Cu-CDs after 12 min of exposure to light, indicating successful PDT activation. Conversely, the signals of CDs and water were relatively diminished under both dark and light conditions. Therefore, the results from the EPR spectroscopy demonstrated an amplified signal for Cu-CDs while observing weakened signals for CDs and water in the presence of light during PDT. The Cu-CDs showed good photoinduced cytotoxicity and can be used as a versatile photodiagnostic and therapeutic tool in various biological applications. Liu et al. (2020) have synthesized a novel, biodegradable NP composite that can combine four different approaches to cancer treatment like starving therapy, PDT, PTT, and immune based therapy (Entry-5 of Table 1). The NPs, known as γ-PGA@GOx@Mn, Cu-CDs NPs, have an exceptional capacity to selectively target malignant cells and remain within the acidic microenvironment of tumors for a prolonged time. When these NPs exposed to 730 nm laser, they exhibit both photothermal and photodynamic effects, with the added advantage of generating hydrogen peroxide (H_2O_2) *in situ* to reduce tumor hypoxia and improve *in vivo* PDT. Thus, by combination of these therapies results in excellent tumor inhibition, as demonstrated by the high collection of NPs within the tumor tissues, coupled with synergistic effect of starving therapy, PDT and PTT. Moreover, when combined with anti-PDL1 checkpoint blockade treatment, this NP-based combination therapy is able to directly remove primary tumors and target metastatic tumors, leading to the suppression of distant tumors. Jiang et al. (2020) have developed a versatile Nano platform called CuO@CNSs-DOX, which can be used for the combining therapies of PTT, CDT, and CT (Entry-6 of Table 1). During synthesis CuO are adsorbing on carbon nanostructures surface, an enhancement was observed in the efficiency of photothermal conversion for NPs, resulting in an increase from 6.7% to 10.14%. This enhancement can be attributed to the electron transition that occurs between C-2p and Cu-3d. CuO also used as a CDT agent, which is capable of selectively releasing Cu^{2+} ions at the tumor site. These ions can trigger the generation of Hydroxyl radicals (•OH) through Haber-Weiss and Fenton-like reactions, leading to the induction of apoptosis in cancer cells. Additionally, the therapeutic drug DOX was loaded onto CuO@CNSs through electrostatic adhesion. This formulation enables the rapid release of DOX specifically at the tumor site, effectively targeting and eliminating cancer cells. The CuO@CNSs-DOX platform shows promise in improving the effectiveness of cancer treatment by utilizing the synergistic effects of PTT, CDT, and CT. Sun et al. (2020) evaluates the capability of Cu/CC NPs for cancer treatment (Entry-7 of Table 1). The study investigates the synergistic therapeutic effect of combining PDT, PTT and CDT using Cu/CC NPs. The Cu/CC NPs *in vivo*/vitro studies show excellent tumor homing capacity, high photothermal conversion efficiency, enhanced accumulation capability, and PTT efficiency. *In vitro* the cell-toxicity of Cu/CC NPs on normal and cancer cells were investigated. The cell viability was assessed utilizing a cell counting kit-8 (CCK8) assay. The findings revealed that the viability of MRC-5 normal cells remained above eighty percent even when exposed to the highest concentration of Cu/CC NPs (200 mg/mL). In contrast, the viability of 4T1 and A549 cancerous cell line decreased rapidly with increasing concentrations of Cu/CC NPs. Specifically, particularly at a concentration of 200 mg/mL, the viability of A549 cells was observed to be only 51%, while the viability of 4T1 cells was even lower, with only 38% remaining alive, indicating that the nano-assemblies had enhanced cytotoxicity towards cancer cells in comparison to normal cells. The combination therapy leads to significant tumor inhibition, with the highest efficacy observed in the trimodal CDT, PTT and PDT. Yu et al. (2020) design a hollow-structured CuS NPs that were combine with CDs and loaded with the drug bortezomib to target tumors (Entry-8 of Table 1). To increase specificity for cancer cells, the nano-composite were coated with a macrophage membrane hybridized with T7 peptide, which helped them evade the immune system and enter cancer cells through transferrin receptor-mediated endocytosis. The biocompatible and less toxic CuSCD NPs had excellent photothermal conversion efficiency when exposed to laser irradiation of 808 nm. After coating with the macrophage membrane hybridized with T7 peptide, the resulting CuSCDB@MMT7 NC showed increased specificity for cancer cells and improved immune evasion. They used CuSCDB@MMT7-triggered PTT to treat tumors, they observed an increase in tumor cell apoptosis and a decrease in metastasis. This was due to the increased heat-stability of various substrates involved in cell proliferation and survival, which are part of the ubiquitin-dependent proteasomal degradation pathway. Chen et al. (2021) developed a composite of CD and Cu_2O and investigated its anticancer and antiangiogenic properties in various cancerous and normal cells (Entry-9 of Table 1). This finding demonstrated that CDs/Cu_2O displayed enhanced sensitivity towards SKOV3 cells in comparison to HeLa, A549, HT-29, HCT116 cancer cells, as well as normal cells. The IC50 value recorded for SKOV3 cells was 0.85 μg mL−1, which was roughly three times lower than the IC50 values observed for the other tested cancer cells, and approximately 12 times lower than that for normal cells. Furthermore, CDs/Cu_2O demonstrated stronger antitumor activity Compared to commonly used anticancer drugs like artesunate (ART) and oxaliplatin (OXA), the IC50 value of the CDs/Cu_2O NCs was significantly lower. Specifically, the IC50 value for the NCs was approximately 114 times lower than that of ART and approximately 75 times lower than that of OXA. Furthermore, the CDs/Cu_2O NCs demonstrated enhanced antiangiogenic properties in comparison to the commercial antiangiogenic inhibitor, SU5416. This was attributed to the downregulation of VEGFR2 expression. Moreover, the CDs/Cu_2O NCs exhibited the ability to modulate angiogenesis-related genes in SKOV3 cells, specifically impacting genes such as Maspin and TSP1, thereby effectively suppressing angiogenesis Mohammed et al. (2022) synthesize CuO NPs-CNPs NC by pulsed laser ablation in liquid (PLAL) (Entry-11 of Table 1). This NC consisted of CuO NPs decorated C-NPs. The potential anticancer properties of CNP-CuO NPs were investigated in a study conducted on the MCF-7 breast cancer cell line. Additionally, the biocompatibility of these NPs was assessed to ensure their safe application. The results demonstrated that CNP-CuO NPs exhibited a significantly higher cytotoxicity against MCF-7 cells compared to CNPs alone, with the highest anticancer effects reaching almost 85%. These findings suggest that CNP-CuO NPs have high potential as an anticancer agent. Najaflu et al. (2022) have successfully synthesized 3 nm Cu-CDs with a green synthesis approach (Entry-12 of Table 1). The resulting Cu-CDs nanospheres demonstrated strong thermal ablation effects on 4T1 cells upon exposure to an 808 nm NIR laser irradiation. Importantly, the Cu-CDs showed low cytotoxicity *in vitro*, and their photothermal conversion efficiency was measured to be 39.3%. These findings suggest that Cu-CDs can be internalized by cells causing induce cell thermal death when exposed to 800 nm NIR laser irradiation, making them a promising candidate for cell PTT.

2.2.2 Cancer therapy based on Ag-CDs

Sachdev et al. (2015) developed a CD-Ag@ZnO NCs, which have significant potential in effectively monitoring the internalization of substances by MCF-7 and A549 cancer cells, as well as triggering programmed cell death (apoptosis) in these cells (Entry-13 of Table 1). *In vitro* studies have shown that the concentration-dependent cytotoxic effects of CD-Ag@ZnO NCs are attributed to the induction of apoptosis, which is accompanied by a notable rise in the generation of intracellular ROS. The elevation in ROS levels is closely linked to mitochondrial dysfunction, which subsequently triggers the initiation of apoptosis. These findings suggest that CD-Ag@ZnO NCs could be a potential candidate for cancer treatment. Liu et al. (2020) developed a biocompatible and low-toxicity NCs, [CyOH–Ag-NPs/CDs], Act as a nano-photosensitizer with high efficiency for PDT (Entry-14 of Table 1). They conducted experiments on mice in groups with 4T1 tumors to evaluate the therapeutic efficacy of this NC. The growth of tumors was partially suppressed in both the AgNP/CDs and CyOH groups. However, the CyOH–Ag-NPs/CDs group demonstrated remarkable tumor reduction, which can be attributed to the enhanced production of singlet oxygen ($^1O_2$) by this specific NC. The CyOH–Ag-NPs/CDs nano-photosensitizer showcased numerous benefits, such as a substantial production of singlet oxygen, targeted accumulation in mitochondria, improved penetration into tissues under 660 nm laser irradiation, and enhanced specificity towards tumor cells. In comparison to the CyOH dye or AgNP/CDs nanohybrid, it displayed a more potent antitumor effect. Ghosal et al. (2020) have successfully synthesized a natural polysaccharide derived CDs based AgNP NC and exhibits its anticancer activity against breast cancer MCF-7 cells (Entry-15 of Table 1). The synthesis method was *in situ*, facile and green, making it an eco-friendly approach. The anticancer effect of the CD@AgNPs was found to be dose-dependent and attributed to the generation of intracellular ROS leads to cell apoptosis. In addition to its anticancer properties, CDs demonstrated exceptional optical properties, characterized by excitation-dependent multicolor FL emission and remarkable photostability. Priyadarshini et al. (2022) synthesized a nanoconjugate called Ag@CDs, made up of Ag and CDs, and tested its efficacy against HeLa cells, a type of cervical cancer cell (Entry-17 of Table 1). A study revealed that the utilization of Ag@CDs resulted in the suppression of HeLa cell proliferation, exhibiting an IC50 value of approximately 50 ± 1: 0 μg/mL, while also inducing apoptosis. The observed mechanism behind this effect can be attributed to the production of ROS, which can induce harm to cellular structures and activate pathways leading to cell death. This indicates that Ag@CDs has a potential to be a promising anticancer drug with potent therapeutic effects, making it a promising candidate for further development and testing.

2.2.3 Cancer therapy based on Au-CDs

Wang et al. (2015) developed a Fe_3O_4@PC-CDs-Au NPs offer therapeutic potential and drug delivery carriers because of their remarkable ability to convert light into heat at a highly efficient rate and drug loading capacity (Entry-18 of Table 1). To test the photothermal performance of Fe_3O_4@PC-CDs-Au NPs they studied PT effect of water, aqueous dispersion of Fe_3O_4@PC-CDs template NPs and Fe_3O_4@PC-CDs-Au hybrid NPs under NIR irradiation, and the results show that upon exposure to same NIR irradiation for 5 minutes, the temperature of water increased by 5°C, followed by Fe_3O_4@PC-CDs 25°C and Fe_3O_4@PC-CDs-Au hybrid NPs 34°C. The template NPs of Fe_3O_4 coated with CDs already demonstrate excellent photothermal conversion capability. Moreover, by incorporating Au nanocrystals onto the carbon shell, the photothermal effect of the resulting hybrid NPs (Fe_3O_4@PC-CDs-Au) can be greatly intensified. That's why the Fe_3O_4@PC-CDs-Au hybrid NPs is ideal candidate for PTT. Furthermore, the NPs can be easily dispersed in water and carry drug molecules via their hydrophilic hydroxyl/carboxyl surface functional groups and porous carbon structure. They also found the loading capacity of DOX molecules into the NPs, which is approximately 71.9 wt%, which can be attributed to the various interactions between the DOX molecules and the NPs. Including π-stacking, hydrogen bonding, and electrostatic attractions. Additionally, the work mention that the drug molecule can be released from NPs can exhibit altered behavior when exposed to a magnetic field or NIR light. These NPs can be modified with targeting ligands to improve their specificity towards cancer cells. Gedda et al. (2017) synthesized a (10^{-9}) composite consisting of Au and Gd-CDs (Entry-22 of Table 1). These NPs exhibit low levels of toxicity and favorable biocompatibility, even at high concentrations, as observed in both *in vitro* experiments using HeLa cells and *in vivo* experiments conducted on zebrafish embryos. Furthermore, the explored the potential application of the NC as a photothermal agent (PTA) for cancer therapy. This is attributed to the NCs capability to absorb NIR light and convert it into thermal energy. The NC was found to have a high photothermal conversion efficiency and was photostable under laser irradiation. *In vitro* experiments showed that the NC had low toxicity and could kill cancer cells in a concentration-dependent manner when exposed to NIR laser irradiation. The trypan blue staining and MTT assay results were consistent and indicated that the NC could induce cell death through localized hyperthermia. In addition, when the concentration reached 2 mg/mL or higher, the solutions exhibited the ability to raise temperatures above 42°C. This temperature elevation proved effective in eliminating tumor cells. Wang et al. (2017) synthesized Au@C/CaP NPs was produced, which are core-shell NP consists of an Au core, a carbon shell and a Ca-phosphate coating (Entry-23 of Table 1). The Au@C/CaP NPs exhibit pH- and

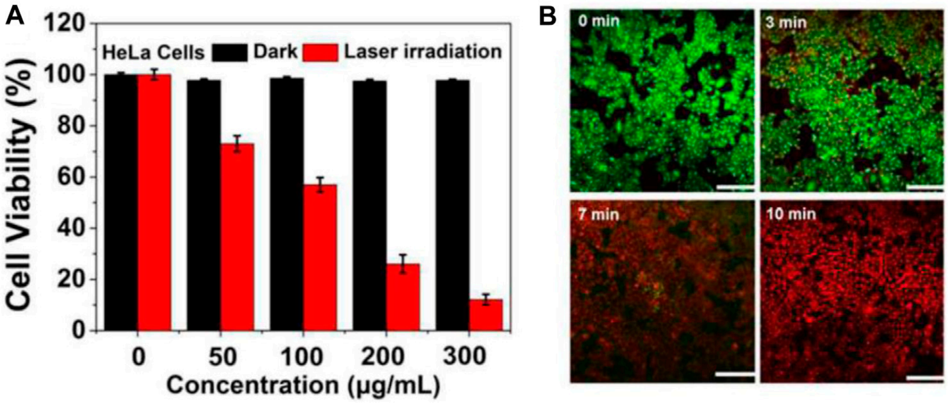

FIGURE 3
MTT assay and PTT effects reproduced from reference (Hou et al., 2018). **(A)** Relative viability of HeLa cells incubated with gradually increasing concentrations of CDs@Au nanoflowers before and after irradiation by a 750 nm laser (2 W/cm^2) for 10 min. **(B)** Under a 750 nm laser irradiation (2 W/cm^2) from 0–10 min, the time-dependent confocal images of HeLa cells incubated with 300 μg/mL of C-dots@Au nanoflowers and co-stained by calcein-AM/PI. Scale bar: 100 nm.

NIR-responsive drug release properties (Mean it can carry a drug inside them and release it when they are exposed to acidic conditions (like in cancer cells) or NIR light). The Au@C/CaP NPs can also enhance photothermal conversion efficiency by heat up when absorb near infrared light, which can kill cancer cells. The study demonstrates that Au@C/CaP NPs can be loaded with DOX, an extensively employed anti-cancer medication, and can effectively deliver DOX to cancer cells under acidic or NIR stimuli. The paper also shows that the Au@C/CaP NPs can induce synergistic CT and PTT of cancer cells by combining DOX-mediated cytotoxicity and NIR-induced hyperthermia. Hou et al. (2018) developed CDs@Au that exhibit efficient PT properties under laser irradiation of 750 nm, this study also evaluates the potential of using localized hyperthermia to facilitate PTT in HeLa cells (Entry-24 of Table 1). They achieved a photothermal conversion efficiency of around 22.5% and examined the effectiveness of CDs@Au nanoflowers in inducing PTT and assessing their impact on HeLa cells. Notably, the nanoflowers exhibited minimal toxicity to HeLa cells across a range of concentrations (0-300 μg/mL), indicating their low cytotoxicity.

However, when HeLa cells were exposed to a 750 nm laser at a power density of 2 W/cm^2 for a duration of 10 min, the viability of the cells decreased significantly. The decrease in cell viability was observed with increasing concentrations of CDs@Au nanoflowers, and the highest concentration tested, 300 μg/mL, resulted in approximately 90% cell death (Figures 3A). To assess the PTT efficacy of CDs@Au nanoflowers, a staining technique involving calcein-AM (green) and PI (red) was employed. The results indicated (Figures 3B) that cell death was dependent on the duration of laser irradiation. Following a 3-min irradiation, cells exhibited signs of heating caused by the CDs@ Au nanoflowers. Prolonging the irradiation time to 7 min led to the destruction of the majority of cells. After 10 min of irradiation, nearly all cells were eradicated. These findings demonstrate the effective performance of CDs@Au nanoflowers in PTT, highlighting their potential application in cancer treatment.

Gong et al. (2019) developed a mitochondrial oxidative stress amplifier (MitoCAT-g), a therapeutic agent (Entry-27 of Table 1). Which has the ability to selectively target and enter mitochondria, the powerhouses of cells. Once inside, it catalyzes reactions involving oxygen and glutathione, resulting in the generation of ROS that can cause irreversible mitochondrial damage and programmed cell death (apoptosis) in cancer cells. Interestingly, *in vivo* MitoCAT-g demonstrated remarkable efficacy in inhibiting tumor growth in both subcutaneous and orthotopic HCC PDX (hepatocellular carcinoma patient-derived xenograft) models, without any toxic activity. Li et al. (2022) have developed a novel nanohybrid called Au@CDs, which consists of Au and CDs (Entry-32 of Table 1). These nanohybrids demonstrate enzyme-like catalytic activity when exposed to NIR light and have excellent SERS properties. The Au@CDs nanohybrids possess NIR-photoinduced peroxidase-like catalytic processes via a SERS strategy, which can be utilized for cancer treatments. They also have glutathione oxidase-like activities that can enhanced the effects of ROS and other cancer treatments, making cancer cells more susceptible to damage. The work also shows the nanohybrids potential for PDT by promoting apoptosis in cancerous cells in just 3 min. SERS is utilized to watch the ROS activity of the TME, and this work shows that after the NIR light source is removed for 33 min, the presence of glutathione counteracts and eliminates the ROS activity of the TME. This research has significant implications for the development of artificial enzymes to be used in therapeutic strategies targeting ROS. Additionally, it introduces a novel spectroscopic tool that can be employed to evaluate the effectiveness of catalytic therapy in treating tumors.

3 Conclusion

Since their discovery with less than 20 years ago, the fluorescent Carbon Quantum Dots have emerged as effective alternate to other conventional quantum dots in the biomedical applications including imaging and therapy mainly because of their easy and simple synthesis, non-toxicity, enhanced biocompatibility and outstanding optical properties including high photostability, multi-color emission based on excitation, Near Infra-Red light absorbing ability and excellent upconversion photoluminescence. However, the interesting feature is their easy integration/doping with other metals and nanomaterials which enhances their physicochemical properties.

In this manuscript we have presented a summary of current applications of group-11 (Cu-, Ag- and Au)-Carbon Dots as innovative tools for cancer treatment. The metal-CDs nanocomposites, nanohybrids or heterostructures have shown remarkable and encouraging applications in the field of cancer theranostics. A detailed overview of the literature is given of group-11 metals-doped carbon dots having application in cancer imaging and therapy with potential candidates for clinical use. Both *in-vivo* and *in-vitro* anti-cancer studies show promising and encouraging results based on their biocompatibility, cytotoxicity and photostability. Different precursors as sources of CDs can be employed in doping, nano-composites formation, nano-hybrids formation or heterostructures with the mentioned metals.

In summary, this review demonstrates Ag-, Cu- and Au-doped-Carbon Dots as a new emerging class of C-based nano fluorescent materials for cancer diagnosis and therapy. However, from a perspective to be well-established in this direction few challenges need to be addressed.

4 Current challenges and future perspective

Despite their improved performance for cancer treatment based on novel methods of synthesis these group-11 metals doped carbon dots still have some challenges as follows:

1. Rapid microwave-assisted and sonochemical methods of synthesis needs to be established.
2. Although FL imaging is now well established, however, MRI, PAT and NIR based *in-vivo* and *ex-vivo* models have yet to be studied in more details.
3. Compared to photothermal therapy, photodynamic therapy has not been explored to the required extent.
4. Detailed characterization of formation mechanism of these metal-based-doped CDs using *in situ* techniques is necessary better understanding and useful application in cancer treatment.
5. To explain structure-performance correlation, more advanced techniques like SXR (synchronous X-ray radiation), TR-EPR (time-resolved electron paramagnetic resonance), SAC-STEM (spherical-aberration correction scanning/transmission electron microscopy), MALDI-TOF/MS matrix-assisted laser desorption ionization time-of-flight mass spectroscopy) needs to be used on regular basis for better understanding.
6. Regarding the excellent biocompatibility and almost zero toxicity carbon dots emitting deep red to NIR (650–1700 nm) that are excited by deep red to NIR light are desirable in future photo-theranostics in clinical applications. Therefore, more systematic research work is required in this direction.
7. There are many unanswered questions regarding different aspects of metal-doped carbon-dots that will for sure inspire multi-disciplinary research work looking into the rich future of these fluorescent nanomaterials.

Author contributions

IU: Data curation, Formal Analysis, Investigation, Software, Writing–original draft, Conceptualization, Methodology, Project administration, Resources, Supervision, Validation, Visualization, Writing–review and editing. HS: Data curation, Formal Analysis, Investigation, Software, Writing–original draft. MA: Data curation, Validation, Visualization, Writing–review and editing. O-U-RA: Data curation, Validation, Visualization, Writing–review and editing. MS: Data curation, Validation, Visualization, Writing–review and editing. MU: Data curation, Validation, Visualization, Writing–review and editing. AH: Data curation, Validation, Visualization, Writing–review and editing. MO: Data curation, Validation, Visualization, Writing–review and editing.

Funding

The author(s) declare that no financial support was received for the research, authorship, and/or publication of this article.

Acknowledgments

Support and cooperation of Muhammad Yaqub is highly acknowledged.

Conflict of interest

The authors declare that the research was conducted in the absence of any commercial or financial relationships that could be construed as a potential conflict of interest.

Publisher's note

References

Abdelhamid, H. N., Talib, A., and Wu, H. F. (2017). One pot synthesis of gold - carbon dots nanocomposite and its application for cytosensing of metals for cancer cells. *Talanta* 166, 357–363. doi:10.1016/j.talanta.2016.11.030

Ahmad Khera, R., Ahmad, R., Ullah, I., Abid, O.-U.-R., Fatunsin, O., Sher, M., et al. (2010). Cyclization vs. Elimination reactions of 5-Aryl-5-hydroxy 1,3-diones: one-pot synthesis of 2-Aryl-2,3-dihydro-4H-pyran-4-ones. *Helvetica Chim. Acta* 93 (9), 1705–1715. doi:10.1002/hlca.201000015

Alarfaj, N. A., El-Tohamy, M. F., and Oraby, H. F. (2018). CA 19-9 pancreatic tumor marker fluorescence immunosensing detection via immobilized carbon quantum dots conjugated gold nanocomposite. *Int. J. Mol. Sci.* 19 (4), 1162. doi:10.3390/ijms19041162

Ali, A., Ullah, I., Sher, M., Villinger, A., and Langer, P. (2009). Synthesis of sterically encumbered biaryls based on a ‘copper(I)-catalyzed arylation/[3+3] cyclocondensation’ strategy. *Tetrahedron Lett.* 50 (1), 118–120. doi:10.1016/j.tetlet.2008.10.093

Ali, I., Siyo, B., Hassan, Z., Malik, I., Ullah, I., Ali, A., et al. (2013). Synthesis of trifluoromethyl-substituted bi- and terphenyls by site-selective Suzuki–Miyaura reactions of various dihalogenated trifluoromethyl-benzene derivatives. *J. Fluor. Chem.* 145, 18–34. doi:10.1016/j.jfluchem.2012.11.005

Ali, M., Mir, S., Abid, O.-U.-R., Yawer, M. A., Ullah, I., and Roy, S. (2022). Nanoclay reinforced ternary blends based on biodegradable polymers for drug delivery application. *Int. J. biomaterials* 2022, 1–15. doi:10.1155/2022/6585305

Arshad, F., and Sk, M. P. (2020). Luminescent sulfur quantum dots for colorimetric discrimination of multiple metal ions. *ACS Appl. Nano Mater.* 3 (3), 3044–3049. doi:10.1021/acsanm.0c00394

Bao, Y. W., Hua, X. W., Li, Y. H., Jia, H. R., and Wu, F. G. (2018). Hyperthemia-promoted cytosolic and nuclear delivery of copper/carbon quantum dot-crosslinked nanosheets: multimodal imaging-guided photothermal cancer therapy. *ACS Appl. Mater Interfaces* 10 (2), 1544–1555. doi:10.1021/acsami.7b15332

Behi, M., Naficy, S., Chandrawati, R., and Dehghani, F. (2020). Nanoassembled peptide biosensors for rapid detection of matrilysin cancer biomarker. *Small* 16 (16), e1905994. doi:10.1002/smll.201905994

Bray, F., Ferlay, J., Soerjomataram, I., Siegel, R. L., Torre, L. A., and Jemal, A. (2018). Global cancer statistics 2018: GLOBOCAN estimates of incidence and mortality worldwide for 36 cancers in 185 countries. *CA A Cancer J. Clin.* 68 (6), 394–424. doi:10.3322/caac.21492

Chen, D., Li, B., Lei, T., Na, D., Nie, M., Yang, Y., et al. (2021). Selective mediation of ovarian cancer SKOV3 cells death by pristine carbon quantum dots/Cu(2)O composite through targeting matrix metalloproteinases, angiogenic cytokines and cytoskeleton. *J. Nanobiotechnology* 19 (1), 68. doi:10.1186/s12951-021-00813-8

Chopra, I. J. (2007). The increasing use of silver-based products as antimicrobial agents: a useful development or a cause for concern? *J. Antimicrob. Chemother.* 59 (4), 587–590. doi:10.1093/jac/dkm006

Dhar, S., Daniel, W. L., Giljohann, D. A., Mirkin, C. A., and Lippard, S. J. J. (2009). Polyvalent oligonucleotide gold nanoparticle conjugates as delivery vehicles for platinum (IV) warheads. *J. Am. Chem. Soc.* 131 (41), 14652–14653. doi:10.1021/ja9071282

El-Sayed, I. H., Huang, X., and El-Sayed, M. A. J. N. (2005). Surface plasmon resonance scattering and absorption of anti-EGFR antibody conjugated gold nanoparticles in cancer diagnostics: applications in oral cancer. *Nano Lett.* 5 (5), 829–834. doi:10.1021/nl050074e

Fang, Q., Dong, Y., Chen, Y., Lu, C.-H., Chi, Y., Yang, H.-H., et al. (2017). Luminescence origin of carbon based dots obtained from citric acid and amino group-containing molecules. *Carbon* 118, 319–326. doi:10.1016/j.carbon.2017.03.061

Farrer, N. J., and Sadler, P. J. J. (2008). Photochemotherapy: targeted activation of metal anticancer complexes. *Aust. J. Chem.* 61 (9), 669–674. doi:10.1071/ch08088

Gao, P., Liu, S., Su, Y., Zheng, M., and Xie, Z. (2020). Fluorine-doped carbon dots with intrinsic nucleus-targeting ability for drug and dye delivery. *Bioconjugate Chem.* 31 (3), 646–655. doi:10.1021/acs.bioconjchem.9b00801

Gedda, G., Yao, Y. Y., Chen, S. H., Ghule, A. V., Ling, Y. C., and Chang, J. Y. (2017). Facile synthesis of gold/gadolinium-doped carbon quantum dot nanocomposites for magnetic resonance imaging and photothermal ablation therapy. *J. Mater Chem. B* 5 (31), 6282–6291. doi:10.1039/c7tb01139c

George, N., Faoagali, J., and Muller, M. J. B. J. (1997). Silvazine (silver sulfadiazine and chlorhexidine) activity against 200 clinical isolates. *Burns* 23 (6), 493–495. doi:10.1016/s0305-4179(97)00047-8

Ghosal, K., Ghosh, S., Ghosh, D., and Sarkar, K. (2020). Natural polysaccharide derived carbon dot based *in situ* facile green synthesis of silver nanoparticles: synergistic effect on breast cancer. *Int. J. Biol. Macromol.* 162, 1605–1615. doi:10.1016/j.ijbiomac.2020.07.315

Giang, N. N., Won, H. J., Lee, G., and Park, S. Y. (2021). Cancer cells targeted visible light and alkaline Phosphatase-Responsive TiO2/Cu2+ carbon Dots-Coated wireless electrochemical biosensor. *Chem. Eng. J.* 417, 129196. doi:10.1016/j.cej.2021.129196

Gong, N., Ma, X., Ye, X., Zhou, Q., Chen, X., Tan, X., et al. (2019). Carbon-dot-supported atomically dispersed gold as a mitochondrial oxidative stress amplifier for cancer treatment. *Nat. Nanotechnol.* 14 (4), 379–387. doi:10.1038/s41565-019-0373-6

Guo, X.-L., Ding, Z.-Y., Deng, S.-M., Wen, C.-C., Shen, X.-C., Jiang, B.-P., et al. (2018). A novel strategy of transition-metal doping to engineer absorption of carbon dots for near-infrared photothermal/photodynamic therapies. *Carbon* 134, 519–530. doi:10.1016/j.carbon.2018.04.001

Hadad, C., González-Domínguez, J. M., Armelloni, S., Mattinzoli, D., Ikehata, M., Istif, A., et al. (2021). Graphene quantum dots: from efficient preparation to safe renal excretion. *Nano Res.* 14 (3), 674–683. doi:10.1007/s12274-020-3096-y

Hassan, Z., Ullah, I., Ali, I., Khera, R. A., Knepper, I., Ali, A., et al. (2013). Synthesis of tetraaryl-p-benzoquinones and 2,3-diaryl-1,4-naphthoquinones via Suzuki–Miyaura cross-coupling reactions. *Tetrahedron* 69 (2), 460–469. doi:10.1016/j.tet.2012.11.040

He, C., Lin, X., Mei, Y., Luo, Y., Yang, M., Kuang, Y., et al. (2022). Recent advances in carbon dots for *in vitro*/Vivo fluorescent bioimaging: a mini-review. *Front. Chem.* 10, 905475. doi:10.3389/fchem.2022.905475

Hou, C., Chen, S., and Wang, M. (2018). Facile preparation of carbon-dot-supported nanoflowers for efficient photothermal therapy of cancer cells. *Dalton Trans.* 47 (6), 1777–1781. doi:10.1039/c8dt00026c

Huang, X., Zhang, F., Zhu, L., Choi, K. Y., Guo, N., Guo, J., et al. (2013). Effect of injection routes on the biodistribution, clearance, and tumor uptake of carbon dots. *ACS Nano* 7 (7), 5684–5693. doi:10.1021/nn401911k

Ibad, M. F., Hussain, M., Abid, O.-U.-R., Ali, A., Ullah, I., Zinad, D. S., et al. (2010). One-Pot synthesis of unsymmetrical 2,3-diarylindoles by site-selective suzuki-miyaura reactions of N-Methyl-2,3-dibromoindole. *Synlett* 2010 (03), 411–414. doi:10.1055/s-0029-1219201

Jiang, F., Ding, B., Zhao, Y., Liang, S., Cheng, Z., Xing, B., et al. (2020). Biocompatible CuO-decorated carbon nanoplatforms for multiplexed imaging and enhanced antitumor efficacy via combined photothermal therapy/chemodynamic therapy/chemotherapy. *Sci. China Mater.* 63 (9), 1818–1830. doi:10.1007/s40843-019-1397-0

Jiao, M., Wang, Y., Wang, W., Zhou, X., Xu, J., Xing, Y., et al. (2022). Gadolinium doped red-emissive carbon dots as targeted theranostic agents for fluorescence and MR imaging guided cancer phototherapy. *Chem. Eng. J.* 440, 135965. doi:10.1016/j.cej.2022.135965

Kar, A., Dagar, P., Kumar, S., Singh Deo, I., Vijaya Prakash, G., and Ganguli, A. K. (2023). Photoluminescence and lifetime studies of C-dot decorated CdS/ZnFe2O4 composite designed for photoelectrochemical applications. *J. Photochem. Photobiol. A Chem.* 439, 114612. doi:10.1016/j.jphotochem.2023.114612

Kaurav, H., Verma, D., Bansal, A., Kapoor, D. N., and Sheth, S. (2023). Progress in drug delivery and diagnostic applications of carbon dots: a systematic review. *Front. Chem.* 11, 1227843. doi:10.3389/fchem.2023.1227843

Khan, M. E., Mohammad, A., and Yoon, T. (2022). State-of-the-art developments in carbon quantum dots (CQDs): photo-catalysis, bio-imaging, and bio-sensing applications. *Chemosphere* 302, 134815. doi:10.1016/j.chemosphere.2022.134815

Khera, R. A., Ullah, I., Ahmad, R., Riahi, A., Hung, N. T., Sher, M., et al. (2010). Synthesis of functionalized triarylmethanes by combination of FeCl3-catalyzed benzylations of acetylacetone with [3+3] cyclocondensations. *Tetrahedron* 66 (9), 1643–1652. doi:10.1016/j.tet.2010.01.022

Leonardi, A. A., Lo Faro, M. J., Petralia, S., Fazio, B., Musumeci, P., Conoci, S., et al. (2018). Ultrasensitive label- and PCR-free genome detection based on cooperative hybridization of silicon nanowires optical biosensors. *ACS Sensors* 3 (9), 1690–1697. doi:10.1021/acssensors.8b00422

Li, L., Yang, J., Wei, J., Jiang, C., Liu, Z., Yang, B., et al. (2022). SERS monitoring of photoinduced-enhanced oxidative stress amplifier on Au@carbon dots for tumor catalytic therapy. *Light Sci. Appl.* 11 (1), 286. doi:10.1038/s41377-022-00968-5

Li, L.-p., Ren, X.-f., Bai, P.-r., Liu, Y., Xu, W.-y., Xie, J., et al. (2021). Near-infrared emission carbon dots for bio-imaging applications. *New Carbon Mater.* 36 (3), 632–638. doi:10.1016/s1872-5805(21)60041-0

Li, R. S., Gao, P. F., Zhang, H. Z., Zheng, L. L., Li, C. M., Wang, J., et al. (2017a). Chiral nanoprobes for targeting and long-term imaging of the Golgi apparatus. *Chem. Sci.* 8 (10), 6829–6835. doi:10.1039/c7sc01316g

Li, W., Zhang, H., Zheng, Y., Chen, S., Liu, Y., Zhuang, J., et al. (2017b). Multifunctional carbon dots for highly luminescent orange-emissive cellulose based composite phosphor construction and plant tissue imaging. *Nanoscale* 9 (35), 12976–12983. doi:10.1039/c7nr03217j

Liu, J., Li, R., and Yang, B. (2020a). Carbon dots: a new type of carbon-based nanomaterial with wide applications. *ACS Cent. Sci.* 6 (12), 2179–2195. doi:10.1021/acscentsci.0c01306

Liu, P., Wang, L., Zhao, K., Liu, Z., Cao, H., Ye, S., et al. (2020b). High luminous efficiency Au@CDs for sensitive and label-free electrochemiluminescent detection of circulating tumor cells in serum. *Sensors Actuators B Chem.* 316, 128131. doi:10.1016/j.snb.2020.128131

Liu, R., Yang, Z., Zhang, L., Zhao, J., Hou, C., and Zhao, S. (2020c). A near infrared dye-coated silver nanoparticle/carbon dot nanocomposite for targeted tumor imaging and enhanced photodynamic therapy. *Nanoscale Adv.* 2 (1), 489–494. doi:10.1039/c9na00596j

Liu, R., Zhang, L., Zhao, J., Hou, C., Huang, Y., Huang, Z., et al. (2019). A distinctive spinach-based carbon nanomaterial with chlorophyll-rich and near-infrared emission for simultaneous *in vivo* Biothiol imaging and dual-enhanced photodynamic therapy of tumor. *Adv. Ther.* 2, 1900011. doi:10.1002/adtp.201900011

Liu, S., Cao, H., Wang, Z., Tu, W., and Dai, Z. (2015). Label-free photoelectrochemical cytosensing via resonance energy transfer using gold nanoparticle-enhanced carbon dots. *Chem. Commun. (Camb)* 51 (75), 14259–14262. doi:10.1039/c5cc04092b

Mohammadi, S., Salimi, A., Hamd-Ghadareh, S., Fathi, F., and Soleimani, F. (2018). A FRET immunosensor for sensitive detection of CA 15-3 tumor marker in human serum sample and breast cancer cells using antibody functionalized luminescent carbon-dots and AuNPs-dendrimer aptamer as donor-acceptor pair. *Anal. Biochem.* 557, 18–26. doi:10.1016/j.ab.2018.06.008

Mohammed, S. A. A., Khashan, K. S., Jabir, M. S., Abdulameer, F. A., Sulaiman, G. M., Al-Omar, M. S., et al. (2022). Copper oxide nanoparticle-decorated carbon nanoparticle composite colloidal preparation through laser ablation for antimicrobial and antiproliferative actions against breast cancer cell line, MCF-7. *Biomed. Res. Int.* 2022, 1–13. doi:10.1155/2022/9863616

Naik, K., Chaudhary, S., Ye, L., and Parmar, A. S. (2022). A strategic review on carbon quantum dots for cancer-diagnostics and treatment. *Front. Bioeng. Biotechnol.* 10, 882100. doi:10.3389/fbioe.2022.882100

Najaflu, M., Shahgolzari, M., Bani, F., and Khosroushahi, A. Y. (2022). Green synthesis of near-infrared copper-doped carbon dots from alcea for cancer photothermal therapy. *ACS Omega* 7 (38), 34573–34582. doi:10.1021/acsomega.2c04484

Nawaz, M., Ullah, I., Abid, O.-u.-R., Ali, A., Patonay, T., Saghyan, A. S., et al. (2012). Synthesis of functionalized para- and meta-terphenyls based on site-selective Suzuki cross-coupling reactions of bis(triflates) of methyl 2,5-dihydroxybenzoate and methyl 2,4-dihydroxybenzoate. *Can. J. Chem.* 91 (11), 1–11. doi:10.1139/cjc-2012-0201

Nawaz, M., Ullah, I., Abid, O.-U.-R., Villinger, A., and Langer, P. (2011). Synthesis of 2′,4-diarylbenzophenones through site-selective suzuki–miyaura reactions of bis(triflates) of 2′,4-dihydroxybenzophenones. *Eur. J. Org. Chem.* 2011 (33), 6670–6684. doi:10.1002/ejoc.201100762

Nekoueian, K., Amiri, M., Sillanpää, M., Marken, F., Boukherroub, R., and Szunerits, S. (2019). Carbon-based quantum particles: an electroanalytical and biomedical perspective. *Chem. Soc. Rev.* 48 (15), 4281–4316. doi:10.1039/c8cs00445e

Nie, S. (2010). Understanding and overcoming major barriers in cancer nanomedicine. *Nanomedicine* 5 (4), 523–528. doi:10.2217/nnm.10.23

Nocito, G., Calabrese, G., Forte, S., Petralia, S., Puglisi, C., Campolo, M., et al. (2021). Carbon dots as promising tools for cancer diagnosis and therapy. *Cancers (Basel)* 13 (9), 1991. doi:10.3390/cancers13091991

Pal, A., Arshad, F., and Sk, M. P. (2020). Emergence of sulfur quantum dots: unfolding their synthesis, properties, and applications. *Adv. Colloid Interface Sci.* 285, 102274. doi:10.1016/j.cis.2020.102274

Park, J. H., Yu, K., Min, J. Y., Chung, Y. H., and Yoon, J. Y. (2021). A dual-functional lactate sensor based on silver nanoparticle-coated carbon dots. *Bull. Korean Chem. Soc.* 42 (5), 767–772. doi:10.1002/bkcs.12257

Priyadarshini, E., Meena, R., Bohidar, H. B., Sharma, S. K., Abdellattif, M. H., Saravanan, M., et al. (2022). Comparative *in vitro* cytotoxicity study of carbon dot-based organometallic nanoconjugates: exploration of their cell proliferation, uptake, and localization in cancerous and normal cells. *Oxid. Med. Cell. Longev.* 2022, 1–11. doi:10.1155/2022/3483073

Raubenheimer, H. G., and Schmidbaur, H. J. (2014). The late start and amazing upswing in gold chemistry. *J. Chem. Educ.* 91 (12), 2024–2036. doi:10.1021/ed400782p

Rosi, N. L., Giljohann, D. A., Thaxton, C. S., Lytton-Jean, A. K., Han, M. S., and Mirkin, C. A. J. S. (2006). Oligonucleotide-modified gold nanoparticles for intracellular gene regulation. *Science* 312 (5776), 1027–1030. doi:10.1126/science.1125559

Sachdev, A., Matai, I., and Gopinath, P. (2015). Dual-functional carbon dots-silver@ zinc oxide nanocomposite: *in vitro* evaluation of cellular uptake and induction of apoptosis. *J. Mater Chem. B* 3 (7), 1217–1229. doi:10.1039/c4tb02043j

Safaei, R., and Howell, S. B. J. C. (2005). Copper transporters regulate the cellular pharmacology and sensitivity to Pt drugs. *Crit. Rev. Oncol. Hematol.* 53 (1), 13–23. doi:10.1016/j.critrevonc.2004.09.007

Scheiber, I., Dringen, R., and Mercer, J. F. B. (2013). *Copper: effects of deficiency and overload. Interrelations between essential metal ions and human diseases*. Dordrecht: Springer Netherlands, 359–387.

Shao, J., Zhu, S., Liu, H., Song, Y., Tao, S., and Yang, B. (2017). Full-color emission polymer carbon dots with quench-resistant solid-state fluorescence. *Adv. Sci.* 4 (12), 1700395. doi:10.1002/advs.201700395

Soumya, R. S., and Hela, P. G. J. D. P. L. (2013). Nano silver based targeted drug delivery for treatment of cancer. *Nanomater. (Basel)* 5 (4), 189–197.

Sun, S., Chen, Q., Tang, Z., Liu, C., Li, Z., Wu, A., et al. (2020). Tumor microenvironment stimuli-responsive fluorescence imaging and synergistic cancer therapy by carbon-dot-Cu(2+) nanoassemblies. *Angew. Chem. Int. Ed. Engl.* 59 (47), 21041–21048. doi:10.1002/anie.202007786

Sun, S., Guan, Q., Liu, Y., Wei, B., Yang, Y., and Yu, Z. (2019). Highly luminescence manganese doped carbon dots. *Chin. Chem. Lett.* 30 (5), 1051–1054. doi:10.1016/j.cclet.2019.01.014

Sunbal, M. A., OmerAbid, M. M., Ullah, I., Abid, O. U. R., and Sohail, M. (2023). Chemical insights into the synthetic chemistry of five-membered saturated heterocycles—a transition metal–catalyzed approach. *Front. Chem.* 11, 1185669. doi:10.3389/fchem.2023.1185669

Tejwan, N., Saini, A. K., Sharma, A., Singh, T. A., Kumar, N., and Das, J. (2021). Metal-doped and hybrid carbon dots: a comprehensive review on their synthesis and biomedical applications. *J. Control Release* 330, 132–150. doi:10.1016/j.jconrel.2020.12.023

Ullah, I., Ilyas, M., Omer, M., Alamzeb, M., Adnan, H., and Sohail, M. (2022). Fluorinated triazoles as privileged potential candidates in drug development—focusing on their biological and pharmaceutical properties. *Front. Chem.* 10, 926723. doi:10.3389/fchem.2022.926723

Ullah, I., Khera, R. A., Hussain, M., Villinger, A., and Langer, P. (2009). Synthesis of tetraaryl-p-benzoquinones by Suzuki–Miyaura cross-coupling reactions of tetrabromo-p-benzoquinone. *Tetrahedron Lett.* 50 (32), 4651–4653. doi:10.1016/j.tetlet.2009.05.115

Ullah, I., Nawaz, M., Villinger, A., and Langer, P. (2011a). Synthesis of 8,9-disubstituted fluoranthenes by domino two-fold Heck/electrocyclization/dehydrogenation of 1,2-dibromoacenaphthylene. *Tetrahedron Lett.* 52 (16), 1888–1890. doi:10.1016/j.tetlet.2011.02.032

Ullah, I., Nawaz, M., Villinger, A., and Langer, P. (2011b). Synthesis of trifluoromethyl-substituted di- and terphenyls by site-selective suzuki-miyaura reactions of 1,4-Dibromo-2-trifluoromethyl-benzene. *Synlett* 2011 (13), 1895–1899. doi:10.1055/s-0030-1260956

Ullah, I., Sher, M., Khera, R. A., Ali, A., Ibad, M. F., Villinger, A., et al. (2010a). Chelation-control in the formal [3+3] cyclization of 1,3-bis-(silyloxy)-1,3-butadienes with 1-hydroxy-5-silyloxy-hex-4-en-3-ones. One-pot synthesis of 3-aryl-3,4-dihydroisocoumarins. *Tetrahedron* 66 (10), 1874–1884. doi:10.1016/j.tet.2010.01.019

Ullah, I., Sher, M., Khera, R. A., Ali, A., Nawaz, M., Shkoor, M., et al. (2010b). Synthesis of of sterically encumbered biaryls based on a 'copper(I)-catalyzed arylation/[3+3] cyclocondensation' strategy. *Tetrahedron* 66 (21), 3824–3835. doi:10.1016/j.tet.2010.03.054

Wang, H., Cao, G., Gai, Z., Hong, K., Banerjee, P., and Zhou, S. (2015). Magnetic/NIR-responsive drug carrier, multicolor cell imaging, and enhanced photothermal therapy of gold capped magnetite-fluorescent carbon hybrid nanoparticles. *Nanoscale* 7 (17), 7885–7895. doi:10.1039/c4nr07335e

Wang, H., Zhang, M., Zhang, L., Li, S., Li, L., Li, X., et al. (2017). Near-infrared light and pH-responsive Au@carbon/calcium phosphate nanoparticles for imaging and chemo-photothermal cancer therapy of cancer cells. *Dalton Trans.* 46 (43), 14746–14751. doi:10.1039/c7dt02274c

Wang, J., Xu, M., Wang, D., Li, Z., Primo, F. L., Tedesco, A. C., et al. (2019a). Copper-doped carbon dots for optical bioimaging and photodynamic therapy. *Inorg. Chem.* 58 (19), 13394–13402. doi:10.1021/acs.inorgchem.9b02283

Wang, W., Wang, Y., Pan, H., Cheddah, S., and Yan, C. (2019b). Aptamer-based fluorometric determination for mucin 1 using gold nanoparticles and carbon dots. *Mikrochim. Acta* 186 (8), 544. doi:10.1007/s00604-019-3516-4

Yang, S.-T., Cao, L., Luo, P. G., Lu, F., Wang, X., Wang, H., et al. (2009). Carbon dots for optical imaging *in vivo*. *J. Am. Chem. Soc.* 131 (32), 11308–11309. doi:10.1021/ja904843x

Yu, Y., Song, M., Chen, C., Du, Y., Li, C., Han, Y., et al. (2020). Bortezomib-encapsulated CuS/carbon dot nanocomposites for enhanced photothermal therapy via stabilization of polyubiquitinated substrates in the proteasomal degradation pathway. *ACS Nano* 14 (8), 10688–10703. doi:10.1021/acsnano.0c05332

Yue, J.-s., Yuan, F.-y., Qiu, H.-x., Li, Y., Li, J., Xue, Y.-h., et al. (2023). A review of fluorescent carbon dots: synthesis, photoluminescence mechanism, solid-state photoluminescence and applications in white light-emitting diodes. *New Carbon Mater.* 38 (3), 478–492. doi:10.1016/s1872-5805(23)60742-5

Zhai, Y., Wang, Y., Li, D., Zhou, D., Jing, P., Shen, D., et al. (2018). Red carbon dots-based phosphors for white light-emitting diodes with color rendering index of 92. *J. Colloid Interface Sci.* 528, 281–288. doi:10.1016/j.jcis.2018.05.101

Zhang, L., Wang, D., Huang, H., Liu, L., Zhou, Y., Xia, X., et al. (2016). Preparation of gold–carbon dots and ratiometric fluorescence cellular imaging. *ACS Appl. Mater. Interfaces* 8 (10), 6646–6655. doi:10.1021/acsami.5b12084

Zhang, X., Wei, X., Qi, J., Shen, J., Xu, J., Gong, G., et al. (2022). Simultaneous detection of bladder cancer exosomal MicroRNAs based on inorganic nanoflare and DNAzyme walker. *Anal. Chem.* 94 (11), 4787–4793. doi:10.1021/acs.analchem.1c05588

Zheng, D.-W., Li, B., Li, C.-X., Fan, J.-X., Lei, Q., Li, C., et al. (2016). Carbon-Dot-decorated carbon nitride nanoparticles for enhanced photodynamic therapy against hypoxic tumor via water splitting. *ACS Nano* 10 (9), 8715–8722. doi:10.1021/acsnano.6b04156

frontiers | Frontiers in Bioengineering and Biotechnology

TYPE Mini Review
PUBLISHED 21 December 2023
DOI 10.3389/fbioe.2023.1332993

OPEN ACCESS

EDITED BY
Palashuddin Sk,
Aligarh Muslim University, India

REVIEWED BY
Atikur Hassan,
Indian Institute of Technology Patna, India
Amaresh Kumar Sahoo,
Indian Institute of Information Technology, India

*CORRESPONDENCE
Li Zhou,
✉ zhouli@glut.edu.cn
Guangming Lu,
✉ lugm33@163.com

RECEIVED 04 November 2023
ACCEPTED 07 December 2023
PUBLISHED 21 December 2023

CITATION
Huang Y, Lu G and Zhou L (2023), A mini review on selenium quantum dots: synthesis and biomedical applications. *Front. Bioeng. Biotechnol.* 11:1332993. doi: 10.3389/fbioe.2023.1332993

A mini review on selenium quantum dots: synthesis and biomedical applications

Yanhua Huang, Guangming Lu* and Li Zhou*

Guangxi Key Laboratory of Optical and Electronic Materials and Devices, Guangxi Colleges and Universities Key Laboratory of Natural and Biomedical Polymer Materials, and College of Materials Science and Engineering, Guilin University of Technology, Guilin, China

In recent years, the demand for advanced biomedical nanomaterials has seen a noticeable surge. Among the essential trace elements in the human body, selenium has gained recognition for its anti-cancer, antioxidant, and immune regulatory properties. However, traditional selenium-based semiconductor quantum dots (QDs) are often comprised of heavy metal elements that tend to be toxic, thereby limiting their usage in biomedical applications. Fortunately, the advent of elemental selenium quantum dots (SeQDs), a new kind of fluorescent nanomaterial with unique physicochemical properties, has provided a solution to this problem. These SeQDs are known for their low toxicity and good biocompatibility, making them a promising candidate for biomedical applications. In this mini-review, we delve into the synthesis methods of fluorescent SeQDs and the latest progress in their applications in bioimaging, biosensing, and diagnosis treatment. Finally, we identify the major challenges and future prospects in the field of SeQDs.

KEYWORDS

selenium quantum dots, fluorescence, bioimaging, biosensing, diagnosis

Introduction

Recent years have witnessed a surge of interest in fluorescent quantum dots (QDs), which are tiny structures made of semiconductor nanocrystals. The QDs offer striking advantages, such as remarkable optical, electrical, electrochemical, and catalytic properties, thus proving to be highly versatile for an array of practical applications (Lin et al., 2022; Triana et al., 2022). However, the conventional QDs typically contain heavy metals from the II-IV or III-V groups of the periodic table, making them unsuitable for applications in biological and environmental fields due to their toxic nature. Consequently, there is an urgent need to develop alternative QDs that are composed of non-toxic materials and that can be used in a variety of new application areas (Yao et al., 2018; Gao et al., 2020; Ruan and Zhou, 2022). As such, the development of metal-free fluorescent QDs, such as carbon QDs (Zhou et al., 2013; Liao et al., 2016; Lu et al., 2018), graphene QDs (Zhou et al., 2017), sulfur QDs (Song et al., 2019; Wang et al., 2019; Arshad and Sk, 2020; Gao et al., 2022), and silicon QDs (Yang et al., 2023) has garnered significant interest as they present viable alternatives to traditional semiconductor QDs, with the added benefit of being non-toxic and able to be applied in diverse fields.

Selenium (Se) is considered to be one of the essential trace elements for the human body (Huang et al., 2020b). However, the practical applications of semiconductor quantum dots containing selenium elements, such as cadmium selenide quantum dots, lead selenide quantum dots, silver selenide quantum dots, and others (He et al., 2017; Sousa et al., 2020; Yuan et al., 2022), are severely restricted due to their toxicity, mainly caused by the presence of heavy metal

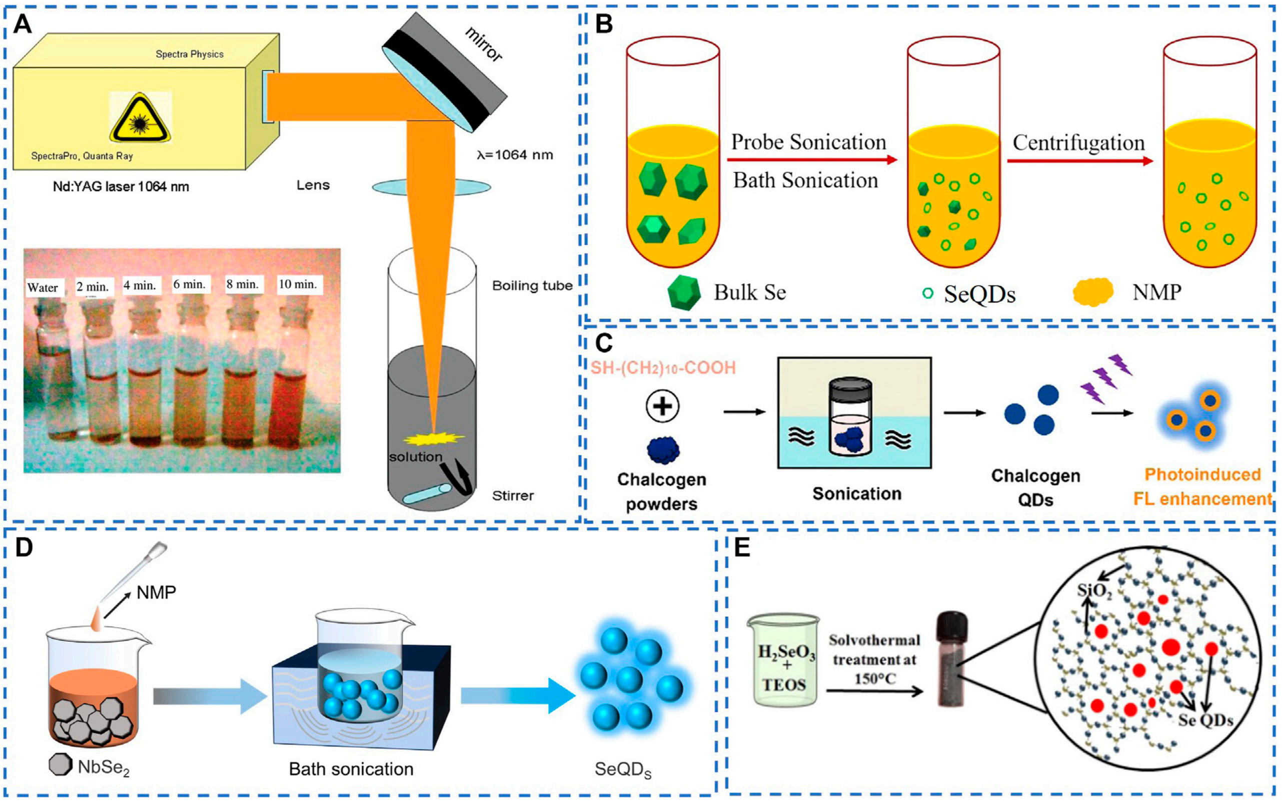

FIGURE 1
(A) Schematic diagram of preparation of SeQDs by laser irradiation. Reproduced, with permission, from Singh et al. (2010). Copyright 2010, American Chemical Society. **(B)** Ultrasonic assisted synthesis of SeQDs from bulk selenium powder. Reproduced, with permission, from Jiang et al. (2020). Copyright 2020, American Chemical Society. **(C)** Preparation of SeQDs by ultrasonic treatment of bulk selenium powder in the presence of thiolates. Reproduced, with permission, from Zhang et al. (2021). Copyright 2021, American Chemical Society. **(D)** Preparation of SeQDs by sonication treatment of $NbSe_2$. **(E)** Solvothermal synthesis of SeQDs in the presence of TEOS. Reproduced, with permission, from Anupama et al. (2021). Copyright 2021, American Chemical Society.

ions. Recently, metal-free elemental selenium QDs (SeQDs) have emerged as a new type of fluorescent nanomaterial with the potential to replace traditional selenium-based QDs. This is due to their unique physicochemical properties, low cytotoxicity and good biocompatibility (Deng et al., 2023; Lv et al., 2023). Currently, there has been a dearth of literature discussing the properties and potential applications of SeQDs, despite their importance in biomedical applications. As such, there is a need to write a review paper to consolidate the research progress made in SeQDs. This mini review aims to provide an overview of the various approaches for synthesis of SeQDs, followed by discussions on their toxicity and biomedical applications, including bioimaging, biosensing, and disease therapy. The challenges and opportunities in SeQDs research, specifically in terms of synthesis and biomedical applications, are also discussed. Overall, this mini review hopes to shed light on SeQDs and encourage further research and practical applications by researchers.

Synthesis

The synthesis of SeQDs can be achieved through two strategies: the "top-down" and the "bottom-up" strategies, similar to other reported fluorescent QDs. The "top-down" strategy entails crushing the bulk selenium powder using physical forces, resulting in the production of SeQDs ranging in size from 2 to 10 nm. Singh et al. dispersed bulk selenium powder into a boiling tube filled with double steamed water and subjected it to irradiation using a pulsed Nd:YAG laser for 15 min. They successfully obtained SeQDs with a particle size of 2.74 nm (Singh et al., 2010). Similarly, Guisbiers et al. dispersed bulk selenium powder in ethanol and exposed it to laser beams at three different wavelengths, namely, 355, 532, and 1,064 nm. They discovered that the SeQDs obtained after 4–6 h of irradiation at any of the three wavelengths were all smaller than 4 nm (Guisbiers et al., 2015) (Figure 1A). Furthermore, they noted that the size and optical properties of the synthesized SeQDs were highly reliant on the duration of irradiation. Nevertheless, the efficiency of SeQDs preparation *via* laser irradiation is low, and it poses certain risks to human health. In addition to laser irradiation treatment, preparation of SeQDs through ultrasonication liquid-phase exfoliation of bulk selenium powder has also been reported. A study by Jiang et al. involved adding bulk selenium powder to N-methylpyrrolidone (NMP) solvent and subjecting the mixture to ultrasonic bath treatment at a temperature of 5 °C and ultrasonic power of 400 W (Jiang et al., 2020) (Figure 1B). This led to the successful synthesis of SeQDs with an average diameter of 4.9 nm, opening up new method for SeQDs synthesis. Another study by Zhang et al. also used bulk selenium powder in the presence of thiolates and NMP solvent to prepare SeQDs through ultrasonication treatment (Zhang et al., 2021) (Figure 1C). Initially, the 100 W power bath sonication was employed, followed by the application of 110 W tip sonication for the treatment process. They found that NMP was the most effective solvent among other solvents due to its surface tension matching with the surface energy of selenium powder. Furthermore, the SeQDs exhibited exceptional photostability, accompanied by a notable increase in fluorescence intensity with extended ultraviolet light irradiation time. This intriguing result presents a promising avenue for optimizing the optical properties of SeQDs.

Conversely, the "bottom-up" strategy involves the direct synthesis of SeQDs from selenium-based precursors by chemical reaction (Huang et al., 2020a). Thus far, two types of precursors have been utilized: elemental selenium powder and selenium-containing compounds. For instance, Yang and colleagues have successfully synthesized SeQDs by introducing selenium powder into a sodium sulfite solution along with bovine serum albumin. After adjusting the pH of the reaction mixture to 6, the mixture was incubated at varying temperatures and time intervals. It was discovered that amorphous SeQDs could be achieved by incubating the mixture at 20 °C for 12 h. On the other hand, crystalline SeQDs were obtained by incubating the mixture at 80 °C for 24 h. The average sizes of the amorphous and crystalline SeQDs acquired were reported to be 2.25 nm and 4.10 nm, respectively (Wang et al., 2016; Zhu et al., 2019). In addition, SeQDs with a mean size of 4.6 nm can be synthesized by introducing a mixture of selenium powder, potassium hydroxide, and hydrazine hydrate into a solution of κ-carrageenan (κ-CG) after heating at 70 °C under an argon atmosphere for 30 min (Lesnichaya et al., 2019). The authors proposed that hydrazine hydrate acts as a reducing agent, converting selenium powder into highly reactive selenide anions (Se^{2-}) in an alkaline environment. It was observed that an aqueous solution of κ-CG can then oxidize the Se^{2-} anions to zero valent Se atoms.

Alternatively, the direct oxidation or reduction of selenium-containing compounds, such as H_2SeO_3 and $NbSe_2$, to zero-valent Se atoms, has also been employed in the synthesis of SeQDs. For instance, Fujishima et al. demonstrated that UV irradiation of ethanol and methanol solutions containing H_2SeO_3 can yield highly dispersed SeQDs on the surface of TiO_2. Interestingly, the average size of the SeQDs was found to increase as the irradiation time increased. Following a 2 h irradiation period, the average size of the SeQDs reached 8.7 nm (Fujishima et al., 2014). However, this method necessitates specific instrumentation and entails a complex operational procedure. Qian and colleagues utilized $NbSe_2$, which is constrained with weak van der Waals forces, as a selenium precursor and added it to NMP. The mixture was then subjected to continuous high power ultrasonication of 500 W for 4 h. The resulting dispersion was then centrifuged, and the supernatant was collected to obtain SeQDs with an average size of 2.95 nm and a remarkable photoluminescence quantum yield of 22.7%, which is the highest reported quantum yield so far (Qian et al., 2017) (Figure 1D). Similarly, Guo and colleagues reported the synthesis of SeQDs by dissolving $NbSe_2$ in distilled water and subjecting it to an autoclave reaction at 60 °C for 4 h. Vitamin C was subsequently added, and ultrasound treatment was performed at pH 8.0 for 3 h to yield SeQDs with an average size of approximately 5 nm. The prepared SeQDs exhibited favorable colloidal stability and maintain their size in pure water, PBS buffer (pH = 7.4), and cell culture medium. However, the time-consuming synthesis and intricate post-processing steps pose significant challenges for scalable production of SeQDs (Guo et al., 2021). To satisfy the need for solid-state fluorescent quantum dots (QDs) with anti-self-quenching properties, Anupama et al. utilized a solvation-assisted sol-gel approach to fabricate solid-state luminescent SeQDs with an average size between 3 and 8 nm (Anupama et al., 2021) (Figure 1E). Their findings suggest that the solvothermal decomposition of selenite leads to nucleation of triangular selenium nanocrystalline in the presence of tetraethyl orthosilicate (TEOS).

Various physical and chemical approaches have been developed for the synthesis of fluorescent SeQDs based on "top-down" and "bottom-up" strategies (Ruan and Zhou, 2022; Yang et al., 2023). Physical methods, such as laser irradiation and ultrasound, require advanced equipment and have high energy consumption but relatively low yield (Huang et al., 2023). Chemical methods, such as wet chemistry, offer higher yields but may involve the use of toxic ingredients, high temperatures, and high pressures, posing certain production risks (Yao et al., 2018; Gao et al., 2020). Therefore, there is a strong need for the development of a facile and effective approach to enable scalable synthesis of highly fluorescent SeQDs. On the other hand, biosynthesis technique is widely recognized as a clean, efficient, safe, and promising method for preparing nanoparticles. However, the biosynthesis of SeQDs has not been reported to date. It is anticipated that this technique will be employed in the future for the synthesis of fluorescent SeQDs.

Biomedical applications

The increasing interest in the biomedical application of SeQDs has highlighted the importance of evaluating their potential toxicity. To assess SeQDs toxicity, researchers have broadly utilized cell viability tests with specific assays like MTT, CCK-8, and WST-1 (Kundu et al., 2019; Ahmadi et al., 2022). For example, in a study by Guo et al., MTT assays were employed to evaluate the cytotoxicity of SeQDs on SH-SY5Y cells, demonstrating that SeQDs had much lower cytotoxicity than elemental selenium powder (Guo et al., 2021) (Figure 2A). Likewise, Zhang and colleagues examined the toxic effects of SeQDs on HeLa and HEK-293 cells and found that even after incubation with 1 mg/mL SeQDs for 24 h, the cell viability remained at 80% (Zhang et al., 2021). The results of these studies provide a solid foundation for further research on the biomedical applications of SeQDs, as their low cytotoxicity suggests a promising safety profile.

Currently, SeQDs find wide application in the field of biomedicine, particularly in bioimaging, biosensing, and diagnosing treatment. Bioimaging plays a critical role in enhancing our comprehension of cellular structures and physiological processes in organisms. Among the diverse range of fluorescent nanomaterials, SeQDs stand out due to their unique photoluminescence properties. What sets SeQDs apart is the fact that selenium is a necessary trace element in the body (Lian et al., 2019; Zhou et al., 2022a), enhancing their significance in bioimaging.

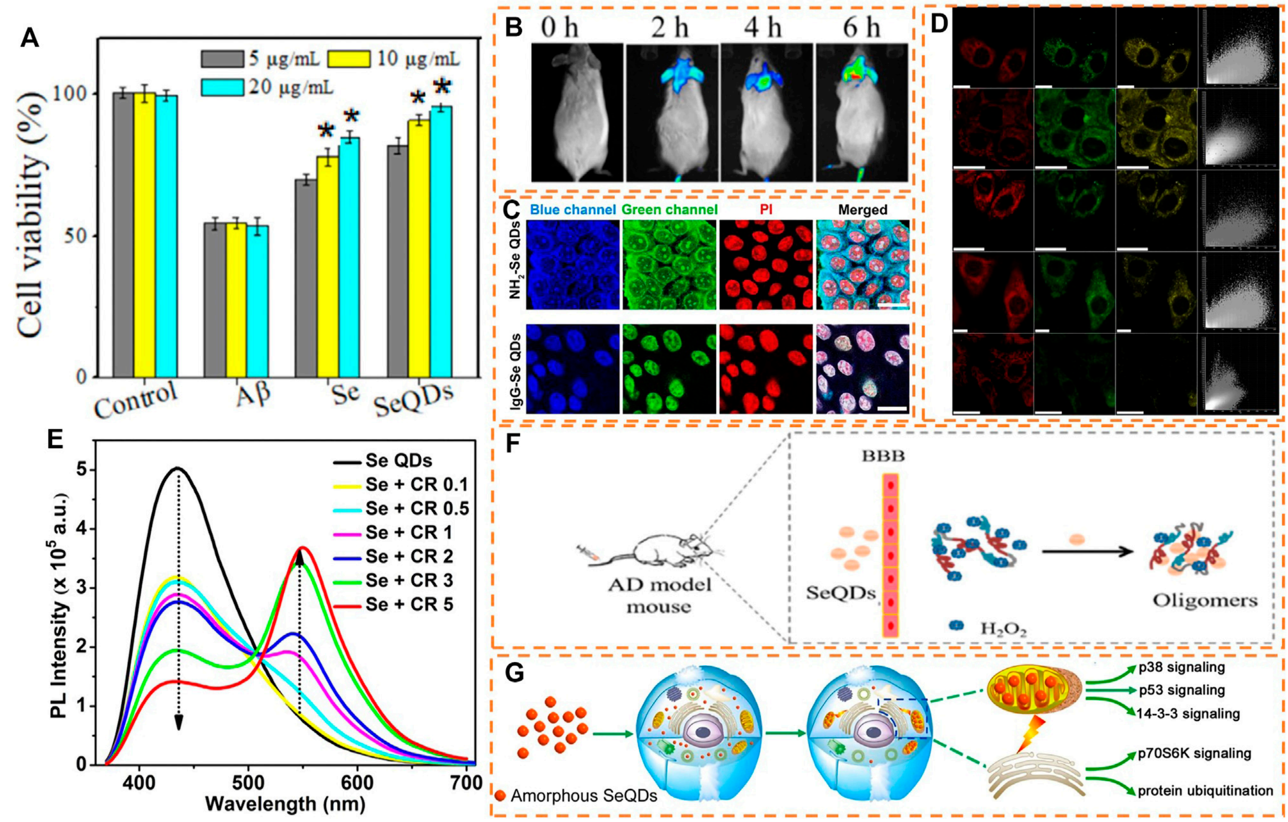

FIGURE 2
(A) Cytotoxicity assessment of SeQDs and **(B)** *in vivo* fluorescence imaging with SeQDs. Reproduced, with permission, from Guo et al. (2021). Copyright 2021, American Chemical Society. **(C)** LSCM fluorescence images of fixed/permeated cells treated with NH$_2$-SeQDs and IgG-SeQDs. Reproduced, with permission, from Zhang et al. (2021). Copyright 2021, American Chemical Society. **(D)** LSCM fluorescence images of different cells incubated with SeQDs. Reproduced, with permission, from Wang et al. (2016). Copyright 2016, Springer Nature. **(E)** Fluorescence detection of curcumin by SeQDs. Reproduced, with permission, from Anupama et al. (2021). Copyright 2021, American Chemical Society. **(F)** Using SeQDs for dissociating Aβ fibrils and balancing ROS level to treat AD. Reproduced, with permission, from Guo et al. (2021). Copyright 2021, American Chemical Society. **(G)** Mechanism of anti-proliferation effect of SeQDs on cancer cells. Reproduced, with permission, from Wang et al. (2016). Copyright 2016, Springer Nature.

Guo et al. conducted a comprehensive study by injecting SeQDs into mice, which resulted in the observation of the fluorescent signal of SeQDs entering the brain 2 h later (Guo et al., 2021) (Figure 2B). With the progress of time, the fluorescence signal in the brain gradually intensified, eventually reaching its highest value at 6 h. Notably, the organs of the SeQDs-treated mice demonstrated an intact structure, without any pathological changes or damage to organs when compared to the control group. These results provide evidence for the exceptional biosafety of SeQDs *in vivo*, as well as establish their effectiveness as a fluorescent probe for bioimaging. Zhang et al. synthesized IgG tailored SeQDs (IgG-SeQDs) and utilized them in immunofluorescence imaging (Figure 2C) (Zhang et al., 2021). The laser scanning confocal microscope (LSCM) images clearly demonstrated the successful binding of IgG to SeQDs and their excellent co-localization with the nucleo-stained propyl iodide (PI), confirming the exceptional nuclear staining ability of IgG-SeQDs. In a separate study, Wang et al. employed SeQDs as a fluorescent probe for imaging HeLa cells. Figure 2D illustrates the intense blue and green fluorescence observed in the HeLa cells after incubation with SeQDs, upon excitation by 405 nm and 488 nm laser irradiation, respectively (Wang et al., 2016). However, most reported SeQDs can only emit blue and green fluorescence, limiting their potential for bioimaging. Additionally, the spontaneous fluorescence of cells and biological tissues may interfere with the fluorescence of SeQDs. Therefore, it is necessary to develop fluorescent SeQDs with long wavelength emissions, such as red fluorescence and near-infrared fluorescence.

The unique optical properties and surface characteristics of SeQDs make them a valuable fluorescent nanomaterial for biosensing applications (Huang et al., 2021). For example, Anupama et al. demonstrated the use of SeQDs as a fluorescent probe for sensing curcumin (CR) (Figure 2E) (Anupama et al., 2021). The addition of CR led to a significant decrease in the fluorescence intensity of SeQDs, which was attributed to the presence of the internal filtration effect (IFE). This effect occurs when the absorption spectrum of CR overlaps well with the excitation and emission spectra of SeQDs. Additionally, selenium is an essential co-contributor to the optimal function of the antioxidant enzyme glutathione peroxidase, thereby playing a crucial role as a redox regulator in maintaining cellular homeostasis. Consequently, SeQDs hold great potential for anticancer activity and pro-oxidation properties in the treatment of various diseases (Liu et al., 2020; Zhou et al., 2022a; Zhou et al., 2022b). The unique attributes of SeQDs enable them to be utilized both as a fluorescent probe and a therapeutic agent in practical applications. For instance, Guo et al. have explored the potential of SeQDs as a valuable tool for detecting and monitoring Alzheimer's disease (AD) (Guo et al., 2021). By employing fluorescence tracking technology, the researchers discovered that SeQDs entered the brain within approximately 2 h of their injection in mice. The fluorescence signals in the brain steadily increased over time and peaked after 6 h, indicating that SeQDs can efficiently traverse the blood-brain barrier (BBB) and steadily accumulate in the brain (Figure 2F). Aside from its ability to inhibit amyloid-beta (Aβ) aggregation, which is the culprit behind AD, SeQDs can also reduce Aβ-mediated cytotoxicity, thus blocking the progression of AD. This, in turn, helps minimize oxidative stress, restore mitochondrial function, maintain nerve cell stability and safeguard nerve cells against oxidative stress. In addition, the researchers observed higher levels of fluorescence signals in the livers and kidneys of mice that were injected with SeQDs, indicating that most of the selenium is rapidly metabolized after entering the body. Additionally, H&E staining of the heart, liver, spleen, lung, and kidney of mice revealed that compared to the control group, the organs of the SeQDs-treated mice were structurally intact, and no pathological changes were evident. This finding suggests that SeQDs are unlikely to cause any damage to various tissues and organs. Hence, SeQDs have an edge over conventional single-target drugs in the treatment of AD, providing a fresh avenue towards the prevention and treatment of neurodegenerative diseases. The anti-cancer activity of Se-containing nanoparticles may be strongly influenced by their surface and crystalline characteristics. As reported by Chen's group, the use of L-glutathione modified Se nanoparticles leads to a higher reduction in reactive oxygen species and mitochondrial breakage compared to D-glutathione modified ones. This, in turn, prevents the oxidative damage of INS-1 cells caused by palmitic acid. (Huang et al., 2020b). Similarly, Wang and colleagues observed that amorphous-SeQDs exert their anti-cancer effects primarily through their uptake and localization in mitochondria. This leads to severe damage to mitochondrial membranes, depletion of mitochondrial potential, induction of apoptosis, and cell cycle arrest in the S phase, which ultimately hinder the growth and proliferation of tumor cells. Conversely, crystalline-SeQDs were found to have a weaker impact (Wang et al., 2016). Furthermore, these effects were attributed to the unique ability of SeQDs to differentially regulate 61 proteins and several signaling pathways related to stress response, protein synthesis, cell migration, and cell cycle (Figure 2G). These findings provide a deeper understanding of the mechanisms driving the anti-proliferative effects of nanoparticles on cancer cells, and suggest that SeQDs may represent a promising nanomaterial for cancer treatment. Atherosclerosis is a condition characterized by the accumulation of a lipid layer in the arterial wall, reducing artery elasticity and narrowing the arterial lumen (Dong et al., 2020). Endothelial dysfunction is a leading cause of atherosclerotic plaque and a risk factor for myocardial infarction rupture (Zhao et al., 2023). Zhu and colleagues found that SeQDs can inhibit the activity of Na+/H+ exchanger 1 (NHE1) and impair calcium ion/calpain signaling, effectively improving endothelial cell relaxation, preventing endothelial dysfunction, and limiting the growth of atherosclerotic plaques (Zhu et al., 2019). Overall, SeQDs have demonstrated remarkable potential in the treatment of various diseases, including cancer, Alzheimer's disease, and atherosclerosis, resulting in increased interest and attention from researchers in this field.

Conclusion and perspectives

Conventional semiconductor QDs that contain selenium element, such as CdSe QDs, Ag_2Se QDs, and PbSe QDs, suffer from high toxicity. Consequently, their application in biomedical fields remains limited. However, SeQDs, being a novel form of fluorescent nanomaterial, possess several advantages such as low toxicity, small particle size, and unique optical and surface properties. Moreover, selenium is a requisite trace element in the human body, which makes SeQDs more preferable as fluorescent QDs in *in-vivo* research, potentially avoiding rejection between the nanomaterial and organisms. Therefore, SeQDs possess substantial potential in biomedical research, especially in biological imaging, sensing, diagnosis, and treatment.

While researchers have made remarkable progress in their studies, SeQDs still possess certain limitations. Notably, their photostability diminishes significantly when exposed to excitation light for prolonged periods, leading to a decline in fluorescence. Although several methods have been developed to improve their photostability, the task of generating stable SeQDs on a larger scale to meet the growing demand remains challenging. Furthermore, achieving scalable synthesis of highly fluorescent SeQDs is yet another hurdle. Existing approaches reported so far can only produce minimal quantities of SeQDs, falling short of practical application requirements. When considering bioimaging applications, it is important to note that SeQDs generally emit in the blue-green light range. Unfortunately, this range of light can be absorbed by organisms, and the fluorescence from the organism may impact imaging accuracy. Therefore, exploring new SeQDs that emit in the red or near-infrared range is imperative for more precise bioimaging. Additionally, SeQDs can be paired with specific targeted molecules to produce efficient and sensitive bioprobes that allow for the monitoring of molecular-level reactions in organisms through advanced optical imaging technology. This aspect is also a vital direction for SeQDs research. While SeQDs have proven to be effective biosensors for various substances such as metal ions and drug molecules, their application in this field remains limited. Further research in this area could lead to potentially groundbreaking discoveries. Furthermore, SeQDs have shown promising advantages in the realms of diagnosis and treatment, but clinical trials have yet to be conducted, presenting a pressing issue that requires urgent attention. Additionally, SeQDs may find utility in agriculture by improving the cultivation of plants and vegetables, resulting in an abundance of produce that is rich in selenium. As such, using SeQDs as a selenium supplement to prevent various diseases is also an emerging trend in the field. In addition, SeQDs possess unique properties that make them promising for use in active food packaging. Their exceptional antibacterial and antioxidant properties offer a potential solution to enhance the functionality of conventional packaging by providing extended food shelf life during transportation and storage while preserving food quality.

Author contributions

YH: Conceptualization, Writing–original draft. GL: Writing–review and editing. LZ: Funding acquisition, Writing–review and editing.

Funding

The author(s) declare financial support was received for the research, authorship, and/or publication of this article. The authors acknowledge financial support from the National Natural Science Foundation of China (No. U21A2097), Guangxi Science and Technology Base and Talent Project (No. AA23026001), Natural Science Foundation of Guangxi Province (No. 2017GXNSFFA198002), and Scientific Research and Technological Development Plan of Guilin (No. 20220103-2).

Conflict of interest

The authors declare that the research was conducted in the absence of any commercial or financial relationships that could be construed as a potential conflict of interest.

Publisher's note

References

Ahmadi, A., Sokunbi, M., Patel, T., Chang, M. W., Ahmad, Z., and Singh, N. (2022). Influence of critical parameters on cytotoxicity induced by mesoporous silica nanoparticles. *Nanomaterials* 12, 2016. doi:10.3390/nano12122016

Anupama, K., Paul, T., and Ann Mary, K. A. (2021). Solid-state fluorescent selenium quantum dots by a solvothermal-assisted sol-gel route for curcumin sensing. *ACS Omega* 6, 21525–21533. doi:10.1021/acsomega.1c02441

Arshad, F., and Sk, M. P. (2020). Luminescent sulfur quantum dots for colorimetric discrimination of multiple metal ions. *ACS Appl. Nano Mat.* 3, 3044–3049. doi:10.1021/acsanm.0c00394

Deng, S., Long, J., Dai, X., Wang, G., and Zhou, L. (2023). Simultaneous detection and adsorptive removal of Cr(VI) ions by fluorescent sulfur quantum dots embedded in chitosan hydrogels. *ACS Appl. Nano Mat.* 6, 1817–1827. doi:10.1021/acsanm.2c04768

Dong, Y., Lee, Y., Cui, K., He, M., Wang, B., Bhattacharjee, S., et al. (2020). Epsin-mediated degradation of IP3R1 fuels atherosclerosis. *Nat. Commun.* 11, 3984. doi:10.1038/s41467-020-17848-4

Fujishima, M., Tanaka, K., Sakami, N., Wada, M., Morii, K., Hattori, T., et al. (2014). Photocatalytic current doubling-induced generation of uniform selenium and cadmium selenide quantum dots on titanium(IV) oxide. *J. Phys. Chem. C* 118, 8917–8924. doi:10.1021/jp410794j

Gao, P. X., Huang, Z. Y., Tan, J. S., Lv, G. S., and Zhou, L. (2022). Efficient conversion of elemental sulfur to robust ultrabright fluorescent sulfur quantum dots using sulfur-ethylenediamine precursor. *ACS Sustain. Chem. Eng.* 10, 4634–4641. doi:10.1021/acssuschemeng.2c00036

Gao, P. X., Wang, G., and Zhou, L. (2020). Luminescent sulfur quantum dots: synthesis, properties and potential applications. *Chemphotochem* 4, 5235–5244. doi:10.1002/cptc.202000158

Guisbiers, G., Wang, Q., Khachatryan, E., Arellano-Jimenez, M. J., Webster, T. J., Larese-Casanova, P., et al. (2015). Anti-bacterial selenium nanoparticles produced by UV/VIS/NIR pulsed nanosecond laser ablation in liquids. *Laser Phys. Lett.* 12, 016003. doi:10.1088/1612-2011/12/1/016003

Guo, X., Lie, Q., Liu, Y., Jia, Z., Gong, Y., Yuan, X., et al. (2021). Multifunctional selenium quantum dots for the treatment of alzheimer's disease by reducing aβ-neurotoxicity and oxidative stress and alleviate neuroinflammation. *ACS Appl. Mat. Interfaces* 13, 30261–30273. doi:10.1021/acsami.1c00690

He, L., Zeng, L., Mai, X., Shi, C., Luo, L., and Chen, T. (2017). Nucleolin-targeted selenium nanocomposites with enhanced theranostic efficacy to antagonize glioblastoma. *J. Mat. Chem. B* 5, 3024–3034. doi:10.1039/c6tb03365b

Huang, W. C., Wang, M. M., Hu, L. P., Wang, C., Xie, Z. J., and Zhang, H. (2020a). Recent advances in semiconducting monoelemental selenium nanostructures for device applications. *Adv. Funct. Mat.* 30, 2003301. doi:10.1002/adfm.202003301

Huang, Y., Chen, Q., Zeng, H., Yang, C., Wang, G., and Zhou, L. (2023). A review of selenium (Se) nanoparticles: from synthesis to applications. *Part. Part. Syst. Charact.* 40, 2300098. doi:10.1002/ppsc.202300098

Huang, Y., Fu, Y., Li, M., Jiang, D., Kutyreff, C. J., Engle, J. W., et al. (2020b). Chirality-driven transportation and oxidation prevention by chiral selenium nanoparticles. *Angew. Chem. Int. Ed.* 59, 4406–4414. doi:10.1002/anie.201910615

Huang, Z., Gao, Y., Huang, Z., Chen, D., Sun, J., and Zhou, L. (2021). Sulfur quantum dots: a novel fluorescent probe for sensitive and selective detection of Fe^{3+} and phytic acid. *Microchem. J.* 170, 106656. doi:10.1016/j.microc.2021.106656

Jiang, X., Huang, W., Wang, R., Li, H., Xia, X., Zhao, X., et al. (2020). Photocarrier relaxation pathways in selenium quantum dots and their application in UV-vis photodetection. *Nanoscale* 12, 11232–11241. doi:10.1039/c9nr10235c

Kundu, M., Sadhukhan, P., Ghosh, N., Chatterjee, S., Manna, P., Das, J., et al. (2019). pH-responsive and targeted delivery of curcumin via phenylboronic acid-functionalized ZnO nanoparticles for breast cancer therapy. *J. Adv. Res.* 18, 161–172. doi:10.1016/j.jare.2019.02.036

Lesnichaya, M. V., Shendrik, R., and Sukhov, B. G. (2019). Relation between excitation dependent luminescence and particle size distributions for the selenium nanoparticles in κ-carrageenan shell. *J. Lumin.* 211, 305–313. doi:10.1016/j.jlumin.2019.03.056

Lian, X., Wei, M. Y., and Ma, Q. (2019). Nanomedicines for near-infrared fluorescent lifetime-based bioimaging. *Front. Bioeng. Biotechnol.* 7, 386. doi:10.3389/fbioe.2019.00386

Liao, J., Cheng, Z. H., and Zhou, L. (2016). Nitrogen-doping enhanced fluorescent carbon dots: green synthesis and their applications for bioimaging and label-free detection of Au^{3+} ions. *ACS Sustain. Chem. Eng.* 4, 3053–3061. doi:10.1021/acssuschemeng.6b00018

Lin, J., Xu, L., Zheng, Y., Wu, D., and Yue, J. (2022). Imitation-mussel fluorescent silicon quantum dots for selective labeling and imaging of bacteria and biofilms. *Front. Bioeng. Biotechnol.* 10, 971682. doi:10.3389/fbioe.2022.971682

Liu, T., Xu, L. G., He, L. Z., Zhao, J. F., Zhang, Z. H., Chen, Q., et al. (2020). Selenium nanoparticles regulates selenoprotein to boost cytokine-induced killer cells-based cancer immunotherapy. *Nano Today* 35, 100975. doi:10.1016/j.nantod.2020.100975

Lu, M. C., Duan, Y. X., Song, Y. H., Tan, J. S., and Zhou, L. (2018). Green preparation of versatile nitrogen-doped carbon quantum dots from watermelon juice for cell imaging, detection of Fe^{3+} ions and cysteine, and optical thermometry. *J. Mol. Liq.* 269, 766–774. doi:10.1016/j.molliq.2018.08.101

Lv, G., Dai, X., Lu, G., Ye, L., Wang, G., and Zhou, L. (2023). Facile fabrication of portable electrospun poly(vinyl alcohol)/sulfur quantum dots film sensor for sensitive and selective detection of Fe^{3+}. *Opt. Mat.* 135, 113227. doi:10.1016/j.optmat.2022.113227

Qian, F. L., Li, X. M., Tang, L. B., Lai, S. K., Lu, C. Y., and Lau, S. P. (2017). Selenium quantum dots: preparation, structure, and properties. *Appl. Phys. Lett.* 110, 53104. doi:10.1063/1.4975358

Ruan, H., and Zhou, L. (2022). Synthesis of fluorescent sulfur quantum dots for bioimaging and biosensing. *Front. Bioeng. Biotechnol.* 10, 909727. doi:10.3389/fbioe.2022.909727

Singh, S. C., Mishra, S. K., Srivastava, R. K., and Gopal, R. (2010). Optical properties of selenium quantum dots produced with laser irradiation of water suspended Se nanoparticles. *J. Phys. Chem. C* 114, 17374–17384. doi:10.1021/jp105037w

Song, Y., Tan, J., Wang, G., Gao, P., Lei, J., and Zhou, L. (2019). Oxygen accelerated scalable synthesis of highly fluorescent sulfur quantum dots. *Chem. Sci.* 11, 772–777. doi:10.1039/c9sc05019a

Sousa, F. L. N., Souza, B. A. S., Jesus, A. C. C., Azevedo, W. M., Mansur, H. S., Freitas, D. V., et al. (2020). Aqueous electrosynthesis of silver indium selenide nanocrystals and their photothermal properties. *Green Chem.* 22, 1239–1248. doi:10.1039/c9gc03647d

Triana, M. A., Hsiang, E.-L., Zhang, C., Dong, Y., and Wu, S.-T. (2022). Luminescent nanomaterials for energy-efficient display and healthcare. *ACS Energy Lett.* 7, 1001–1020. doi:10.1021/acsenergylett.1c02745

Wang, G., Guo, Y., Yang, G., Yang, L., Ma, X., Wang, K., et al. (2016). Mitochondria-mediated protein regulation mechanism of polymorphs-dependent inhibition of nanoselenium on cancer cells. *Sci. Rep.* 6, 31427. doi:10.1038/srep31427

Wang, H., Wang, Z., Xiong, Y., Kershaw, S. V., Li, T., Wang, Y., et al. (2019). Hydrogen peroxide assisted synthesis of highly luminescent sulfur quantum dots. *Angew. Chem. Int. Ed.* 58, 7040–7044. doi:10.1002/anie.201902344

Yang, D., Cui, Z., Wen, Z., Piao, Z., He, H., Wei, X., et al. (2023). Recent updates on functionalized silicon quantum-dot-based nanoagents for biomedical applications. *ACS Mat. Lett.* 5, 985–1008. doi:10.1021/acsmaterialslett.2c01225

Yao, J., Li, P., Li, L., and Yang, M. (2018). Biochemistry and biomedicine of quantum dots: from biodetection to bioimaging, drug discovery, diagnostics, and therapy. *Acta Biomater.* 74, 36–55. doi:10.1016/j.actbio.2018.05.004

Yuan, M., Hu, H., Wang, Y., Xia, H., Zhang, X., Wang, B., et al. (2022). Cation-exchange enables *in situ* preparation of PbSe quantum dot ink for high performance solar cells. *Small* 18, e2205356. doi:10.1002/smll.202205356

Zhang, X., Chen, X., Guo, Y., Gu, L., Wu, Y., Bindra, A. K., et al. (2021). Thiolate-assisted route for constructing chalcogen quantum dots with photoinduced fluorescence enhancement. *ACS Appl. Mat. Interfaces* 13, 48449–48456. doi:10.1021/acsami.1c15772

Zhao, H., Dan, P., Xi, J., Chen, Z., Zhang, P., Wei, W., et al. (2023). Novel soybean polypeptide dglycin alleviates atherosclerosis in apolipoprotein E-deficient mice. *Int. J. Biol. Macromol.* 251, 126347. doi:10.1016/j.ijbiomac.2023.126347

Zhou, J., Zhang, D., Lv, X., Liu, X., Xu, W., Chen, L., et al. (2022a). Green synthesis of robust selenium nanoparticles via polysaccharide-polyphenol interaction: design principles and structure-bioactivity relationship. *ACS Sustain. Chem. Eng.* 10, 2052–2062. doi:10.1021/acssuschemeng.1c06048

Zhou, L., He, B., and Huang, J. (2013). Amphibious fluorescent carbon dots: one-step green synthesis and application for light-emitting polymer nanocomposites. *Chem. Commun.* 49, 8078–8080. doi:10.1039/c3cc43295e

Zhou, L., Wu, F., Yu, J., Deng, Q., Zhang, F., and Wang, G. (2017). Titanium carbide ($Ti_3C_2T_X$) MXene: a novel precursor to amphiphilic carbide-derived graphene quantum dots for fluorescent ink, light-emitting composite and bioimaging. *Carbon* 118, 50–57. doi:10.1016/j.carbon.2017.03.023

Zhou, W., Yin, L., Zhang, X., Liang, T., Guo, Z., Liu, Y., et al. (2022b). Recent advances in small molecule dye-based nanotheranostics for NIR-II photoacoustic imaging-guided cancer therapy. *Front. Bioeng. Biotechnol.* 10, 1002006. doi:10.3389/fbioe.2022.1002006

Zhu, M. L., Wang, G., Wang, H., Guo, Y. M., Song, P., Xu, J., et al. (2019). Amorphous nano-selenium quantum dots improve endothelial dysfunction in rats and prevent atherosclerosis in mice through Na(+)/H(+) exchanger 1 inhibition. *Vasc. Pharmacol.* 115, 26–32. doi:10.1016/j.vph.2019.01.005

frontiers | Frontiers in Bioengineering and Biotechnology

TYPE Original Research
PUBLISHED 22 December 2023
DOI 10.3389/fbioe.2023.1326254

OPEN ACCESS

EDITED BY
Md Palashuddin Sk,
Aligarh Muslim University, India

REVIEWED BY
Satyapriya Bhandari,
University of North Bengal, India
Sahnawaz Ahmed,
National Institute of Pharmaceutical Education and Research, Kolkata, India

*CORRESPONDENCE
Pengju Lv,
✉ pengjulv@163.com
Han Yue,
✉ yuehan1000@126.com

RECEIVED 23 October 2023
ACCEPTED 05 December 2023
PUBLISHED 22 December 2023

CITATION
Wang J, Sun G, Li F, Zhu Z, Sun L, Lv P and Yue H (2023), Development of ZnCdSe/ZnS quantum dot-based fluorescence immunochromatographic assay for the rapid visual and quantitative detection 25-hydroxyvitamins D in human serum. *Front. Bioeng. Biotechnol.* 11:1326254. doi: 10.3389/fbioe.2023.1326254

Development of ZnCdSe/ZnS quantum dot-based fluorescence immunochromatographic assay for the rapid visual and quantitative detection 25-hydroxyvitamins D in human serum

Jianfa Wang[1], Guoshao Sun[1], Fang Li[1], Zhi Zhu[1], Lei Sun[2], Pengju Lv[2]* and Han Yue[2]*

[1]Department of Orthopedics, Zhengzhou Central Hospital Affiliated Zhengzhou University, Zhengzhou, Henan, China, [2]Center of Stem Cell and Regenerative Medicine, Zhengzhou Central Hospital Affiliated Zhengzhou University, Zhengzhou, Henan, China

Vitamin D deficiency is associated with various diseases such as obesity, digestive problems, osteoporosis, depression, and infections, and has therefore emerged as a topic of great interest in public healthcare. The quantitative assessment of 25-hydroxyvitamin D (25-OH VD) in human serum may accurately reflect the nutritional status of vitamin D in the human body, which is significant for the prevention and treatment of vitamin D-deficient patients. In this study, we developed an assay for quantitative detection of 25-OH VD based on the 25-OH VD monoclonal antibody (mAb), and identified the optimal process parameters. The following process settings were found to be suitable for the test strips: pH of 7.6, 1-Ethyl-3-(3-dimethylaminopropyl) carbodiimide (EDC) ratio of 1:2000, and the anti-25-OH VD mAb ratio was 1:8. The equilibration time of the immune dynamic assay was 15 min. Under optimal conditions, the quantum dot nanoparticle-based fluorescent immunochromatographic assay (QDs-FICA) exhibited dynamic linear detection of 25-OH VD in PBS, from 5 ng/mL to 100 ng/mL, and the strip quantitative curve could be represented by the following regression equation: $y = -0.02088 \log x) + 1.444$ (R2 = 0.9050). The IC50 of the QDs-FICA was 39.6 ± 1.33 ng/mL. The specificity of the QDs-FICA was evaluated by running several structurally related analogues, including 25-OH VD_2, 25-OH VD_3, 1,25-OH_2VD_3, 1,25-OH_2VD_2, VD_2, and VD_3. The coefficients of variation were all below 10%. The shelf life of the test strips in this study was about 160 days at room temperature. Briefly, this study is the first to perform QDs-FICA for the rapid visual and quantitative detection of 25-OH VD, with great potential significance for clinical diagnosis of vitamin D-associated diseases.

KEYWORDS

25-hydroxyvitamin D, ZnCdSe/ZnS, quantum dots, fluorescence immunochromatographic assay, quantitative detection

Introduction

Vitamin D is an essential fat-soluble steroid derivative that exerts its physiological effects after undergoing hydroxylation twice and binding specifically to the intracellular vitamin D receptor (VDR) (Janjusevic et al., 2021). 25-Hydroxyvitamin D was first reported as a marker of bone metabolism in a Nordic study (Revez et al., 2020). Studies have found that a lack of adequate sunlight exposure can cause serious disruption to the normal growth of adolescents and even lead to rickets (McIntosh et al., 1982; Bouillon et al., 2022). Furthermore, in middle-aged and elderly people, vitamin D deficiency can result in osteoporosis, which can easily lead to fractures and other problems (Reid et al., 2014). In addition, studies have shown that vitamin D deficiency can cause diseases related to the skeletal system, cardiovascular system, glucose metabolism, nervous system, muscular system, cell proliferation, immune system, endocrine system, and tumorigenesis (Di Somma et al., 2017; Liu et al., 2018; Gouni-Berthold and Berthold, 2021).

The biomarkers of bone metabolism, namely, osteocalcin (BGP), parathyroid hormone (PTH), 25-OH VD, and type 1 procollagen amino terminal extender peptide (P1NP) are sensitive, specific, and non-invasive clinical aids to the diagnosis of osteoporosis, and can enable accurate evaluation of bone turnover at the level of intact bone tissue (Balsan et al., 1986). Among them, 25-OH VD is now widely used in the experimental diagnosis of osteoporosis and the assessment of growth and development of children (Garabédian et al., 1983; Holick, 2023). For vitamin D-deprived individuals who take high-dose vitamin D supplementation, it is even more important to regularly and accurately monitor 25-OH VD levels in the body to prevent overdose and consequent toxicity (Vieth, 1999; Binkley et al., 2010). Serum 25-OH VD concentration testing has been found to be the most reasonable and reliable indicator of overall vitamin D status (Mano et al., 2023). The deficiency of 25-OH VD is highly prevalent worldwide; as a result, regular testing of 25-OH VD levels to ensure its adequacy is important for disease prevention.

The current 25-OH VD assay methodology is based on liquid chromatography-tandem mass spectrometry (LC-MS/MS) and ELISA (Su et al., 2014; Yun et al., 2015). LC-MS/MS is recognized as the gold standard for assays and is also used as a reference for validation of other assays, with very high sensitivity, specificity, and accuracy. However, the instruments used are expensive, require high professionalism of operators, and require self-developed assays. At present, most hospitals in China are not equipped with the required instruments and professional staff, which limits the clinical application of LC-MS/MS methods. Fluorescence immunochromatographic assay (FICA) is a rapid diagnostic technique developed in the early 1980s, which is a classical rapid test based on the immunoreaction of antigens and antibodies (Lin et al., 2015). Simultaneously, Compared with LC-MS/MS methods, immunochromatography is easy and fast to operate. Quantum dots (QDs) have attracted wide interest in bioimaging and biosensing (Geszke-Moritz and Moritz, 2013; Yang et al., 2022). Because of their unique optoelectronic properties relative to traditional labeling reagents (organic and protein-based fluorophores), and significant progress has been made in the development of complex surface-coating technologies (Monteiro et al., 2017; Koo et al., 2022). Applications in clinical diagnostics, food safety, environmental protection, and pesticide residues are widespread.

Quantum dot rapid immunochromatographic assay is a new labeled immunoassay technique combining luminescence reaction with immunoassay for the detection of trace antigens or antibodies. This technique has the advantages of high stability, good reproducibility, high sensitivity, high specificity, and rapid detection (Wang et al., 2021; Chen et al., 2022; Su et al., 2022). T The immunoassay is suitable to be carried out in mid-level and primary hospitals because of the small amount of sample used, relatively inexpensive assay equipment, and simple instrument operation (Li et al., 2022). In the rapid development of point-of-care tests (POCT), user needs such as test accuracy, sensitivity, and stability are high. In this context, fluorescence immunochromatography technology meets the need for rapid detection and is easy to operate (Ahmad Najib et al., 2022; Singh et al., 2020; Zhang et al., 2019). Therefore, in this study, a quantum dot nanoparticle-based fluorescent immunochromatographic assay (QDs-FICA) for the detection of 25-OH VD was established using the quantum dot rapid immunochromatographic technique. The assay was tested and found to be extremely sensitive and specific, with potential utility in the serological detection of 25-OH VD and clinical application for the diagnosis of vitamin D-related diseases.

Materials and methods

Materials and clinical samples

Carboxy water-soluble QDs-COOH (ZnCdSe/ZnS, core/shell) with a size of 12 nm were obtained from Wuhan Jiayuan Quantum Dots Corporation, Ltd. (Wuhan, China). Staphylococcal protein-A (SPA) was purchased from Beijing Solarbio Science & Technology Corporation, Ltd. Fetal calf serum (FCS) was bought from Tian hang Biological Technology Co., Ltd. (Zhejiang, China). The following substances were purchased from Sigma-Aldrich Chemical Co. (St. Louis, MO): 25-OH VD antigen, bovine serum albumin (BSA), staphylococcal protein-A (SPA), and N-(3-dimethylaminopropyl)-N′-ethylcarbodiimide hydrochloride (EDC). 25-OH VD monoclonal antibody was purchased from Bioventix Biotechnology, United Kingdom. Vitamin D and 25-OH VD standards were purchased from Hanzun Biological Co., LTD. 25-OH VD derivative were purchased from Xiamen Tongrenxin Gong Department. The nitrocellulose membrane, sample pad, backing card, absorbent pad and the filter membrane were from Millipore, US. The commercial Chemiluminescence Immunoassay (CLIA) kit for 25-OH VD quantitative analysis was from Immunodiagnostic Systems Holdings PLC (IDS), United Kingdom. Millipore's Milli-Q filtration system was used to create ultrapure water. One-hundred clinical samples were collected from patients who visited the outpatient clinic or physical examination center of Zhengzhou Central Hospital in

TABLE 1 Optimization of the concentration of 25-OH VD-BSA and the d the volume of QB-mAbs by using a checkerboard titration (n = 3).

NO	Concentration of 25-OH VD-BSA (mg/mL)	Volume of QD-mAbs	FI_T	FT_C	FI_T/FI_C	Inhibition ratio (%)
1	0.2	1.0	1,260 ± 62	1,556 ± 268	0.82 ± 0.10	72.88 ± 0.03
2	0.2	1.5	1,469 ± 70	1,507 ± 89	1.01 ± 0.06	60.97 ± 0.05
3	0.2	2.0	2,306 ± 39	1,318 ± 41	1.74 ± 0.04	71.24 ± 0.01
4[a]	0.4	1.0	642 ± 23	815 ± 12	0.78 ± 0.03	80.27 ± 0.02
5	0.4	1.5	918 ± 40	1,168 ± 58	0.78 ± 0.02	72.94 ± 0.02
6	0.4	2.0	1,123 ± 115	1,108 ± 42	1.12 ± 0.04	63.39 ± 0.04
7	0.8	1.0	765 ± 28	681 ± 19	0.97 ± 0.01	38.05 ± 0.07
8	0.8	1.5	1725 ± 87	987 ± 88	1.75 ± 0.12	72.78 ± 0.01
9	0.8	2.0	1,151 ± 79	645 ± 41	1.78 ± 0.16	74.32 ± 0.03

[a]The optimal condition under the concentration of 1.0 ng/mL serum 25-OH VD.

2023. Each patient underwent a health interview and was asked to sign an informed consent form.

Bioconjugation QDs-COOH with 25-OH VD mAb

The synthesis of QDs-mAb conjugates was carried out as described in an earlier study (Zhou et al., 2021). In this study, improved synthesis conditions were used for the 25-OH VD probes. A reaction vessel was filled with 12.5 µL of the QDs-COOH (ZnCdSe/ZnS) (8 µM) and 30 µL of the EDC (4.0 mg/mL), and the mixture was incubated for 30 min at room temperature 25°C. EDC solution was then used to activate the QDs-COOH. Next, 30 µL of 25-OH VD mAb (4.0 mg/mL) in borate-buffered saline (BBS, 10 mM, pH = 7.6) was added to the reaction. A shaking incubator was used to allow the mixture to continue to react for an additional 2 hours at 25°C. At the end of the reaction, the reaction was centrifuged at 8,000 rpm for 3 min to remove any agglomerates and supernatant was discarded. The sample was concentrated and purified five times using ultrafiltration tubes, and the final product was redissolved in the appropriate target coupling buffer. QDs-mAb conjugates were saved in a new brown microcentrifuge tube and stored at 4°C for future use.

Preparation of the QDs-FICA strip

The QDs-FICA consists of five main parts: sample pad, conjugate pad, nitrocellulose membrane, absorbent pad, and backing card. The 25-OH VD-BSA conjugate and SPA solution were immobilized on NC membranes as the test T) and control C) lines using a BioDot XYZ3050 dispensing platform (Irvine, CA, United States). The NC membranes was then dried in an electric blast oven at 40°C for 4 hours. The distance between the T and C lines was roughly 5 mm. Next, the test strips were assembled in the order of the sample pad, conjugate pad, NC membrane, and absorption pad. They were then packaged in a plastic cassette after being sliced into 2.8 mm-wide test strips using a BioDot CM 4000 Guillotine Cutter. They were then stored with desiccant and sealed in aluminum foil at 4°C.

Optimization of conjugating conditions

The inputs of EDC, 25-OH VD mAb, and pH value play a crucial role during the conjugation process. These conditions were optimized by an orthogonal experiment, which is described in Table 1. The fluorescence intensity on the test paper and the peaks of the fluorescence spectral curves were recorded using an MD-980 Multi-channel Fluorescent Immunoassay Analyzer (Micro detection Corporation, Ltd., Nanjing, China). The measurements were used to determine the best set of conjugation conditions.

Standardizing 25-OH VD QDs-FICA

The 25-OH VD stock solution was diluted with 0.01 mol/L PBS buffer solution to achieve final concentrations of 0, 5, 10, 20, 30, 40, 60, 80, and 100 ng/mL. Then, 100 µL of each standard solution was incubated for 3 min with 3 µL of standard immunoprobe before being applied to the spiking wells of the test strips. The T/C ratios of the strips were measured using a gold standard reader after 15 min. Each concentration was tested five times. The sensitivity, IC_{50} value, and linear quantification range of 25-OH VD immunochromatographic strips were determined by plotting the standard curve with the logarithm of 25-OH VD concentration as the horizontal coordinate and the T/C value as the vertical coordinate. The sensitivity was computed by subtracting the mean value for the negative samples from their triple standard deviation.

Limit of detection the QDs-FICA

The 25-OH VD stock solution was diluted with 0.01 mol/L PBS buffer solution to the series standard concentration of 0, 12.5, 5, 7.5, 15, 25, 50, 60, 80, 100, 125, 130, 140, and 150 ng/mL. The FI_T/FI_C ratio of the test strip was detected using the fluorescence instrument, and each concentration was measured in parallel five times. The FI_T/FI_C ratio of the test strip with a concentration of 0 ng/mL of added 25-OH VD was denoted as B0 and the FIT/FIc ratios of the other added concentration was denoted as B. The competition inhibition curve of 25-OH VD strips with PBS as the sample matrix was plotted by logarithmic mapping of the B/B0 value of the 25-OH VD concentration, and the IC_{50} value and linear quantitative range of the strips were determined at this time.

Cross-reactivity of the QDs-FICA

To evaluate the specificity of 25-OH VD colloidal gold quantitative test strips, six common 25-OH VD structural analogs, namely, 25-OH VD_2, 25-OH $VD_{3,}$ 125-OH_2VD_3, 125-OH_2VD_2, VD2, and VD3, were selected for cross-reaction experiments. A series of standards concentration with final concentrations of 0, 5, 10, 20, 30, 40, 60, 80, and 100 ng/L were prepared in the stock solution, and the above solutions were detected with 25-OH VD colloidal gold strips. Each concentration was measured three times in parallel, and the standard curve was drawn according to the T/C ratio measured by the colloidal gold reader. The IC_{50} of each competitor was obtained, and the cross-reaction rate of each analogue with 25-OH VD was calculated according to the following formula: (Cr) %= (25-OH VD IC_{50}) (cross analogue IC_{50}) 100%.

Interruptibility of the QDs-FICA

The test was repeated twice with the same dilution of the interference test samples; then, the samples of low, medium, and high concentration levels were used as the base samples. We divided each base sample into five portions, one of which was added to the sample dilution, without interfering substances, as the control sample. The other four portions were added in equal volumes, with different concentrations of interfering substances, as the analysis sample. The measurement was repeated three times to determine the average value of each sample to calculate the interference rate, using the following formula: Interference rate = (average concentration of analyzed sample average concentration of base sample)/average concentration of base sample × 100%. The interference effect between the addition of interferon and the absence of interferon was calculated, and ≤10% bias was used as the judgment standard.

Accuracy and precision of the QDs-FICA

The 25-OH VD standard was added into 0.01 mol/mL PBS buffer solution until the final concentration was 25, 50, and 100 ng/mL. The same batch of test strips was used to detect the three concentrations of low, medium, and high levels; measurement was performed every 3 days and repeated three times for each sample. To evaluate the accuracy and precision of the test strips, the recovery rate of each concentration and the difference between batches of the test strips was calculated.

Stability of the QDs-FICA

Stability experiments were performed by randomly selecting 100 test strips from the same batch and placing them in the oven at 60.1°C. The experiments were designed according to the Arrhenius formula, the time intervals for which 60.1°C needs to be tested are the Day 0, Day 1, Day 2, Day 4 and Day 8 (about 0 days, 40 days, 80 days, 160 days, and 320 days at 25°C). Three standard antibody dilutions of 1:500, 1:2,000, and 1:5,000 were measured and three parallels were set up for each sample. The average FI_T/FI_C values were calculated. The QDs solution with a concentration of 0.5 mg/mL was configured and directly scribed to the T-line position of the NC membrane using a membrane scribe, assembled into a test card and then placed in the tester for 100 consecutive readings to compare the average lifetimes of the QDs and mAb QDs.

QDs-FICA for 25-OH VD qualitative and quantitative detection

For construction of the quantitative standard curve for 25-OH VD detection, the extract was mixed with 25-OH VD to make standard solutions (0, 0.01, 0.05, 0.1, 0.5, 1.0, 2.5, 5.0, 10, and 50 ng/mL). 25-OH VD standard solution detection was performed using fluorescent test strips. The cut-off value, i.e., the lowest 25-OH VD concentration that caused T line fluorescent band invisibility, was used to evaluate the qualitative performance of QDs-FICA. The T line fluorescence intensity dropped as the 25-OH VD concentration increased, disappearing under a handheld UV light. The MD-800 multiple immunochromatographic test strip analyzer measured the T line, C line, and FI ratio (FI_T/FI_C) fluorescence intensity three times for each standard test for quantitative detection.

Results

Characterization of QDs and mAb-QDs conjugates

The QDs were synthesized by encapsulating ZnCdSe/ZnS using a microemulsion method as previously reported (Shen et al., 2015). Agarose gel electrophoresis (AGE) and sodium dodecyl sulfate polyacrylamide gel electrophoresis (SDS-PAGE) experiments indicated that anti-25-OH VD-mAb-QDs have a large molecular weight, which slows down their migration in agarose gels (Figure 1A). When anti-25-OH VD-mAb were coupled to QDs, the excitation and emission wavelengths remained unchanged at about 605 nm, but the fluorescence intensity was weaker than that of QDs, which may be attributed to the effect of the antibody on fluorescence detection or the occurrence of fluorescence burst during the coupling process (Figure 1B). The particle size distribution and potential variation of the nanoparticles were measured by dynamic light scattering (DLS), as shown in (Figures 1C,D), The mAb-QDs conjugates reached a size of 160.82 nm, and the polymer dispersity index (PDI) value of mAb-QDs conjugates was 0.372. In comparison, the QDs were only 19.27 nm in size, and the PDI value of the QDs was 0.187. As a result, the size of the hydrated QDs was significantly smaller than that of the mAb-QDs. Furthermore, Figures 1E,F show the zeta potential (ζ potential) values of the anti-25-OH VD-mAb-QDs conjugates and QDs. While the potential

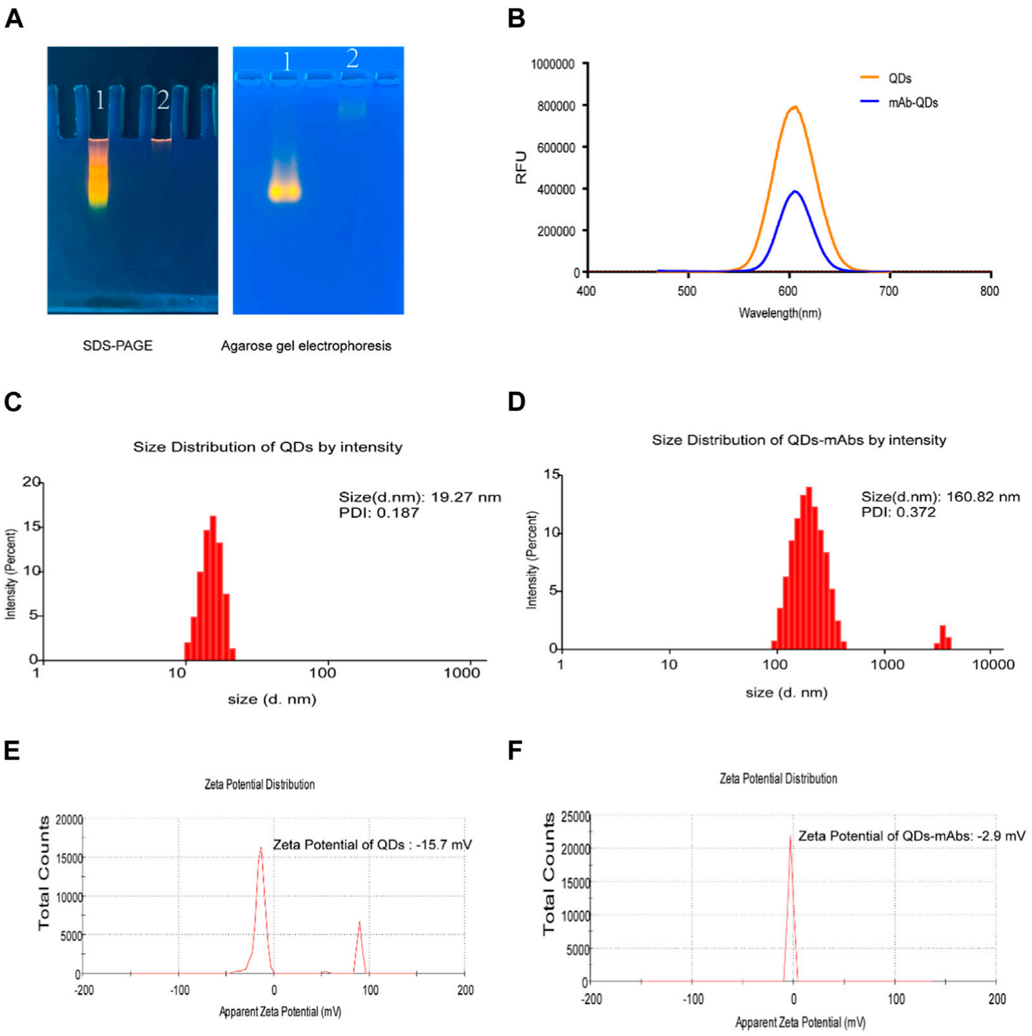

FIGURE 1
Fluorescent Probe Validation. **(A)** SDS-PAGE and Agarose gel electrophoresis. 1. QDs; 2. Anti-25-OH VD-mAb-QDs. **(B)** QDs and anti-25-OH VD-mAb-QDs fluorescence emission spectrum (Excitation wavelength 450nm, emission wavelength 585 nm). **(C, D)** Hydrodynamic diameter of the QDs and mAb-QDs by a Malvern laser particle size analyzer. **(E, F)** Size and ζ potential distributions of the QDs and anti-25-OH VD-mAb-QDs by a Malvern laser particle size analyzer.

of QDs was detected by DLS to be −15.7mV, the potential of anti-25-OH VD-mAb-QDs was −2.9 mV. Transmission electron microscopy (TEM) images showed (Supplementary Figure S1) that the prepared anti-25-OH VD-mAb-QDs had a regular spherical shape with a relatively uniform particle size distribution. High-resolution TEM images of individual particles showed that a large number of oil-soluble ZnCdSe/ZnS QDs were tightly embedded in the polymer. The above several sets of data indicate that there is effective coupling between the QDs and anti-25-OH VD-mAb, confirming successful synthesis of the immunofluorescence probe.

Detection of 25-OH VD using QDs-FICA platform

QDs-FICA is a straightforward and visually appealing approach for validating the bioactivity of mAb-QDs. A schematic illustration for the detection of 25-OH VD using the QDs-FICA-based platform is shown in Figure 2. Briefly, QDs were used to replace colloidal gold particles as signal markers. QDs were coupled with the corresponding antibody of 25-OH VD to be tested, and then sprayed on the binding pad. Immunochromatographic test strips were made by assembling the sample pad, the binding pad, the reaction membrane, and the absorbent pad. The FICA technique revealed that QDs could not selectively interact with the T line (25-OH VD-BSA) and C line (SPA). However, anti-25-OH VD-mAb -QDs underwent strong interactions with the C and T lines when exposed to ultraviolet light from a portable UV lamp with an excitation wavelength of 365 nm.

Optimization of coupling conditions

Because of the pH, EDC and anti-25-OH VD mAbs can have a significant effect on the stability and biological activity of the

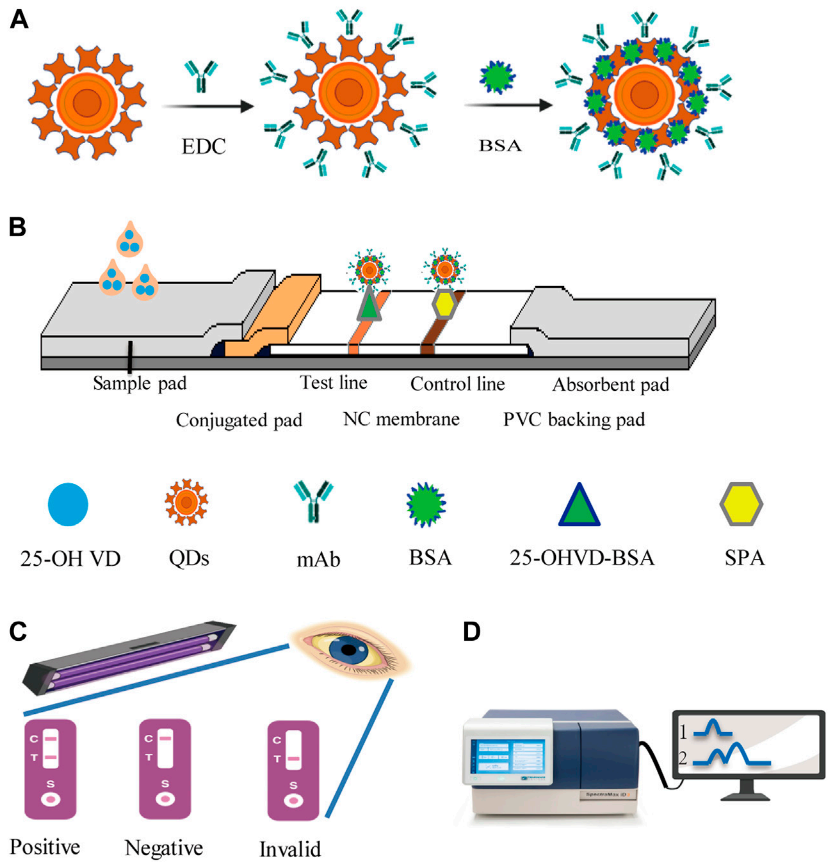

FIGURE 2
Schematic representation of the sandwich procedure for the detection of 25-OH VD using QDs-ICA platform. **(A)** Schematic illustration of the anti-25-OH VD-mAb-QDs probes preparation. **(B)** The five components assembly of conventional ICA sensor, the positive tests consequence consisting of a test line (T) and a control line (C). **(C)** Immunochromatographic assay shows a negative result with the presence of control line. **(D)** The fluorescence strip readera. 1, QDs; 2 anti-25-OH VD-mAb-QDs.

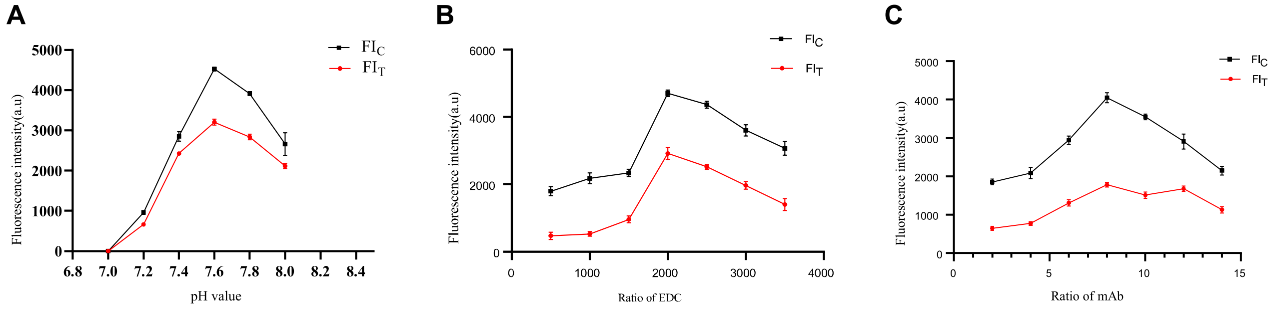

FIGURE 3
Optimization of coupling conditions for QDs-mAb. **(A)** Determine the optimal pH of the label. **(B)** Determine the optimal amount of label led activator EDC. **(C)** Determine the optimal amount of labelled anti-25-OH VD-mAb.

conjugate. Therefore, coupling conditions were optimized in this study. As shown in Figure 3A, when the pH was 7.6, the highest values of both FI_T and FI_C were obtained. When the molar ratio of QDs to EDC is 1:2000, FI_T and FI_C are saturated (Figure 3B). The excessive amount of EDC would lead to a large amount of conjugate aggregation, which is unfavorable for mutual coupling. In addition, the results showed that FI_T and FI_C were saturated when the molar ratio of QDs to the anti-25-OH VD mAb was 1:8 (Figure 3C). The optimal coupling conditions were as follows: a pH of 7.6, an EDC ratio of 1:2000, and a 25-OH VD:mAb ratio was 1:8.

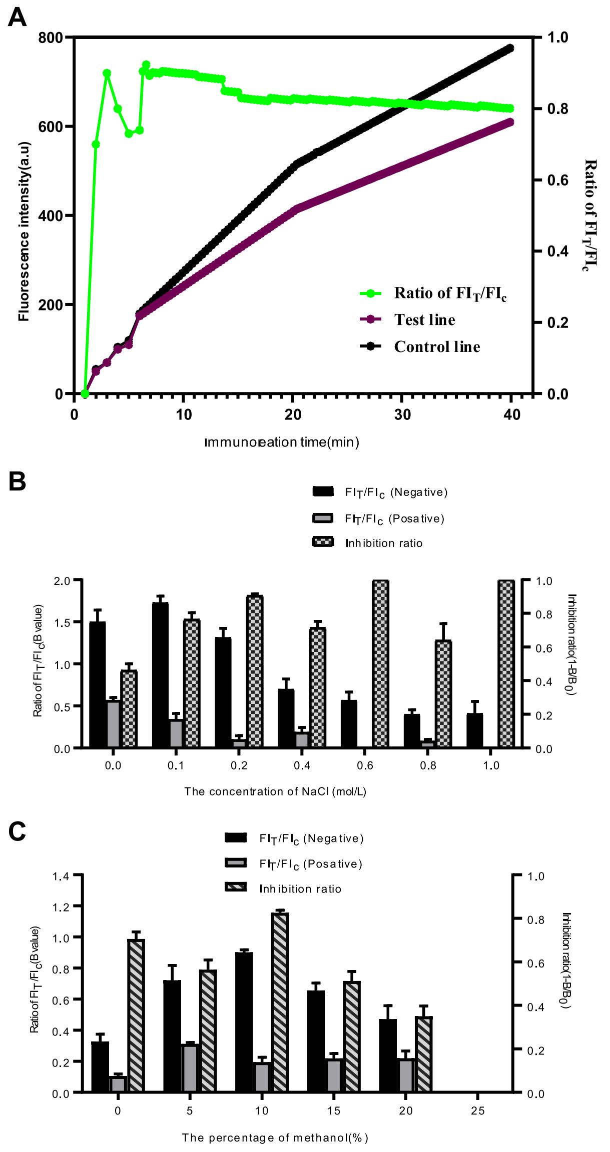

FIGURE 4
Optimization detection conditions of the QDs-FICA. **(A)** Kinetic curves of immunoreaction on test line, control line and FI_T/FI_C of QDs-based immunochromatographic strip. **(B)** Effect of ion strength in samples on the T/C ratio. **(C)** Effect of ethanol in samples on FI_T/FI_C and competitive inhibition rate.

Optimization of the QDs-FICA

The dosages of 25-OH VD-BSA and anti-25-OH VD mAb-QDs are particularly important for optimal sensitivity and fluorescence intensity of the FICA. The experimental results are presented in Table 1. Which shows that the fluorescence intensity of the T and C lines of the test strips was stronger when the concentration of 25-OH VD-BSA was 0.4 mg/mL and the immunoprobe dosage was 1.0 μL (group 4), The FI_T and FI_C were 642 ± 23 and 815 ± 12, respectively. The competition inhibition rate of 1.0 ng/mL positive samples was as high as 80.27 ± 0.02 (n = 3), which indicated the best detection effect relative to the rest of the groups. Therefore, the optimization results for group 4 were determined as the best quantitative analysis conditions for the test strips.

Optimization of detection conditions

In order to achieve the best performance of the QDs-FICA platform, we further optimised the immunoreaction time of the assay, the salt ions and the ethanol content of the sample solution. As shown in Figure 4A, The FI_T and FI_C improved continuously within 45 min The fluorescence signals of T and C lines were gradually strengthened after 10 min of spiking, and the FI_T/FIc ratio tended to be 0.8 when the immunoreaction time reached 15 min. Specific experimental results are shown in Figure 4B. When the salt ion concentration is 0.2 mol/L, the T/C value of the negative sample is 1.365, and the T/C value of the positive sample is 0.028. The competitive inhibition rate reaches 92.5%. The maximum values of FI_T/FI_C for negative samples and competitive inhibition for positive samples were reached when the concentration of ethanol in the samples was 10%. When the concentration of ethanol is greater than 10%, FI_T/FI_C and the competitive inhibition rate decrease rapidly (Figure 4C). The reason is that the concentration of organic solution exceeds the capacity of protein, which will lead to the loss of protein activity.

Sensitivity and stability of the QDs-FICA

The stability results showed that the detection efficiency of the test strips stored at 60.1°C for 4 days (160 days, 25°C) was weakened, and only 1:500 high concentration antibody standards could be measured. So it was inferred that the storage time of the test strips in this study was about 160 days at room temperature. See Supplementary Figure S2. The fluorescence lifetime measurement results show that although the fluorescence intensity of anti-25-OH VD-mAb-QDs is slightly lower than that of QDs, the fluorescence intensity of 100 consecutive measurements of the T-line remains basically unchanged. This demonstrates that the lifetime of anti-25-OH VD-mAb-QDs can satisfy normal clinical detection applications (Supplementary Figure S3).

Analytical performance and validation of QDs-FICA

The standard curve was shown in Figure 5, its linear regression equation is y = −0.02088 logx)+1.444 (R^2 = 0.9050). The concentration of 25-OH VD shows a very good linear relationship between 5 ng/mL and 100 g/mL, according to the linear regression equation. It is concluded that the IC_{50} of the test strip was 39.6 ± 1.33 ng/mL (n = 3). Table 2 showed the cross-reaction rates of 25-OH VD_3, 125-OH_2VD_3, and 125-OH_2VD_2 with the strip were 26%, 11%, and 25%, respectively. The cross-reaction rates of VD_3 and VD_2 were less than 1% with the test strip. Therefore, the fluorescence test strip has good specificity.

As shown in Supplementary Table S1, the interference rate is less than 8%. This indicates that the method is more resistant to strong

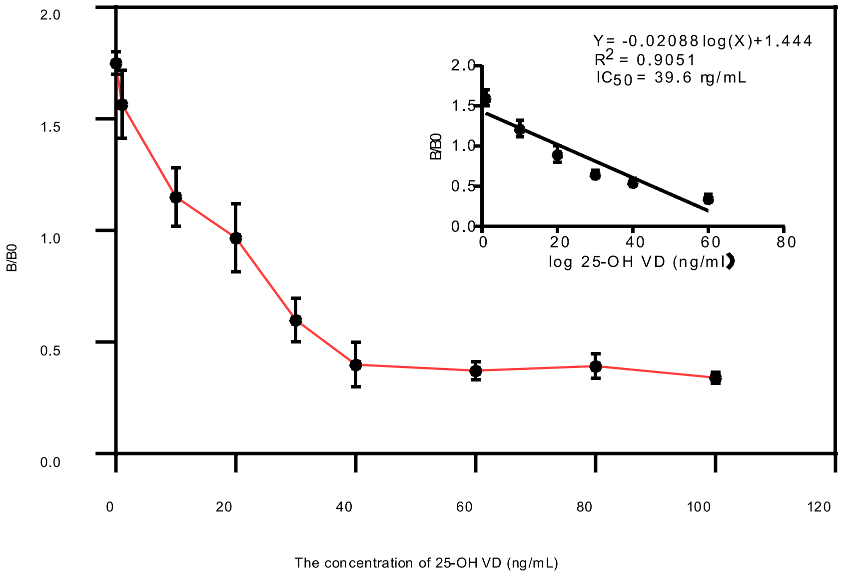

FIGURE 5
Evaluation of the test strips using 25-OH VD standards, Calibration curve for quantitative detection of 25-OH VD by QDs-FICA.

TABLE 2 Specificity tests against structurally related analogies.

Name	Cross-reaction rate (%)
25-OH VD2	100
25-OH VD3	26
125-OH2VD3	11
125-OH2VD2	25
VD2	<1
VD3	<1

interference. The test results for the 25-OH VD immunochromatographic strips between batches and within batches are shown in Table 3. The recovery rates of 25-OH VD addition samples at different concentrations in the test strip range from 80.48% to 93.41%, and the coefficient of variation for the test strip ranged from 1.78% to 9.96%. The recoveries of the 25-OH VD addition samples were 85.35%–100.65%, and the coefficient of variation was between 2.39% and 9.35%. The results show that the 25-OH VD QD fluorescent microsphere strip has good precision and accuracy.

Comparison of QDs-FICA and commercial chemiluminescence immunoassay (CLIA) methodology

We collected 100 human serum samples from Zhengzhou Central Hospital. For comparison with the chemiluminescence immunoassay method, a semi-quantitative commercial ELISA kit was purchased from DiaSorin. The results were presented in Figures 6A, B, the serum results were compared with the results for the control reagents. The regression equation was Y = 1.455X+13.89, and the correlation with DiaSorin was R^2 = 0.9438. The positive samples containing a high viral load showed color very quickly (5–10 min) at the T lines; this was statistically significant, and confirms that the results of the tests are in good agreement.

Discussion

Vitamin D has become more popular in recent years as people's living circumstances have improved (Aloia et al., 2010). Vitamin D is one of the most vital nutrients for maintaining human life activities. UV radiation exposure converts 7-dehydrocholesterol in the skin to vitamin D, which then plays a crucial function in blood circulation throughout the body (Ahmed et al., 2020). At present, the methodology involved in the 25-OH VD detection kit mainly includes six methods (Tripathi et al., 2022). Because 25-OH VD is not found in free form in human serum, but rather in conjunction with vitamin D binding protein (VDBP), the test strips are utilized to evaluate genuine human blood samples (Zhu et al., 2022). LC-MS/MS method instruments are expensive and have strict installation conditions, requiring a larger area to meet the requirements (Ko et al., 2021; Gao et al., 2022). In recent years, QDs technology is a development after the tracer marker colloidal gold Immunological testing methods (Geszke-Moritz and Moritz, 2013). Fluorescent microspheres are used in different technologies, such as electrochemical technology, immunochromatography technology, and other detection technologies (Shivalkar et al., 2022). Xiang et al. (2011) used self-assembly technology to alternately assemble quantum dot fluorescent microspheres, which were combined with electrochemical methods for the determination of urethral pathogens. They obtained a sensitivity more than ten times higher than other fluorescent substances such as colloidal gold.

TABLE 3 Accuracy and precision of the QD immunochromatographic test strip.

Spiked 25-OHVD (ng/mL)	Intra-assay			Inter-assay[a]		
	Test[b]	CV (%)	Recovery (%)	Test[b]	CV (%)	Recovery (%)
20	20.12 ± 0.019	1.78	80.48	21.34 ± 0048	4.34	85.35
50	46.09 ± 0.014	1.84	92.18	50.13 ± 0.019	2.39	100.26
100	93.41 ± 0.057	9.96	93.41	100.65 ± 0.054	9.35	10,065

[a] Assay was completed every 3 days for 15 days continuously.

[b] Mean value of three replicates at each 25-OHVD, spiked concentration.

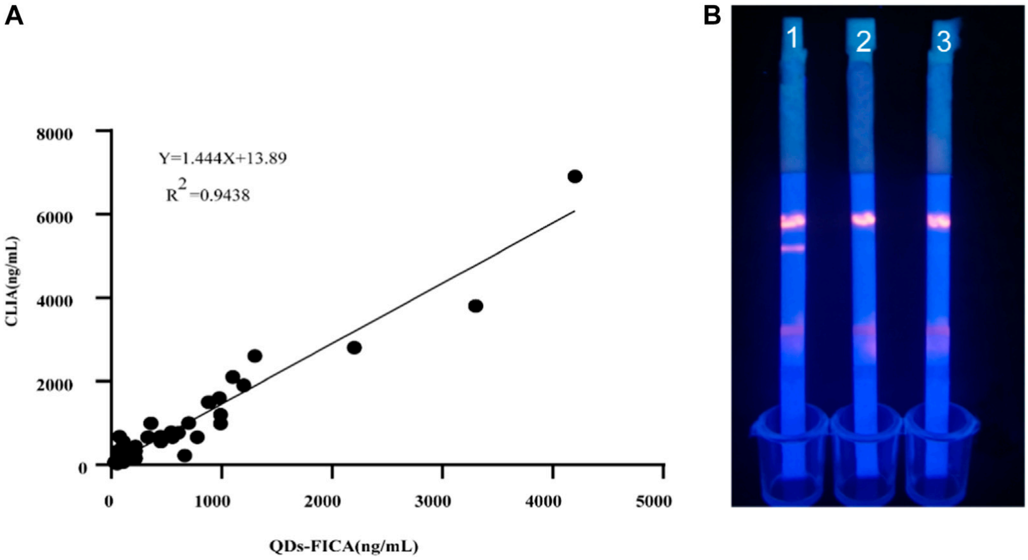

FIGURE 6
Evaluation of the QDs-FICA platform with clinical sample. **(A)** 25-OH V D-positive serum samples were quantified using both QDs-FICA and a commercially available human 25-OH VD CLIA kit. **(B)** QDs-FICA visual readout. 1, positive sample; 2, negative sample; CK, blank control with double-distilled water.

In this study, quantum dots were used as labeling materials to label 25-OH VD, and QDs-FICA provided a new detection method for 25-OH VD. We used several methods to verify whether the coupling was successful. High-resolution TEM images of individual particles showed that a large number of oil-soluble ZnCdSe/ZnS QDs were tightly embedded in the polymer. The data indicate that there is effective coupling between the QDs and the 25-OH VD monoclonal antibody, and confirm successful synthesis of the immunofluorescence probe. When mAb are coupled to QDs, the excitation and emission wavelengths remained unchanged, but the fluorescence intensity was weaker than that of QDs, which may be related to the effect of the antibody on the fluorescence detection or the occurrence of fluorescence burst during the coupling process. Although EDC reactions are usually carried out in acidic buffer solutions (pH 4.7–5.5), effective coupling can also be achieved in high-pH buffer solutions. After repeated verification, the optimal pH of ZnCdSe/ZnS core-shell QDs and anti-25-OH VD mAb was 7.6. The ideal reading time of the test strip was 15 min The concentration of 0.2 mol/L of NaC1 solution was determined as the optimal salt ion concentration. A solution with 10% ethanol mass fraction was selected for this experiment. The QDs-FICA exhibited dynamic linear detection of 25-OH VD in PBS from 5 ng/mL to 100 ng/mL and the strip quantitative curves could be represented by the following regression equation: $y = -0.02088 \log x)+1.444$ ($R^2 = 0.9050$). The IC_{50} of the QDs-FICA was achieved at 39.6 ± 1.33 ng/mL. The cross-reaction rate between the test strip and 25-OH VD_2 was 100%, indicating that the affinity of the antibody to 25-OH VD_2 was equal to 25-OH VD. The cross-reaction rates of 25-OH $VD_{3,}$ 125-OH_2VD_3, and125-OH_2VD_2 with the strip were 28%, 10%, and 22%, respectively. The cross-reaction rate VD_3 and VD_2 were less than 1% with the test strip. The intra-batch spiking recoveries ranged between 85.6% and 90.76%, with coefficients of variance ranging between 7.0% and 23.72%. The recovery rates of the intra- and inter-assays for the spiked samples ranged from 80.48% to 93.41%, and the coefficients of variation were all below 10%. The test strips were used to determine the presence of 25-OH VD in human serum.

These findings indicate that the QDs-FICA exhibit superior performance to colloidal gold; this may be due to the low capture rate of positive results observed by colloidal gold immunochromatography through observation with the naked eye in contrast, fluorescent materials such as QDs can be collected and read by instruments through fluorescence emission, resulting in higher reliability of the results. In addition, the superior performance of QDs enables their widespread application in the field of immunochromatography. The QDs-FICA established in this study is suitable for the rapid clinical detection of vitamin D at the community level and in remote areas. The study also meets the demands for visualization inspection, providing a good choice for screening and surveillance of in the future.

Conclusion

In summary, in this study, we applied QDs-FICA to 25-OH VD detection for the first time. Compared with traditional immune detection methods, this method provides a new detection method for 25- OH VD. The 25-OH VD magnetic particle chemiluminescence immunoassay established in this study can be applied to quantitative clinical detection of 25-OH VD content in human serum, and its accuracy, precision, linearity, cross-reactivity, anti-interference ability, and stability meet clinical requirements. Besides, the QDs-FICA established in this study is suitable for the rapid clinical detection of vitamin D at the community level and in remote areas, providing a good choice for disease screening and surveillance.

Data availability statement

The original contributions presented in the study are included in the article/Supplementary Material, further inquiries can be directed to the corresponding authors.

Ethics statement

All donors provided written informed consent, and the present study was approved by the Ethics Committee of Zhengzhou Central Hospital Affiliated to Zhengzhou University (Ethics No. 202112).

Author contributions

HY: Funding acquisition, Supervision, Writing–review and editing. JW: Conceptualization, Data curation, Formal Analysis, Investigation, Methodology, Project administration, Software, Validation, Writing–original draft. GS: Data curation, Investigation, Project administration, Software, Writing–original draft. FL: Methodology, Supervision, Writing–original draft. ZZ: Formal Analysis, Project administration, Supervision, Conceptualization, Writing–original draft. LS: Conceptualization, Data curation, Resources, Software, Writing–original draft. PL: Data curation, Methodology, Project administration, Validation, Writing–original draft.

Funding

The author(s) declare financial support was received for the research, authorship, and/or publication of this article. This work was supported by the henan province medical science and technology project (grant numbers LHGJ20200767), this work was also supported by the Henan Province science and technology research and development projects (grant numbers 222102310032).

Acknowledgments

We thank clinical laboratory of Zhengzhou central hospital for providing blood samples.

Conflict of interest

The authors declare that the research was conducted in the absence of any commercial or financial relationships that could be construed as a potential conflict of interest.

Publisher’s note

Supplementary material

The Supplementary Material for this article can be found online at: https://www.frontiersin.org/articles/10.3389/fbioe.2023.1326254/full#supplementary-material

References

Ahmad Najib, M., Selvam, K., Khalid, M. F., Ozsoz, M., and Aziah, I. (2022). Quantum dot-based lateral flow immunoassay as point-of-care testing for infectious diseases: a narrative review of its principle and performance. *Diagn. (Basel)* 12 (9). doi:10.3390/diagnostics12092158

Ahmed, S., Goldberg, G. R., Raqib, R., Roy, S. K., Haque, S., Braithwaite, V. S., et al. (2020). Aetiology of nutritional rickets in rural Bangladeshi children. *Bone* 136, 115357. doi:10.1016/j.bone.2020.115357

Aloia, J. F., Chen, D. G., Yeh, J. K., and Chen, H. (2010). Serum vitamin D metabolites and intestinal calcium absorption efficiency in women. *Am. J. Clin. Nutr.* 92 (4), 835–840. doi:10.3945/ajcn.2010.29553

Balsan, S., Garabédian, M., Larchet, M., Gorski, A. M., Cournot, G., Tau, C., et al. (1986). Long-term nocturnal calcium infusions can cure rickets and promote normal mineralization in hereditary resistance to 1,25-dihydroxyvitamin D. *J. Clin. Invest.* 77 (5), 1661–1667. doi:10.1172/jci112483

Binkley, N., Ramamurthy, R., and Krueger, D. (2010). Low vitamin D status: definition, prevalence, consequences, and correction. *Endocrinol. Metab. Clin. North Am.* 39 (2), 287–301. table of contents. doi:10.1016/j.ecl.2010.02.008

Bouillon, R., Manousaki, D., Rosen, C., Trajanoska, K., Rivadeneira, F., and Richards, J. B. (2022). The health effects of vitamin D supplementation: evidence from human studies. *Nat. Rev. Endocrinol.* 18 (2), 96–110. doi:10.1038/s41574-021-00593-z

Chen, P., Zhou, M., Chen, X., Xiong, S., Su, Y., Zhou, H., et al. (2022). Quantum dot bead-based competitive immunochromatographic assay for enterotoxin aureus A detection in pasteurized milk. *J. Dairy Sci.* 105 (6), 4938–4945. doi:10.3168/jds.2021-21568

Di Somma, C., Scarano, E., Barrea, L., Zhukouskaya, V., Savastano, S., Mele, C., et al. (2017). Vitamin D and neurological diseases: an endocrine view. *Int. J. Mol. Sci.* doi:10.3390/ijms18112482

Gao, W., Wei, L., Zhao, J., Yang, X., Han, Y., Liu, Y., et al. (2022). The measurement of 25-hydroxyvitamin-D in chronic HBV patients using LC-MS/MS. *Clin. Lab.* 68 (7). doi:10.7754/Clin.Lab.2021.211034

Garabédian, M., Vainsel, M., Mallet, E., Guillozo, H., Toppet, M., Grimberg, R., et al. (1983). Circulating vitamin D metabolite concentrations in children with nutritional rickets. *J. Pediatr.* 103 (3), 381–386. doi:10.1016/s0022-3476(83)80407-7

Geszke-Moritz, M., and Moritz, M. (2013). Quantum dots as versatile probes in medical sciences: synthesis, modification and properties. *Mater Sci. Eng. C Mater Biol. Appl.* 33 (3), 1008–1021. doi:10.1016/j.msec.2013.01.003

Gouni-Berthold, I., and Berthold, H. K. (2021). Vitamin D and vascular disease. *Curr. Vasc. Pharmacol.* doi:10.2174/1570161118666200317151955

Holick, M. F. (2023). The one-hundred-year anniversary of the discovery of the sunshine vitamin D(3): historical, personal experience and evidence-based perspectives. *Nutrients* 15 (3). doi:10.3390/nu15030593

Janjusevic, M., Gagno, G., Fluca, A. L., Padoan, L., Beltrami, A. P., Sinagra, G., et al. (2021). The peculiar role of vitamin D in the pathophysiology of cardiovascular and neurodegenerative diseases. *Life Sci.* doi:10.1016/j.lfs.2021.120193

Ko, D. H., Jun, S. H., Nam, Y., Song, S. H., Han, M., Yun, Y. M., et al. (2021). Multiplex LC-MS/MS for simultaneous determination of 25-hydroxyvitamin D, 24,25-dihydroxyvitamin D(3), albumin, and vitamin D-binding protein with its isoforms: One-step estimation of bioavailable vitamin D and vitamin D metabolite ratio. *J. Steroid Biochem. Mol. Biol.* 206, 105796. doi:10.1016/j.jsbmb.2020.105796

Koo, J. J., Jung, K. H., Park, K., Min, W. J., Yu, K. S., Kim, Z. H., et al. (2022). Characterization of the interfacial structures of core/shell CdSe/ZnS QDs. *J. Phys. Chem. Lett.* 13 (31), 7220–7227. doi:10.1021/acs.jpclett.2c01923

Li, Z., Wang, A., Zhou, J., Chen, Y., Liu, H., Liu, Y., et al. (2022). A universal fluorescent immunochromatography assay based on quantum dot nanoparticles for the rapid detection of specific antibodies against SARS-CoV-2 nucleocapsid protein. *Int. J. Mol. Sci.* 23 (11). doi:10.3390/ijms23116225

Lin, R., Skandarajah, A., Gerver, R. E., Neira, H. D., Fletcher, D. A., and Herr, A. E. (2015). A lateral electrophoretic flow diagnostic assay. *Lab. Chip* 15 (6), 1488–1496. doi:10.1039/c4lc01370k

Liu, W., Zhang, L., Xu, H.-J., Li, Y., Hu, C.-M., Yang, J.-Y., et al. (2018). The anti-inflammatory effects of vitamin D in tumorigenesis. *Int. J. Mol. Sci.* doi:10.3390/ijms19092736

Mano, H., Kushioka, T., Kise, S., Nagao, C., Iijima, A., Nishikawa, M., et al. (2023). Development of nanoluciferase-based sensing system that can specifically detect 1α,25-dihydroxyvitamin D in living cells. *J. Steroid Biochem. Mol. Biol.* 227, 106233. doi:10.1016/j.jsbmb.2022.106233

McIntosh, N., Livesey, A., and Brooke, O. G. (1982). Plasma 25-hydroxyvitamin D and rickets in infants of extremely low birthweight. *Archives Dis. Child.* doi:10.1136/adc.57.11.848

Monteiro, T. O., Tanaka, A. A., Damos, F. S., and Luz, R. C. (2017). Photoelectrochemical determination of tert-butylhydroquinone in edible oil samples employing CdSe/ZnS quantum dots and LiTCNE. *Food Chem.* 227, 16–21. doi:10.1016/j.foodchem.2017.01.089

Reid, I. R., Bolland, M. J., and Grey, A. (2014). Effects of vitamin D supplements on bone mineral density: a systematic review and meta-analysis. *Lancet* 383 (9912), 146–155. doi:10.1016/s0140-6736(13)61647-5

Revez, J. A., Lin, T., Qiao, Z., Xue, A., Holtz, Y., Zhu, Z., et al. (2020). Genome-wide association study identifies 143 loci associated with 25 hydroxyvitamin D concentration. *Nat. Commun.* doi:10.1038/s41467-020-15421-7

Shen, J., Zhou, Y., Fu, F., Xu, H., Lv, J., Xiong, Y., et al. (2015). Immunochromatographic assay for quantitative and sensitive detection of hepatitis B virus surface antigen using highly luminescent quantum dot-beads. *Talanta* 142, 145–149. doi:10.1016/j.talanta.2015.04.058

Shivalkar, S., Arshad, F., Sahoo, A. K., and Sk, M. P. (2022). Visible light-mediated photoactivated sulfur quantum dots as heightened antibacterial agents. *ACS Omega.* doi:10.1021/acsomega.2c03968

Singh, S., Dhawan, A., Karhana, S., Bhat, M., and Dinda, A. K. (2020). Quantum dots: an emerging tool for point-of-care testing. *Micromachines (Basel)* 11 (12). doi:10.3390/mi11121058

Su, R., Wu, Y. T., Doulkeridou, S., Qiu, X., Sørensen, T. J., Susumu, K., et al. (2022). A nanobody-on-quantum dot displacement assay for rapid and sensitive quantification of the epidermal growth factor receptor (EGFR). *Angew. Chem. Int. Ed. Engl.* 61 (33), e202207797. doi:10.1002/anie.202207797

Su, Z., Narla, S. N., and Zhu, Y. (2014). 25-Hydroxyvitamin D: analysis and clinical application. *Clin. Chim. Acta* 433, 200–205. doi:10.1016/j.cca.2014.03.022

Tripathi, A., Ansari, M., Dandekar, P., and Jain, R. (2022). Analytical methods for 25-hydroxyvitamin D: advantages and limitations of the existing assays. *J. Nutr. Biochem.* 109, 109123. doi:10.1016/j.jnutbio.2022.109123

Vieth, R. (1999). Vitamin D supplementation, 25-hydroxyvitamin D concentrations, and safety. *Am. J. Clin. Nutr.* 69 (5), 842–856. doi:10.1093/ajcn/69.5.842

Wang, C., Yang, X., Zheng, S., Cheng, X., Xiao, R., Li, Q., et al. (2021). Development of an ultrasensitive fluorescent immunochromatographic assay based on multilayer quantum dot nanobead for simultaneous detection of SARS-CoV-2 antigen and influenza A virus. *Sens. Actuators B Chem.* 345.130372. doi:10.1016/j.snb.2021.130372

Xiang, Y., Zhang, H., Jiang, B., Chai, Y., and Yuan, R. (2011). Quantum dot layer-by-layer assemblies as signal amplification labels for ultrasensitive electronic detection of uropathogens. *Anal. Chem.* 83 (11), 4302–4306. doi:10.1021/ac200564r

Yang, E., Zhang, Y., and Shen, Y. (2022). Quantum dots for electrochemiluminescence bioanalysis - a review. *Anal. Chim. Acta* 1209.339140. doi:10.1016/j.aca.2021.339140

Yun, C., Chen, J., Yang, C., Piao, J., and Yang, X. (2015). [Comparison for ELISA and CLIA of serum 25-hydroxy vitamin D determination]. *Wei Sheng Yan Jiu* 44 (3), 435–439.

Zhang, J., Shikha, S., Mei, Q., Liu, J., and Zhang, Y. (2019). Fluorescent microbeads for point-of-care testing: a review. *Mikrochim. Acta* 186 (6), 361. doi:10.1007/s00604-019-3449-y

Zhou, J., Yang, Q., Liang, C., Chen, Y., Zhang, X., Liu, Z., et al. (2021). Detection of ochratoxin A by quantum dots-based fluorescent immunochromatographic assay. *Anal. Bioanal. Chem.* 413 (1), 183–192. doi:10.1007/s00216-020-02990-1

Zhu, A., Kuznia, S., Boakye, D., Schöttker, B., and Brenner, H. (2022). Vitamin D-binding protein, bioavailable, and free 25(OH)D, and mortality: a systematic review and meta-analysis. *Nutrients* 14. doi:10.3390/nu1419389

Frontiers in Bioengineering and Biotechnology

TYPE Review
PUBLISHED 22 January 2024
DOI 10.3389/fbioe.2023.1333752

OPEN ACCESS

EDITED BY
Sameer Hussain,
Xi'an Jiaotong University, China

REVIEWED BY
Kafeel Ahmad,
Sungkyunkwan University, Republic of Korea
Ansar Abbas,
Xi'an Jiaotong University, China
Siavash Iravani,
Independent Researcher, Isfahan, Iran

*CORRESPONDENCE
Surya Das,
dassurya394@gmail.com
Somnath Mondal,
somomsom@gmail.com
Dhiman Ghosh,
dhiman.ghosh@phys.chem.ethz.ch

†These authors have contributed equally to this work

RECEIVED 05 November 2023
ACCEPTED 29 December 2023
PUBLISHED 22 January 2024

CITATION
Das S, Mondal S and Ghosh D (2024), Carbon quantum dots in bioimaging and biomedicines. *Front. Bioeng. Biotechnol.* 11:1333752.
doi: 10.3389/fbioe.2023.1333752

Carbon quantum dots in bioimaging and biomedicines

Surya Das[1]*†, Somnath Mondal[2]*† and Dhiman Ghosh[3]*†

[1]Department of Chemistry, University of Kalyani, Kalyani, India, [2]Department of Chemistry, Pennsylvania State University, State College, PA, United States, [3]Department of Chemistry and Applied Biosciences, Zurich, Switzerland

Carbon quantum dots (CQDs) are gaining a lot more attention than traditional semiconductor quantum dots owing to their intrinsic fluorescence property, chemical inertness, biocompatibility, non-toxicity, and simple and inexpensive synthetic route of preparation. These properties allow CQDs to be utilized for a broad range of applications in various fields of scientific research including biomedical sciences, particularly in bioimaging and biomedicines. CQDs are a promising choice for advanced nanomaterials research for bioimaging and biomedicines owing to their unique chemical, physical, and optical properties. CQDs doped with hetero atom, or polymer composite materials are extremely advantageous for biochemical, biological, and biomedical applications since they are easy to prepare, biocompatible, and have beneficial properties. This type of CQD is highly useful in phototherapy, gene therapy, medication delivery, and bioimaging. This review explores the applications of CQDs in bioimaging and biomedicine, highlighting recent advancements and future possibilities to increase interest in their numerous advantages for therapeutic applications.

KEYWORDS

carbon quantum dots, biocompatible quantum dots, bioimaging, biomedicine, metal-doped CQD, CQD-polymer composite (CPD), graphene-based carbon dots (GQD), carbon dots

1 Introduction

An element's properties are determined by its electronic configuration, but Quantum phenomena emerge when matter is reduced to nanoscale dimensions due to matter size (Cotta, 2020; García de Arquer et al., 2023). The Chemistry Nobel Prize for 2023 recognizes the discovery and evolution of quantum dots (QDs) and is jointly awarded to Aleksey Yekimov (created size-dependent quantum effects in coloured glass), Louis Brus (first to demonstrate size-dependent particle quantum effects), Moungi Bawendi (revolutionized the chemical productions of QD) (NobelPrize. org., 2024). QDs are tiny nanoparticles with properties determined by size. Quantum dots, the nanotechnology components offer significant benefits to humanity, including tiny sensors, flexible electronics, encrypted quantum communication, thinner solar cells, and surgery to guide tissue removal (Gangasani and Student, 2007; Cheki et al., 2013; Knoblauch et al., 2014; Zhao and Zhu, 2016).

Carbon nanomaterials have drawn great interest due to their simple surface functionalization, easy synthesis methods, biodegradability, and no toxicity. Carbon-based quantum dots or Carbon quantum dots (CQDs) are submicron-sized nanomaterials with zero dimensions that were initially produced in 2004 while purifying single-walled carbon nanotubes (SWCNTs) (Xu et al., 2004). Following this, CQDs have been applied to a broad range of applications because of their inexpensive preparation cost and advantageous qualities, which include solubility in aqueous medium, chemical inertness, biocompatibility, and non-toxicity (Wang et al., 2014; Lim et al., 2015; Sousa et al., 2021). CQDs exhibit unique and fascinating properties, with their colours varying based on their size (Mai et al., 2020). CQDs are largely employed in biological applications due to their intrinsic fluorescence, stability, biocompatibility, ease of manufacture, and lack of adverse effects (Lan et al., 2017; Pourmadadi et al., 2023). Carbon nanotubes, graphene, and fullerenes have low aqueous solubility resulting in no fluorescence emission in visible regions and having limited applications (Sahu et al., 2012; Liang et al., 2013; Yang et al., 2013). On the other hand, CQDs are not having such limitations. CQDs, with their unique optical and electronic properties, are increasingly used in electronics, sensors, solar cells, catalysis, supercapacitors, and energy conversion gadgets (Wang and Hu, 2014; Lim et al., 2015; Ahmad et al., 2017; Pal et al., 2019). Most CQD molecules are typically composed of a sp^2/sp^3 hybridized carbon core with various surface functional groups (Bhunia et al., 2013; Zhao et al., 2015). The water-soluble nature of CQDs is attributed to the presence of functional groups that contain oxygen, namely, carboxyl (-COOH) and hydroxyl (-OH), on their surface (Zhu et al., 2015). In addition to providing fluorescence characteristics, these functional groups on CQDs assist their solubility and enable them to generate durable colloids in water or polar solvents. Their significant quantum yield (QY) of fluorescence and stable red and near-infrared emission properties make them used in various applications in biology and medicine, particularly in bioimaging and biomedicines (Bhunia et al., 2013; Luo et al., 2013; Zuo et al., 2015). CQDs have also been employed to understand the interactions with various proteins, like other biocompatible nanomaterials (Mondal et al., 2015; 2016; Mondal, 2017; Malik et al., 2019). This opens a new avenue for understanding the significance of CQD in nanomedicines with possible interactions and their outcomes with various human proteins. CQDs' distinct chemistry and optical and physical characteristics render them a potential candidate for advanced nanomaterials research for bioimaging and biomedicines (Nazir et al., 2014; Sasaki et al., 2021; Sangjan et al., 2022; Gedda et al., 2023).

CQDs and polymer composite materials are efficient for biological, biochemical, and biomedical applications due to their ease of preparation, biocompatibility, and economical (Kausar, 2019; Molaei, 2019; Feng et al., 2021; Wang et al., 2022; Pathak et al., 2023). To create photoluminescent materials, careful tuning of their surface-level chemical groups and size is necessary for proper electrical structure tuning (Pal et al., 2019; Abbas et al., 2023; Yang et al., 2023). CQDs can be synthesized from various sources and mixed with polymers to create composites. Developing better CQD/polymer composite materials utilizing ligand exchange, grafting, and capping, leads to commend biocompatibility and optoelectrical features is a growing research topic (Qi and Gao, 2008; Kausar, 2019; Pathak et al., 2023). A variety of *in vivo* biological obstacles, such as glomerular filtration barriers, blood-brain barriers, and ion channels, can be overcome by them due to their small size (Yang et al., 2009). This type of CQD has great applications in bioimaging, phototherapy, drug delivery, and gene therapy (Ross et al., 2020; Pathak et al., 2023; Soumya et al., 2023).

We present a concise overview of the applications of CQDs in bioimaging and biomedicine. This review will explore recent advances, future possibilities, and various applications of CQDs and CQDs-based composites in the field of bioimaging and biomedicines, aiming to increase interest in numerous advantages of CQDs in these fields.

2 Synthesis of CQDs

Through the purification method of single-walled carbon nanotubes, Scrivens et al. obtained luminous carbon nanoparticles for the first time in 2004. Since then, several synthetic routes have been reported for the synthesis of CQDs varying in size and surface functional groupings. In general, CQDs can be synthesized using either of two primary methods: top-down or bottom-up (Figure 1) (Niu N. et al., 2017; Yadav et al., 2023). Top-down approaches use physical or chemical mechanisms to split up bigger carbon structures into smaller ones. For instance, arc discharge, laser ablation, and electrochemical oxidation can be utilised to cut graphite or carbon nanotubes into CQDs. These techniques have the potential to yield high-quality CQDs with uniform size distribution and good crystallinity, but they also come with a cost and could produce hazardous byproducts. Conversely, using thermal or chemical reactions, CQDs are assembled from smaller carbon precursors in bottom-up approaches. To create CQDs from organic molecules or biomass, for instance, hydrothermal treatment, solvothermal synthesis, and microwave pyrolysis can be applied (Ren R. et al., 2019). These techniques can provide CQDs with different functional groups and doping components, however, they could also lead to poor size control and low yield. To enhance the characteristics and functionality of CQDs, post-treatment procedures such as doping, surface passivation, and purification can be applied to both top-down and bottom-up approaches. The intended uses and properties of CQDs influence the synthesis technique selection.

2.1 Top-down method

The top-down process incorporates arc discharge, laser ablation, and acidic oxidation to break down the larger carbon resources into smaller components. This method generally employs carbon structures having sp^2 hybridization that don't have effective energy gaps or band gaps as precursor materials. The top-down method is very beneficial and effective for microsystem industries, but there are certain restrictions regarding the uniform size and shape distributions of CQDs, impurity, and costs (Table 1).

2.1.1 Laser ablation

This approach uses a high-energy laser pulse to illuminate the surface of the starting material. Consequently, it reaches a thermodynamic state characterized by incredibly high temperatures (>900°C) and pressures (75 KPa), leading to heating up quickly and condensing into a plasma state in which CQDs are formed by vapour crystallization. The first report of a laser ablation approach was made in 2006 by Sun and colleagues (Sun et al., 2006). The pulsed laser ablation method described by Ren X. et al., 2019 was utilized to produce N-doped micro-pore CQDs (NM-CQDs). NM-CQD was used for cellular staining and imaging and showed good internalization in various cells. Dual-beam laser ablation was described by Cui et al., 2020 as a means of producing carbon quantum dots (CQDs) from inexpensive carbon fabrics for utilization in bioimaging. The laser ablation method yields more PL emissions.

2.1.2 Arc discharge

This process utilizes gas plasma generated in a sealed reactor inside an anodic electrode to reorganize carbon molecules as they break into smaller segments from bulk carbon sources. When the electric current is present, the reactor's temperature can reach −3,700°C, resulting in massively energetic plasma. Carbon vapour accumulates in the cathode to produce CQDs (Su et al., 2014). When Xu and colleagues used the arch discharge approach first to isolate and purify a single-wall carbon nanotube, they unintentionally discovered fluorescent carbon quantum dots (Xu et al., 2004). The CQDs can exhibit blue-green, orange, or yellow fluorescence at a wavelength of 365 nm. Using HNO3, the carboxyl moiety (hydrophilic) was added to the CQD surface.

2.1.3 Acidic oxidation

It was reported in 2014 that hetero-atom-doped CQDs may be synthesized on a wide scale via hydrothermal reduction and acidic oxidation. To begin, carbon nanoparticles were oxidized using a mixture of H_2SO_4, HNO_3, and $NaClO_3$. (Dong et al., 2010). Subsequently, the oxidized CQDs underwent hydrothermal reactions with sources of selenium, sulfur, and nitrogen. Precursors such as sodium hydrosulfide (NaHS), sodium selenide (NaHSe), and dimethyl formamide (DMF) have each been employed. The generated S-CQDs, Se-CQDs, and N-CQDs, have demonstrated tunable extended fluorescence life-span, improved good quantum yield (QY), and PL activity in contrast to pure CQDs (Yan et al., 2014). CQDs are also used to prepare drug delivery applications and electrochemical sensors once they are generated using the acidic oxidation process.

2.1.4 Electrochemical

The electrochemical method, primarily introduced by Zhou and coworkers in 2007, was used to fabricate blue luminescent CQDs deriving out of multiwall carbon nanotubes. This method involves larger carbon precursors shredding into smaller parts through electrochemical oxidation, with a reference electrode. Zhang et al. have developed water-soluble CQDs exhibiting tunable luminescence (Hou et al., 2015). Deng et al., 2014 utilized this method to synthesize CQDs utilising low-molecular-weight alcohol. However, this technique needs surface passivation, and has a tedious purification process, making it the least frequently used technique.

2.1.5 Ultrasonication

The CQDs preparation process is easy and economical with the use of ultrasonic technology. It creates waves of alternating high- and low-pressure causing tiny bubbles in liquid to evolve and burst. To achieve varied properties, researchers can alter the reaction time, ultrasonic power, and ratio of carbon source to solvent. CQDs have been produced using this technique from various carbon materials, such as graphite, MWCNTs, and carbon fibre. CQDs exhibit blue luminous emission and range in diameter from 1 to 5 nm (Park et al., 2014). The ultrasonic method can also be used to create heteroatom-doped CQDs (Huang et al., 2018). CQDs can also be made using other waste materials that contain carbon (Feng and Zhang, 2019). Food waste and ethanol can be combined to create water-soluble CQDs, which have several benefits including low cytotoxicity, strong photoluminescence, and high Photostability for *in vitro* bioimaging.

2.2 Bottom-up method

The top-down approach for CQDs synthesis utilizes techniques like combustion, hydrothermal/solvothermal, microwave irradiation, template, and pyrolysis (Table 2). The shape and size of CQDs depend on factors like precursor molecular structures, solvent, and reaction conditions. The reaction condition is important as it affects the reactants as well as the incredibly random nucleation and escalation process of the CQDs. This approach has great advantages in material chemistry, is easy to operate, has lower costs, and is easier for large-scale production. Precursors for CQD synthesis can be chemical or biological, with chemical precursors including glucose, citric acid, sucrose, and natural sources like Azadirachta indica leaves, rice husks, and aloe vera.

2.2.1 Combustion

The combustion method gained popularity for its ease of scaling up, accurate precursor molecule design, affordability, and environmentally friendly features to enhance the bottom-up methods for producing CQDs. The method of synthesizing CQDs using combustion was initially published by Liu et al., 2007. This process uses oxidative acid treatments to adjust the fluorescence characteristics, improve water solubility, and aggregate tiny carbon resources into CQDs. Liu and Coworkers clarified that the process of partially burning a candle with aluminium foil and refluxing it in a solution of nitric acid produced candle ashes, followed by dissoluting the candle ashes in a neutral medium, centrifuging the mixture, and using a dialysis technique to obtain Pure CQDs. Researchers have developed combustion methods for producing fluorescent CQDs, such as combusting citric acid, followed by surface functionalization with carboxyl groups through acetic acid moiety conjugation at elevated temperatures (Yang et al., 2023). The combustion approach synthesizes CQDs with poor QY but good fluorescence without doping.

2.2.2 Hydrothermal

The hydrothermal process includes pouring the precursor materials into an aqueous media, then adding the mixture to a stainless-steel autoclave lined with Teflon and heating it to high pressure for many hours. Zhang et al., 2010 initially introduced the use of the hydrothermal method to prepare 2 nm-diameter fluorescent CQDs by employing L-ascorbic acid as a carbon precursor. The hydrothermal process, which has attracted major interest recently owing to its cost-effectiveness and environmental friendliness, produces CQDs from tiny molecules (amino acids, saccharides, sucrose, proteins, glucose, polymers, polyols, discarded peels or juice, etc.) in a single, environment friendly, and cost-effective way. Carbon quantum dots

TABLE 1 Top-down method of carbon quantum dots synthesis.

Synthetic pathway	Precursors	Utilization	Ref	Advantages	Disadvantages
Laser ablation	Graphite powder and cement	Bioimaging	Sun et al. (2006)	(a) Scalable (b) easy and convenient synthesis process (c) Ability to develop a range of nanostructures	(a) Expensive (b) a large amount of carbon material is needed (c) multi-step process (d) harsh reaction conditions (e) low control over size (f) low QY (quantum yield)
	Nano-carbon materials	Biology and imaging	Li et al. (2011)		
	Carbon cloth	Cell bio-imaging	Cui et al. (2020)		
	Carbon microparticles	Cell labelling and visualization	Doñate-Buendía et al. (2020)		
	Platanus biomass	Engineering and biomedical imaging	Ren et al. (2019b)		
Arc discharge	Graphite electrodes	Optical activity	Biazar et al. (2018)	(a) Most obtainable method	(a) Required purification (b) Low QY (quantum yield) (c) Harsh reaction conditions
	Graphite	energy technologies	Dey et al. (2014)		
	Carbon byproducts	Optoelectronics	Su et al. (2014)		
Ultrasonication	Food waste	Optoelectronics, biomedical imaging, and plant seed germination and growth	Park et al. (2014)	(a) simple to use (b) Mild condition required for the experiment (c) Cost- effective	(a) Low QY (quantum yield), (b) difficult to dope
	Cigarette ash	Cell imaging and cytotoxicity evaluation	Huang et al. (2018)		
	Coke	Applied in light emitting devices	Feng and Zhang (2019)		
Electrochemical Method	Sodium citrate and urea	Selective sensing for mercury ion	Hou et al. (2015)	(a) no surface passivation is required (b) less expensive (c) easy purification method (d) sustainable and environmentally friendly process	(a) allow only a few small precursors (b) tedious purifying process (c) Complex procedure (d) Time-consuming process (e) tough to determine the CQDs concentration
	Amino acids	Cell imaging, fibre staining and specific sensitive detection towards ferric ion	Niu et al. (2017a)		
	Low-molecular-weight alcohols (ethanol)	Cell imaging	Deng et al. (2014)		
	Graphite rods	Applied in catalysis, bioscience and energy technology	Li et al. (2010)		
Chemical oxidation	Activated carbon	Detecting metronidazole drugs using a chemiluminescence technique involving flow injection	Yan et al. (2014)	(a) Higher yield (b) Highly pure	(a) Poor quantum yield (b) Pollution of the environment
	Coal	Applied in various optical devices and materials	Li et al. (2015)		
	Activated carbon	ECL (electrochemiluminescent) biosensing and bioimaging	Dong et al. (2010)		

(CQDs) were made sustainably from biowaste obtained from banana peels incorporating a simple hydrothermal process by Lee et al. (Atchudan et al., 2020). When exposed to UV light (365 nm), these CQDs generate a strong blue fluorescence with a 20% quantum yield (QY). NS-CQDs (QY 53.19%) were also produced utilizing this process from L-lysine and thiourea to detect the concentration of picric acid in water. A solvothermal approach is also involved in synthesizing CQDs in which alcohol, ammonia, and other organic and inorganic solvents are employed in place of water (Zuo et al., 2015).

2.2.3 Microwave

CQDs can be produced efficiently and economically via microwave synthesis, which employs electromagnetic radiation with a broad wavelength that ranges from 1 mm to 1 m (Ahmad et al., 2018). This radiation can provide sufficient energy to disrupt the chemical bonds of the reaction's precursor components. In comparison to other techniques, this process is easy, straightforward, quick, and ecologically friendly, resulting in higher quantum yield for the CQDs formation. Zhu et al., 2009 and co-workers developed fluorescent CQDs having electrochemiluminescence abilities for the very first time by heating a clear aqueous solution of saccharides and PEG 200 in a 500 W microwave oven for 2–10 min utilizing this simple and affordable method.

2.2.4 Pyrolysis

The pyrolysis technique is a thermal decomposition of a precursor, typically over 430°C, to create nanoscale colloidal particles. It offers practicality, repeatability, simplicity, and

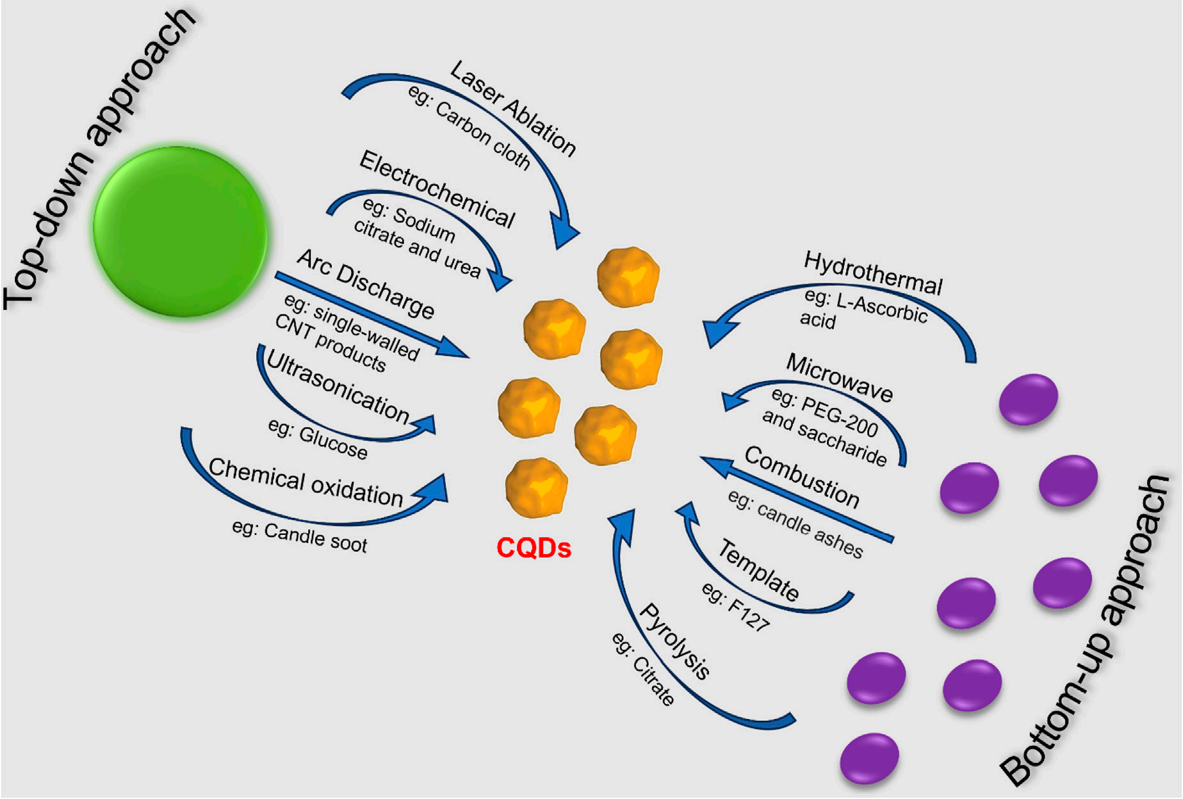

FIGURE 1
Top-down and bottom-up methods for CQD synthesis via various routes.

high quantum yield (QY). In the presence of a strong acid concentration and an alkali as a catalyst, the carbon precursor cleaves into colloidal nanoparticles. However, separating small precursors from raw materials is challenging. In 2009, Liu et al., 2009 developed a method for preparing CQDs using resol (source of Carbon) with surfactant-modified silica spheres. The CQDs were stable in a broad pH range and showed blue fluorescence. Xue et al., 2016 synthesized N-doped carbon quantum dots (CQDs) from peanut shell waste using an economical carbonization method, which shows excitation-dependent fluorescence emission. Praneerad et al., 2019 produced fluorescent CQDs from durian peel biomass waste, which was used for constructing a composite electrode with higher specific capacitance than a Carbon electrode.

2.2.5 Template

Another commonly used approach for producing nano-sized CQDs is the template-assisted technique which provides higher quantum yields and even size distribution. In this method, CQDs are prepared via two steps. The first step involved calcination, which produced CQDs in the suitable silicon sphere or mesoporous template and the second step involved etching, which removed the supporting components. As a beneficial methodology for CQDs, this procedure is simple, accessible, inhibit particle agglomeration, appropriate for surface passivation, and regulates CQD size (Liu et al., 2009). Mesoporous silica spheres were used as nanoreactors by Zhong and colleagues in 2011 to generate carbon dots with exceptional luminescence characteristics. Templates can be made of hard elements like silica, metal-organic framework, layered host matrices, and zeolite, or soft elements like surfactants. Yang et al., 2013 created a novel soft-hard template technique for photoluminescent CQDs synthesized from organic molecules. The soft template in this report is Pluronic P123, while the hard template is OMS (ordered mesoporous silica) SBA-15. The drawback of the template method is that certain templates are challenging to extract from the CQDs, and the fluorescence activity of the CQDs could be impacted when the templates are removed by heating or acid-base etching. Besides all these techniques discussed here, CQDs can also be synthesized from porous organic polymer following a suitable method for various applications (Pan et al., 2019; Das et al., 2022a).

3 Characteristics of CQDs

Depending on whether sp^2 carbon is present, the core-shell architectures of carbon quantum dots (CQDs) can have either an amorphous or graphitic crystalline structure. These tiny (2–3 nm) cores vary in size based on the synthesis method, precursors, and additional factors (Pathak et al., 2023; Yadav et al., 2023). Precursors, methods, and other factors are used to classify cores. The core structure of CQDs is ascertained using

TABLE 2 Bottom-up method of carbon quantum dots synthesis.

Synthetic pathway	Precursors	Utilization	Reference	Advantages	Disadvantages
Hydrothermal	L-Ascorbic acid	Biological labelling, bioimaging, and diagnosis of disease	Zhang et al. (2010)	(a) Cheap (b) eco-friendly (c) controllable (d) non-toxic	(a) Low yield (b) low purity (c) Poor size control
	Glucosamine hydrochloride	Biomedical, catalysis and chromatography	Yang et al. (2011)		
	Citric-acid, and ethylenediamine	Printing inks, biosensors for detecting Fe^{3+}, and Bioimaging	Zhu et al. (2013)		
	Phosphoric acid and folic acid	Biosensor for Pt^{4+} detection	Campos et al. (2016)		
	Glycerol and (3-aminopropyl) triethoxysilane (APTS)	intracellular Cu^{2+} imaging in cells	Zou et al. (2016)		
	Citric acid and poly (ethylenimine)	Clinical and biochemical assays; morin detection in urine samples	Li et al. (2017a)		
	Tetraphenyl porphyrin and 1,2-ethanediamine (EDA)	Multicolour bioimaging and biosensors for Fe^{3+} ions detection	Wu et al. (2017)		
	Ethylene glycol, Folic acid	Biosensor for Hg^{2+} detection	Zhang and Chen (2014)		
Microwave	Diethylene glycol	antibacterial activity	Verma et al. (2020)	(a) Rapid, convenient and scalable (b) Inexpensive (c) Environmentally friendly	Poor size control
	PEG-200 and saccharide	Biological labelling and biosensors	Zhu et al. (2009)		
	Citric acid, branched polyethyleneimine	*In vivo* gene delivery	Pierrat et al. (2015)		
	Citric acid, urea	Screening of oxygen-states in CQDs	Dong et al. (2017)		
	Raw cashew gum	*In vivo* imaging	Pires et al. (2015)		
	Crab shell	Drug Delivery and Bioimaging	Yao et al. (2017)		
	Eggshell membrane	Sample detection and biotechnology	Wang et al. (2012)		
Combustion	Candle soot	Multicolor imaging	Liu et al. (2007)	(a) Large-scale synthesis (b) Exhibited good PL intensity (c) Simple, inexpensive, and eco-friendly method (d) displayed good fluorescence without doping	low quantum yield
Template	F127	Bioimaging agents	Liu et al. (2009)	Simple to manipulate CQD's size	(a) Time taking method (b) Cost -effective method (c) Limited quantum yield (d) Difficult steps
	Pluronic P123 and OMS (ordered mesoporous silica) SBA-15	Bioimaging	Yang et al. (2013)		
Pyrolysis	Durian peel waste	Supercapacitor	Praneerad et al. (2019)	(a) Rapid process (b) Repeatable, practicable, and simple	Broad size distribution
	Peanut shells	Multicolor cell imaging	Xue et al. (2016)		
	Watermelon peel	Optical imaging probes and cell imaging	Zhou et al. (2012)		

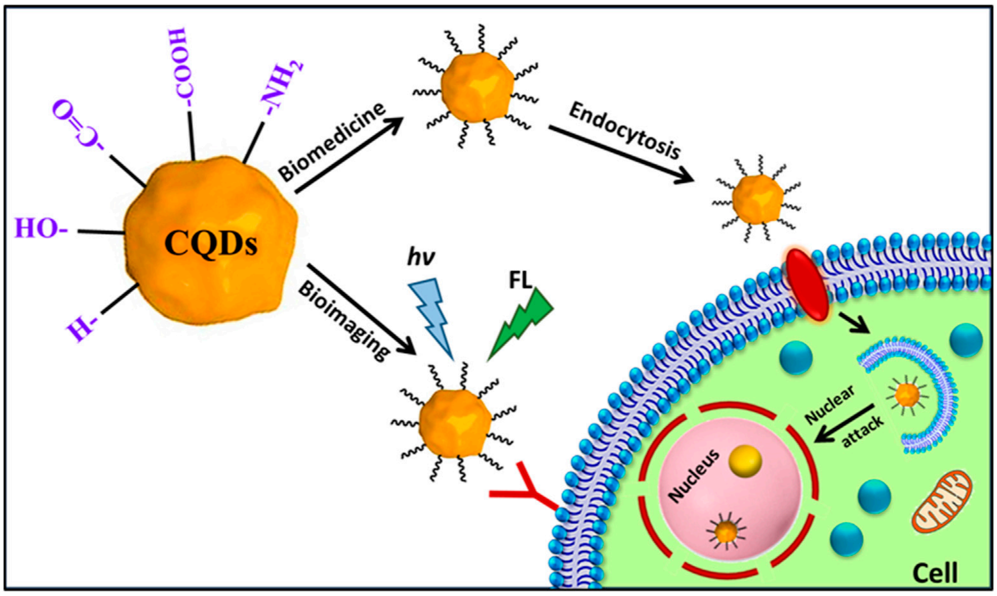

FIGURE 2
Schematic of the mechanism of actions of fluorescent carbon quantum dots inside the cells in bioimaging and biomedicine.

instrumental methods such as Nuclear magnetic resonance (NMR), Raman spectroscopy, X-ray diffraction (XRD), TEM, and SEM. X-ray photoelectron spectroscopy (XPS), elemental analysis (EA), and Fourier transform infrared (FT-IR) are further methods. NMR can also be employed to understand the interactions and relaxation studies of CQDs with various proteins (Jaipuria et al., 2012; 2022; Mondal et al., 2013; Dubey et al., 2016; Werbeck et al., 2020). Nitrogen sorption analysis is used to determine the surface area of carbon nanoparticles (Verma et al., 2020). Using zeta potential, the existence of functional groups on the outer layer is verified. The PL characteristics of CQD fluorescence emission arising out of the conjugated p domain are determined by the quantum-confinement effect from p-conjugated electrons within the sp^2 atomic structure (Zhu et al., 2015). Fluorescence emission is caused by surface imperfections such as sp^2 and sp^3 hybridized carbon, and the size of CQDs influences the characteristics of PL (Luo et al., 2014; Zuo et al., 2015). Fluorescence emission and peak placement in CQDs can be impacted by surface imperfections and irregularities. CQDs can be created using the entire spectrum of sunlight (Ahmad et al., 2018). Moreover, photoexcited electron transfer is aided by the CQDs-based composites' capacity to harvest light, which raises photocatalytic efficiency.

Carbon quantum dots, in contrast to semiconductor QDs, can exist in an amorphous form because of their predominant sp^2 and sp^3 molecular orbitals (Wang et al., 2014). Carbon QDs are often modified by surface passivation and functionalization with a particular organic ligand. As a result, several organic functional groups, including carboxylic, carbonyl, hydroxyl, and hydrocarbon, are capped on the surface (Cui et al., 2021). The carbon core is covalently linked to every member of this functional group. This effect makes CQD more soluble in water and makes preparing it for use in a variety of applications easier.

4 Properties of CQDs

CQDs are characterized by a "core-shell" nanostructure that is made up of surface functional groups and a nanoscale carbon core (Pourmadadi et al., 2023). Their various structural configurations and quantum confinement effect also affect their catalytic, optical, and electronic behaviours. These properties can further be modified utilizing surface passivation or doping the CQD (Yang et al., 2023). The bandgap and electronic structure are modified by doping and the presence of heteroatoms.

CQDs prepared out of various precursors, exhibit varying absorption spectra in different solvents (Wang et al., 2014). They have similar UV-visible absorption, with absorption peaks in the UV region ranging from 260 nm to 320 nm. The absorption peak in the 280–350 nm range is attributed to electronic transitions from C–O or C=O bonds to π* orbitals. The absorption peak in the 350–600 nm range is attributed to surface chemical moieties. Some CQDs display long-wavelength absorption ranging from 600 to 800 nm, originating out of the aromatic ring-containing structures (Cui et al., 2021). Surface modification or passivation can influence absorption properties. Carbon quantum dots (CQDs) can have their optical characteristics modified by surface passivation, functional groups, and heteroatom doping or co-doping (Yadav et al., 2023). The CQDs are shielded from impurity adherence and extra stability by the protective layer that surface passivation creates on their surface. When surface-passivating chemicals are added to CQDs, they exhibit increased quantum yields and fluorescence, making them highly optically active. Longer wavelength absorption can also be enhanced by surface passivation. Covalent bonds between functionalizing agents and CQDs can produce materials with exceptional photo reversibility, low toxicity, high stability, and strong biocompatibility (Gao et al., 2018). By modifying the π-π* energy level, the dopant modifies the bandgap, electrical structure, and optical characteristics of CQDs.

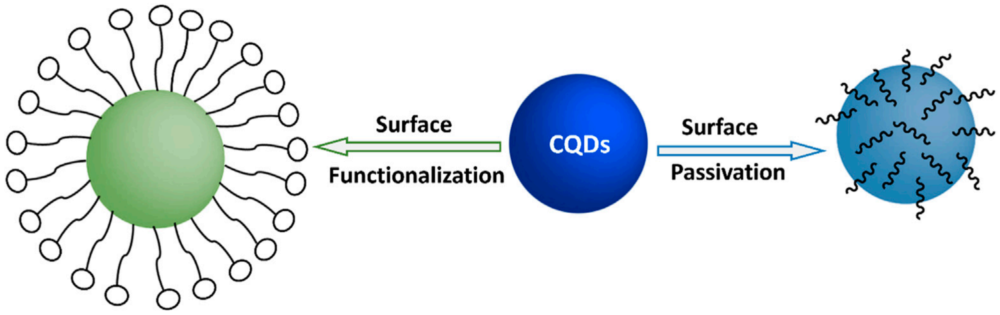

FIGURE 3
Schematic for surface functionalization and surface passivation on CQDs.

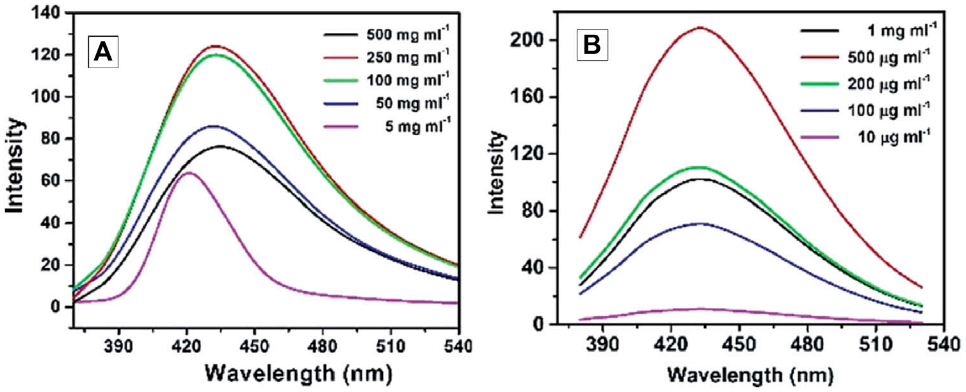

FIGURE 4
Fluorescence emission spectra (with excitation at 346 nm) of hydrophilic CQD **(A)** and hydrophobic CQD **(B)** prepared from sucrose and Octadecyl-amine/octadecene respectively. Reprinted (adapted) with permission from Mondal *et al.* (Mondal et al., 2015) Copyright (2015) Royal Society of Chemistry.

Various processes (as mentioned in Section 2) can be utilized to create such heteroatom-doped CQDs, which have better photocatalytic activity, increased electron transfer, and higher QYs.

Fluorescent CQDs have great applications in sensing, bioimaging and biomedicines (Figure 2). There are various mechanisms to understand the fluorescence in CQDs (Yang et al., 2023). Fluorescence phenomena in CQDs are primarily produced by two mechanisms: (a) surface defects, surface passivation/functionalization (Figure 3), carbon core state, quantum size effect, and (b) band gaps of π-conjugated domains (sp^2 hybridized) which resemble aromatic molecules incorporating certain energy band gaps regarding absorption and emission (Song et al., 2014). On the other hand, surface defects arise in CQD owing to the unsymmetrical arrangement of sp^2 and sp^3 carbon atoms, and the presence of hetero atoms like N, B, P, or S. Due to the surface defect, the solid host creates an environment like aromatic molecules resulting in absorbing UV light to exhibit various colour emissions. The two emission forms are seen in CQDs: excitation-independent emission because of the highly ordered graphitic structure, and excitation-dependent emission (tunable emission) because of different emission sites and particle size distribution (Figure 4). In contrast to conventional organic dyes, CQDs have high photostability and steady fluorescence.

Recent studies have explored the photoluminescence (PL) emission in carbon quantum dots (CQDs), which has gained interest in photocatalysis with other fields (Yang et al., 2023). PL emission wavelengths are larger than the excitation wavelength and can be attributed to band-gap transitions incorporated in conjugated π-domains or deficiencies in graphene structures. Research has shown that excitation-dependent emission of fluorescent CQDs with surface modifications and one-step thermal treatment of 4-amino antipyrine emit excitation-dependent PL emission in 525–660 nm. The investigation looks at the PL emission of CQD, with a particular emphasis on size modification. CQDs were created by an electrochemical method assisted by alkali, and their diameters ranged from 1.2 to 3.8 nm (Hasanzadeh et al., 2021). The PL characteristics fluctuated with particle size, as revealed by optical views, suggesting a highly reliant HOMO-LUMO gap (Zhu et al., 2015). Particles with sizes smaller than 3 nm are more likely to emit visible spectrum light because the band gap narrows with increasing particle size. PL emission from CQD produced from alkyl-gallates is independent of size. In this review, we will discuss the recent advancements in bioimaging and biomedical applications

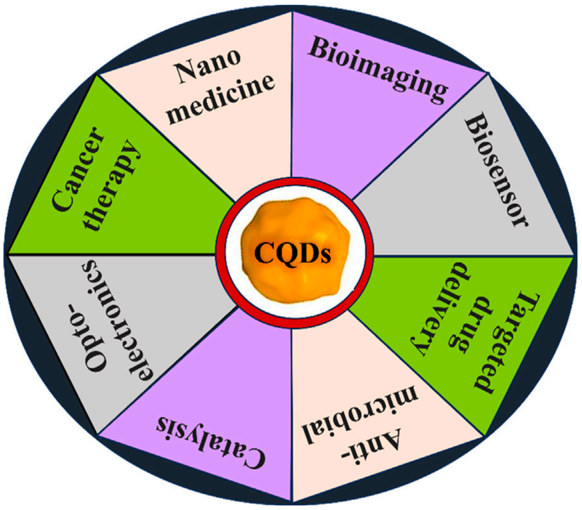

FIGURE 5
Various applications of CQDs. We discussed recent advancements in bioimaging and biomedical applications using CQDs in our review.

employing all these features and various modifications of CQDs (Figure 5).

5 CQDs in bioimaging

Bioimaging enables real-time, non-invasive imaging of biological phenomena. It is a technique of utmost importance in healthcare units for the diagnosis of human health diseases. The intrinsic fluorescence property of CQDs, great stability, and great advantage of modification with various functional groups offer a suitable candidate for bioimaging (Bhunia et al., 2013; Luo et al., 2014; Liu et al., 2020b; Su et al., 2020). In addition, multi-wavelength emissions, excellent photostability, resistance to photobleaching, and quick and easy methods of preparation, establish CQDs to be the fluorescent probes of the next-generation for *in vitro* and *in vivo* imaging (Wegner and Hildebrandt, 2015; Wang et al., 2022; Gedda et al., 2023). Other conventional quantum dots like metal quantum dots and organic dyes are toxic, mostly prohibiting their uses in bioimaging (Su et al., 2020; Wang et al., 2022). Three-dimensional visualization of the biological subcellular compartments as well as tissues and organisms can be obtained with various biocompatible carbon quantum dots (Table 3).

Biocompatible CQDs can readily penetrate various cells through endocytosis, a macropinocytosis-like cell-penetration mechanism based on the shape, surface functionalization, and type of the cells (Magesh et al., 2022; Wang et al., 2022). Bioimaging of such cellular compartments and organelles can lead to a broader understanding of early symptoms and progression of different diseases like Alzheimer's, Parkinson's, diabetes, cancers, and many others (Kabanov and Gendelman, 2007; Guerrero et al., 2021). CQD can be employed to understand the interactions with various proteins and track the changes through Bioimaging (Bhunia et al., 2013; Luo et al., 2013; Wang et al., 2022). The unique properties of CQDs, such as their outstanding photostability, low cytotoxicity, conspicuous biocompatibility, and multicolour emission profile, make them a prime option for fluorescence imaging (Luo et al., 2014). Up until recently, almost all CQDs have essentially labelled the cytoplasm and cell membrane without any special alterations. CQDs were used for intracellular imaging with HeLa cells, MCF-7 cells, Caco-2 cells, HepG2 cells, PC12 cells, lung cancer cells, and pancreas stem cells (Li et al., 2018; Xia et al., 2019; Shi et al., 2020; Tian et al., 2020; El-brolsy et al., 2022; Havrdová et al., 2022). Besides, researchers have systematically tracked the biodistribution of CQD in mice cells through *in vivo* imaging (Shi et al., 2020; Tian et al., 2020). Tao et al., 2012 performed *in vivo* fluorescence imaging investigations (Figure 6) on CQD-M derived from MWNTs. The researchers labelled CQD-M I^{125}. When the radiolabeling stability was examined in mouse plasma, the amount of I^{125} detachment from CQDs was found to be satisfactory. The biodistribution and blood radioactivity levels were used to measure the pharmacokinetics of CQDs. According to the study, following intravenous injection, CQDs were mostly collected in the liver and spleen. Early on, there was a significant level of kidney uptake of CQDs, indicating that they might pass through the glomerulus and be eliminated by urine. This study indicates that both renal and faecal excretion could lead to the clearance of CQDs (Tao et al., 2012).

Using CQDs in polymer matrices (Carbonized Polymer Dot or CPD) is an additional new field of study with a broad range of possible applications (Feng et al., 2021). CQDs with polyethyleneimine (PEI) functionalization display tunable fluorescence with multiple wavelength emissions (Chen et al., 2019). The ternary nano-assembly of CD-PEI/Au-PEI/pDNA renders an effective transfecting agent as observed from a fluorescence microscope (Kim et al., 2013). CQD is functionalised with quaternary ammonium groups employed in L929 and NIH/3T3 cell lines of healthy mice and imaged with fluorescence microscopy (Havrdová et al., 2021). This study reveals the intranuclear uptake of the functionalised CQDs utilising their intrinsic fluorescence properties. Photoacoustic (PA) imaging and near-infrared fluorescence are displayed by large amino acid mimicking (LAAM) CQDs synthesised from 1,4,5,8-tetraminoanthraquinone and citric acid (Li et al., 2020). LAAM CQDs can selectively image tumours. CQDs prepared from o-phenylenediamine and terephthalic acid applied for near-infrared (NIR) bioimaging (Ding et al., 2020; Moniruzzaman et al., 2022; Marković et al., 2023). A donor-acceptor (D-π-A) structural approach was introduced for the synthesis of this CQD. CQD-PEG was developed by choosing polyethylene glycol as a passivating agent for the increment in functionality and photoluminescence (PL) properties of CQDs (Peng et al., 2020). CQD-PEG were exceptionally photoresponsive and photoluminescent after the surface modification. PEG passivated CQDs were initially used to stain Caco 2 cells for cellular bioimaging, rendering CQD a potential fluorescent label of the cells. Red emissive CQDs (absorption: 400–750 nm) were prepared using polythiophene phenyl propionic acid (Ge et al., 2015; Liu et al., 2020a; Ding et al., 2020). The red emissive CQDs exhibit a high photothermal conversion efficiency ($\eta \sim 38.5\%$) and a strong photoacoustic response. These special qualities allow the red emissive CQDs to be utilised as photoacoustic, multifunctional fluorescent, and biomedicines

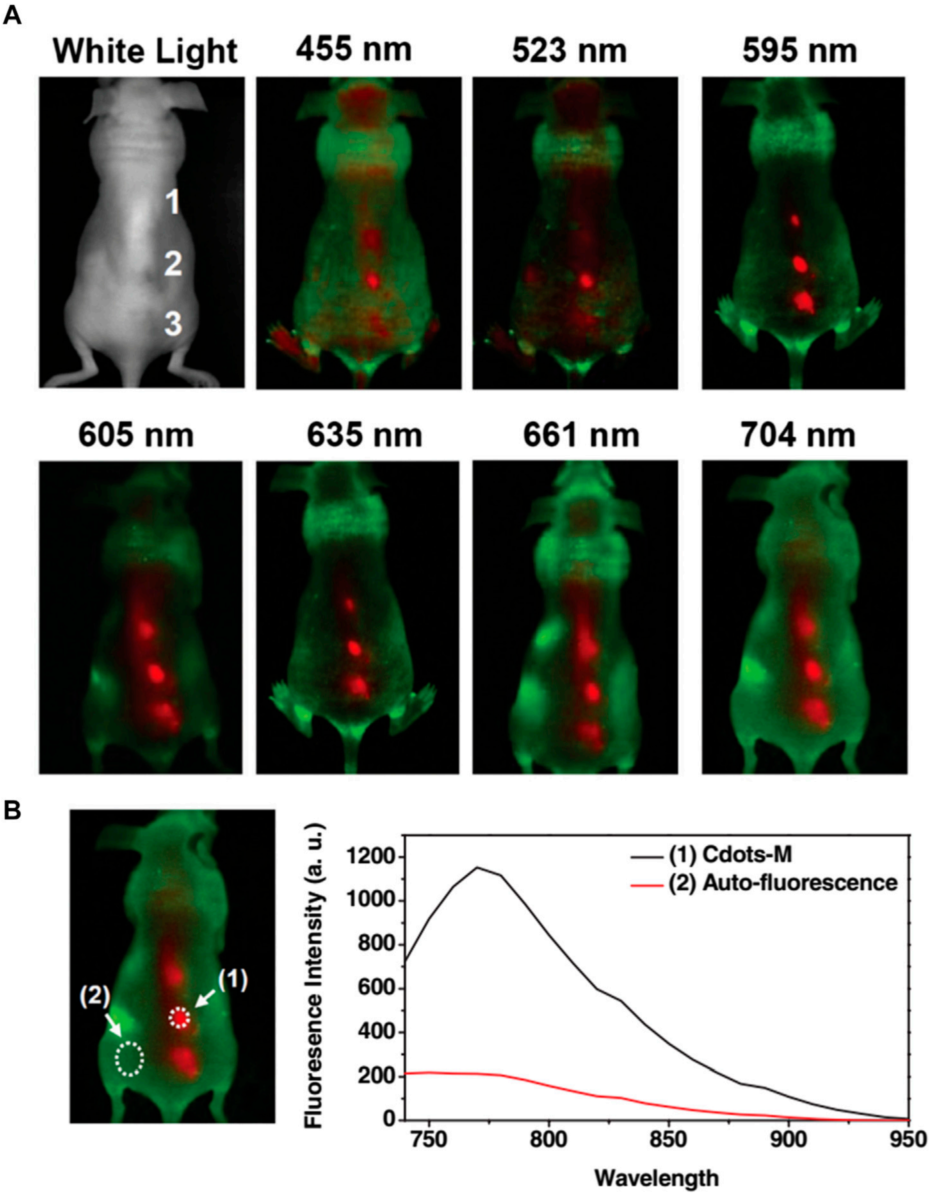

FIGURE 6
(A) Fluorescence imaging *in vivo*. *In vivo* fluorescence photos of a mouse administered with CQD. The pictures were captured at 455, 523, 595, 605, 635, 661, and 704 nm at different excitation wavelengths. Tissue autofluorescence and CQD fluorescent signals are shown in red and green, respectively. **(B)** The spectral picture obtained with NIR (704 nm) excitation has a signal-to-background separation. The background of tissue autofluorescence was clearly distinguished from the CQD fluorescence. High radioactivity of I^{125} was found in the urine and faeces of the mouse, indicating that both renal and faecal excretions may have contributed to the CQD's clearance. Reprinted with permission from Tao et al. (2012) Reprinted (adapted) with permission from Liu et al. Copyright (2012) Wiley.

(discussed in the next section). Most CQDs are synthesized from graphite-based materials (GQD) that exhibit characteristics of graphene and can be utilized for bioimaging applications (Kortel et al., 2020). In the past, some techniques have been used to obtain mitochondrial imaging, such as labelling tumour cells with aptamer AS1411 and causing CQDs to collect at the mitochondrial and lysosomal sites. For imaging the nucleus, graphene-based CQD-PEI (Polyethyleneamine) was used (Tian et al., 2020). Following the addition of CQD/hydrogel loaded without and with 5-fluorouracil, bioimaging of A549 cells was carried out. CQDs were functionalized after being produced with citric acid using hydrothermal carbonization involving RGERPPR and maleimide-polyethylene glycol-amino succinimide succinate (Mal-PEG-NHS) (Gao et al., 2018). The resulting CQD was utilized for bioimaging. Gadolinium-encapsulated carbon dots can exhibit high T1 relaxivity (16.0×10^{-3} M^{-1} S^{-1}, 7T) and intense fluorescence, enabling an imaging probe with intrinsically dual-mode (Jiao et al., 2022). The increased permeability and retention effect of these carbon dots helps them to accumulate readily in tumours and the unbound Gadolinium excretes from the host via the renal system.

Hydrophilic and hydrophobic CQDs can be obtained with the preferred synthetic routes (Section 2) which is not common for

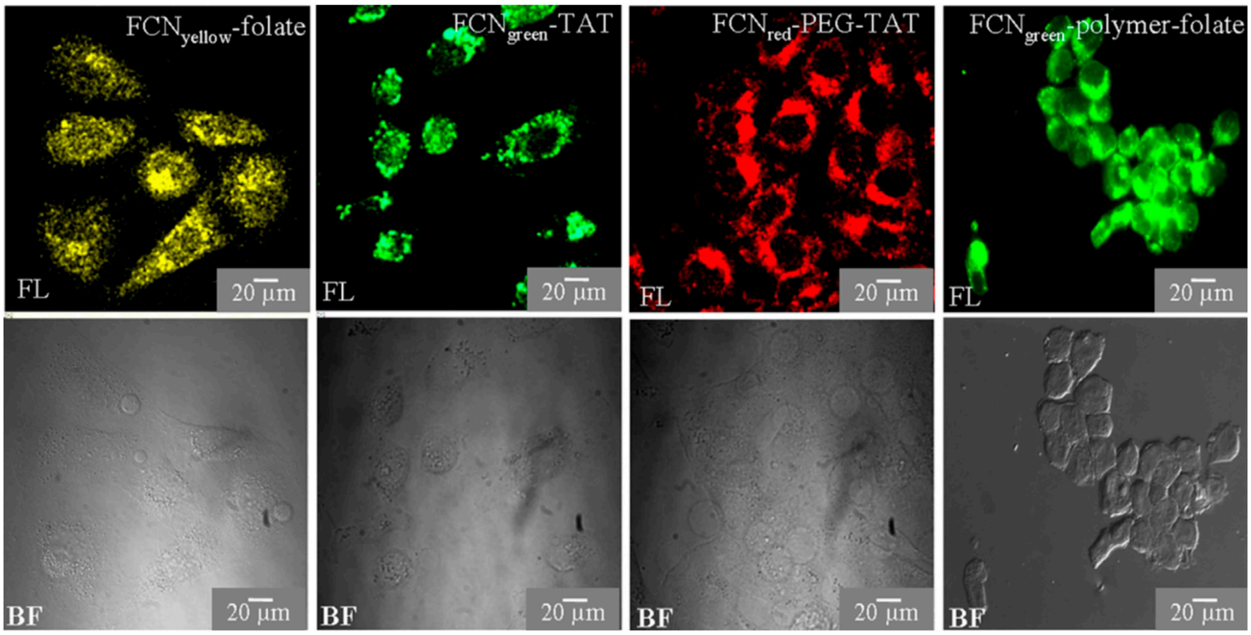

FIGURE 7
CQD as a fluorescent marker of cells. HeLa cells are cultured in CQDs for three to 6 hours, after which the labelled cells are observed under a fluorescent microscope. Using a confocal or Apotome microscope, cells are observed in bright field (BF) and fluorescence (FL) modes. Reprinted (adapted) with permission from Bhunia et al., 2013 Copyright (2013) Nature.

other metal quantum dots for biological applications. Hydrophobic CQDs in parallel to hydrophilic CQDs offer a wide range of applications for the study of membrane proteins and other biological systems. The application of functionalized CQDs as fluorescent cell labels were studied by Bhunia et al., 2013 (Figure 7). They discovered that the CQDs may be imaged with TAT peptide- or folate-functionalization utilizing a standard microscope and can be labelled in one to 2 hours. Because of the low surface charge and tiny hydrodynamic diameter, CQDs have poor non-specific binding to cells which gets improved by this functionalization. The cellular and *in vivo* imaging applications of fluorescent CQDs are demonstrated by the fact that they are non-toxic at dosages higher than typical concentrations as concluded from MTT assays (Bhunia et al., 2013).

Hetero-atom-doped CQDs offer a wide range of wavelengths with multicolour fluorescence properties, increasing the stability and perfect for real-time cellular bioimaging (Sekar et al., 2022; Khoshnood et al., 2023; Mousa et al., 2023). In addition, when CQDs are co-doped with two heteroatoms from Nitrogen, Boron, or Phosphorus, the resulting CQD becomes more biocompatible with a much higher quantum yield (Atchudan et al., 2020; Kalaiyarasan et al., 2020; Tummala et al., 2021; Sekar et al., 2022). When o-phenylenediamine was treated with boric acid, the hydrothermal reaction yielded N, B-CQDs which is yellow fluorescent (Wei et al., 2020). N, B-CQDs were incorporated with HeLa cells to obtain fluorescence bioimaging. N or B plays a significant role in electrical modification and a remodelled surface pattern in co-doping that advances intense radiation features in N and B-CQDs (Wei et al., 2020). Fluorescent N, P-CQD derived from hydrothermal synthesis of *Ganoderma lucidum* was utilised for *in vivo* imaging (Tu et al., 2020). Photoluminescent CQDs produced from alginate have enormous potential as bioimaging probes (Zhou et al., 2016). The functional effect of various element dopants on CQDs in generating multiwavelength emission is still under investigation. Bao et al. looked at the *in vivo* biodistribution of the CQDs utilizing NIR FL imaging of mice without and with tumours to determine if it would be feasible to use CQDs for tumour diagnosis and treatment (Bao X. et al., 2018). Following intravenous infusion of CQDs into mice with H22 tumours, each mouse's entire body progressively displayed intense near-infrared fluorescence. The whole-body NIR fluorescence intensity had significantly dropped 3 hours after injection, and the tumour area's NIR fluorescence signal stood out sharply from the surrounding tissues (Figure 8) (Bao X. et al., 2018). Graphene-based CQDs can also be utilized for red and NIR fluorescence bioimaging.

The need for efficient multimodal imaging probes is growing, combining various imaging modalities like magnetic resonance (MRI), photoacoustic (PA), and imaging using computed tomography (CT) (Prabhuswamimath, 2022; Rajasekar et al., 2022; Kanungo et al., 2023; Latha et al., 2023). PA imaging is a hybrid method of imaging that combines optical and ultrasonic modalities for deep tissue penetration and great spatial resolution (Rajasekar et al., 2022; Latha et al., 2023). CQDs exhibit substantial absorption coefficients in the red to near-infrared spectrum when used as PA contrast agents and can transform light into heat (Ge et al., 2015; Prabhuswamimath, 2022). Doping MRI/CT probes into CQDs allows for the formation of further multimodal CQDs as discussed in this section earlier. The spatial resolution and the limited penetration depth with multi-modal CQDs are still under investigation for application in PA, MRI, and CT imaging (Louie, 2010; Zheng et al., 2016; Morato et al., 2021). CQDs have a lot of

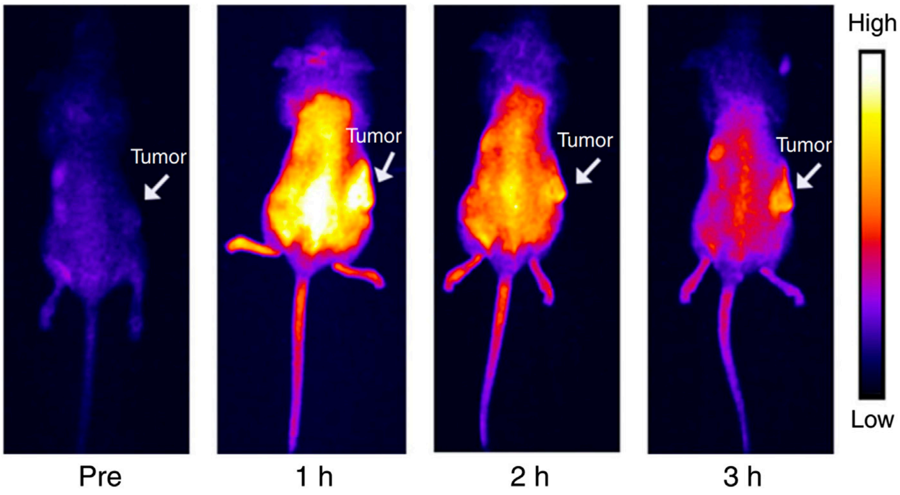

FIGURE 8
NIR emitting CQDs for *in vivo* imaging: Mouse bodies were imaged using NIR fluorescence at different time intervals following intravenous administration of CQDs (0.2 mL, 1000 μg mL^{-1}). Reprinted (adapted) with permission from Bao X. et al., 2018 Copyright (2018) Nature.

TABLE 3 Bioimaging applications of various carbon quantum dots.

Type of CQDs	Precursors	Synthesis method	Ref
CQDs	Wheat straw and bamboo	Hydrothermal	Huang et al. (2019)
CQDs	Graphite powder, Cement, Poly-(propionyl ethylenimine-*co*-ethylenimine)	Microwave-assisted pyrolysis	Cao et al. (2007)
Pure red emissive CQDs	Urea and citric acid	Solvothermal	Zhang et al. (2022)
N, S, P-CQDs	Thiamine pyrophosphate (ThPP)	Hydrothermal	Nasrin et al. (2020)
CQDs	Citric acid and para-phenylenediamine	Hydrothermal	Huo et al. (2022)
N-CQDs	Tetraphenyl porphyrin	Hydrothermal	Wu et al. (2017)
CQDs	Aconitic acid	Hydrothermal	Qian et al. (2018)
CQD	Maltose and NaOH	Microwave-assisted Method	Shereema et al. (2015)
L-CQDs	Citric acid and ethanediamine	Hydrothermal	Xue et al. (2019)
CQDs	Walnut shells	Carbonization	Cheng et al. (2017)
N, Cl- CQDs	Urea and choline chloride-glycerine deep eutectic solvent	Microwave-assisted method	Wang et al. (2018)
CQDs	*Eleocharis dulcis*	Hydrothermal	Bao et al. (2018a)
N, P-CQDs	H_3PO_4, Cyanobacteria and $C_2H_8N_2$	Hydrothermal	Wang et al. (2021)
N-CQDs	Guanidinium chloride and citric acid	Pyrolysis method	Mingcong et al. (2017)
CQDs	Banana peel	Hydrothermal	Atchudan et al. (2020)
Si-CQDs	Hydroquinone	Solvothermal	Qian et al. (2014)
N, P-CQDs	Ganoderma lucidum	Hydrothermal	Tu et al. (2020)
CQDs	Cynodon dactylon	Microwave-assisted method	Gurung et al. (2023)

potential applications in biological imaging as optical nanoprobes in the future (Wang et al., 2022). These findings suggested that cell imaging as an effective technique for *in vivo* imaging has a bright future. Subsequent research endeavours ought to concentrate on augmenting the QY of CQDs and generating structurally, compositionally, and geometrically well-defined CQDs. When CQD development is unrestricted by size, it can reach incredible ranges of applications.

6 CQDs in biomedicines

Nanotechnology is gaining attention in biomedical applications, particularly in nano-drug delivery systems and nano-cancer imaging (NCI) (Koutsogiannis et al., 2020). In the case of CQDs, the nano-drug delivery methods provide efficient delivery at a fixed rate and time, whilst the latter has the advantage of CQDs providing high sensitivity, improved contrast, and high precision (Azam et al., 2021; Cui et al., 2021; Zhu et al., 2022). The unique photophysical and physicochemical properties of CQDs along with their biocompatibility and facile synthetic route of preparation render CQDs an enticing nanomaterial candidate for biomedical application (Arshad et al., 2020; Azam et al., 2021; Adam et al., 2022). So CQDs have great applications in clinical research. The use of CQDs in drug delivery, gene therapy, and combatting the recent COVID-19 pandemic has been discussed below (Table 4).

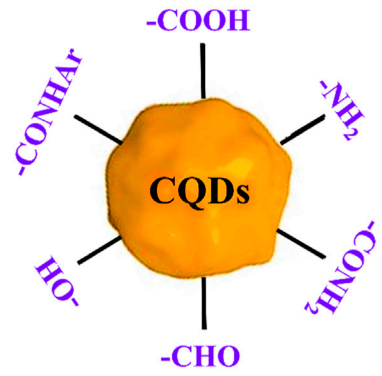

FIGURE 9
Schematic of different functional moieties on CQD which can be synthesized via any preferred methods as discussed in Section 2.

6.1 Drug delivery

Like other nanomaterials, CQD-based drug delivery involves drugs onto CQDs through binding or adsorption, for site-specific delivery of the drugs with minimal side effects (Lim et al., 2015; Zhu et al., 2015; Guerrero et al., 2021). The bond between CQD and the drug gets cleaved in the CQD-drug complex in an acidic environment of the diseased site or other stimulating factors (Li et al., 2020). This allows the controlled release of the drug to specific sites. Free CQDs easily get excreted through the renal or hepatobiliary system afterwards (Tian et al., 2020). The controllable surface modification for varying functions, small size, low cost, biocompatibility, and almost no side effects make CQDs an easy choice for the drug target (Figure 9) (Zhang et al., 2018; Lu et al., 2019a). To date, several anticancer and antibacterial drugs have been delivered successfully utilising various modified CQDs (Verma et al., 2020; Mahani et al., 2021).

CQDs play a significant part in both the diagnosis and treatment of cancer-like diseases (Palashuddin Sk et al., 2015; Wang et al., 2015; Zhao and Zhu, 2016; Gao et al., 2017; Ghosh et al., 2019a). Doxorubicin is a common chemotherapy medication that has been licensed by the FDA (Li S. et al., 2016). Doxorubicin can be combined using enzymes associated with DNA from malignant cells to speed up DNA base pair intercalation in tumours and inhibit the growth of cancer cells, making it a typical first-line treatment for a variety of malignancies (Tacar et al., 2013). A combination of CQDs and doxorubicin, cisplatin, and docetaxel-like cancer drugs has been developed that exhibits considerable tumour targeting, improved anti-tumour effectiveness, and minimal side effects (Yang et al., 2016; Mahani et al., 2021; Mahani et al., 2021; Sawpari et al., 2023). Carbonized Polymer Dot or CPD has various medical applications (Zhu et al., 2015). CQD/polymer composites exhibit self-release patterns and have important biomedical utilisations in treating cancer (Zhao and Zhu, 2016; Adam et al., 2022; Soumya et al., 2023). They are used in drug delivery systems such as insulin-smart nanocarriers and chemotherapeutic medicines (Devi et al., 2019; Alaghmandfard et al., 2021). The N-doped carbon dots (FN-CQDs) with folic acid are endocytosed specifically (specific cellular absorption rate >93.40%) and remain in autophagic vacuoles in cancer cells for an extended period (Khoshnood et al., 2023). Released FN-CQDs have been proven to effectively kill tumour cells and to be effective against 26 different types of tumour cells by activating the extrinsic and intrinsic apoptotic signalling pathways. Selective tumour targeting of the human glioblastoma cell line (U87MG) was successful in utilizing surface charge modulation of CQD-Doxorubicin incorporating a coating of octylamine-modified polyacrylic acid (cRGD-PAA-OA) and cRGD (Gao et al., 2018). Zhou et. al. produced intensely red emissive CQDs with several coupled α-carboxyl and amino groups to improve drug delivery efficiency and tumour-specific imaging (Liu et al., 2020a; Ding et al., 2020). These CQDs could target tumours such as gliomas because of the large neutral amino acid transporter 1’s multivalent interaction (Liu et al., 2018). Consequently, the CQDs could likewise be used to treat brain tumours by fluorescence/PA imaging while combining with topotecan hydrochloride (Huang et al., 2013; Huang et al., 2013; Li S. et al., 2016; Deng et al., 2018; Li et al., 2020). The schematic representation of CQD-mediated drug delivery is shown in Figure 9 above. CQD on the Porous polycaprolactone (PCL) matrix strengthens the bioactivity for biomineralization and can be used for bone tissue engineering (Luo et al., 2014). Stem cell biology is a significant advancement in biomedicine, with researchers exploring the use of untapped stem cells. Mukherjee et al. propose a strategy using biogenic carbon quantum dots (CQDs) out of garlic peels as a biogenic precursor (Figure 10) (Majood et al., 2023). These CQDs can image mesenchymal stem cells without cytotoxicity and can form reactive oxygen species (ROS) to influence stem cell migration and chondrocyte differentiation without chondrogenic induction factors. The study suggests garlic peel-generated CQDs as a major advancement in stem cell biology.

PEGylation is a common surface functionalization approach used in the CQDs assembly; (CQDs-Pt (IV) @PEG-(PAH/DMMA)), a cisplatin-based platform that stimulates the electrostatic repulsion mechanism that releases positively charged CQDs-Pt (IV) (Feng et al., 2016). *In-vivo* trials highlight the potential of CQDs for excellent tumour suppression efficacy and few side effects by emphasizing the efficiency of CQDs for transporting cisplatin-based drugs to the site-specific organs for maximal therapeutic effect. Cur-CPDs, CQDs prepared from curcumin, have anti-cancer, and antibacterial, anti-inflammatory, antioxidant properties (Lin et al., 2019). Insulin-smart nanocarriers,

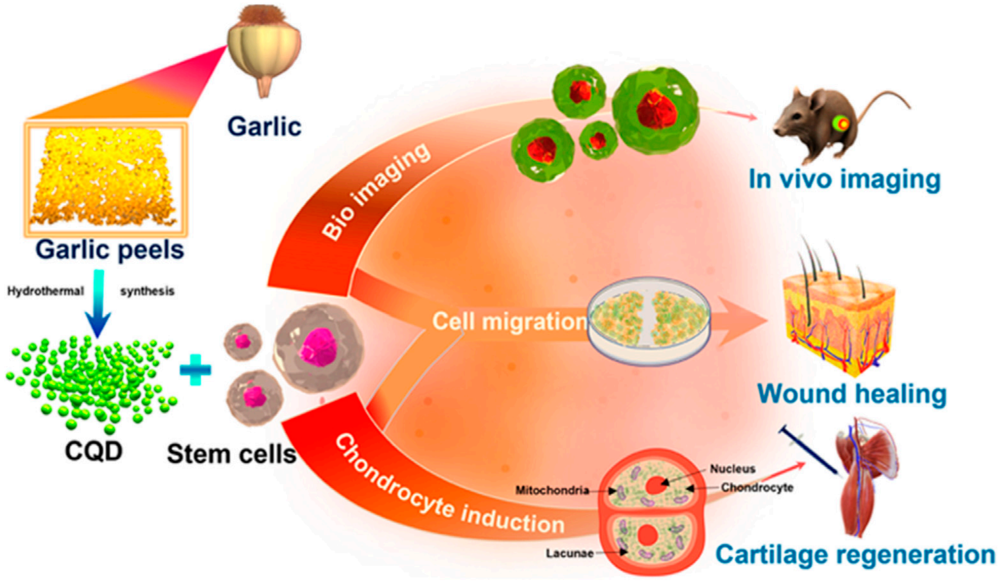

FIGURE 10
CQDs as a biogenic precursor for stem cell biology, demonstrating their ability to mesenchymal stem cell imaging without cytotoxicity and generate reactive oxygen species. Reprinted (adapted) with permission from Majood et al., 2023 (ACS Appl. Mater. Interfaces 2023, 15, 16, 19997–20011) Copyright (2023) ACS.

a self-release pattern developed by adding insulin to CQD/polymer hydrogels that contain phenyl-boronic acid are widely used in biomedical applications (Adam et al., 2022). An agarose-poly (vinyl alcohol) copolymer and CQDs as a cross-linker were used to generate a pH-responsive hydrogel nanocomposite, and this biodegradable nanocomposite released the antibacterial medication norfloxacin (Date et al., 2020). CQDPAs (Carbon quantum dot polyamines), a highly cationic form of Carbon quantum dot, are used to treat bacterial keratitis and infections due to their potent antibacterial properties (Jian et al., 2017). When compared to negatively charged CQDs, both uncharged and positively charged CQDs demonstrated superior bactericidal action synthesised from ethylene glycol and various amine sources (Verma et al., 2020). CQDs are synthesized from graphene-based materials (GQD) that exhibit characteristics of graphene and can be utilized for biomedical applications. Graphene-based CQDs have a lot of carboxylic groups, which enable them to be functionalized with active biomolecules (Kortel et al., 2020). This makes them useful for developing therapies and delivering drugs (Figure 11). The effectiveness of employing graphene-based CQDs as a low-cytotoxicity inhibitor for the aggregation of Aß peptides as they adhere to the hydrophobic centre of the peptides was demonstrated by Liu et al., 2015. Functionalized GQDs have demonstrated significant effectiveness in recognizing cancer receptors, transporting chemotherapeutic agents—like doxorubicin (DOX) or cisplatin—selectively to the cell nucleus while advancing the cytotoxicity, obstructing the agents' unintentional transportation into normal cell tissues, and prohibiting drug resistance (Deng et al., 2018). Graphene-based CQDS widely used in photodynamic treatment (PDT) has shown significant therapeutic benefit (Choi et al., 2014). The molecules may be put into the system with the aid of the CQDs, opening the way to the prospect of drug administration with bioimaging capabilities. The functionalized CQDs' biocompatibility remains a crucial concern for their future use in living cells, tissues, and animals (Tian et al., 2020). This could potentially be a disadvantage for the clinical testing of these CQDs in therapeutic applications in some cases. The disadvantages also include the synthesis of CQDs using different methods such as the need for costly ingredients, severe reaction conditions, and extended reaction times (Section 2).

6.2 Gene therapy

Gene therapy s the technique of modifying a person's genes to treat or cure an illness (Pham et al., 2023). Gene therapy is regarded as a long-term and potentially curable therapeutic method for a variety of disorders (Dunbar et al., 2018). In this technique, the vector with excellent efficiency of gene transfection can transfer genetic components within the cells. According to reports from the past few years, CQDs can be employed as gene nanocarriers that can be tracked via imaging (Ghosh et al., 2019a; Han and Na, 2019; Pham et al., 2023). Therefore, among various nanoparticles, CQDs take considerable attention in gene therapy as a non-viral vector. Various research has revealed that desirable CQDs/polymeric nanostructures can be a suitable competitor for gene delivery in specific areas like tumours (Molaei, 2019). A hybrid nano-gene vector-based CQDs (CQD-PEI), produced utilizing glycerol along with the branched PEI25k through microwave-aided pyrolysis, has the superior capability to gene transfer because of the outer positive charged polymer layer on the CQDs (Liu et al., 2012). CQDs were employed as a gene carrier for chondrogenesis from fibroblasts (Molaei, 2019). The development of multifunctional nano-carriers has demonstrated potential for use in diagnostics and gene therapy. CQD complexed with PEI and unlabeled plasmid DNA presented real-time monitoring for gene delivery (Kim et al., 2013). While

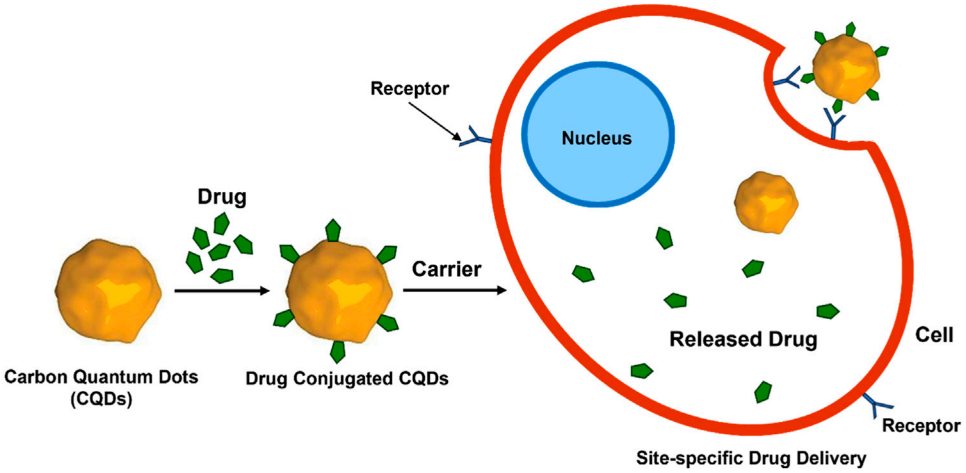

FIGURE 11
CQD-mediated drug delivery to the cells. Drug molecules are conjugated with CQDs followed by binding to the receptor on the cell surface and release of the drug molecules inside the cells.

plasmid DNA and polymeric vectors can be labelled with organic dyes and inorganic QDs, research has demonstrated health issues and instability. When compared to PEI alone, CQDs capped with PEI matrix allowed plasmid DNA for a greater transfection into COS-7 and HepG2 cells (Zhu et al., 2022). The hydrogel demonstrated intriguing simultaneous imaging capabilities with several excitation wavelengths, suggesting potential applications for near-infrared emissions imaging *in vivo*.

Kisor et al. developed CQD-PAMAM conjugates (CDPs) by synthesizing CQDs using peels of sweet lemon as a renewable source and conjugating them with several generations of polyamidoamine (PAMAM) dendrimers (Ghosh et al., 2019b). Between the conjugates of CDP, CDP3 is a potential gene transfer vector for TNBC (triple negative breast cancer) gene therapy because of its better gene complexation along with protection abilities, low level of toxicity, compatibility of blood, and enhanced gene transfection effectiveness, resulting in an intriguing theranostic technique for future therapy (Ghosh et al., 2019b). Furthermore, CDP3 demonstrated extremely specific Cu (II) ion detection, which could assist in determining the metastatic stage of TNBC, which has a larger concentration of Cu (II) ions. To function as an effective pseudo-homogeneous gene transfer vehicle, Ehsan et al. constructed CQDs from chitosan which were functionalized with arginine (Rezaei and Hashemi, 2021). Due to robust photoluminescence properties in both solid and solution states under physiological environments and excellent cellular intake in the human embryonic kidney −293T (HEK-293T) cells without any toxicity, the CQDs decorated with poly-l-lysine (PLL), namely, CQD/PLL core-shell NPs, show significant potential in the application of gene delivery (Hasanzadeh et al., 2021). CQDs, made from sodium alginate, were successfully employed as an effective non-viral gene carrier (Zhou et al., 2016). These CQDs displayed transfection effectiveness that was comparable to lipofectamine, but they also had the added benefits of cell imaging, extremely minimal cytotoxicity, and good biocompatibility. It was also found that multifunctional nanoparticles of polyethyleneimine-based carbon quantum dots (PCD) have the potential to transmit genes within cells. Both sodium alginate-based CQD and PCD can bioimaging probes discussed earlier (Zhou et al., 2016; Han and Na, 2019).

6.3 Combatting COVID-19

COVID-19, a pulmonary viral disease causing severe pulmonary distress with fever, has led to massive global deaths recently (Zhou and Ye, 2021). Scientists are working on rapid diagnosis and therapy when immune cells produce mediators (i.e., interleukins, α-defensins) that induce inflammation (Zhou and Ye, 2021; Soltani-Zangbar et al., 2022). CQDs are employed to diagnose and treat the disease (Xue et al., 2022). The herbs are more effective than medical plants as the precursor of CQDs to fight COVID-19 (Łoczechin et al., 2019; Naik et al., 2022). As an example, curcumin-derived CQDs were effective against enterovirus (EV-71) and garlic-derived CQDs were later found to diminish inflammatory cytokines while reducing coronavirus attachment and penetration (Lin et al., 2019; Kalkal et al., 2021). CQDs have been synthesized by hydrothermal treatment of ethylenediamine and citric acid as precursors of carbon and post-modification with boronic acid ligands, which exhibited concentration-dependent coronaviral inactivation (Łoczechin et al., 2019). The nanoporous membranes made of carbon dots and poly-(vinylidene fluoride) for self-sterilized, recyclable facemasks to combat the virus have been reported (Singh et al., 2021). The composite films have a hydrophobic surface, compact nanopore network, and efficient filtering of particles larger than 100 nm. CQDs have had a significant role in combatting COVID-19.

Systems based on CQDs may find use in the future in antiviral and antibacterial applications. Targeted delivery of medicinal medications loaded on CQDs, biological dye, and biological nanotransporters will become more and more significant.

TABLE 4 Biomedicinal applications of different carbon quantum dots.

Type of CQDs	Precursors	Synthesis method	Application	Ref
N-CQDs	Osmanthus leaves/Tea Leaves/Milk vetch	Hydrothermal	Antibacterial activity against *E. coli* and *S. aureus*	Ma et al. (2020)
CQD_{Spds}	Spermidine powder	Pyrolysis	Bacterial keratitis treatment	Jian et al. (2017)
N, S-CQDs	Amino acids (Arginine, Lysine, Histidine, Cysteine, and Methionine)	microwave irradiation	Hemolysis and blood clotting tests	Sahiner et al. (2019)
Levofloxacin-CQDs	Levofloxacin hydrochloride	hydrothermal Hethod	Poor drug resistance and significant antibacterial activities	Wu et al. (2022)
Quaternized CQDs	Glucose and DDA (dimethyl diallyl ammonium chloride)	Carbonization	Wound treatment for multiple bacterial infections	Zhao et al. (2022)
N-CQDs	Diethylenetriamine and glucose	Hydrothermal	Antibacterial properties against *Staphylococcus*	Zhao et al. (2019)
CD-PEI-IBAm	Polyethylenimine (PEI) and glycerol and isobutyric amide	Pyrolysis	Biomedical treatment	Yin et al. (2013)
NHF-CQDs	*N*-hydroxy phthalimide	Pyrolysis	Treatment for metastatic breast cancer	Tiron et al. (2020)
Cur-CQDs	Curcumin	Pyrolysis	Significant antimicrobial efficacy against Enterovirus 71 (EV71) infection	Lin et al. (2019)
CQDs	κ-carrageenan and folic acid	Hydrothermal process	Nano-vehicle for cancer cell targeting, biomedical research, and anticancer drugs	Das et al. (2019)
QCQD	Diallyl dimethylammonium chloride and 2,3-epoxypropyltrimethylammonium chloride	Solvothermal	Therapy for pneumonia in mice infected with MRSA	Zhao et al. (2020)
CQDs	Gallic acid (GA), citric acid (CA), ethane diamine (EDA)	Microwave assisted method	Antitumor treatment	Lu et al. (2019b)
CQDs	Silk fibroin	Microwave assisted method	Biomedical	Ko et al. (2017)
CQD/Ag NPs	Cow milk	Hydrothermal	Antibacterial activity	Han et al. (2015)
CQDs	Diethylene glycol and amine	Microwave-assisted synthesis	Antibacterial activity	Verma et al. (2020)
CQDs	Sodium citrate dehydrate, Urea	Carbonization	Intracellular drug delivery	Sun et al. (2020)
CQDs	Ammonium citrate	Pyrolysis	Microbicide to treat MRSA infection	Li et al. (2016b)

Enhanced photocatalytic antibacterial activity of covalent organic frameworks (COFs) is reported for CQDs as an electron extractant, which encompasses a great possibility for collaboration among material scientists and biochemical researchers for advanced biological and bio-environmental applications (Das et al., 2022b; 2023; Liang et al., 2022).

7 Conclusion

This review provides insight into the various synthetic methods of CQDs, their structure and properties, and the applications of CQDs in bioimaging and biomedicine. The article focuses on recent advancements, future possibilities, and various applications of CQDs and CQDs-based composites, hetero-atom-doped modifications in the field of bioimaging and biomedicines.

The CQDs were found in 2004 during the purification of single-walled carbon nanotubes (SWCNTs) and sanitizing them. Since that time, there have been a lot of techniques reported for the synthesis of CQDs. In general, CQDs can be synthesized using either of two primary methods: top-down or bottom-up. Top-down approaches use physical or chemical mechanisms to split up bigger carbon structures into smaller ones (Wang et al., 2014). Because of their low preparation costs and various advantageous qualities, such as their solubility in aqueous medium, chemical inertness, biocompatibility, and non-toxicity, CQDs have since been used in a wide variety of applications. Right electron doping and right surface passivation on CQDs are utilised in drug delivery due to their biocompatible properties and fluorescent properties. CQDs can be used as carriers for drug delivery, tracking continuous fluorescence emission. We emphasized new applications of CQDs, focusing on the precursors, properties, and synthesis of CQDs following their uses in bioimaging and biomedicine. A variety of biomedical applications have come to rely on CQDs and carbon-based composite materials because of their distinct physiochemical, immune-quiescent, biocompatible, and other characteristics. The powerful light-absorbing ability of CQDs allows the targeted destruction of tumour cells and microorganisms in photothermal therapy, photodynamic therapy, and PTT/PDT combo treatments (Juzenas et al., 2008; Choi et al., 2014). This review's primary contribution is the suggested framework for the future incorporates ascertaining diverse sources yielding CQDs with adaptable biomedical uses, comprehending the mechanism of action and eventual secretion through renal process from the body.

We have put a special emphasis on highlighting nanocomposites comprising CQDs and composites, featuring efficient uses for bioimaging and biomedicines. The fluorescence off/on the mode of CQD/polymer composites may be applied to detect bioanalytics, hence bringing information from the laboratory scale to commercial and industrial domains (Li W. et al., 2017; Ma et al., 2018; Adam et al., 2022). Preclinical research indicates promise for medication delivery, on-chip labs, cancer therapy, and non-invasive diagnostics. CQDs enable real-time monitoring of the subcellular and tissues, which makes it a quick and easy way to assess patients' health and an area of great focus in research. Investigations into antivirals based on CQDs are still in their early stages. Currently, targeting and utilizing CQDs to prevent certain viruses is difficult. Research on CQDs-based single-atom nanomedicine aims to clarify the exact mechanism for bio applications and enhance complicated selectivity and loading efficiency. CQDs in polymer matrices (Carbonized Polymer Dot or CPD) and CQDs synthesized from graphene-based materials (GQD) are utilized for various bioimaging and biomedical applications (Liu et al., 2015; Pathak et al., 2023). This helps in the imaging process incorporating various wavelengths, red and NIR wavelengths, easing the drug delivery process, and gene therapy.

More research is needed on CQDs, which offer new applications in bioimaging and biomedicines. Although the synthesis methodologies and potential applications are greatly explored, tuning the sizes of CQDs for desired fluorescence properties and functionalization on CQDs in some cases in a simple, environmentally friendly method is challenging. Future research would focus on raising the QY of CQDs and developing clearly defined geometrically, compositionally, and structurally CQDs. Many unknown features in CQDs might open their extensive use in bioimaging and biomedicines to combat a range of threats in the future.

Author contributions

SD: Writing–original draft, Writing–review and editing. SM: Writing–original draft, Writing–review and editing. DG: Writing–original draft, Writing–review and editing.

Funding

The author(s) declare financial support was received for the research, authorship, and/or publication of this article. Open access funding by ETH Zurich.

Conflict of interest

The authors declare that the research was conducted in the absence of any commercial or financial relationships that could be construed as a potential conflict of interest.

Publisher's note

References

Abbas, A., Zhang, C., Hussain, S., Li, Y., Gao, R., Li, J., et al. (2023). A robust switchable oil-in-water emulsion stabilized by electrostatic repulsions between surfactant and similarly charged carbon dots. *Small* 19, e2206621. doi:10.1002/smll.202206621

Adam, G. O., Sharker, S. M., and Ryu, J. H. (2022). Emerging biomedical applications of carbon dot and polymer composite materials. *Appl. Sci. Switz.* 12, 10565. doi:10.3390/app122010565

Ahmad, K., Gogoi, S. K., Begum, R., Sk, M. P., Paul, A., and Chattopadhyay, A. (2017). An interactive quantum dot and carbon dot conjugate for pH-sensitive and ratiometric Cu2+ sensing. *ChemPhysChem* 18, 610–616. doi:10.1002/cphc.201601249

Ahmad, K., Pal, A., Pan, U. N., Chattopadhyay, A., and Paul, A. (2018). Synthesis of single-particle level white-light-emitting carbon dots: via a one-step microwave method. *J. Mater Chem. C Mater* 6, 6691–6697. doi:10.1039/c8tc01276h

Alaghmandfard, A., Sedighi, O., Tabatabaei Rezaei, N., Abedini, A. A., Malek Khachatourian, A., Toprak, M. S., et al. (2021). Recent advances in the modification of carbon-based quantum dots for biomedical applications. *Mater. Sci. Eng. C* 120, 111756. doi:10.1016/j.msec.2020.111756

Arshad, F., Pal, A., Alam, T., Khan, J. A., and Sk, M. P. (2020). Luminescent carbogenic dots for the detection and determination of hemoglobin in real samples. *New J. Chem.* 44, 6213–6221. doi:10.1039/D0NJ00401D

Atchudan, R., Edison, T. N. J. I., Perumal, S., Muthuchamy, N., and Lee, Y. R. (2020). Hydrophilic nitrogen-doped carbon dots from biowaste using dwarf banana peel for environmental and biological applications. *Fuel* 275, 117821. doi:10.1016/j.fuel.2020.117821

Azam, N., Najabat Ali, M., and Javaid Khan, T. (2021). Carbon quantum dots for biomedical applications: review and analysis. *Front. Mater* 8. doi:10.3389/fmats.2021.700403

Bao, R., Chen, Z., Zhao, Z., Sun, X., Zhang, J., Hou, L., et al. (2018a). Green and facile synthesis of nitrogen and phosphorus co-doped carbon quantum dots towards fluorescent ink and sensing applications. *Nanomaterials* 8, 386. doi:10.3390/nano8060386

Bao, X., Yuan, Y., Chen, J., Zhang, B., Li, D., Zhou, D., et al. (2018b). *In vivo* theranostics with near-infrared-emitting carbon dots—highly efficient photothermal therapy based on passive targeting after intravenous administration. *Light Sci. Appl.* 7, 91. doi:10.1038/s41377-018-0090-1

Bhunia, S. K., Saha, A., Maity, A. R., Ray, S. C., and Jana, N. R. (2013). Carbon nanoparticle-based fluorescent bioimaging probes. *Sci. Rep.* 3, 1473. doi:10.1038/srep01473

Biazar, N., Poursalehi, R., and Delavari, H. (2018). Optical and structural properties of carbon dots/TiO2 nanostructures prepared via DC arc discharge in liquid. *AIP Conf. Proc.* 1920 (1), 020033. doi:10.1063/1.5018965

Campos, B. B., Oliva, M. M., Contreras-Cáceres, R., Rodriguez-Castellón, E., Jiménez-Jiménez, J., da Silva, J. C. G. E., et al. (2016). Carbon dots on based folic acid coated with PAMAM dendrimer as platform for Pt(IV) detection. *J. Colloid Interface Sci.* 465, 165–173. doi:10.1016/j.jcis.2015.11.059

Cao, L., Wang, X., Meziani, M. J., Lu, F., Wang, H., Luo, P. G., et al. (2007). Carbon dots for multiphoton bioimaging. *J. Am. Chem. Soc.* 129, 11318–11319. doi:10.1021/ja073527l

Cheki, M., Moslehi, M., and Assadi, M. (2013). Marvelous applications of quantum dots. *Eur. Rev. Med. Pharmacol. Sci.* 17, 1141–1148.

Chen, L., Raohao, F., Changchang, Z., Xiang, L., and Changhua, Z. (2019). Fluorescent enhancement of polyethyleneimine nano-polymers and the application in cellar imaging. *Polym. Degrad. Stab.* 163, 7–14. doi:10.1016/j.polymdegradstab.2019.01.013

Cheng, C., Shi, Y., Li, M., Xing, M., and Wu, Q. (2017). Carbon quantum dots from carbonized walnut shells: structural evolution, fluorescence characteristics, and intracellular bioimaging. *Mater. Sci. Eng. C* 79, 473–480. doi:10.1016/j.msec.2017.05.094

Choi, Y., Kim, S., Choi, M.-H., Ryoo, S.-R., Park, J., Min, D.-H., et al. (2014). Highly biocompatible carbon nanodots for simultaneous bioimaging and targeted photodynamic therapy *in vitro* and *in vivo*. *Adv. Funct. Mat.* 24, 5781–5789. doi:10.1002/adfm.201400961

Cotta, M. A. (2020). Quantum dots and their applications: what lies ahead? *ACS Appl. Nano Mater* 3, 4920–4924. doi:10.1021/acsanm.0c01386

Cui, L., Ren, X., Sun, M., Liu, H., and Xia, L. (2021). Carbon dots: synthesis, properties and applications. *Nanomaterials* 11, 3419. doi:10.3390/nano11123419

Cui, L., Ren, X., Wang, J., and Sun, M. (2020). Synthesis of homogeneous carbon quantum dots by ultrafast dual-beam pulsed laser ablation for bioimaging. *Mater. Today* 12, 100091. doi:10.1016/j.mtnano.2020.100091

Das, P., Ganguly, S., Agarwal, T., Maity, P., Ghosh, S., Choudhary, S., et al. (2019). Heteroatom doped blue luminescent carbon dots as a nano-probe for targeted cell labeling and anticancer drug delivery vehicle. *Mater Chem. Phys.* 237, 121860. doi:10.1016/j.matchemphys.2019.121860

Das, S., Chowdhury, I. H., Chakraborty, A., Naskar, M. K., Sarkar, M., and Manirul Islam, S. K. (2022a). Porous organic polymer (POP) nanosheets: an efficient photo-catalyst for visible-light assisted CO2 reduction. *Mater Adv.* 3, 3165–3173. doi:10.1039/d1ma01021b

Das, S., Hazra Chowdhury, I., Hazra Chowdhury, A., Singh, N., Sarkar, M., and Islam, Sk. M. (2022b). Metal-free covalent organic framework for facile production of solar fuel via CO2 reduction. *Ind. Eng. Chem. Res.* 61, 17044–17056. doi:10.1021/acs.iecr.2c02902

Das, S., Sarkar, P., Goswami, M., Ali, S. M., Mollah, M. R., and Islam, S. M. (2023). A sustainable strategy for the visible-light-driven facile N-formylation of amines using a Co(ii)-embedded covalent organic framework as an efficient photocatalyst. *Mater Chem. Front.* 7, 3349–3364. doi:10.1039/D3QM00042G

Date, P., Tanwar, A., Ladage, P., Kodam, K. M., and Ottoor, D. (2020). Carbon dots-incorporated pH-responsive agarose-PVA hydrogel nanocomposites for the controlled release of norfloxacin drug. *Polym. Bull.* 77, 5323–5344. doi:10.1007/s00289-019-03015-3

Deng, J., Lu, Q., Mi, N., Li, H., Liu, M., Xu, M., et al. (2014). Electrochemical synthesis of carbon nanodots directly from alcohols. *Chem. – A Eur. J.* 20, 4993–4999. doi:10.1002/chem.201304869

Deng, T., Zhang, R., Wang, J., Song, X., Bao, F., Gu, Y., et al. (2018). Carbon dots-cluster-DOX nanocomposites fabricated by a Co-Self-Assembly strategy for tumor-targeted bioimaging and therapy. *Part. Part. Syst. Charact.* 35. doi:10.1002/ppsc.201800190

Devi, P., Saini, S., and Kim, K.-H. (2019). The advanced role of carbon quantum dots in nanomedical applications. *Biosens. Bioelectron.* 141, 111158. doi:10.1016/j.bios.2019.02.059

Dey, S., Govindaraj, A., Biswas, K., and Rao, C. N. R. (2014). Luminescence properties of boron and nitrogen doped graphene quantum dots prepared from arc-discharge-generated doped graphene samples. *Chem. Phys. Lett.* 595–596, 203–208. doi:10.1016/j.cplett.2014.02.012

Ding, H., Zhou, X. X., Wei, J. S., Li, X. B., Qin, B. T., Chen, X. B., et al. (2020). Carbon dots with red/near-infrared emissions and their intrinsic merits for biomedical applications. *Carbon N. Y.* 167, 322–344. doi:10.1016/j.carbon.2020.06.024

Doñate-Buendía, C., Fernández-Alonso, M., Lancis, J., and Mínguez-Vega, G. (2020). Pulsed laser ablation in liquids for the production of gold nanoparticles and carbon quantum dots: from plasmonic to fluorescence and cell labelling. *J. Phys. Conf. Ser.* 1537, 012013. doi:10.1088/1742-6596/1537/1/012013

Dong, S., Yuan, Z., Zhang, L., Lin, Y., and Lu, C. (2017). Rapid screening of oxygen states in carbon quantum dots by chemiluminescence probe. *Anal. Chem.* 89, 12520–12526. doi:10.1021/acs.analchem.7b03711

Dong, Y., Zhou, N., Lin, X., Lin, J., Chi, Y., and Chen, G. (2010). Extraction of electrochemiluminescent oxidized carbon quantum dots from activated carbon. *Chem. Mater.* 22, 5895–5899. doi:10.1021/cm1018844

Dubey, A., Mondal, S., Chandra, K., and Atreya, H. S. (2016). Rapid identification of amino acid types in proteins using phase modulated 2D HN(CACB) and 2D HN(COCACB). *J. Magnetic Reson.* 267, 22–29. doi:10.1016/j.jmr.2016.04.004

Dunbar, C. E., High, K. A., Joung, J. K., Kohn, D. B., Ozawa, K., and Sadelain, M. (2018). Gene therapy comes of age. *Sci. Wash. D.C. U. S.)* 359, eaan4672. doi:10.1126/science.aan4672

El-brolsy, H. M. E. M., Hanafy, N. A. N., and El-Kemary, M. A. (2022). Fighting non-small lung cancer cells using optimal functionalization of targeted carbon quantum dots derived from natural sources might provide potential therapeutic and cancer bio image strategies. *Int. J. Mol. Sci.* 23, 13283. doi:10.3390/ijms232113283

Feng, T., Ai, X., An, G., Yang, P., and Zhao, Y. (2016). Charge-convertible carbon dots for imaging-guided drug delivery with enhanced *in vivo* cancer therapeutic efficiency. *ACS Nano* 10, 4410–4420. doi:10.1021/acsnano.6b00043

Feng, X., and Zhang, Y. (2019). A simple and green synthesis of carbon quantum dots from coke for white light-emitting devices. *RSC Adv.* 9, 33789–33793. doi:10.1039/c9ra06946a

Feng, Z., Adolfsson, K. H., Xu, Y., Fang, H., Hakkarainen, M., and Wu, M. (2021). Carbon dot/polymer nanocomposites: from green synthesis to energy, environmental and biomedical applications. *Sustain. Mater. Technol.* 29, e00304. doi:10.1016/j.susmat.2021.e00304

Gangasani, S., and Student, B. E. (2007). A study on quantum dot and its applications. *Int. J. Innovative Res. Sci. Eng. Technol.* 5, 3297. doi:10.15680/IJIRSET.2016.0505119

Gao, G., Jiang, Y. W., Yang, J., and Wu, F. G. (2017). Mitochondria-targetable carbon quantum dots for differentiating cancerous cells from normal cells. *Nanoscale* 9, 18368–18378. doi:10.1039/c7nr06764j

Gao, L., Zhao, X., Wang, J., Wang, Y., Yu, L., Peng, H., et al. (2018). Multiple functionalized carbon quantum dots for targeting glioma and tissue imaging. *Opt. Mater (Amst)* 75, 764–769. doi:10.1016/j.optmat.2017.11.044

García de Arquer, F. P., Talapin, D. V., Klimov, V. I., Arakawa, Y., Bayer, M., and Sargent, E. H. (2023). Semiconductor quantum dots: technological progress and future challenges. *Science* 373, eaaz8541. doi:10.1126/science.aaz8541

Ge, J., Jia, Q., Liu, W., Guo, L., Liu, Q., Lan, M., et al. (2015). Red-emissive carbon dots for fluorescent, photoacoustic, and thermal theranostics in living mice. *Adv. Mater.* 27, 4169–4177. doi:10.1002/adma.201500323

Gedda, G., Sankaranarayanan, S. A., Putta, C. L., Gudimella, K. K., Rengan, A. K., and Girma, W. M. (2023). Green synthesis of multi-functional carbon dots from medicinal plant leaves for antimicrobial, antioxidant, and bioimaging applications. *Sci. Rep.* 13, 6371. doi:10.1038/s41598-023-33652-8

Ghosh, S., Ghosal, K., Mohammad, S. A., and Sarkar, K. (2019a). Dendrimer functionalized carbon quantum dot for selective detection of breast cancer and gene therapy. *Chem. Eng. J.* 373, 468–484. doi:10.1016/j.cej.2019.05.023

Ghosh, S., Ghosal, K., Mohammad, S. A., and Sarkar, K. (2019b). Dendrimer functionalized carbon quantum dot for selective detection of breast cancer and gene therapy. *Chem. Eng. J.* 373, 468–484. doi:10.1016/j.cej.2019.05.023

Guerrero, E. D., Lopez-Velazquez, A. M., Ahlawat, J., and Narayan, M. (2021). Carbon quantum dots for treatment of amyloid disorders. *ACS Appl. Nano Mater* 4, 2423–2433. doi:10.1021/acsanm.0c02792

Gurung, S., Neha, Arun, N., Joshi, M., Jaiswal, T., Pathak, A. P., et al. (2023). Dual metal ion (Fe3+ and As3+) sensing and cell bioimaging using fluorescent carbon quantum dots synthesised from Cynodon dactylon. *Chemosphere* 339, 139638. doi:10.1016/j.chemosphere.2023.139638

Han, J., and Na, K. (2019). Transfection of the TRAIL gene into human mesenchymal stem cells using biocompatible polyethyleneimine carbon dots for cancer gene therapy. *J. Ind. Eng. Chem.* 80, 722–728. doi:10.1016/j.jiec.2019.02.015

Han, S., Zhang, H., Xie, Y., Liu, L., Shan, C., Li, X., et al. (2015). Application of cow milk-derived carbon dots/Ag NPs composite as the antibacterial agent. *Appl. Surf. Sci.* 328, 368–373. doi:10.1016/j.apsusc.2014.12.074

Hasanzadeh, A., Mofazzal Jahromi, M. A., Abdoli, A., Mohammad-Beigi, H., Fatahi, Y., Nourizadeh, H., et al. (2021). Photoluminescent carbon quantum dot/poly-L-Lysine core-shell nanoparticles: a novel candidate for gene delivery. *J. Drug Deliv. Sci. Technol.* 61, 102118. doi:10.1016/j.jddst.2020.102118

Havrdová, M., Urbančič, I., Bartoň Tománková, K., Malina, L., Štrancar, J., and Bourlinos, A. B. (2021). Self-targeting of carbon dots into the cell nucleus: diverse mechanisms of toxicity in NIH/3T3 and l929 cells. *Int. J. Mol. Sci.* 22, 5608. doi:10.3390/ijms22115608

Havrdová, M., Urbančič, I., Tománková, K. B., Malina, L., Poláková, K., Štrancar, J., et al. (2022). Intracellular trafficking of cationic carbon dots in cancer cell lines MCF-7 and HeLa—time lapse microscopy, concentration-dependent uptake, viability, DNA damage, and cell cycle profile. *Int. J. Mol. Sci.* 23, 1077. doi:10.3390/ijms23031077

Hou, Y., Lu, Q., Deng, J., Li, H., and Zhang, Y. (2015). One-pot electrochemical synthesis of functionalized fluorescent carbon dots and their selective sensing for mercury ion. *Anal. Chim. Acta* 866, 69–74. doi:10.1016/j.aca.2015.01.039

Huang, C., Dong, H., Su, Y., Wu, Y., Narron, R., and Yong, Q. (2019). Synthesis of carbon quantum dot nanoparticles derived from byproducts in bio-refinery process for cell imaging and *in vivo* bioimaging. *Nanomaterials* 9, 387. doi:10.3390/nano9030387

Huang, H., Cui, Y., Liu, M., Chen, J., Wan, Q., Wen, Y., et al. (2018). A one-step ultrasonic irradiation assisted strategy for the preparation of polymer-functionalized carbon quantum dots and their biological imaging. *J. Colloid Interface Sci.* 532, 767–773. doi:10.1016/j.jcis.2018.07.099

Huang, X., Zhang, F., Zhu, L., Choi, K. Y., Guo, N., Guo, J., et al. (2013). Effect of injection routes on the biodistribution, clearance, and tumor uptake of carbon dots. *ACS Nano* 7, 5684–5693. doi:10.1021/nn401911k

Huo, X., Liu, L., Bai, Y., Qin, J., Yuan, L., and Feng, F. (2022). Facile synthesis of yellowish-green emitting carbon quantum dots and their applications for phoxim sensing and cellular imaging. *Anal. Chim. Acta* 1206, 338685. doi:10.1016/j.aca.2021.338685

Jaipuria, G., Krishnarjuna, B., Mondal, S., Dubey, A., and Atreya, H. S. (2012). Amino acid selective labeling and unlabeling for protein resonance assignments. *Adv. Exp. Med. Biol.* 992, 95–118. doi:10.1007/978-94-007-4954-2_6

Jaipuria, G., Shet, D., Malik, S., Swain, M., Atreya, H. S., Galea, C. A., et al. (2022). IGF-dependent dynamic modulation of a protease cleavage site in the intrinsically disordered linker domain of human IGFBP2. *Proteins* 90, 1732–1743. doi:10.1002/prot.26350

Jian, H.-J., Wu, R.-S., Lin, T.-Y., Li, Y.-J., Lin, H.-J., Harroun, S. G., et al. (2017). Super-cationic carbon quantum dots synthesized from spermidine as an eye drop formulation for topical treatment of bacterial keratitis. *ACS Nano* 11, 6703–6716. doi:10.1021/acsnano.7b01023

Jiao, M., Wang, Y., Wang, W., Zhou, X., Xu, J., Xing, Y., et al. (2022). Gadolinium doped red-emissive carbon dots as targeted theranostic agents for fluorescence and MR imaging guided cancer phototherapy. *Chem. Eng. J.* 440, 135965. doi:10.1016/j.cej.2022.135965

Juzenas, P., Chen, W., Sun, Y. P., Coelho, M., Generalov, R., Generalova, N., et al. (2008). Quantum dots and nanoparticles for photodynamic and radiation therapies of cancer. *Adv. Drug Deliv. Rev.* 60, 1600–1614. doi:10.1016/j.addr.2008.08.004

Kabanov, A. V., and Gendelman, H. E. (2007). Nanomedicine in the diagnosis and therapy of neurodegenerative disorders. *Prog. Polym. Sci. Oxf.* 32, 1054–1082. doi:10.1016/j.progpolymsci.2007.05.014

Kalaiyarasan, G., Joseph, J., and Kumar, P. (2020). Phosphorus-doped carbon quantum dots as fluorometric probes for iron detection. *ACS Omega* 5, 22278–22288. doi:10.1021/acsomega.0c02627

Kalkal, A., Allawadhi, P., Pradhan, R., Khurana, A., Bharani, K. K., and Packirisamy, G. (2021). Allium sativum derived carbon dots as a potential theranostic agent to combat the COVID-19 crisis. *Sensors Int.* 2, 100102. doi:10.1016/j.sintl.2021.100102

Kanungo, S., Gupta, N., Rawat, R., Jain, B., Solanki, A., Panday, A., et al. (2023). Doped carbon quantum dots reinforced hydrogels for sustained delivery of molecular cargo. *J. Funct. Biomater.* 14, 166. doi:10.3390/jfb14030166

Kausar, A. (2019). Polymer/carbon-based quantum dot nanocomposite: forthcoming materials for technical application. *J. Macromol. Sci. Part A* 56, 341–356. doi:10.1080/10601325.2019.1578614

Khoshnood, A., Farhadian, N., Abnous, K., Matin, M. M., Ziaee, N., and Yaghoobi, E. (2023). N doped-carbon quantum dots with ultra-high quantum yield photoluminescent property conjugated with folic acid for targeted drug delivery and bioimaging applications. *J. Photochem Photobiol. A Chem.* 444, 114972. doi:10.1016/j.jphotochem.2023.114972

Kim, J., Park, J., Kim, H., Singha, K., and Kim, W. J. (2013). Transfection and intracellular trafficking properties of carbon dot-gold nanoparticle molecular assembly conjugated with PEI-pDNA. *Biomaterials* 34, 7168–7180. doi:10.1016/j.biomaterials.2013.05.072

Knoblauch, C., Griep, M., and Friedrich, C. (2014). Recent advances in the field of bionanotechnology: an insight into optoelectric bacteriorhodopsin, quantum dots, and noble metal nanoclusters. *Sensors (Basel)* 14, 19731–19766. doi:10.3390/s141019731

Ko, N., Nafiujjaman, M., Cherukula, K., Lee, S., Hong, S.-J., Lim, H.-N., et al. (2017). Microwave-assisted synthesis of biocompatible silk fibroin-based carbon quantum dots. *Part. Part. Syst. Charact.* 35, 1700300. doi:10.1002/ppsc.201700300

Kortel, M., Mansuriya, B. D., Santana, N. V., and Altintas, Z. (2020). Graphene quantum dots as flourishing nanomaterials for bio-imaging, therapy development, and micro-supercapacitors. *Micromachines (Basel)* 11, 866. doi:10.3390/MI11090866

Koutsogiannis, P., Thomou, E., Stamatis, H., Gournis, D., and Rudolf, P. (2020). Advances in fluorescent carbon dots for biomedical applications. *Adv. Phys. X* 5, 1758592. doi:10.1080/23746149.2020.1758592

Lan, M., Zhao, S., Zhang, Z., Yan, L., Guo, L., Niu, G., et al. (2017). Two-photon-excited near-infrared emissive carbon dots as multifunctional agents for fluorescence imaging and photothermal therapy. *Nano Res.* 10, 3113–3123. doi:10.1007/s12274-017-1528-0

Latha, B. D., Soumya, K., More, N., Mounika, C., Guduru, A. T., Singh, G., et al. (2023). Fluorescent carbon quantum dots for effective tumor diagnosis: a comprehensive review. *Biomed. Eng. Adv.* 5, 100072. doi:10.1016/j.bea.2023.100072

Li, C., Wang, Y., Zhang, X., Guo, X., Kang, X., Du, L., et al. (2018). Red fluorescent carbon dots with phenylboronic acid tags for quick detection of Fe(III) in PC12 cells. *J. Colloid Interface Sci.* 526, 487–496. doi:10.1016/j.jcis.2018.05.017

Li, H., He, X., Kang, Z., Huang, H., Liu, Y., Liu, J., et al. (2010). Water-soluble fluorescent carbon quantum dots and photocatalyst design. *Angew. Chem. Int. Ed.* 49, 4430–4434. doi:10.1002/anie.200906154

Li, J.-Y., Liu, Y., Shu, Q.-W., Liang, J.-M., Zhang, F., Chen, X.-P., et al. (2017a). One-Pot hydrothermal synthesis of carbon dots with efficient up- and down-converted photoluminescence for the sensitive detection of morin in a dual-readout assay. *Langmuir* 33, 1043–1050. doi:10.1021/acs.langmuir.6b04225

Li, M., Hu, C., Yu, C., Wang, S., Zhang, P., and Qiu, J. (2015). Organic amine-grafted carbon quantum dots with tailored surface and enhanced photoluminescence properties. *Carbon N. Y.* 91, 291–297. doi:10.1016/j.carbon.2015.04.083

Li, S., Amat, D., Peng, Z., Vanni, S., Raskin, S., De Angulo, G., et al. (2016a). Transferrin conjugated nontoxic carbon dots for doxorubicin delivery to target pediatric brain tumor cells. *Nanoscale* 8, 16662–16669. doi:10.1039/c6nr05055g

Li, S., Su, W., Wu, H., Yuan, T., Yuan, C., Liu, J., et al. (2020). Targeted tumour theranostics in mice via carbon quantum dots structurally mimicking large amino acids. *Nat. Biomed. Eng.* 4, 704–716. doi:10.1038/s41551-020-0540-y

Li, W., Zhang, H., Zheng, Y., Chen, S., Liu, Y., Zhuang, J., et al. (2017b). Multifunctional carbon dots for highly luminescent orange-emissive cellulose based composite phosphor construction and plant tissue imaging. *Nanoscale* 9, 12976–12983. doi:10.1039/c7nr03217j

Li, X., Wang, H., Shimizu, Y., Pyatenko, A., Kawaguchi, K., and Koshizaki, N. (2011). Preparation of carbon quantum dots with tunable photoluminescence by rapid laser passivation in ordinary organic solvents. *Chem. Commun.* 47, 932–934. doi:10.1039/C0CC03552A

Li, Y.-J., Harroun, S. G., Su, Y.-C., Huang, C.-F., Unnikrishnan, B., Lin, H.-J., et al. (2016b). Synthesis of self-assembled spermidine-carbon quantum dots effective against multidrug-resistant bacteria. *Adv. Healthc. Mat.* 5, 2545–2554. doi:10.1002/adhm.201600297

Liang, J., Li, W., Chen, J., Huang, X., Liu, Y., Zhang, X., et al. (2022). Carbon dots as an electron extractant for enhanced photocatalytic antibacterial activity of covalent organic frameworks. *J. Mater Chem. A Mater* 451, 23384–23394. doi:10.1039/d2ta03978h

Liang, Q., Ma, W., Shi, Y., Li, Z., and Yang, X. (2013). Easy synthesis of highly fluorescent carbon quantum dots from gelatin and their luminescent properties and applications. *Carbon N. Y.* 60, 421–428. doi:10.1016/j.carbon.2013.04.055

Lim, S. Y., Shen, W., and Gao, Z. (2015). Carbon quantum dots and their applications. *Chem. Soc. Rev.* 44, 362–381. doi:10.1039/c4cs00269e

Lin, C., Chang, L., Chu, H., Lin, H., Chang, P., Wang, R. Y. L., et al. (2019). High amplification of the antiviral activity of curcumin through transformation into carbon quantum dots. *Small* 15, 1902641. doi:10.1002/smll.201902641

Liu, C., Zhang, P., Zhai, X., Tian, F., Li, W., Yang, J., et al. (2012). Nano-carrier for gene delivery and bioimaging based on carbon dots with PEI-passivation enhanced fluorescence. *Biomaterials* 33, 3604–3613. doi:10.1016/j.biomaterials.2012.01.052

Liu, H., Ye, T., and Mao, C. (2007). Fluorescent carbon nanoparticles derived from candle soot. *Angew. Chem. - Int. Ed.* 46, 6473–6475. doi:10.1002/anie.200701271

Liu, J., Geng, Y., Li, D., Yao, H., Huo, Z., Li, Y., et al. (2020a). Deep red emissive carbonized polymer dots with unprecedented narrow full width at half maximum. *Adv. Mater.* 32, e1906641. doi:10.1002/adma.201906641

Liu, J., Li, R., and Yang, B. (2020b). Carbon dots: a new type of carbon-based nanomaterial with wide applications. *ACS Cent. Sci.* 6, 2179–2195. doi:10.1021/acscentsci.0c01306

Liu, R., Wu, D., Liu, S., Koynov, K., Knoll, W., and Li, Q. (2009). An aqueous route to multicolor photoluminescent carbon dots using silica spheres as carriers. *Angew. Chem. Int. Ed. Engl.* 48, 4598–4601. doi:10.1002/anie.200900652

Liu, Y., Liu, J., Zhang, J., Li, X., Lin, F., Zhou, N., et al. (2018). Noninvasive brain tumor imaging using red emissive carbonized polymer dots across the blood-brain barrier. *ACS Omega* 3, 7888–7896. doi:10.1021/acsomega.8b01169

Liu, Y., Xu, L.-P., Dai, W., Dong, H., Wen, Y., and Zhang, X. (2015). Graphene quantum dots for the inhibition of β amyloid aggregation. *Nanoscale* 7, 19060–19065. doi:10.1039/C5NR06282A

Łoczechin, A., Séron, K., Barras, A., Giovanelli, E., Belouzard, S., Chen, Y. T., et al. (2019). Functional carbon quantum dots as medical countermeasures to human coronavirus. *ACS Appl. Mater Interfaces* 11, 42964–42974. doi:10.1021/acsami.9b15032

Louie, A. (2010). Multimodality imaging probes: design and challenges. *Chem. Rev.* 110, 3146–3195. doi:10.1021/cr9003538

Lu, S., Liu, L., Wang, H., Zhao, W., Li, Z., Qu, Z., et al. (2019a). Synthesis of dual functional gallic-acid-based carbon dots for bioimaging and antitumor therapy. *Biomater. Sci.* 7, 3258–3265. doi:10.1039/c9bm00570f

Lu, S., Liu, L., Wang, H., Zhao, W., Li, Z., Qu, Z., et al. (2019b). Synthesis of dual functional gallic-acid-based carbon dots for bioimaging and antitumor therapy. *Biomater. Sci.* 7, 3258–3265. doi:10.1039/C9BM00570F

Luo, P. G., Sahu, S., Yang, S.-T., Sonkar, S. K., Wang, J., Wang, H., et al. (2013). Carbon "quantum" dots for optical bioimaging. *J. Mater Chem. B* 1, 2116. doi:10.1039/c3tb00018d

Luo, P. G., Yang, F., Yang, S. T., Sonkar, S. K., Yang, L., Broglie, J. J., et al. (2014). Carbon-based quantum dots for fluorescence imaging of cells and tissues. *RSC Adv.* 4, 10791. doi:10.1039/c3ra47683a

Ma, C., Dai, K., Hou, H., Ji, X., Chen, L., Ivey, D. G., et al. (2018). High ion-conducting solid-state composite electrolytes with carbon quantum dot nanofillers. *Adv. Sci.* 5, 1700996. doi:10.1002/advs.201700996

Ma, Y., Zhang, M., Wang, H., Wang, B., Huang, H., Liu, Y., et al. (2020). N-doped carbon dots derived from leaves with low toxicity via damaging cytomembrane for broad-spectrum antibacterial activity. *Mater Today Commun.* 24, 101222. doi:10.1016/j.mtcomm.2020.101222

Magesh, V., Sundramoorthy, A. K., and Ganapathy, D. (2022). Recent advances on synthesis and potential applications of carbon quantum dots. *Front. Mater* 9. doi:10.3389/fmats.2022.906838

Mahani, M., Pourrahmani-Sarbanani, M., Yoosefian, M., Divsar, F., Mousavi, S. M., and Nomani, A. (2021). Doxorubicin delivery to breast cancer cells with transferrin-targeted carbon quantum dots: an *in vitro* and *in silico* study. *J. Drug Deliv. Sci. Technol.* 62, 102342. doi:10.1016/j.jddst.2021.102342

Mai, X.-D., Phan, Y. T. H., and Nguyen, V.-Q. (2020). Excitation-independent emission of carbon quantum dot solids. *Adv. Mater. Sci. Eng.* 2020, 1–5. doi:10.1155/2020/9643168

Majood, M., Selvam, A., Agrawal, O., Chaurasia, R., Rawat, S., Mohanty, S., et al. (2023). Biogenic carbon quantum dots as a neoteric inducer in the game of directing chondrogenesis. *ACS Appl. Mater Interfaces* 15, 19997–20011. doi:10.1021/acsami.3c02007

Malik, S. A., Mondal, S., and Atreya, H. S. (2019). Enhanced stability of an intrinsically disordered protein against proteolytic cleavage through interactions with silver nanoparticles. *RSC Adv.* 9 (49), 28746–28753. doi:10.1039/c9ra05514b

Marković, Z. M., Budimir, M. D., Danko, M., Milivojević, D. D., Kubat, P., Zmejkoski, D. Z., et al. (2023). Structural, optical, and bioimaging characterization of carbon quantum dots solvothermally synthesized from o -phenylenediamine. *Beilstein J. Nanotechnol.* 14, 165–174. doi:10.3762/bjnano.14.17

Mingcong, R., Feng, Y., Wang, Y., and Chen, X. (2017). One-pot solid phase pyrolysis synthesis of nitrogen-doped carbon dots for Fe3+ sensing and bioimaging. *Sens. Actuators B Chem.* 245, 868–874. doi:10.1016/j.snb.2017.02.014

Molaei, M. J. (2019). Carbon quantum dots and their biomedical and therapeutic applications: a review. *RSC Adv.* 9, 6460–6481. doi:10.1039/c8ra08088g

Mondal, S. (2017). *Structural and dynamic studies of protein-nanomaterial interactions*.

Mondal, S., Shet, D., Prasanna, C., and Atreya, H. S. (2013). High yield expression of proteins in *E. coli* for NMR studies. *Adv. Biosci. Biotechnol.* 04, 751–767. doi:10.4236/abb.2013.46099

Mondal, S., Thirupathi, R., and Atreya, H. S. (2015). Carbon quantum dots as a macromolecular crowder. *RSC Adv.* 5, 4489–4492. doi:10.1039/c4ra14019b

Mondal, S., Thirupathi, R., Rao, L. P., Atreya, H. S., Dreyer, D. R., Park, S., et al. (2016). Unraveling the dynamic nature of protein–graphene oxide interactions. *RSC Adv.* 6, 52539–52548. doi:10.1039/C6RA03759C

Moniruzzaman, M., Dutta, S. D., Lim, K. T., and Kim, J. (2022). Perylene-derived hydrophilic carbon dots with polychromatic emissions as superior bioimaging and NIR-responsive photothermal bactericidal agent. *ACS Omega* 7, 37388–37400. doi:10.1021/acsomega.2c04130

Morato, Y. L., Paredes, K. O., Chamizo, L. L., Marciello, M., and Filice, M. (2021). Recent advances in multimodal molecular imaging of cancer mediated by hybrid magnetic nanoparticles. *Polym. (Basel)* 13, 2989. doi:10.3390/polym13172989

Mousa, M. A., Abdelrahman, H. H., Fahmy, M. A., Ebrahim, D. G., and Moustafa, A. H. E. (2023). Pure and doped carbon quantum dots as fluorescent probes for the detection of phenol compounds and antibiotics in aquariums. *Sci. Rep.* 13, 12863. doi:10.1038/s41598-023-39490-y

Naik, K., Chaudhary, S., Ye, L., and Parmar, A. S. (2022). A strategic review on carbon quantum dots for cancer-diagnostics and treatment. *Front. Bioeng. Biotechnol.* 10, 882100. doi:10.3389/fbioe.2022.882100

Nasrin, A., Hassan, M., Mann, G., and Gomes, V. G. (2020). Conjugated ternary doped carbon dots from vitamin B derivative: multispectral nanoprobes for targeted melanoma bioimaging and photosensitization. *J. Lumin* 217, 116811. doi:10.1016/j.jlumin.2019.116811

Nazir, S., Hussain, T., Ayub, A., Rashid, U., and MacRobert, A. J. (2014). Nanomaterials in combating cancer: therapeutic applications and developments. *Nanomedicine* 10, 19–34. doi:10.1016/j.nano.2013.07.001

Niu, F., Xu, Y., Liu, J., Song, Z., Liu, M., and Liu, J. (2017a). Controllable electrochemical/electroanalytical approach to generate nitrogen-doped carbon quantum dots from varied amino acids: pinpointing the utmost quantum yield and the versatile photoluminescent and electrochemiluminescent applications. *Electrochim Acta* 236, 239–251. doi:10.1016/j.electacta.2017.03.085

Niu, N., Ma, Z., He, F., Li, S., Li, J., Liu, S., et al. (2017b). Preparation of carbon dots for cellular imaging by the molecular aggregation of cellulolytic enzyme lignin. *Langmuir* 33, 5786–5795. doi:10.1021/acs.langmuir.7b00617

Pal, A., Ahmad, K., Dutta, D., and Chattopadhyay, A. (2019). Boron doped carbon dots with unusually high photoluminescence quantum yield for ratiometric intracellular pH sensing. *ChemPhysChem* 20, 1018–1027. doi:10.1002/cphc.201900140

Palashuddin Sk, M., Goswami, U., Ghosh, S. S., and Chattopadhyay, A. (2015). Cu2+-embedded carbon nanoparticles as anticancer agents. *J. Mater Chem. B* 3, 5673–5677. doi:10.1039/C5TB00567A

Pan, Q., Xu, Z., Deng, S., Zhang, F., Li, H., Cheng, Y., et al. (2019). A mechanochemically synthesized porous organic polymer derived CQD/chitosan-graphene composite film electrode for electrochemiluminescence determination of dopamine. *RSC Adv.* 9, 39332–39337. doi:10.1039/c9ra06912g

Park, S. Y., Lee, H., Park, E., Lee, S., Lee, J., Jeong, S., et al. (2014). Photoluminescent green carbon nanodots from food-waste-derived sources: large-scale synthesis, properties, and biomedical applications. *ACS Appl. Mater Interfaces* 6, 3365–3370. doi:10.1021/am500159p

Pathak, R., Punetha, V. D., Bhatt, S., and Punetha, M. (2023). Multifunctional role of carbon dot-based polymer nanocomposites in biomedical applications: a review. *J. Mater Sci.* 58, 6419–6443. doi:10.1007/s10853-023-08408-4

Peng, Z., Ji, C., Zhou, Y., Zhao, T., and Leblanc, R. M. (2020). Polyethylene glycol (PEG) derived carbon dots: preparation and applications. *Appl. Mater Today* 20, 100677. doi:10.1016/j.apmt.2020.100677

Pham, Q. D. M., Thomson, S. M., Schaible, B. N., Mills, K. D., Atala, A., Porada, C. D., et al. (2023). Acceptability of prenatal diagnosis and prenatal treatment of haemophilia using cell and gene therapies within US haemophilia community. *Haemophilia* 29, 1024–1031. doi:10.1111/hae.14805

Pierrat, P., Wang, R., Kereselidze, D., Lux, M., Didier, P., Kichler, A., et al. (2015). Efficient invitro and invivo pulmonary delivery of nucleic acid by carbon dot-based nanocarriers. *Biomaterials* 51, 290–302. doi:10.1016/j.biomaterials.2015.02.017

Pires, N. R., Santos, C. M. W., Sousa, R. R., De Paula, R. C. M., Cunha, P. L. R., and Feitosa, J. P. A. (2015). Novel and fast microwave-assisted synthesis of carbon quantum dots from raw cashew gum. *J. Braz Chem. Soc.* 26, 1274–1282. doi:10.5935/0103-5053.20150094

Pourmadadi, M., Rahmani, E., Rajabzadeh-Khosroshahi, M., Samadi, A., Behzadmehr, R., Rahdar, A., et al. (2023). Properties and application of carbon quantum dots (CQDs) in biosensors for disease detection: a comprehensive review. *J. Drug Deliv. Sci. Technol.* 80, 104156. doi:10.1016/j.jddst.2023.104156

Prabhuswamimath, S. C. (2022). "Chapter 9 - PA Imaging: a promising tool for targeted therapeutic implications in Cancer," in *Biomedical imaging instrumentation*. Editors M. Suar, N. Misra, and N. S. Bhavesh (Academic Press), 131–160. doi:10.1016/B978-0-323-85650-8.00009-7

Praneerad, J., Nueangnoraj, K., In, I., and Paoprasert, P. (2019). Environmentally friendly supercapacitor based on carbon dots from durian peel as an electrode. *Key Eng. Mater* 803, 115–119. doi:10.4028/www.scientific.net/KEM.803.115

Qi, L., and Gao, X. (2008). Emerging application of quantum dots for drug delivery and therapy. *Expert Opin. Drug Deliv.* 5, 263–267. doi:10.1517/17425247.5.3.263

Qian, J., Quan, F., Zhao, F., Wu, C., Wang, Z., and Zhou, L. (2018). Aconitic acid derived carbon dots: conjugated interaction for the detection of folic acid and fluorescence targeted imaging of folate receptor overexpressed cancer cells. *Sens. Actuators B Chem.* 262, 444–451. doi:10.1016/j.snb.2018.01.227

Qian, Z., Shan, X., Chai, L., Ma, J., Chen, J., and Feng, H. (2014). Si-doped carbon quantum dots: a facile and general preparation strategy, bioimaging application, and multifunctional sensor. *ACS Appl. Mater Interfaces* 6, 6797–6805. doi:10.1021/am500403n

Rajasekar, B., Nirmala, P., Bhuvaneswari, P., Radhika, R., Asha, S., Kavitha, K. R., et al. (2022). A feasible multimodal photoacoustic imaging approach for evaluating the clinical symptoms of inflammatory arthritis. *Biomed. Res. Int.* 2022, 1–12. doi:10.1155/2022/7358575

Ren, R., Zhang, Z., Zhao, P., Shi, J., Han, K., Yang, Z., et al. (2019a). Facile and one-step preparation carbon quantum dots from biomass residue and their applications as efficient surfactants. *J. Dispers. Sci. Technol.* 40, 627–633. doi:10.1080/01932691.2018.1475239

Ren, X., Zhang, F., Guo, B., Gao, N., and Zhang, X. (2019b). Synthesis of N-doped Micropore carbon quantum dots with high quantum yield and dual-wavelength photoluminescence emission from biomass for cellular imaging. *Nanomaterials* 9, 495. doi:10.3390/nano9040495

Rezaei, A., and Hashemi, E. (2021). A pseudohomogeneous nanocarrier based on carbon quantum dots decorated with arginine as an efficient gene delivery vehicle. *Sci. Rep.* 11, 13790. doi:10.1038/s41598-021-93153-4

Ross, S., Wu, R. S., Wei, S. C., Ross, G. M., and Chang, H. T. (2020). The analytical and biomedical applications of carbon dots and their future theranostic potential: a review. *J. Food Drug Anal.* 28, 678–696. doi:10.38212/2224-6614.1154

Sahiner, N., Suner, S. S., Sahiner, M., and Silan, C. (2019). Nitrogen and sulfur doped carbon dots from amino acids for potential biomedical applications. *J. Fluoresc.* 29, 1191–1200. doi:10.1007/s10895-019-02431-y

Sahu, S., Behera, B., Maiti, T. K., and Mohapatra, S. (2012). Simple one-step synthesis of highly luminescent carbon dots from orange juice: application as excellent bio-imaging agents. *Chem. Commun. (Camb)* 48, 8835–8837. doi:10.1039/c2cc33796g

Sangjan, A., Boonsith, S., Sansanaphongpricha, K., Thinbanmai, T., Ratchahat, S., Laosiripojana, N., et al. (2022). Facile preparation of aqueous-soluble fluorescent polyethylene glycol functionalized carbon dots from palm waste by one-pot hydrothermal carbonization for colon cancer nanotheranostics. *Sci. Rep.* 12, 10550. doi:10.1038/s41598-022-14704-x

Sasaki, D., Kusamori, K., Takayama, Y., Itakura, S., Todo, H., and Nishikawa, M. (2021). Development of nanoparticles derived from corn as mass producible bionanoparticles with anticancer activity. *Sci. Rep.* 11, 22818. doi:10.1038/s41598-021-02241-y

Sawpari, R., Samanta, S., Banerjee, J., Das, S., Dash, S. S., Ahmed, R., et al. (2023). Recent advances and futuristic potentials of nano-tailored doxorubicin for prostate cancer therapy. *J. Drug Deliv. Sci. Technol.* 81, 104212. doi:10.1016/j.jddst.2023.104212

Sekar, R., Basavegowda, N., Jena, S., Jayakodi, S., Elumalai, P., Chaitanyakumar, A., et al. (2022). Recent developments in heteroatom/metal-doped carbon dot-based image-guided photodynamic therapy for cancer. *Pharmaceutics* 14, 1869. doi:10.3390/pharmaceutics14091869

Shereema, R. M., Sankar, V., Raghu, K. G., Rao, T. P., and Shankar, S. S. (2015). One step green synthesis of carbon quantum dots and its application towards the bioelectroanalytical and biolabeling studies. *Electrochim Acta* 182, 588–595. doi:10.1016/j.electacta.2015.09.145

Shi, X., Hu, Y., Meng, H.-M., Yang, J., Qu, L., Zhang, X.-B., et al. (2020). Red emissive carbon dots with dual targetability for imaging polarity in living cells. *Sens. Actuators B Chem.* 306, 127582. doi:10.1016/j.snb.2019.127582

Singh, S., Shauloff, N., Sharma, C. P., Shimoni, R., Arnusch, C. J., and Jelinek, R. (2021). Carbon dot-polymer nanoporous membrane for recyclable sunlight-sterilized facemasks. *J. Colloid Interface Sci.* 592, 342–348. doi:10.1016/j.jcis.2021.02.049

Soltani-Zangbar, M. S., Parhizkar, F., Abdollahi, M., Shomali, N., Aghebati-Maleki, L., Shahmohammadi Farid, S., et al. (2022). Immune system-related soluble mediators and COVID-19: basic mechanisms and clinical perspectives. *Cell Commun. Signal.* 20, 131. doi:10.1186/s12964-022-00948-7

Song, Y., Zhu, S., and Yang, B. (2014). Bioimaging based on fluorescent carbon dots. *RSC Adv.* 4, 27184. doi:10.1039/c3ra47994c

Soumya, K., More, N., Choppadandi, M., Aishwarya, D. A., Singh, G., and Kapusetti, G. (2023). A comprehensive review on carbon quantum dots as an effective photosensitizer and drug delivery system for cancer treatment. *Biomed. Technol.* 4, 11–20. doi:10.1016/j.bmt.2023.01.005

Sousa, H. B. A., Martins, C. S. M., and Prior, J. A. V. (2021). You don't learn that in school: an updated practical guide to carbon quantum dots. *Nanomaterials* 11, 611–688. doi:10.3390/nano11030611

Su, W., Wu, H., Xu, H., Zhang, Y., Li, Y., Li, X., et al. (2020). Carbon dots: a booming material for biomedical applications. *Mater Chem. Front.* 4, 821–836. doi:10.1039/c9qm00658c

Su, Y., Xie, M., Lu, X., Wei, H., Geng, H., Yang, Z., et al. (2014). Facile synthesis and photoelectric properties of carbon dots with upconversion fluorescence using arc-synthesized carbon by-products. *RSC Adv.* 4, 4839–4842. doi:10.1039/C3RA45453C

Sun, Y., Zheng, S., Liu, L., Kong, Y., Zhang, A., Xu, K., et al. (2020). The cost-effective preparation of green fluorescent carbon dots for bioimaging and enhanced intracellular drug delivery. *Nanoscale Res. Lett.* 15, 55. doi:10.1186/s11671-020-3288-0

Sun, Y.-P., Zhou, B., Lin, Y., Wang, W., Fernando, K. A. S., Pathak, P., et al. (2006). Quantum-sized carbon dots for bright and colorful photoluminescence. *J. Am. Chem. Soc.* 128, 7756–7757. doi:10.1021/ja062677d

Tacar, O., Sriamornsak, P., and Dass, C. R. (2013). Doxorubicin: an update on anticancer molecular action, toxicity and novel drug delivery systems. *J. Pharm. Pharmacol.* 65, 157–170. doi:10.1111/j.2042-7158.2012.01567.x

Tao, H., Yang, K., Ma, Z., Wan, J., Zhang, Y., Kang, Z., et al. (2012). *In vivo* NIR fluorescence imaging, biodistribution, and toxicology of photoluminescent carbon dots produced from carbon nanotubes and graphite. *Small* 8, 281–290. doi:10.1002/smll.201101706

NobelPrize.org. (2024). Nobel Prize Outreach AB. Available at: https://www.nobelprize.org/prizes/chemistry/2023/summary/.

Tian, X., Zeng, A., Liu, Z., Zheng, C., Wei, Y., Yang, P., et al. (2020). Carbon quantum dots: *in vitro* and *in vivo* studies on biocompatibility and biointeractions for optical imaging. *Int. J. Nanomedicine* 15, 6519–6529. doi:10.2147/IJN.S257645

Tiron, C. E., Luta, G., Butura, M., Zugun-Eloae, F., Stan, C. S., Coroaba, A., et al. (2020). NHF-derived carbon dots: prevalidation approach in breast cancer treatment. *Sci. Rep.* 10, 12662. doi:10.1038/s41598-020-69670-z

Tu, Y., Wang, S., Yuan, X., Wei, Y., Qin, K., Zhang, Q., et al. (2020). A novel fluorescent nitrogen, phosphorus-doped carbon dots derived from Ganoderma Lucidum for bioimaging and high selective two nitrophenols detection. *Dyes Pigments* 178, 108316. doi:10.1016/j.dyepig.2020.108316

Tummala, S., Lee, C. H., and Ho, Y. P. (2021). Boron, and nitrogen co-doped carbon dots as a multiplexing probe for sensing of p-nitrophenol, Fe (III), and temperature. *Nanotechnology* 32, 265502. doi:10.1088/1361-6528/abeeb6

Verma, A., Arshad, F., Ahmad, K., Goswami, U., Samanta, S. K., Sahoo, A. K., et al. (2020). Role of surface charge in enhancing antibacterial activity of fluorescent carbon dots. *Nanotechnology* 31, 095101. doi:10.1088/1361-6528/ab55b8

Wang, B., Cai, H., Waterhouse, G. I. N., Qu, X., Yang, B., and Lu, S. (2022). Carbon dots in bioimaging, biosensing and therapeutics: a comprehensive review. *Small Sci.* 2. doi:10.1002/smsc.202200012

Wang, L.-W., Peng, C.-W., Chen, C., and Li, Y. (2015). Quantum dots-based tissue and *in vivo* imaging in breast cancer researches: current status and future perspectives. *Breast Cancer Res. Treat.* 151, 7–17. doi:10.1007/s10549-015-3363-x

Wang, N., Zheng, A.-Q., Liu, X., Chen, J.-J., Yang, T., Chen, M.-L., et al. (2018). Deep eutectic solvent-assisted preparation of nitrogen/chloride-doped carbon dots for intracellular biological sensing and live cell imaging. *ACS Appl. Mater Interfaces* 10, 7901–7909. doi:10.1021/acsami.8b00947

Wang, Q., Liu, X., Zhang, L., and Lv, Y. (2012). Microwave-assisted synthesis of carbon nanodots through an eggshell membrane and their fluorescent application. *Analyst* 137, 5392–5397. doi:10.1039/c2an36059d

Wang, X., Gao, S., Xu, N., Xu, L., Chen, S., Mei, C., et al. (2021). Facile synthesis of phosphorus-nitrogen doped carbon quantum dots from cyanobacteria for bioimaging. *Can. J. Chem. Eng.* 99, 1926–1939. doi:10.1002/cjce.23927

Wang, Y., and Hu, A. (2014). Carbon quantum dots: synthesis, properties and applications. *J. Mater Chem. C Mater* 2, 6921. doi:10.1039/C4TC00988F

Wang, Y., Hu, A., Xu, X., Ray, R., Gu, Y., Ploehn, H. J., et al. (2014). Carbon quantum dots: synthesis, properties and applications. *J. Mater Chem. C Mater* 2, 6921. doi:10.1039/C4TC00988F

Wegner, K. D., and Hildebrandt, N. (2015). Quantum dots: bright and versatile *in vitro* and *in vivo* fluorescence imaging biosensors. *Chem. Soc. Rev.* 44, 4792–4834. doi:10.1039/C4CS00532E

Wei, Y., Chen, L., Wang, J., Liu, X., Yang, Y., and Yu, S. (2020). Rapid synthesis of B-N co-doped yellow emissive carbon quantum dots for cellular imaging. *Opt. Mater (Amst)* 100, 109647. doi:10.1016/j.optmat.2019.109647

Werbeck, N. D., Shukla, V. K., Kunze, M. B. A., Yalinca, H., Pritchard, R. B., Siemons, L., et al. (2020). A distal regulatory region of a class I human histone deacetylase. *Nat. Commun.* 11, 3841. doi:10.1038/s41467-020-17610-w

Wu, F., Su, H., Wang, K., Wong, W.-K., and Zhu, X. (2017). Facile synthesis of N-rich carbon quantum dots from porphyrins as efficient probes for bioimaging and biosensing in living cells. *Int. J. Nanomedicine* 12, 7375–7391. doi:10.2147/IJN.S147165

Wu, L.-N., Yang, Y.-J., Huang, L.-X., Zhong, Y., Chen, Y., Gao, Y.-R., et al. (2022). Levofloxacin-based carbon dots to enhance antibacterial activities and combat antibiotic resistance. *Carbon N. Y.* 186, 452–464. doi:10.1016/j.carbon.2021.10.020

Xia, J., Kawamura, Y., Suehiro, T., Chen, Y., and Sato, K. (2019). Carbon dots have antitumor action as monotherapy or combination therapy. *Drug Discov. Ther.* 13, 114–117. doi:10.5582/ddt.2019.01013

Xu, X., Ray, R., Gu, Y., Ploehn, H. J., Gearheart, L., Raker, K., et al. (2004). Electrophoretic analysis and purification of fluorescent single-walled carbon nanotube fragments. *J. Am. Chem. Soc.* 126, 12736–12737. doi:10.1021/ja040082h

Xue, B., Yang, Y., Sun, Y., Fan, J., Li, X., and Zhang, Z. (2019). Photoluminescent lignin hybridized carbon quantum dots composites for bioimaging applications. *Int. J. Biol. Macromol.* 122, 954–961. doi:10.1016/j.ijbiomac.2018.11.018

Xue, M., Zhan, Z., Zou, M., Zhang, L., and Zhao, S. (2016). Green synthesis of stable and biocompatible fluorescent carbon dots from peanut shells for multicolor living cell imaging. *New J. Chem.* 40, 1698–1703. doi:10.1039/C5NJ02181B

Xue, Y., Liu, C., Andrews, G., Wang, J., and Ge, Y. (2022). Recent advances in carbon quantum dots for virus detection, as well as inhibition and treatment of viral infection. *Nano Converg.* 9, 15. doi:10.1186/s40580-022-00307-9

Yadav, P. K., Chandra, S., Kumar, V., Kumar, D., and Hasan, S. H. (2023). Carbon quantum dots: synthesis, structure, properties, and catalytic applications for organic synthesis. *Catalysts* 13, 422. doi:10.3390/catal13020422

Yan, Z., Xiao, A., Lu, H., Liu, Z., and Chen, J. (2014). Determination of metronidazole by a flow-injection chemiluminescence method using ZnO-doped carbon quantum dots. *New Carbon Mater.* 29, 216–224. doi:10.1016/S1872-5805(14)60136-0

Yang, H.-L., Bai, L.-F., Geng, Z.-R., Chen, H., Xu, L.-T., Xie, Y.-C., et al. (2023). Carbon quantum dots: preparation, optical properties, and biomedical applications. *Mater Today Adv.* 18, 100376. doi:10.1016/j.mtadv.2023.100376

Yang, L., Wang, Z., Wang, J., Jiang, W., Jiang, X., Bai, Z., et al. (2016). Doxorubicin conjugated functionalizable carbon dots for nucleus targeted delivery and enhanced therapeutic efficacy. *Nanoscale* 8, 6801–6809. doi:10.1039/c6nr00247a

Yang, S. T., Cao, L., Luo, P. G., Lu, F., Wang, X., Wang, H., et al. (2009). Carbon dots for optical imaging *in vivo*. *J. Am. Chem. Soc.* 131, 11308–11309. doi:10.1021/ja904843x

Yang, Y., Wu, D., Han, S., Hu, P., and Liu, R. (2013). Bottom-up fabrication of photoluminescent carbon dots with uniform morphology via a soft–hard template approach. *Chem. Commun.* 49, 4920–4922. doi:10.1039/C3CC38815H

Yang, Z.-C., Li, X., and Wang, J. (2011). Intrinsically fluorescent nitrogen-containing carbon nanoparticles synthesized by a hydrothermal process. *Carbon N. Y.* 49, 5207–5212. doi:10.1016/j.carbon.2011.07.038

Yao, Y.-Y., Gangaraju, G., Girma, W., Yen, C.-L., Ling, Y., and Chang, J.-Y. (2017). Magnetofluorescent carbon dots derived from crab shell for targeted dual-modality bioimaging and drug delivery. *ACS Appl. Mater Interfaces* 9, 13887–13899. doi:10.1021/acsami.7b01599

Yin, J.-Y., Liu, H.-J., Jiang, S., Chen, Y., and Yao, Y. (2013). Hyperbranched polymer functionalized carbon dots with multistimuli-responsive property. *ACS Macro Lett.* 2, 1033–1037. doi:10.1021/mz400474v

Zhang, B., Liu, C., and Liu, Y. (2010). A novel one-step approach to synthesize fluorescent carbon nanoparticles. *Eur. J. Inorg. Chem.* 2010, 4411–4414. doi:10.1002/ejic.201000622

Zhang, F., Zhang, M., Zheng, X., Tao, S., Zhang, Z., Sun, M., et al. (2018). Berberine-based carbon dots for selective and safe cancer theranostics. *RSC Adv.* 8, 1168–1173. doi:10.1039/c7ra12069a

Zhang, H., Wang, G., Zhang, Z., Lei, J. H., Liu, T. M., Xing, G., et al. (2022). One step synthesis of efficient red emissive carbon dots and their bovine serum albumin composites with enhanced multi-photon fluorescence for *in vivo* bioimaging. *Light Sci. Appl.* 11, 113. doi:10.1038/s41377-022-00798-5

Zhang, R., and Chen, W. (2014). Nitrogen-doped carbon quantum dots: facile synthesis and application as a "turn-off" fluorescent probe for detection of Hg2+ ions. *Biosens. Bioelectron.* 55, 83–90. doi:10.1016/j.bios.2013.11.074

Zhao, A., Chen, Z., Zhao, C., Gao, N., Ren, J., and Qu, X. (2015). Recent advances in bioapplications of C-dots. *Carbon N. Y.* 85, 309–327. doi:10.1016/j.carbon.2014.12.045

Zhao, C., Wang, X., Wu, L., Wu, W., Zheng, Y., Lin, L., et al. (2019). Nitrogen-doped carbon quantum dots as an antimicrobial agent against Staphylococcus for the treatment of infected wounds. *Colloids Surf. B Biointerfaces* 179, 17–27. doi:10.1016/j.colsurfb.2019.03.042

Zhao, C., Wang, X., Yu, L., Wu, L., Hao, X., Liu, Q., et al. (2022). Quaternized carbon quantum dots with broad-spectrum antibacterial activity for the treatment of wounds infected with mixed bacteria. *Acta Biomater.* 138, 528–544. doi:10.1016/j.actbio.2021.11.010

Zhao, C., Wu, L., Wang, X., Weng, S., Ruan, Z., Liu, Q., et al. (2020). Quaternary ammonium carbon quantum dots as an antimicrobial agent against gram-positive bacteria for the treatment of MRSA-infected pneumonia in mice. *Carbon N. Y.* 163, 70–84. doi:10.1016/j.carbon.2020.03.009

Zhao, M.-X., and Zhu, B.-J. (2016). The research and applications of quantum dots as nano-carriers for targeted drug delivery and cancer therapy. *Nanoscale Res. Lett.* 11, 207. doi:10.1186/s11671-016-1394-9

Zheng, D. W., Li, B., Li, C. X., Fan, J. X., Lei, Q., Li, C., et al. (2016). Carbon-dot-decorated carbon nitride nanoparticles for enhanced photodynamic therapy against hypoxic tumor via water splitting. *ACS Nano* 10, 8715–8722. doi:10.1021/acsnano.6b04156

Zhou, J., Deng, W., Wang, Y., Cao, X., Chen, J., Wang, Q., et al. (2016). Cationic carbon quantum dots derived from alginate for gene delivery: one-step synthesis and cellular uptake. *Acta Biomater.* 42, 209–219. doi:10.1016/j.actbio.2016.06.021

Zhou, J., Sheng, Z., Han, H., Zou, M., and Li, C. (2012). Facile synthesis of fluorescent carbon dots using watermelon peel as a carbon source. *Mater Lett.* 66, 222–224. doi:10.1016/j.matlet.2011.08.081

Zhou, X., and Ye, Q. (2021). Cellular immune response to COVID-19 and potential immune modulators. *Front. Immunol.* 12, 646333. doi:10.3389/fimmu.2021.646333

Zhu, H., Wang, X., Li, Y., Wang, Z., and Yang, X. (2009). Microwave synthesis of fluorescent carbon nanoparticles with electrochemiluminescence properties. *Chem. Commun. (Camb)* 4, 5118–5120. doi:10.1039/b907612c

Zhu, P., Wang, S., Zhang, Y., Li, Y., Liu, Y., Li, W., et al. (2022). Carbon dots in biomedicine: a review. *ACS Appl. Bio Mater* 5, 2031–2045. doi:10.1021/acsabm.1c01215

Zhu, S., Meng, Q., Wang, L., Zhang, J., Song, Y., Jin, H., et al. (2013). Highly photoluminescent carbon dots for multicolor patterning, sensors, and bioimaging. *Angew. Chem. Int. Ed.* 52, 3953–3957. doi:10.1002/anie.201300519

Zhu, S., Song, Y., Zhao, X., Shao, J., Zhang, J., and Yang, B. (2015). The photoluminescence mechanism in carbon dots (graphene quantum dots, carbon nanodots, and polymer dots): current state and future perspective. *Nano Res.* 8, 355–381. doi:10.1007/s12274-014-0644-3

Zou, C., Foda, M. F., Tan, X., Shao, K., Wu, L., Lu, Z., et al. (2016). Carbon-dot and quantum-dot-coated dual-emission core–satellite silica nanoparticles for ratiometric intracellular Cu2+ imaging. *Anal. Chem.* 88, 7395–7403. doi:10.1021/acs.analchem.6b01941

Zuo, J., Jiang, T., Zhao, X., Xiong, X., Xiao, S., Zhu, Z., et al. (2015). Preparation and application of fluorescent carbon dots. *J. Nanomater* 2015, 1–13. doi:10.1155/2015/787862

Frontiers in
Bioengineering and Biotechnology

Accelerates the development of therapies, devices, and technologies to improve our lives

A multidisciplinary journal that accelerates the development of biological therapies, devices, processes and technologies to improve our lives by bridging the gap between discoveries and their application.

Discover the latest Research Topics

See more →

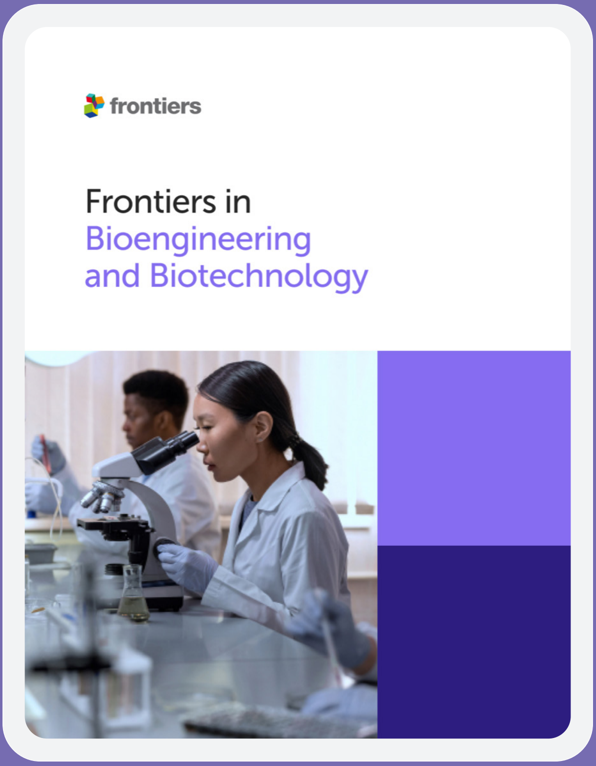

frontiers

Frontiers in
Bioengineering
and Biotechnology

Frontiers

Avenue du Tribunal-Fédéral 34
1005 Lausanne, Switzerland
frontiersin.org

Contact us

+41 (0)21 510 17 00
frontiersin.org/about/contact

frontiers | Research Topics